Damaged Goods: Regional deformation history and structural controls on the Hammond Reef gold deposit, Atikokan, Ontario

Nils Rainer Backeberg

Doctor of Philosophy

Department of Earth and Planetary Sciences

McGill University

Montreal,Quebec

2015-04-13

A thesis submitted to McGill University in partial fulfilment of the requirements of the degree of Doctor of Philosophy

Why “Damaged Goods”? Fluid flow through crustal-scale structures is known to be a major control on ore forming processes. But, it is mostly the fractured (damaged) wall-rocks immediately adjacent to these structures that see the richest metal endowments (goods). This is an important distinction to make when trying to understand the dynamics of fluid flow and looking for ore deposits relative to principal slip surfaces or parent structures.

“Earth has taken 4.6 billion years to shape itself into the way we see it today.
Geologists read the history embedded in the rocks and minerals
and share the story that Earth has to tell.”

My attempt at philosophy...

Nils Backeberg

ABSTRACT

Hammond Reef is a low-grade (< 1 g/t or 1 ppm Au), disseminated gold deposit located in an anastomosing deformation corridor along the western margin of the 3.0 Ga Marmion tonalite gneiss, adjacent to the Marmion Shear Zone. The Marmion Shear Zone separates the Marmion gneiss and Finlayson Lake greenstone belt of the Mesoarchean Wabigoon subprovince. Most known Archean gold deposits are hosted in greenstone belt terranes. This places Hammond Reef in an under-explored environment with respect to gold exploration targets and warrants a detailed understanding of the deposit to elucidate the deformation history of the two adjoined terranes and the events that led to the gold enrichment at Hammond Reef.

The deformation, intrusion and alteration events of the Finlayson Lake greenstone belt and Marmion gneiss cover over 200 million years, from the onset of deformation at 2.92 Ga to the youngest reactivation and fluid flow at around 2.70 Ga. The clockwise pressure–temperature pathway of the greenstone belt during deformation records deep subduction along a cool geothermal gradient ($\sim 20°$C/km), followed by underplating and exhumation. The Finlayson Lake greenstone belt docked with Marmion gneiss during exhumation. The emplacement of the Diversion Stock along the Marmion Shear Zone effectively locked the shear zone and sutured the Marmion gneiss and Finlayson Lake greenstone belt.

The anastomosing deformation corridor in the Marmion gneiss is defined by local foliation that strikes parallel to the Marmion Shear Zone. Cross-cutting structural,

alteration and intrusive relationships indicate that the anastomosing foliation developed after cessation of shear along the Marmion Shear Zone, during the exhumation of the sutured Marmion and Finlayson terrane. Flattening of sericite after altered feldspar was aligned parallel to the shear zone, which suggests that the anastomosing foliation developed in response to a shortening axis perpendicular to the shear zone. The deformation is kinematically correlated to the ~ 2.7 Ga Neoarchean tectonism and accretion of the Wabigoon subprovince to the Wawa subprovince. Therefore, alteration and mineralization along the Marmion Shear Zone and damage aureole occurred during the regional accretion of the Superior Province, even though the Hammond Reef gold deposit is located in a Mesoarchean terrane that experienced peak metamorphism and deformation up to 200 million years earlier.

Throughout the Superior Province, gold deposits are spatially associated with east-west-trending sutures of the ~ 2.7 Ga Neoarchean tectonism. Hammond Reef is located along the northeast-trending Marmion Shear Zone to the north of the Quetico Fault, which is one of these east-west structures. The Wabigoon subprovince was located in a supra-subduction zone setting associated with the northward-directed subduction of the Wawa subprovince. This setting allowed for subduction-related fluids to migrate up through the subvertical Marmion Shear Zone and damage aureole, which led to the alteration and gold mineralization at Hammond Reef along a dormant structure. Future exploration for gold deposits of similar style should include (steep) crustal-scale structures, suitable for reactivation and fluid migration above ancient subduction zones.

RÉSUMÉ

Hammond Reef est un gisement d'or disséminé à faible teneur (< 1 g/t ou 1 ppm Au) situé dans un couloir de déformation anastomosé le long de la bordure ouest du gneiss tonalitique de Marmion, daté à 3.0 Ga, adjacent à la zone de cisaillement de Marmion. Cette dernière sépare le gneiss de Marmion de la ceinture de roches vertes du lac Finlayson de la sous-province mésoarchéenne de Wabigoon. Étant donné que la plupart des gisements aurifères archéens connus se situent dans ceintures de roches vertes, le gisement de Hammond Reef se situe donc dans un environnement sous-exploré en ce qui concerne les cibles d'exploration aurifère. Une compréhension détaillée de ce gisement est donc nécessaire afin de faire la lumière sur l'historique de déformation de ces deux socles adjacents et sur les évènements qui ont mené à l'enrichissement en or à Hammond Reef.

Les divers évènements de déformation, d'intrusion et d'altération de la ceinture de roches vertes du lac Finlayson et du gneiss de Marmion s'étirent sur plus de 200 millions d'années, de la toute première déformation ductile à 2.92 Ga, jusqu'au dernier évènement de réactivation et de circulation de fluides vers 2.70 Ga. Le tracé pression-température rétrograde suivit par la ceinture de roches vertes durant la déformation reflète la subduction profonde de ces roches le long d'un gradient géothermique relativement faible ($\sim 20°C/km$), précédant leur sous-placage et leur exhumation. La ceinture de roches vertes du lac Finlayson s'est arrimée au gneiss de Marmion durant cette exhumation. La mise en place du Diversion Stock le long de la zone de cisaillement de Marmion a permis le verrouillage de cette dernière et a

soudé le gneiss de Marmion à la ceinture de roches vertes du lac Finlayson.

Dans le gneiss de Marmion, le couloir de déformation anastomosée se distingue par une foliation locale orientée parallèlement à la zone de cisaillement de Marmion. Les relations de recoupement entre les éléments structuraux, intrusifs et d'altération indiquent que la foliation localement présente dans le couloir de déformation anastomosée s'est développée après l'arrêt du jeu cisaillant le long de la zone de cisaillement de Marmion, et ce, durant l'exhumation des socles de Marmion et Finlayson fusionnés. La séricite remplaçant du feldspath altéré montre un aplatissement et un alignement parallèles à la zone de cisaillement, ce qui indiquerait que le réseau de foliation dans le couloir de déformation anastomosé s'est formé en réponse à des contraintes régionales caractérisées par un axe de raccourcissement perpendiculaire à la zone de cisaillement. La déformation montre une corrélation sur le plan cinématique avec la tectonique néoarchéenne à $\sim$ 2.7 Ga et l'accrétion de la sous-province de Wabigoon avec la sous-province de Wawa. L'altération et la minéralisation le long de la zone de cisaillement de Marmion et dans l'auréole de dommage se sont donc produites durant l'accrétion régionale de la province du Supérieur, et celà même si le gisement aurifère de Hammond Reef est situé dans un socle mésoarchéen dont le métamorphisme et la déformation ont culminé jusqu'à 200 millions d'années plus tôt.

Dans la province du Supérieur, les gisements aurifères sont spatialement associés aux sutures néoarchéennes orientées est-ouest daté à $\sim$ 2.7 Ga. Hammond Reef est situé le long de la zone de cisaillement de Marmion orientée vers le nord-est, au nord de la faille de Quetico, qui est l'une de ces structures d'orientation est-ouest. La sous-province de Wabigoon était située dans un milieu de supra-subduction associée

à la subduction vers le nord de la sous-province de Wawa. Ce milieu a permis la migration de fluides vers le haut à travers la zone de cisaillement de Marmion et son auréole de dommage, menant à l'altération et la minéralisation aurifère à Hammond Reef, le long d'une structure inactive. L'exploration future axée sur des gisements aurifères du même style devrait cibler des structures d'envergure crustale subverticales qui auraient pu se prêter à une réactivation et à la migration de fluides au-dessus d'anciennes zones de subduction.

CONTRIBUTION OF AUTHORS

Chapters 3, 4 and 5 in this thesis have been written for publication in peer-reviewed journals. Although each chapter contributes to the overall thesis document, the chapters have been presented as stand-alone articles. I am the main author and contributor of the research presented in each article. I have received fieldwork, advisory and editorial assistance in the completion of the research. Christie Rowe is a leading coauthor on all three articles as the project advisor, and her scientific input was crucial in the development of ideas presented throughout the thesis. The contributions of the other coauthors are described below.

Chapter 3 is published in the Journal of Precambrian Research (volume 249) as "Structural and metamorphic evidence for Mesoarchean subduction in the Finlayson Lake greenstone belt, Superior Province, Ontario". This article includes Christie D. Rowe, Vincent J. van Hinsberg and Eric J. Bellefroid as coauthors. Vincent J. van Hinsberg compiled the pseudosection and pressure-temperature constraints from the data I collected of the Finlayson Lake greenstone belt, which greatly strengthened the structural and metamorphic findings. He also provided editorial comments on the manuscript. Eric J. Bellefroid was my field assistant for fieldwork in the Finlayson Lake greenstone belt and provided editorial input for the preparation of the manuscript.

Chapter 4 is submitted to the Journal of Structural Geology as "No Shear Thing: Deformation adjacent to a dormant shear zone". This article includes Christie D.

Rowe and Naomi Barshi as coauthors. Naomi Barshi was my field assistant for fieldwork in the Marmion tonalite gneiss. She also collected additional amphibole and plagioclase pair mineral chemistries, from which she calculated the pressure-temperature constraints of peak metamorphism in the Marmion tonalite gneiss. Naomi provided detailed editorial assistance for the preparation of the manuscript.

Chapter 5 is in preparation for submission to either Lithos or Economic Geology as "Damaged Goods: Structural and tectonic setting of the Hammond Reef gold deposit, Ontario". This article has only been coauthored by Christie D. Rowe, with editorial assistance and scientific discussion.

ACKNOWLEDGEMENTS

This research was funded by Osisko Exploration Ltd. and the Natural Sciences and Engineering Research Council of Canada through a Collaborative Research and Development grant to Christie Rowe. Osisko provided extensive help with field logistics, access to field sites during operational exploration, as well as offered ongoing support throughout the study. A special thank you to Denver Stone, Robert Wares, Anne Charland, Denis Villeneuve, Zoran Madon, Mike Fell, Jami Brown and many other Osisko employees for their discussions and interest during the evolution of the project. Thank you to Boswell Wing and Alain Tremblay for the excellent reviews of the thesis and the suggestions they made that will definitely strengthen aspects towards publications.

I would like to thank Robert Borowski, Aeron Vaillancourt, Kristyn Rodzinyak, Ian Carvalho Campos, Eric Bellefroid and Naomi Barshi of McGill University for their field assistance, as well as further discussions about the development of the project. Thank you to Vincent van Hinsberg for great discussions on Archean tectonism and to Lang Shi for all the help he provided during electron microprobe analyses. Katarina Bjorkman, of the University of Western Australia, and her family in Sapawe were excellent contacts to have during field seasons, sharing their insight and local knowledge of the geology and gold showings. Thank you to Morgann Perrot and Robert Martin for corrections to the french abstract. My biggest thanks goes to Ben Melosh, co-founder of the Babalas Boys, with whom I started at McGill and have worked closely together with through each portion of the PhD study. We have

founded a strong friendship and collaboration inside and outside of geology. To all my newfound friends in Canada and family back home in South Africa, I owe a great thanks for the support they have shown during my stay in Montrèal. And finally, I thank Christie Rowe, a long-time friend, mentor and supervisor. She has been a great mentor during this PhD research. My move to Montréal to work on this exciting research project would not have been possible without her. Christie introduced me to structural geology in 2006 at the University of Cape Town in South Africa, where I was instantly drawn to the structural aspects of geology. Since then we have engaged in a nine-year-long learning curve in South African, Namibian and Canadian geology.

Figure 1: Christie Rowe and myself (Nils Backeberg) during our 2011 field season on the Finlayson Lake in Atikokan, Canada. Coffee close at hand.

TABLE OF CONTENTS

LIST OF TABLES

LIST OF FIGURES

Figure | page

CHAPTER 1
Introduction

1.1 Introduction

The Hammond Reef gold deposit is a low-grade, bulk-tonnage deposit that sits within 3.0 Ga Mesoarchean tonalite, trondhjemite and granodiorites (TTGs) that make up the Marmion gneiss, in the south-central Wabigoon subprovince, Canada. The deposit is hosted immediately adjacent to the Marmion Shear Zone (MSZ), which is a NE-striking structure that separates the Marmion gneiss from the Finlayson Lake greenstone belt. Hammond Reef is unusual among Archean gold deposits in that it is hosted in the TTGs, rather than in the adjacent greenstone belt. Therefore, gold mineralization at Hammond Reef is in a regionally under-explored terrane with respect to gold exploration targets. The Superior Province is well known for significant gold deposits associated with the period of amalgamation at 2.72 - 2.68 Ga, specifically in the greenstone-belt-dominated Abitibi subprovince (Robert *et al.*, 2005; Percival, 2007b). Gold in the Abitibi is found predominantly in quartz-carbonate-hosted vein networks (lode gold) situated along two major shear zones. These occurrences are consistent with the biased gold exploration targets in Archean terranes worldwide that focus on shear zones cutting greenstone belts (Groves *et al.*, 1989; Kerrich & Wyman, 1990; Goldfarb *et al.*, 2001). This model does not explain the occurrence of Hammond Reef (see Chapter 5 for details on gold deposit settings). In this thesis, I explore the structural evolution and deformation histories of the greenstone belt and

TTGs bounded by the Marmion Shear Zone in order to understand the timing and structural controls of gold mineralization at Hammond Reef.

1.2 Regional geological setting

The North American Superior Province exposes the world's largest Archean terrane. The Superior Province is made up of a series of Mesoarchean subprovinces (Figure 1–1) ranging in age from 3.4 Ga to 2.8 Ga (Percival, 2007a). The subprovinces amalgamated between 2.72 and 2.68 Ga during the Kenoran orogeny, which formed the mosaic of Archean terranes that make up the Superior Province (Gower & Clifford, 1981; Card, 1990; Cruden *et al.*, 1998; Tomlinson *et al.*, 2003; Percival, 2007a). Accretion of terranes occurred progressively from north to south with predominantly northward-directed subduction, preserved in northward-facing seismic reflectors (Calvert *et al.*, 1995; Whalen *et al.*, 2002; White *et al.*, 2003; Musacchio *et al.*, 2004). The subprovince boundaries are mapped as regional-scale east-west-trending sutures, or shear zones, that are traceable over large parts of the Superior Province (dashed lines in Figure 1–1). In this thesis, I focus on a single TTG-greenstone belt terrane of the south-central Wabigoon subprovince, located in the southwestern Superior Province (Figure 1–1). The Wabigoon subprovince accreted together with the North Caribou superterrane to the north (Thurston *et al.*, 1991), followed by the northward-directed subduction of the Wawa subprovince from the south (Calvert *et al.*, 1995). These continental and oceanic crustal terranes are separated by east-west-trending highly deformed metasedimentary terranes of the English River terrane to the north and Quetico terrane to the south (Figure 1–1), also referred to as subprovinces. The metasedimentary terranes have been interpreted as

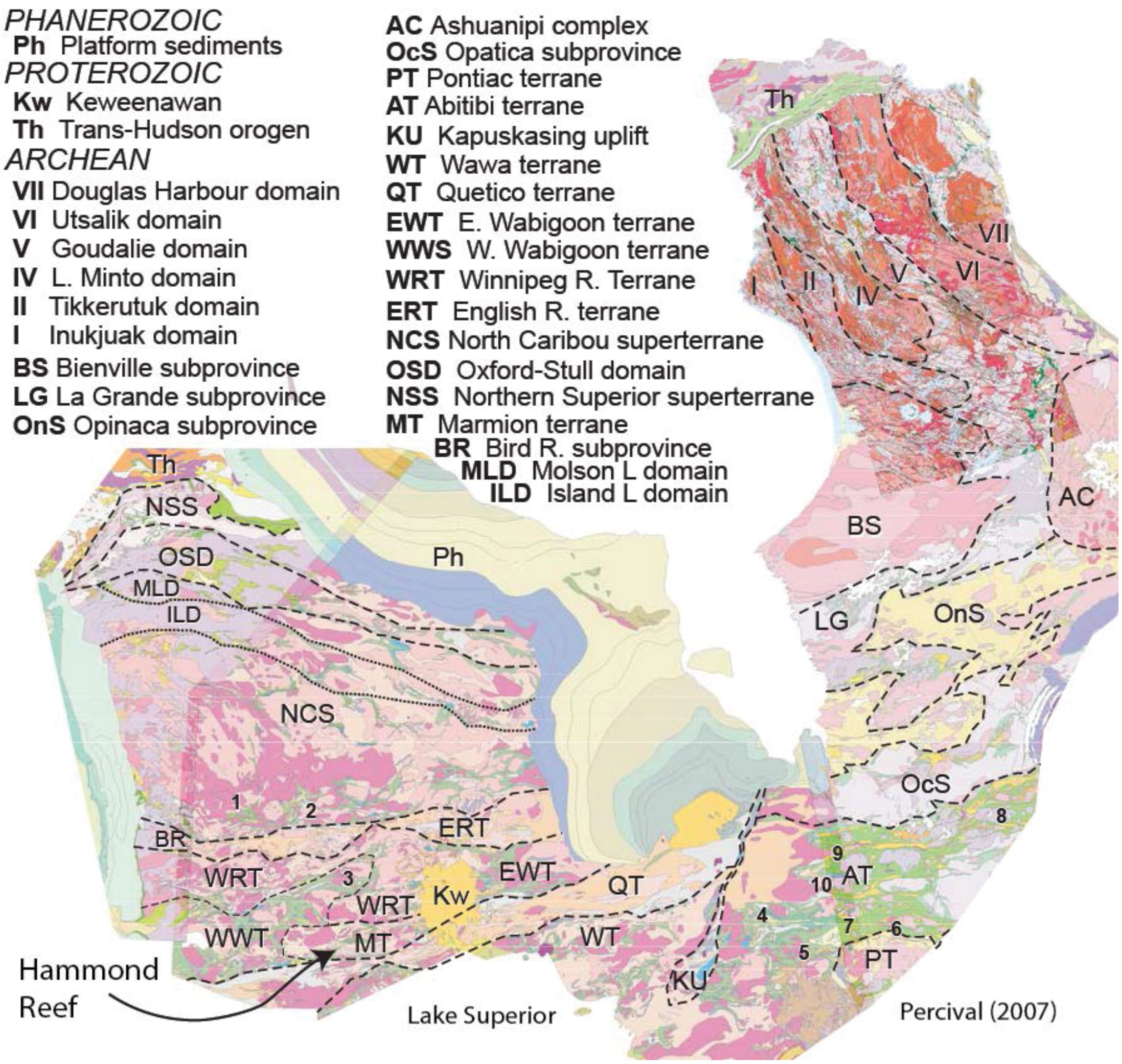

Figure 1–1: Geological map of the Superior Province (Percival, 2007b). Hammond Reef is located in the centre of the Marmion terrane (MT) of the southwestern Superior Province. The Wabigoon subprovince is made up of the Marmion terrane (MT), Winnipeg River terrane (WRT), Western Wabigoon terrane (WWT) and Eastern Wabigoon terrane (EWT).

synorogenic deposits in wedge, fore-arc or back-arc sedimentary basins of an accretionary tectonic setting (Langford & Morin, 1976; Percival & Williams, 1989; Breaks, 1991; Valli *et al.*, 2004).

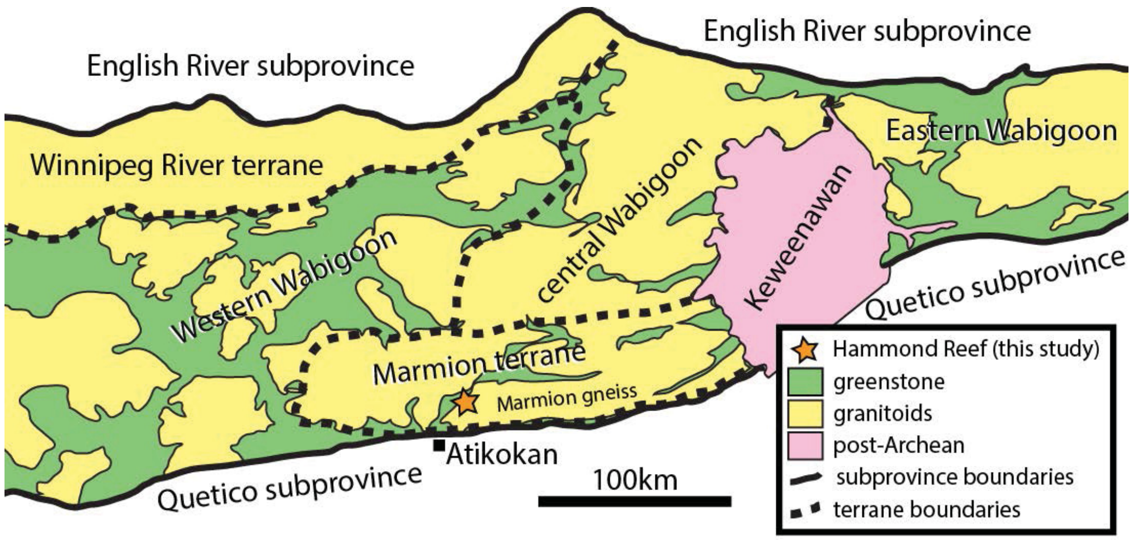

Figure 1–2: Simplified granite-greenstone geology of the Wabigoon subprovince showing terrane boundaries derived from Tomlinson *et al.* (2004) and Percival (2007b). Percival (2007b) included the central Wabigoon terrane as part of the Winnipeg River terrane (Figure 1–1). The Hammond Reef location (this study) is shown by the star in the centre of Marmion terrane, north of the town of Atikokan.

The Wabigoon subprovince represents a Mesoarchean crustal block bounded to the north and south by two east-west-tending terrane boundaries. It is located in the southwestern Superior Province (Figure 1–1). Originally, the subdivisions of the Wabigoon subprovince were based on the prevalence of either plutonic or volcanic rocks (Davis & Jackson, 1988). Regional studies have further subdivided the crustal block into the Marmion, Winnipeg River, eastern Wabigoon, central Wabigoon and western Wabigoon terranes (Figure 1–2) using available U-Pb ages and Nd isotope model ages (Tomlinson *et al.*, 2003). The tectonic evolution of these terranes to form the Wabigoon subprovince is described by the amalgamation of the Marmion, central Wabigoon and Winnipeg River terranes at around 2.92 Ga, followed by the accretion of the western Wabigoon subprovince prior to 2.72 Ga (Tomlinson *et al.*, 2003; Percival & Helmstaedt, 2004; Tomlinson *et al.*, 2004; Percival, 2007a). The Marmion terrane is dominated by TTGs with only a few thin slivers of greenstone belts (Figure 1–2) and is defined by juvenile Mesoarchean magmatism at 3.0 Ga, similar in age and isotope geochemistry to crustal rocks found in the North Caribou terrane to the north (Davis & Jackson, 1988; Tomlinson *et al.*, 2003, 2004). The isotopic signature of the Neoarchean western Wabigoon terrane records juvenile magmatism. The terrane is made up of a high proportion of mafic volcanics (Blackburn *et al.*, 1991; Tomlinson *et al.*, 2003). The Mesoarchean central Wabigoon and Winnipeg River terranes have isotopic signatures that suggest a recycled origin from older 3.4 Ga crustal rocks (Tomlinson *et al.*, 2003; Percival, 2007a). The outline of the Marmion terrane, taken from Tomlinson et al. (2003), is shown in Figure 1–2. However, the literature is vague on exactly which crustal rocks are included in the Marmion terrane. Interpretations for the origin and tectonic assemblage of the Marmion terrane only refer to the 3.0 Ga Marmion tonalite gneiss, also referred to the Marmion batholith (Davis & Jackson, 1988; Tomlinson *et al.*, 2003, 2004; Percival *et al.*, 2006; Percival, 2007a). The Marmion gneiss, however, only occupies one quarter of the proposed Marmion terrane (Figure 1–2). Other TTGs within the proposed Marmion terrane include the Mesoarchean 2.93 Ga Dashwa gneiss and 2.94 Ga Hardtack gneiss, amongst others. The ages of these gneisses contradict the proposed constraints made for the Marmion terrane. No detailed studies of the Dashwa and Hardtack gneisses have been published, which would clarify the associations. In this thesis, I focus on the western edge of the Marmion gneiss and the Finlayson Lake greenstone belt to the west. In order to avoid ambiguity, the term "Marmion terrane" is not used in this thesis. The implications of this study for these predefined terrane boundaries are discussed briefly in the final synthesis and conclusions chapter.

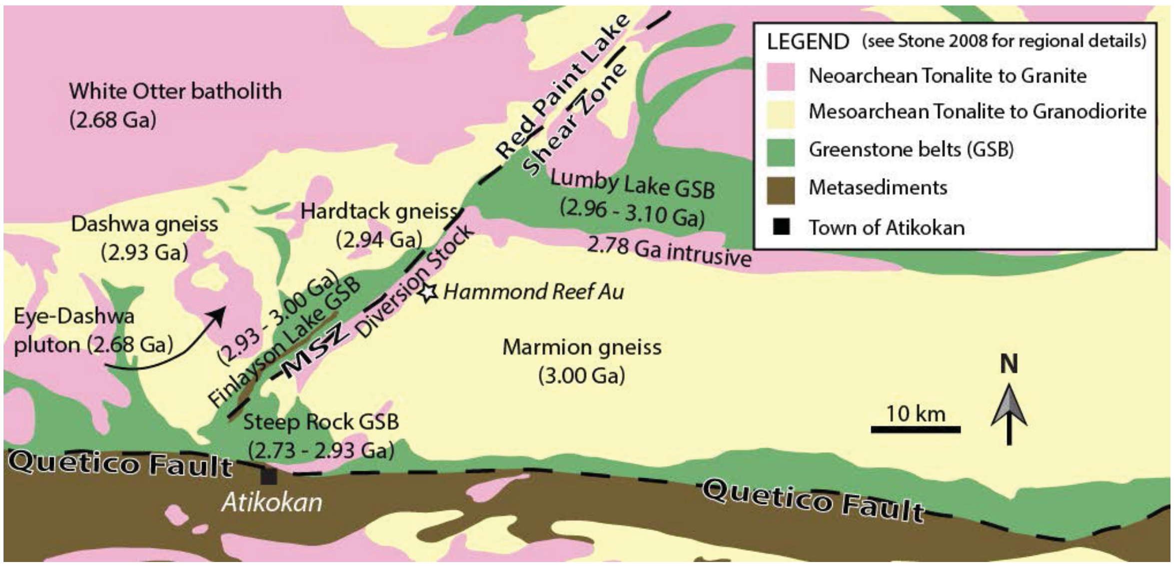

Figure 1–3: Simplified geology showing the distribution of greenstone belts within the TTG-dominated crustal block of the south-central Wabigoon subprovince. The location of the Hammond Reef gold deposit is shown (white star). The Marmion Shear Zone (MSZ), Red Paint Lake Shear Zone and Quetico Fault are shown by dashed lines. Ages and geological outlines of terranes taken from Stone (2008a).

Hammond Reef is located on the western margin of the Marmion gneiss (Figure 1–3). The Marmion gneiss forms an east-west elongate belt over 100 km long (Figure 1–2), and is dated at $\sim$ 3.00 Ga (Davis & Jackson, 1988; Tomlinson *et al.*, 2003). The 2.93 – 3.00 Ga Finlayson Lake greenstone belt separates the Marmion gneiss from the 2.93 Ga Dashwa gneiss and 2.94 Ga Hardtack gneiss (Figure 1–3). The Marmion Shear Zone (MSZ) marks the boundary between the Finlayson Lake greenstone belt and the Marmion gneiss, as the southwestern continuation of the Red Paint Lake Shear Zone (Figure 1–3). The 2.96 – 3.10 Ga Lumby Lake greenstone belt runs along the northern margin of the Marmion gneiss. A younger intrusive, the Diversion Stock, rims the western and northern margin of the Marmion gneiss (Figure 1–3). Samples of the Diversion Stock taken south of Lumby Lake are dated at $\sim$ 2.78 Ga (Buse *et al.*, 2010a). Other Neoarchean intrusions such as the Eye-Dashwa pluton and the White Otter batholith are dated at approximately 2.68 Ga (Stone, 2008a). The Wabigoon subprovince is cut off to the south by the Quetico Fault, which is inferred to have been active at around 2.7 Ga during the accretion of the Superior Province (Corfu & Stott, 1986; Percival & Williams, 1989; Williams, 1990; Bauer *et al.*, 1992; Peterson & Zaleski, 1999). The Quetico Fault separates the metasedimentary Quetico subprovince to the south from the Wabigoon subprovince (Figure 1–2).

1.3 Archean granite-greenstone terranes

The oldest exposed rocks exist within Archean terranes and they have sparked much interest and scientific insight into the chemical and physical processes that existed during early Earth. Archean terranes have a characteristic geometry of narrow belts of supracrustal metabasalt and metasediments pinched between large volumes of crustal tonalite-trondhjemite-granodiorite (TTG) gneisses, also known as granite-greenstone or dome-and-keel terranes (Anhaeusser *et al.*, 1969; Marshak *et al.*, 1992; Kusky & Vearncombe, 1997). The tectonic origin of granite-greenstone terranes is the subject of an ongoing debate, broadly defined by which crustal dynamic process was operating during the hotter Archean earth. Modelling of the melting of komatiites and basalts from greenstone belts suggest that the potential temperature of the mantle during the Archean was approximately 200°C hotter than at present (Nisbet *et al.*, 1993; Labrosse & Jaupart, 2007; Herzberg *et al.*, 2010). The present-day conditions are characterized by plate tectonic geodynamics thought to be driven primarily by slab-pull forces of the subducting lithosphere coupled to the dynamics of mantle convection (Forsyth & Uyeda, 1975; Spence, 1987; Conrad & Lithgow-Bertelloni, 2002; Bercovici, 2003). A higher potential temperature in the mantle results in thicker oceanic plates (crust and depleted lithospheric mantle) due to deeper partial melting (Sleep & Windley, 1982; Vlaar *et al.*, 1994; Van Thienen *et al.*, 2004; van Hunen & Moyen, 2012; Hynes, 2013). The integrated density of oceanic plates at mid-ocean ridges is less dense than the underlying undepleted mantle (positively buoyant), and the density increased with age during thermal cooling of the plate, eventually becoming negatively buoyant (Davies, 1992; Crosby *et al.*, 2006; Hynes, 2013). Hotter, thicker lithospheres have an older neutral buoyancy age and are thought to be more difficult to force down (subduct) into the mantle (Davies, 1992; Vlaar *et al.*, 1994). Therefore, delamination or shallowly dipping subduction zones may have played a more important role in recycling of Archean oceanic crust (Abbott *et al.*, 1994; Foley *et al.*, 2003; Johnson *et al.*, 2014). Recent studies have shown that the physicochemical properties of Archean oceanic plates allow for slab-pull forces in thicker subducted slabs to operate efficiently in a hotter Archean environment, once subduction is initiated (van Hunen & Moyen, 2012; Hynes, 2013). Subduction systems also did not have to be shallow. Numerical models show that steep subduction zones were possible, but owing to the hotter temperatures and inherently weaker strength of the subducted slab, break-off becomes more frequent, resulting in shorter lived, more episodic subduction systems (van Hunen *et al.*, 2008; van Hunen & Moyen, 2012). However, it has mainly been the lack of preserved accretionary wedges, ophiolites, fore-arcs, magmatic arcs and back-arcs in Archean terranes that have been used to argue against subduction in the Archean (Hamilton, 1998; Stern, 2005). Large wedges are characteristic of long-lived and large-scale subduction boundaries in the Phanerozoic (e.g. Reimold & Gibson, 2006; Cawood *et al.*, 2009).

There are researchers that interpret the structural architecture of Archean granite-greenstone terranes based solely on "drifting" plates or microplates in subduction-accretion tectonic settings (Sleep & Windley, 1982; Card, 1990; Schwerdtner, 1990; Kusky & Vearncombe, 1997; de Wit, 1998; Polat *et al.*, 1998; Percival *et al.*, 2004). Alternative proposals for the formation of the dome-and-keel geometry in Archean terranes include gravity-driven vertical tectonics or extensional core complexes (e.g. Marshak *et al.*, 1997). Vertical tectonism is a density-driven process modelled from an originally layered sequence of a thick mafic volcanics package (dense) overlying a deeper, hotter and less dense TTG basement (buoyant) (e.g. Thébaud & Rey, 2013). Tectonic overturn in this model is accommodated by solid-state diapirism, forming granitoid domes and "sagduction" of greenstone belts into synclinal keels (Fyson, 1978; Schwerdtner, 1982; Bloem *et al.*, 1997; Robin & Bailey, 2009). Diapirism remains a strong contender for explaining many of the classical dome-and-keel domains in Archean terranes globally (Fyson, 1978; Ramberg, 1981; Schwerdtner, 1984; Collins, 1989; Minnett & Anhaeusser, 1992; Chardon *et al.*, 1998; Van Kranendonk *et al.*, 2002; Thébaud & Rey, 2013). Extensional core-complex models have also been argued to explain the dome-and-keel geometries in Archean terranes (James & Mortensen, 1992; Marshak *et al.*, 1992, 1997; Marshak, 1999; Zegers *et al.*, 2001; Lana *et al.*, 2010). Core complexes develop by the exhumation of deep crustal rocks beneath detachment faults, driven by extension (Holm & Lux, 1996; Marshak, 1999; Fayon *et al.*, 2004; Yin, 2004; Whitney *et al.*, 2013). The dome shape of crustal gneisses is often associated with the upward arching of a detachment fault during the assent of the hot buoyant crust and is flanked by supracrustal rocks with low, greenschist-facies metamorphic grades (Lister & Baldwin, 1993; Martínez-Martínez *et al.*, 2002; Fayon *et al.*, 2004; Whitney *et al.*, 2013).

No consensus has been reached yet on the mechanisms that led to the final geometries observed for individual granite-greenstone terranes. In many field study cases, structural observations and geochemical data have been used to support both vertical and horizontal tectonic settings for a given terrane, such as the Warawoona greenstone belt in the Pilbara (Collins *et al.*, 1998; Kloppenburg *et al.*, 2001) and the Barberton greenstone belt in the Kaapvaal (de Wit, 1991; Kisters *et al.*, 2003; Van Kranendonk, 2011). The emergence of detailed structural studies of Archean shear zones shows that simultaneous vertical and horizontal kinematics were recorded in polydeformed granite-greenstone terranes (Peterson & Zaleski, 1999; Polat & Kerrich, 1999; Kloppenburg *et al.*, 2001; Lin, 2005; Lin *et al.*, 2005; Kerrich & Polat, 2006; Lin & Beakhouse, 2013). Oblique kinematics in shear zones throughout Earth history is well documented (e.g. White *et al.*, 1980; Jones & Tanner, 1995; Lin *et al.*, 1998). Furthermore, numerical models of Archean tectonic processes suggest that diapirism or core complexes do not necessarily preclude plate-tectonic settings and that these mechanisms can occur simultaneously (diapirs during accretion: Bloem *et al.*, 1997; Rey *et al.*, 2003; Thébaud & Rey, 2013) (core complexes during accretion: Riller *et al.*, 1999; Soula *et al.*, 2001; Whitney *et al.*, 2013). Therefore the discussion about Archean tectonic processes has shifted towards the timing of subduction-accretion plate tectonics as the dominant tectonic process during the evolution of Earth's crust (Ernst, 2009; Van Kranendonk, 2011). Some evidence from synchronous vertical and horizontal kinematics shows that the Mesoarchean Era may be that turning point (Lin, 2005; Lin & Beakhouse, 2013). Most researchers agree that plate tectonics was active during the Neoarchean, and it is widely accepted that the Superior Province amalgamated at $\sim$ 2.7 Ga from the individual subprovinces by accretionary tectonics (Calvert *et al.*, 1995; Whalen *et al.*, 2002; White *et al.*, 2003; Musacchio *et al.*, 2004). A study of inclusions in diamond shows that eclogitic inclusions only appear in diamond younger than 3.0 Ga (Shirey & Richardson, 2011). This suggests that hydrated basaltic oceanic crust was transported to depths and introduced into the subcontinental lithospheric mantle, either by subduction or delamination (Shirey & Richardson, 2011; Van Kranendonk, 2011). Delamination is thought to have occurred throughout Earth history, including the Archean (Zegers & van Keken, 2001; Foley *et al.*, 2003); therefore, the sudden onset of eclogitic inclusions in diamond is thought to be a strong indicator of effective subduction systems (Shirey & Richardson, 2011; Van Kranendonk, 2011).

In this thesis, I do not argue for the prevalence of a specific mechanism of global tectonic processes during early Earth. Rather, I focus on direct field and structural observations, combined with metamorphic assemblages and geochemical signatures, from which the deformation histories of the Mesoarchean Finlayson Lake greenstone belt and adjoining Marmion tonalite gneiss are defined. The structural architecture and deformation histories of these terranes can then be tested against various tectonic processes to argue whether diapirism, subduction or extensional metamorphic core complex models better explain the observations for this study area.

CHAPTER 2
Thesis Organization and Methods

This thesis has been prepared as three alone-standing articles that each contribute to the research goals. Each chapter has been reformatted from its published (or submitted) version into a coherent thesis formatting and numbering. The final chapter of the thesis provides a synthesis of the three articles and an overall conclusion, summarizing the results and implications that have arisen from the findings of this research project. In this chapter, I present the methods, outline, focus and contribution of each chapter within the scope of the overall thesis.

2.1 Chapter 3 – Finlayson Lake greenstone belt

The thesis begins with the research focused on the Finlayson Lake greenstone belt. In contrast to the adjacent Marmion tonalite gneiss, the mafic volcanics have paleo-horizontal surfaces that allow for clearer identification of cross-cutting structural relationships. Data collection is primarily based on field mapping and sampling. This study focuses on detailed structural mapping along transects that run perpendicular to the regional structural fabric. Field data includes lithological paleo way-up orientations (pillow basalts and sediments), strike and dip measurements of foliation and faults, detailed descriptions of field observations and sampling. Structural data were compiled into stereonets for visualisation and kinematic interpretations. All samples were cut and sent for thin section preparation at *Quality Thin Sections*. Thin sections were used for detailed petrographic and microstructural descriptions.

Thin sections were mounted onto a stage for spot mineral analyses measured with the electron microprobe at McGill University under the supervision of Lang Shi. The data from the electron microprobe included a suite of chlorite analyses from across the greenstone belt (Appendix A) and amphibole and plagioclase mineral pairs in the least altered samples for pressure-temperature calculations (data presented in Chapter 3). Selected fresh basalt samples were cleaned by removing the alteration rinds and sent to *Activation Laboratories Ltd*, where the samples were prepared for major and trace element analyses by Inductively Coupled Plasma - Mass Spectrometry (ICP-MS).

The main contributions of this chapter towards the thesis are the deformation history of the greenstone belt and metamorphic constraints on the tectonic setting during deformation. Furthermore, the structural results show a kinematic link to the 2.7 Ga tectonism of the Superior Province during the youngest observed deformation events. Structures in the greenstone belt highlight the cross-cutting relationships of the ductile deformation history of the terrane and set up the framework for the deformation fabrics observed in the adjacent Marmion tonalite gneiss and at Hammond Reef. In this chapter, we also discuss the contributions that can be made by detailed structural and metamorphic studies of greenstone belts, in order to identify the tectonic processes during the Archean that led to the unique geometry of granite-greenstone terranes.

2.2 Chapter 4 – Marmion tonalite gneiss

The Marmion tonalite gneiss was juxtaposed with the Finlayson Lake greenstone belt along the Marmion Shear Zone. The Hammond Reef gold deposit is hosted within an anastomosing deformation corridor within the tonalites that runs parallel to the shear zone. This chapter focuses on the structural fabrics in the tonalites in order to place the deformation history into the regional context established from the adjacent greenstone belt. Methods focused on detailed structural field mapping in order to complement the regional mapping by Stone (2008a,b), who mapped the anastomosing deformation corridor. Field mapping included detailed descriptions of structural fabrics and cross-cutting relationships in the tonalites, strike and dip measurements of foliated tonalites and faults, sampling and detailed descriptions of field observations and drill-core made available through exploration activities. Structural data were compiled into stereonets for visualisation and kinematic interpretations. All samples were cut and sent for thin section preparation at *Quality Thin Sections*. Thin sections were used for detailed petrographic and microstructural descriptions of the tonalites. Spot chemical analyses of plagioclase and amphibole pairs were collected on the election microprobe at McGill University under the supervision of Lang Shi. The composition of amphibole and plagioclase mineral pairs in the least altered tonalites east of the Lynx Head Fault was used for pressure-temperature calculations.

This chapter links the deformation history of the Marmion gneiss to that of the Finlayson Lake greenstone belt from kinematically consistent deformation events in both terranes. The intrusive, structural and alteration cross-cutting relationships contribute to a detailed deformation timeline in the tonalites that is consistent with the results from the Finlayson Lake greenstone belt. The results in the Marmion gneiss expand on the details of the cross-cutting relationships of the younger, brittle deformation history, which was not observed in the Finlayson Lake greenstone belt.

These results confirm interpretations of the late-stage deformation within the regional context of the 2.7 Ga Superior Province. In this chapter, I also contributes to the broader understanding of fluid flow and alteration in damage aureoles around faults. The resulting article is the first to provide a detailed description and interpretation of distributed deformation adjacent to a dormant shear zone.

2.3 Chapter 5 – Hammond Reef gold deposit

The main objective of this research project is to understand the structural controls that led to disseminated gold mineralization in the Marmion tonalites at Hammond Reef. In this chapter, I look at the alteration assemblages at Hammond Reef and place the timing and structural context into the regional deformation history provided in the previous two chapters. Structural data and observations were collected for veins and foliated tonalites to complement the structural data collected regionally in the Marmion gneiss. Samples were collected from fresh surface exposures and drill-core made available from exploration activities and include fresh, unaltered tonalites and various alteration assemblages and alteration intensities observed within and outside of the Hammond Reef gold mineralization. Samples were cut into blocks for preparation for thin sections and bulk-rock geochemistry. Thin sections were prepared commercially for all the samples by *Quality Thin Sections* and used for detailed petrographic and structural descriptions. Bulk-rock geochemical analyses by Inductively Coupled Plasma - Mass Spectrometry (ICP-MS) including Aqua Regia digestion for metal contents were processed commercially, through *Acme Analytical Laboratories (Vancouver) Ltd*, for 39 samples covering the range in alteration assemblages and rock types (Appendix B).

The geochemical data were plotted to illustrate geochemical differences that can be used as a geological signature in identifying rock types (Diversion Stock and Marmion gneiss samples). The alteration assemblages localized at Hammond are documented and contrasted against the regional alteration observed within the anastomosing deformation corridor described in the previous chapter. Results for the timing of mineralization led to the classification of the Hammond Reef gold deposit within the 2.7 Ga regional tectonic setting of the Superior Province. This chapter highlights the ambiguity associated with classifying gold deposits globally based on published classification criteria. The results show the importance of understanding the regional deformation history in order to correctly interpret the structural and local controls of mineralization.

CHAPTER 3
Deformation History of the Finlayson Lake Greenstone Belt

This Chapter focuses on the Finlayson Lake greenstone belt and is published in the Journal of Precambrian Research as *"Structural and metamorphic evidence for Mesoarchean subduction in the Finlayson Lake greenstone belt, Superior Province, Ontario"*. The abstract is as follows:

The unique structural architecture of Archean terranes has generated competing models for early Earth tectonics. Understanding the structural and metamorphic history of an individual terrane allows us to compare the deformation path to that predicted by tectonic models, and determine the best model for matching field observations. The Finlayson Lake greenstone belt is a Mesoarchean terrane lying between three different gneiss terranes in the south-central Wabigoon subprovince in Canada. The belt has been interpreted as either a synformal keel sagducted between rising gneiss diapirs or as three fault-bounded allochthonous sub-belts of different ages. We present a detailed structural field study to define the deformation history of the Finlayson Lake greenstone belt and show that it is not consistent with either previous hypothesis. The Finlayson Lake greenstone belt is a single volcanic package that incorporates detritus from exposed felsic terranes similar in age and composition to the adjacent 3.0 Ga Marmion tonalites. The geometry of the greenstone belt is defined by two outward-facing paleo way-up orientations (anticlinal) and geothermobarometry records a clockwise metamorphic path with a deep prograde event at 820 ± 40

MPa (27-30 km) and 600 ± 45°C, followed by peak metamorphism at 635 ± 165 MPa (21-23 km) and 625 ± 25°C. The deformation history records sinistral transpression during peak metamorphism and continued flattening during retrogression and exhumation from ductile to brittle regimes. The structural and metamorphic results are comparable with modern subduction-accretion style settings. The intensity of both retrogressive and brittle deformation fabrics during exhumation decrease from east to west away from the eastern boundary shear zone, the Marmion Shear Zone. Stronger deformation along the eastern margin of the Finlayson Lake greenstone belt, adjacent to the Marmion Shear Zone, suggest reactivation during exhumation and is likely related to the 2.7 Ga amalgamation of the Superior Province.

3.1 Introduction

The fundamental architecture of Archean continental fragments worldwide is geometrically distinct from Proterozoic and Phanerozoic terranes, leading to various hypotheses for the processes of tectonics during this early part of Earth's history. In Archean terranes, narrow belts of mafic volcanics, intrusives and sediments, usually metamorphosed at greenschist or low-amphibolite facies, are pinched between equant or elliptical domes of tonalite, trondhjemite, and granodiorite gneisses (TTGs), collectively known as TTG-greenstone terranes (Anhaeusser *et al.*, 1969; Marshak *et al.*, 1992; Percival & Helmstaedt, 2004; Percival, 2007a). Archean tectonics and crustal deformation have been addressed by various authors, generating a long-standing debate on when subduction-dominated tectonics took over from vertical diapiric tectonics (Fyson, 1978; Collins, 1989; Schwerdtner, 1990; Lin *et al.*, 1996; Chardon *et al.*, 1998; de Wit, 1998; Hamilton, 1998; Zegers & van Keken, 2001; Van Kranendonk *et al.*, 2004; van Hunen *et al.*, 2008; Kusky *et al.*, 2014). Geometrically different interpretations of the inter-TTG greenstone belts support the different tectonic models, either accretionary terranes from collision-style tectonics (Sleep & Windley, 1982; Card, 1990; Calvert *et al.*, 1995; Kusky & Vearncombe, 1997; Polat *et al.*, 1998; Percival *et al.*, 2004) or as synformal keels sinking or "sagducting" between rising TTG gneiss diapirs (Schwerdtner, 1984; Minnett & Anhaeusser, 1992; Robin & Bailey, 2009). The kinematic signature and deformation history of exposed greenstone belts and adjacent TTG domes should allow us to test these tectonic settings for a given Archean terrane, by interpreting belt-scale architectures from detailed structural studies. The strongest observational evidence for synformal greenstone belts as a result of sagduction during diapiric tectonics comes from structural studies in the Australian Pilbara craton, which show strong flattening fabrics parallel to the greenstone belt margins and steep stretching lineations in the centre of the belt (Collins & Teyssier, 1990; Collins *et al.*, 1998). This architectural model has been adopted for parts of the Superior Province in Canada without the same level of detailed kinematics from greenstone belt field studies.

Thorough kinematic studies on Superior Province Archean terranes are rare (Borradaile & Schwerdtner, 1984; Lin *et al.*, 1996; Polat & Kerrich, 1999; Lin, 2005; Parmenter *et al.*, 2006). Our contribution focuses on the Mesoarchean Finlayson Lake greenstone belt (hereafter referred to as the Finlayson belt), which was deposited over a period of at least 70 million years between 2.93 Ga and 3.00 Ga (Davis & Jackson, 1988; Tomlinson *et al.*, 1999, 2003; Stone, 2010). The Finlayson belt is located in the Marmion terrane of the south-central Wabigoon subprovince of Superior Province

(Percival, 2007b). Three TTG gneiss domes of similar ages border the Finlayson belt: the 3.00 Ga Marmion gneiss; the 2.93 Ga Dashwa gneiss; and the 2.94 Ga Hardtack gneiss (Fig. 3–1a) (Stone, 2008a). The lithologies of the Finlayson belt are dominated by basaltic lava flows, pillow basalts and include finely laminated clastic and chemical sediments, siltstones and graded sandstones with minor conglomerates (Stone, 2008a, 2010). All depositional contacts are tilted to sub-vertical and strike approximately northeast, parallel to the eastern boundary with the Marmion gneiss, defining the dominant structural fabric.

Two contrasting models have been suggested for the tectonic development of the Finlayson belt. Fold axes were inferred from stratigraphic reversals and the Finlayson belt was interpreted as a sagducted synclinal keel (Stone & Kamineni, 1989; Stone *et al.*, 1992). Alternatively, Stone (2008a, 2010) interpreted three fault-bounded allochthonous sub-belts based on the two different measured ages and a third younger age inferred from petrographic similarities to the younger Steep Rock greenstone belt to the south. Due to the lateral heterogeneity of units and lack of marker horizons, lithologic mapping of the Finlayson belt has not resulted in an equivocal structural model. However, a detailed structural and kinematic study of the greenstone belt allows us to test the validity of either hypothesis and explore implications for the regional deformation history of the south-central Wabigoon subprovince. We visited lake-shore exposures throughout the belt and conducted detailed structural mapping (Fig. 3–1). We have produced a structural framework and metamorphic-deformational history that is wholly based on field data and observations. In this paper we compare this framework to the predictions of the competing tectonic models, and place the local deformational history in regional context.

3.2 Geological setting

The Superior Province in Canada preserves one of the largest assemblages of Meso- to Neoarchean terranes. The individual terranes that make up the Superior Province amalgamated progressively from north to south within the 2.72 - 2.68 Ga tectonism known as the Kenoran orogeny (Polat & Kerrich, 2001; Percival *et al.*, 2006; Percival, 2007a), at which time most workers agree that some form of accretionary tectonics was active. Northward dipping fabrics associated with the east-west trending terrane boundaries have been interpreted as northward directed subduction zones active during the accretion period (Calvert *et al.*, 1995; Whalen *et al.*, 2002; White *et al.*, 2003; Musacchio *et al.*, 2004). The Wabigoon subprovince is bounded to the south by the Quetico terrane metasediments, which separate the TTG-greenstone terranes of the Wabigoon and Wawa subprovinces (Percival, 1989; Percival & Williams, 1989; Percival, 2007a). The east-west trending southern margin of the Wabigoon subprovince has been interpreted as a fault with dextral transpression (Williams, 1990; Bauer *et al.*, 1992; Peterson & Zaleski, 1999), known as the Quetico fault (Fig. 3–1a).

The Marmion TTG gneisses are bounded on three sides by greenstone belts: the 2.9 - 3.0 Ga Finlayson belt, the 3.0 Ga Lumby Lake and 2.7 Ga Steep Rock greenstone belts are all bounded by the Marmion TTGs (Fig. 3–1a). The contact relationships between the greenstone belts and the tonalite gneisses are discussed by Tomlinson et al. (2003) and Stone (2010). The younger Steep Rock greenstone

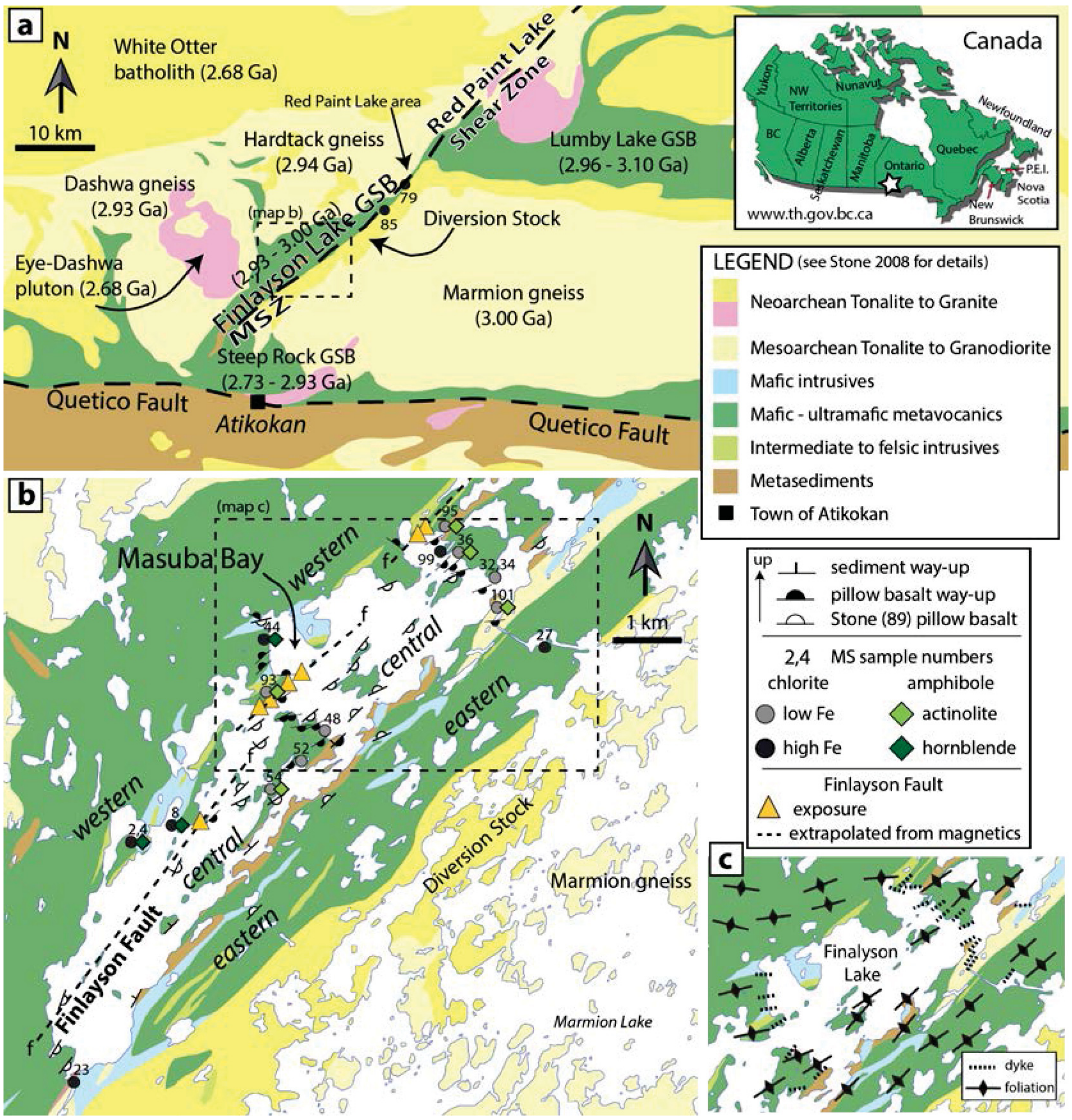

Figure 3–1: Maps of the Finlayson Lake greenstone belt adapted from Stone (2008). Location in Ontario shown by white star on the top right map of Canada. (a) Simplified regional map of the Lumby Lake, Finlayson Lake and Steep Rock greenstone belts (GSB) and associated gneiss domes, also showing the Quetico Fault, Marmion Shear Zone (MSZ) and Red Paint Lake Shear Zone. (b) Enlarged map of the Finlayson belt showing: Pillow basalt way-up orientations; low- and high-Fe chlorite groups (circles) for selected samples (numbers); hornblende or actinolite amphibole occurrence (diamonds), locations with no diamond symbol have no amphibole preserved; mapped locations of altered fault zone (triangles); and extent of fault beneath Finlayson Lake as extrapolated from magnetic data and field exposures. (c) Dashed area outlined in map (b) showing the strike of subvertical foliation and dyke data for that area. White areas (b and c) are lakes.

belt has a documented unconformity at its base, suggesting that it was deposited onto the exposed Marmion TTGs (Wilks & Nisbet, 1988; Stone, 2010). Mapped contact geometries suggest that the Lumby Lake belt is in fault contact with the Marmion gneiss and several major faults parallel to the boundary have been documented within the belt (Tomlinson *et al.*, 1999). The contact between the Finlayson and the Marmion gneiss is named the Marmion Shear Zone (Fig. 3–1a), which links to the north with the Red Paint Lake Shear Zone (Davis & Jackson, 1988; Stone, 2008a) and is cut to the south by the Quetico fault (Bauer *et al.*, 1992; Stone, 2008a). The Marmion shear zone has been intruded by Diversion Stock granitoids and the shear zone core is not exposed (Fig. 3–1b). The western boundary is similarly poorly exposed and separates the Finlayson belt from the Dashwa gneisses in the south and the Hardtack gneisses to the north-west. The dome-shaped Dashwa gneisses have a younger 2.68 Ga intrusive pluton core (the Eye-Dashwa pluton), which along with steep lineations that indicate vertical kinematics of a rising gneiss dome relative to the surrounding greenstone belts (Borowski, 2013) have been suggested to show the strongest evidence for solid state gneiss diapirism in the region (Schwerdtner *et al.*, 1979; Schwerdtner, 1982).

The interpretation of a synformal keel Finlayson belt was derived from a coarse-grid gravity study (Gibb *et al.*, 1988) and inferred synclinal fold axes (Stone & Kamineni, 1989) to explain local pillow way-up reversals. A later interpretation by Stone (2008) subdivided the Finlayson belt into three parallel western-, central- (or Witch Bay) and eastern sub-belts, based on two maximum age dates of a 2.931 Ga felsic tuff and a 3.003 Ga quartz-feldspar volcanic porphyry from the greenstone belt's western and eastern zones, respectively. A youngest zircon detrital age from a conglomerate puts the upper limit on sedimentation in the eastern sedimentary unit at 2.997 Ga (Stone, 2010), which falls within the published age range that spans at least 70 million years. The third belt that separates the eastern and western subdivisions is different, with a lighter shade of green in outcrop, although the lithological assemblages (pillow to massive basalt flows and diverse sediments) are similar. The difference was related to contrasting metamorphic grades with amphibolite facies on the margins and greenschist facies in the centre (Stone, 2010). We test this explanation below, as well as the hypothesis that the petrographic contrasts could represent primary compositional differences across the greenstone belt with associated variations in the extent of low-grade metamorphic overprinting.

3.3 Field and petrographic observations

The Finlayson belt has undergone multiple deformation events causing the development of tectonic structures including folds, faults and grain-scale mineral fabrics. Below we describe each of these and their spatial variations before developing the structural history of the belt. Due to recent lowering of the water level at Finlayson Lake, fresh exposures are found predominantly along the lake-shore outcrops. Our contribution adds detailed, small-scale structural mapping to the regional mapping by Stone (2008). By distinguishing deformational fabrics of different kinematics, metamorphic grade and relative timing, we are able to investigate the structural evolution in more detail.

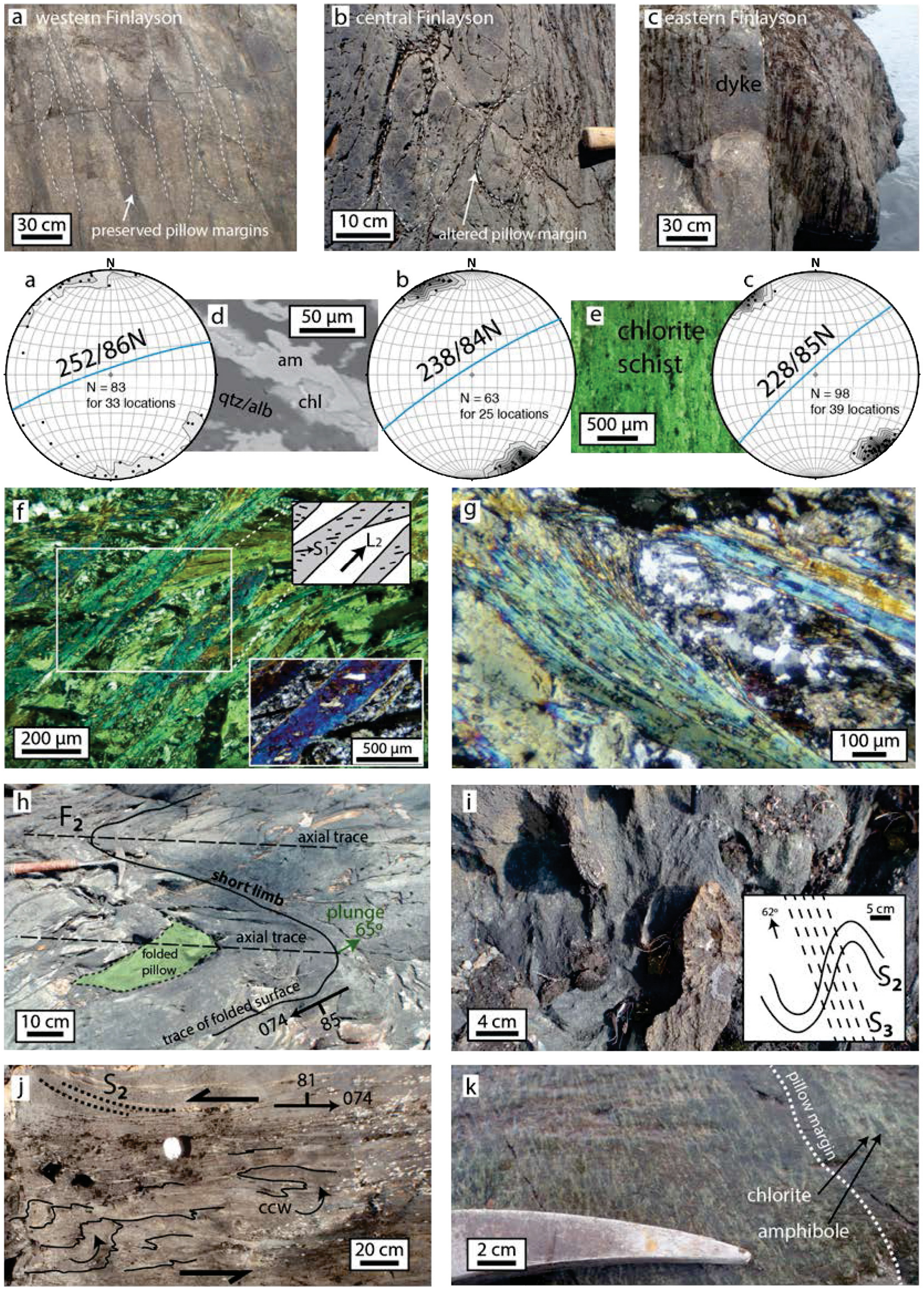

a western Finlayson
30 cm
preserved pillow margins
b central Finlayson
10 cm
altered pillow margin
c eastern Finlayson
dyke
30 cm
N
a
252/86N
N = 83
for 33 locations
d
50 µm
am
qtz/alb
chl
b
238/84N
N = 63
for 25 locations
e
chlorite schist
500 µm
c
228/85N
N = 98
for 39 locations
f
S_1
L_2
200 µm
500 µm
g
100 µm
h
F_2
axial trace
short limb
plunge 65°
axial trace
folded pillow
trace of folded surface
074
85
10 cm
i
62°
5 cm
S_2
S_3
4 cm
j
S_2
81
074
ccw
20 cm
k
pillow margin
chlorite
amphibole
2 cm

Figure 3–2: (Previous page) Field pictures from the Finlayson belt. (a) Pillow basalts in the western Finlayson area showing well preserved pillow margins. Structural fabrics shows a mean strike and dip of 252/86N with a 95% confidence of 17° (stereonet). (b) Pillow basalts in the central portion of the Finlayson belt show partially partially retrogressed pillow margins. Foliation has an average strike and dip of 238/84N with a 95% confidence of 6° (stereonet). (c) Basalts are retrogressed to strongly foliated chlorite schists in the eastern Finlayson and this photo shows a mafic dyke intruding parallel to the dominant structural fabric. Foliation is tightly clustered around 228/85N with a 95% confidence of 3° (stereonet). (d) Backscatter image of a basalt in the western Finlayson area showing partial retrogression of amphibole to chlorite. (e) Plane-polarized transmitted light thin section image of chlorite schist. (f) Two examples from single thin section of coarse gained metagabbro (sample MS008) with coarse lineated hornblende (grey shaded L_2) with aligned inclusions (S_1) within hornblende. (g) Acicular amphibole growth of L_2 hornblende in sample MS008. (h) Sinistral F_2 fold in the Masuba Bay area, showing folded pillow basalts. (i) Cryptic F_2 fold in the central Finlayson visible in hinge zones. (j) Sheared pillow basalts in a sinistral shear zone. Deformed pillow margins (solid lines) and S_2 foliation sheared into parallelism with high-strain zone (dotted lines) show sinistral kinematics. (k) Coarse-grained pillow basalts.

In order to test the hypotheses for the geometry of the greenstone belt, we made detailed structural transects across and along strike, focussing on changes in facing direction, faults, folds, and foliations which preserve kinematic information. Field and microstructural studies have revealed evidence for at least four deformation episodes affecting the Finlayson belt. The structural fabrics and mineral assemblages formed during each deformation are described below.

3.3.1 Belt-scale fabric and dykes

Overall the Finlayson belt has a well defined structural fabric that is easily observed in exposures and aerial photography. The predominant structural fabric and lithological contacts are sub-vertical and strike parallel to the eastern boundary at approximately 040-060° (Fig. 3–2a-c). In the west the mean strike is ENE and becomes more clustered with a NE strike in the eastern portion of the belt (Fig. 3–2a-c), consistent with previous work (Stone, 2008a). Dykes are common throughout the Finlayson belt and consist of mostly mafic with few felsic dykes. Felsic dykes are more common in the eastern portion of the belt (see Section 3.3.6). Predominantly, dykes intrude parallel to the structural fabric (Fig. 3–1c and Fig. 3–2c). Dykes that are at an angle to the structural fabric are folded. The dyke patterns suggest that magmatism was ongoing before, during and after deformation events of the Finlayson belt.

3.3.2 Micro-scale inclusion fabric

The oldest fabric has only been observed as mineral inclusions within younger hornblende crystals. Microscopic observations of a coarse gabbroic unit (sample MS008) show the sub-mm scale inclusion fabric set within aligned hornblende (Fig. 3–2f). The inclusion assemblage consists of plagioclase, quartz and ilmenite that are aligned and parallel across the thin section (Fig. 3–2f). We interpret the alignment on the inclusion mineral assemblage to represents a prograde metamorphic foliation (S_1), that is no longer preserved on the macro scale. The angle between S_1 and lineated hornblende is $\sim 30°$ with variations of $>20°$ related to the variation of the lineation fabric. The kinematic signature of S_1 is not evident in the collected samples. Although the inclusion fabric has been almost entirely overprinted, this inclusion assemblage allowed us to calculate the prograde metamorphic pressure-temperature conditions (see Section 3.5).

3.3.3 Greenstone belt way-up facing orientations

A first-order question for greenstone belt structure is identifying the symmetry across the belt. The sagduction model predicts an overall synclinal symmetry with both outermost limbs facing inward, as was originally proposed for the Finlayson belt by Stone and Kamineni (1989). To test the overall structure of the Finlayson belt we mapped the facing direction for several detailed transects across the belt in as much detail as possible and patterns were detected on multiple scales. Paleo way-up facing orientations can be interpreted from pillow basalts by identifying the lobate tops and downward pointing tails. Due to the high degree of flattening experienced in the Finlayson belt, many pillow basalt exposures are ambiguous with regards to way-up facing direction. Therefore, we only include unambiguous pillow facing orientations from this study and those mapped by Stone et al. (1992) in Figure 3–1b.

Belt-scale pillow reversal

Variations in pillow facing orientations are observed in the Finlayson belt and have previously been reported on geological maps (Stone & Kamineni, 1989). Our detailed transects show two domains of pillow basalt facing orientations. In the western portion of the Finlayson belt, pillows face predominantly northwest, whereas in the central portion of the belt they are southeast facing, such that the two domains face outwards (Fig. 3–1b). Pillow basalts are only locally preserved in the eastern Finlayson belt (see Sections 3.3.4 and 3.3.6). The two domains of pillow facing orientations are separated by a 3 - 7 m wide linear zone of intense foliation and alteration (see triangles in Fig. 3–1b). The alteration assemblage is predominantly ankerite and pyrite and the pre-existing rock structure has been overprinted by an intense foliation. The edges of the most intense alteration can be very sharp ($<$ 1 m), but typically grade to unaltered rock over a distance of 1 - 5 m. Although no kinematic indicators were observed around this feature, the linear geometry and concentrated alteration suggests a belt-scale fault separates the two domains of way-up orientations (Fig. 3–1b). This newly identified fault, here named the Finlayson Fault, may have taken advantage of a pre-existing weakness such as a larger-scale anticline axis, which would be consistent with the belt-scale pillow reversals. The observed fault locations coincide with linear magnetic high features (Ontario Geological Survey, 2009) and in Fig. 3–1b the fault has been traced along the magnetic anomaly that coincides with the observations. The pillow facing orientations are outward, opposite to the facing directions predicted by synclinal symmetry.

Structures leading to local pillow basalt reversals

Sub-vertical lithological units within each way-up facing domain defined above are mostly conformable on traverses perpendicular to the structural fabric. The strike and dip of the lithological contacts are parallel to the strongest foliation. A planar alignment (S_2) of predominantly plagioclase and weakly aligned hornblende is parallel to the lithological contacts. The weak amphibole lineation (L_2) is observed in coarser gabbroic units (Fig. 3–2f) and seen in thin section for finer grained lithologies. Amphiboles in rare meta-gabbros show a mean plunge of 45° to 70° within the S_2 foliation. Co-planarity and definition of these fabrics by alignment of the hornblende motivate us to interpret the weak amphibole lineation as co-genetic with S_2 foliation (S_2-L_2 fabric).

We were not able to identify any repetition of sedimentary or volcanic packages which might support a hypothesis of 100 m-scale folding across the belt. Folds are observed throughout the belt, but these are typically localized and small scale with a wavelength of a few centimetres to 1 m (e.g. Fig. 3–2h - i). The long limbs of the folds are parallel to the S_2 structural fabric (Fig. 3–2h - i) and fold axes across the belt are consistently steeply plunging sub-parallel to L_2 (Fig. 3–3b). Although pillow basalt way-up orientations are mostly consistent in the two domains either side of the Finlayson Fault (Section 3.3.3), reversals have been documented by Stone and

Kamineni (1989) and we observed local zones of paleo way-up reversals. The outcrop in the Masuba Bay area of Finlayson Lake exposes one fold hinge of a larger (20 m wavelength) isoclinal F_2 fold (Fig. 3–3a). The fold asymmetry records sinistral kinematics and within the short limb of the fold, pillow way-up orientations are reversed. A parasitic 1 m wavelength fold shows the same sinistral sense of rotation and folding of preserved pillow basalts around the axial trace (Fig. 3–2h).

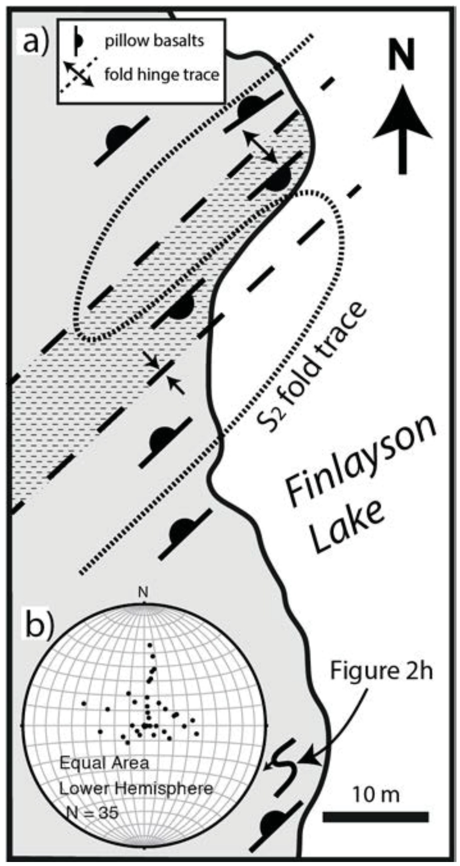

Figure 3–3: (a) Field map of pillow reversal zones in short limbs of sinistral F_2 folds from Masuba Bay area (See Fig. 3–1). Dashed lines show the trace of the fold hinge and dotted line traces out the isoclinal fold. Location of parasitic fold (Fig. 3–2h) is indicated in lower right corner. (b) F_2 fold axes from across the Finlayson belt showing steep to sub-vertical plunges.

The intensity of the S_2 structural fabric is generally consistent across the Finlayson belt. A few discrete small shear zones are observed parallel to the S_2 foliation. One example is a sinistral 50 cm wide shear zones striking sub-parallel to the local S_2 foliation in the central portion of the Finlayson belt (Fig. 3–2j). Figure 3–2j shows sheared pillow margins preserving sinistral kinematics. The shear structure preserves the same sinistral kinematics and amphibole mineralogy as the S_2 foliation and we interpret the two structures to be syn-kinematic. In the eastern portion of the Finlayson belt S_2 structures are only observed in the hinge zones of F_2 folds, where the intersection angle of the fold limbs and later overprinting retrograde foliation (see Section 3.3.4) is increased (Fig. 3–2i).

3.3.4 Schistosity

The dominant structural fabric observed throughout the Finlayson belt is a sub-vertical chlorite foliation (S_3), which is penetrative from belt to thin section scale. The chlorite foliation developed sub-parallel to the S_2 foliation and is defined by retrogressive chlorite replacing amphibole (Fig. 3–2d). The cross-cutting relationship is locally revealed by S_3 overprinting at a moderate angle across the asymmetric F_2 fold hinges (Fig. 3–2i). No mineral lineation is associated with S_3, but intersection lineations of the sub-parallel S_2 and S_3 fabrics are commonly observed in outcrops and easily mistaken for mineral lineations. The intensity of the S_3 foliation is directly proportional to the amount of chlorite growth, which is correlated with the extent of amphibole to chlorite retrogression and is strongest at the eastern boundary (Fig. 3–2a-e). The most intensely foliated units are chlorite schists, where the phyllosilicates form pervasive parallel foliation surfaces and completely overprint the S_2-L_2

structures (Fig. 3–2c and e). These chlorite schists are found within 1 to 2 km of the eastern margin of the Finlayson belt striking sub-parallel to the eastern boundary at 230° with a sub-vertical dip (Fig. 3–2c). To the west the S_3 foliation is weaker, displaying stronger chlorite foliation in fine grained rocks such as pillow margins and weaker overprint in coarse grained rocks. In areas of the weakest S_3 foliation, chlorite retrogression only partially replaces amphiboles as shown in Figure 3–2d. Parallel phyllosilicates and flattened clast symmetry of quartz grains are consistent with pure shear strain within the quartz ductile regime during retrogression.

3.3.5 Mineralogy

Stone (2010) mapped different structural units in the Finlayson belt based on darker green metabasalts in the western and eastern portions and lighter green metabasalts in the central portion (Fig. 3–1b). Stone (2010) attributed these to different metamorphic grades of dark hornblende (amphibolite grade) versus light actinolite (greenschist grade) and used this distinction to correlate parts of the Finlayson to other nearby greenstone belts. Here we relate the paragenesis to the observed structural fabrics described above and combine these observations with electron microprobe mineral analyses in samples from across the belt in order to test the origin of the colour differences.

Sample MS008 (Fig. 3–2f) from the western portion of Finlayson belt (Fig. 3–1b) was selected to represent the best preserved higher grade metamorphic assemblages with only weak retrogression seen as acicular amphiboles (Fig. 3–2g). This sample revealed a mineral assemblage preserved as inclusions (Section 3.3.2; Fig. 3–2f). The inclusion mineral assemblage consists of hornblende, plagioclase, quartz and ilmenite ± epidote. This inclusion assemblage forms with a preferred orientation (S_1) and records a prograde foliation preserved within the S_2-L_2 fabric.

The peak metamorphic paragenesis is variable in units depending on their bulk composition. The assemblages consist of amphibole + plagioclase + ilmenite, amphibole + plagioclase + ilmenite + quartz and amphibole + plagioclase + epidote + ilmenite ± quartz. The least retrogressed units that best preserve the S_2-L_2 fabric are typically gabbroic with weakly lineated amphiboles (L_2). Sample MS008 preserves a peak paragenesis of amphibole + plagioclase + ilmenite, which was used for pressure-temperature and pseudosection calculations (see Section 3.5).

The retrogressive overprinting assemblage, which increases in abundance from west to east includes chlorite, actinolite, albite, quartz, titanite and epidote. The intensity of retrogression varies considerably from weakly altered units with preserved hornblende to intermediate retrogression including partial replacement of hornblende by actinolite and finally to chlorite schists with no preserved amphiboles. The majority of chlorite retrogression is accompanied with the development of the S_3 foliation. Poikilitic and euhedral titanite is common around relict ilmenite grains throughout the Finlayson belt and overgrows both the L_2 fabric of the amphiboles and S_3 chlorite foliation.

We compared the amphibole compositions across the belt in order to test the contrasting metamorphic grades that Stone (2010) proposed. Actinolite is found in the central Finlayson belt and rare remnant actinolite is preserved in the eastern portion of the Finlayson belt (Fig. 3–1b). Hornblende is only preserved in the western portion of the belt (Fig. 3–1b). Therefore, the distribution of actinolite versus hornblende as suggested by Stone (2010) does not explain the occurrence of a colour difference by metamorphic grade within the Finlayson belt. We analysed chlorite (n = 164) and found that chlorite compositions from the lighter and darker metabasalts, as mapped by (Stone, 2010), correspond to a clear division of lower-iron and higher-iron compositions (Fig. 3–4). The chlorite in the darker green volcanics correspond to the high-iron group and have a strong pleochroism and deeper green colour. The data show that the lighter green colour of the basalts in the central Finlayson volcanics (previously named the Witch Bay sub-belt, see Stone (2010)) is coincident with a paler green chlorite with lower iron content (Fig. 3–1b).

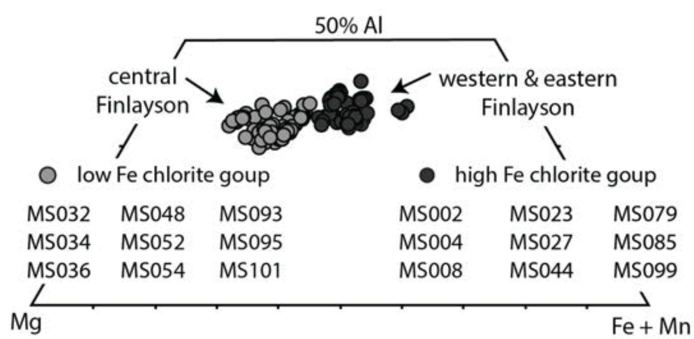

Figure 3–4: Plot of chlorite compositions measured by microprobe for 18 samples and 165 chlorite analyses. Locations of samples are shown in Figure 3–1b. Samples MS079 and MS085 are part of the eastern Finlayson farther north at Red Paint Lake (Fig. 3–1a). Samples are grouped spatially into eastern-western Finlayson (dark circles) and central Finlayson (light circles) as determined from field descriptions of dark or light green basaltic units. Chlorite compositions from western and eastern Finlayson samples show a complete overlap in composition (dark circles). The spatial groupings show a clear separation into higher- (dark circles) and lower- (light circles) iron compositions.

The origin of this chemical difference in the chlorite may reflect different parental sources with primary differences in magnesium-iron ratios. Our limited whole rock geochemistry dataset suggest that the lighter basalts have higher magnesium-iron ratios (n = 2) than the darker basalts (n = 5), consistent with the differences observed in the chlorites. However, the current whole-rock geochemistry dataset is not extensive enough to exclude any other origins for the colour differences, such as preferential sequestering of Fe by other phases, such as pyrite, and the extent of retrogression.

3.3.6 Coarse-grained pillow basalts

Most earlier structures have been overprinted in the eastern portion of the Finlayson belt (see Section 3.3.4). The only preserved lithological structures are pillow basalts that have an unusually coarse-grained texture (Fig. 3–2k) with the primary S_2 fabric preserved. Coarse-grained pillow basalts are found as discrete zones located immediately adjacent to competent felsic intrusive dykes within the region of intensely foliated chlorite schists. The typically dominant S_3 foliation in this region is very weak to absent in the preserved pillow basalts. These pillows have similar aspect ratios to the those in the western portion of the Finlayson belt and were likely also deformed under the same conditions (see Section 3.3.3). However, a coarse grained metamorphic mineral texture is unique to the eastern pillow basalts (Fig. 3–2k). The mineralogy consists mainly of coarse euhedral amphiboles with no preferred orientation. The margins of the amphiboles are retrogressed to chlorite, but no penetrative foliation is developed. The proximity to intrusive dykes suggest that the coarse grained texture may be resultant from contact metamorphism during intrusion of the felsic dykes. This coarse texture is not found beyond 10 - 15 m from the intrusive dykes.

3.3.7 Veins

Veins in the Finlayson belt of multiple generations include monomineralic and polymineralic combinations of quartz, calcite and/or ankerite $\pm$ pyrite, chalcopyrite and accessory monazite. The veins are emplaced predominantly vertically along pre-existing structures and have mutually crosscutting relations between the different populations of veins. Quartz veins are the most common and are boudinaged and folded (Fig. 3–5). Boudinaged quartz veins show pure shear kinematics with stretching in both dip- and strike-parallel axes, parallel to foliation. Deformed quartz veins within the zones of coarse grained pillow basalts (see Section 3.3.6), are emplaced crosscutting the S_2 fabric. The quartz veins are folded and boudinaged axial planar to the S_3 foliation (Fig. 3–5). The felsic dykes that are spatially associated with the coarse pillow basalts show the same generation of folded veins within them (Fig. 3–5b). These veins are recording a shortening that postdates the S_2 fabric. The amount of shortening measured in three quartz veins that post-date S_2 and show only S_3 shortening increases from west to east. Shortening was calculated by measuring the original length (l_0) of the vein and the final folded length (l_1) (see Fig. 3–5b for example). The ratio of final to original quartz vein lengths are 15:41 (63%) at the eastern boundary, 31:67 (54%) at approximately 1 km west of the boundary and 268:541 (50%) for veins 2 km west of the eastern boundary. The trend of increasing shortening toward the east is consistent with the intensity of the chlorite retrogression.

Non-planar and discontinuous ankerite veins are concentrated in zones of intense foliation and can range in thickness from sub-cm to massive 1-3 m wide zones of intense veining and alteration. These veins pinch and swell and are associated with massive sulphides that are scattered throughout the Finlayson belt. Massive ankerite zones entrain abundant foliated volcanic wall rock, suggesting that the fluids used

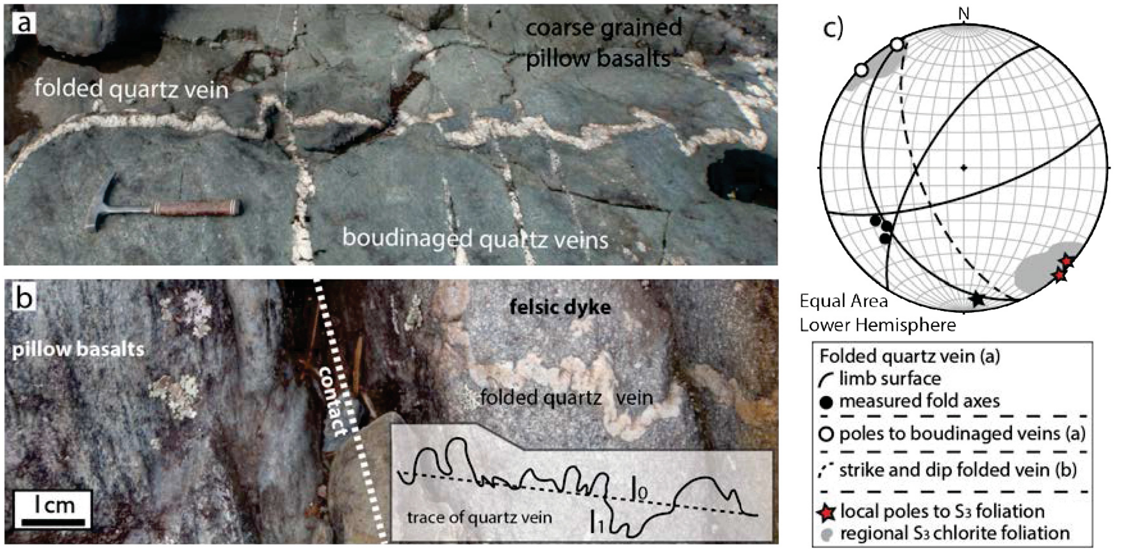

Figure 3–5: Deformed quartz veins in the Finlayson belt. (a) Folded and boudinaged quart veins within coarse grained pillow basalts. (b) Intrusive felsic dyke with folded quartz vein recording shortening. Dashed black line (l_0) shows trace of original length and solid line (l_1) is the trace of the final folded vein. (c) Orientation data for limbs of folded quartz veins (lines) and poles to boudinaged veins (open circles). Regional (shaded area) and local (red star) chlorite foliation is plotted for comparison.

the foliation as a conduit, as seen at the Finlayson Fault. Abundant euhedral coarse pyrite grains grow on the mafic volcanic rafts within the ankerite veins. Calcite veins are the most rarely observed vein-type. Most commonly, the calcite veins form as late sub-horizontal veins in the chlorite schists of the eastern margins of the Finlayson belt. The late calcite veins cut the foliation surfaces as well as pre-existing quartz and/or ankerite veins (Fig. 3–6a). Foliation-parallel calcite veins are also observed, but most commonly in association with quartz as a co-mineralising phase.

3.3.8 Faults and fractures

The youngest structures in the Finlayson belt are faults and fractures, which show brittle deformation of quartz. These faults are most abundant in the eastern portion of the Finlayson belt. Most faults only accommodate small-scale offset

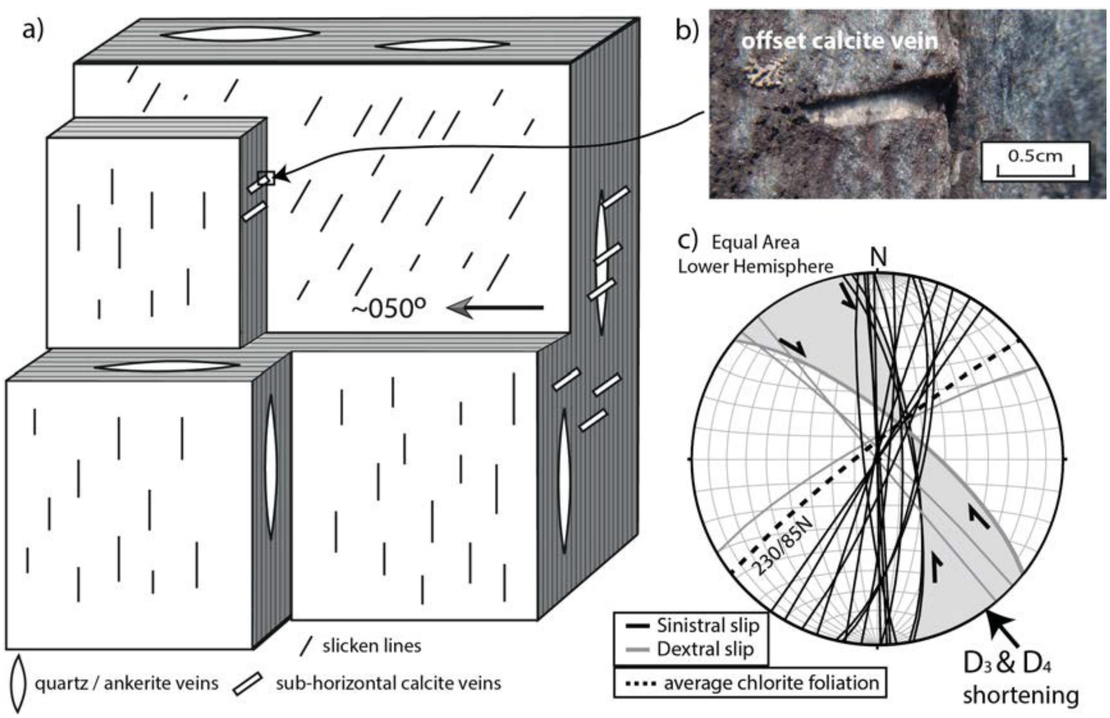

Figure 3–6: (a) Block-sketch of intensely foliated chlorite schists in eastern Finlayson. Exposed foliation surfaces (not to scale) show slickensides with oblique to vertical slip. (b) Sub-horizontal calcite vein showing offset along foliation plane. (c) Sinistral (black lines) and dextral (grey lines) brittle faults from the Finlayson belt. The grey shaded area represents a conjugate set of sinistral and dextral faults at the same outcrop and show the compression field. Dashed line is the average chlorite foliation (230/50N - strike/dip), which separates the orientations of dextral and sinistral structures, suggesting sub-parallel shortening axes for D_3 and D_4.

ranging between 5 cm and 5 m. Slip is localized on earlier planar structures (S_2 and S_3) and displacement is measured from offset dykes and veins. Slickensides are observed on exposed foliation surfaces of the chlorite schists of the eastern Finlayson belt (Fig. 3–6a). Slicks are typically sub vertical and in one outcrop can range in rake between 90° and 70° (Fig. 3–6a). Figure 3–6a shows the relationship of veins, including quartz-ankerite and ankerite veins parallel to the chlorite foliation and sub-horizontal calcite veins cutting the foliation and other vein sets. The calcite veins post-date the S_3 chlorite foliation development (see Section 3.3.7). These calcite veins are displaced along S_3 foliation surfaces that accommodated slip (Fig. 3–6b), showing that the S_3 foliation surfaces were reactivated as (small-scale) slip surfaces.

The predominant sense of strike slip recorded along faults is sinistral with only few dextral faults (Fig. 3–6c). The amount of vertical slip on these faults is not constrained, but if these faults are coeval to the sub vertical slickensides seen on chlorite foliation, we can assume vertical slip is larger than strike-parallel slip. The conjugate orientations of dextral versus sinistral faults are symmetrical around the pole to the chlorite foliation (Fig. 3–6c). Domains of sinistral faults strike between 350° and 050°, whereas dextral faults strike between 230° and 320°, separated across the orientation of S_3 foliation (Fig. 3–6c).

3.3.9 Boundaries of the Finlayson belt

Greenstone belt boundaries are key to unraveling the kinematic history of greenstone-TTG contacts and the tectonic setting that juxtaposed supracrustal with crustal terranes. The ambiguity of the contacts as either large shear zones, slightly faulted nonconformities or both is often difficult to establish in any Archean greenstone-TTG terrane. Here we present the observed constraints focused on the eastern boundary of the Finlayson belt. The western boundary to the Dashwa (Fig. 3–1a) was investigated as part of an unpublished study (Borowski, 2013) and we present evidence for boundary kinematics from his field work and other published studies for completion. The northwestern contact to the Hardtack TTGs was observed at one small exposure in the Red Paint Lake area (Fig. 3–1a).

The eastern boundary

The eastern boundary of the Finlayson belt has been interpreted as the Marmion Shear Zone or Marmion Fault, which marks the southwestern extension of the Red Paint Lake Shear Zone (Fig. 3–1a). The Marmion Shear Zone is not exposed and the structure has been intruded by the Diversion Stock granitoids (Fig. 3–1b), preventing any direct field observations and kinematic interpretations. The only available minimum age constraint for movement along the Marmion Shear Zone is from the approximately 2.7 Ga Quetico Fault that cuts it to the south (Fig. 3–1a). Metasediments close to the eastern margin of the Finlayson belt may include abundant mm-sized feldspar grains and carry rare tonalite blocks up to 20 cm large suggesting that the greenstone belt units were deposited onto or close to exposed felsic basement. The presence of exposed felsic basement is consistent with Marmion-age 3.0 Ga inherited zircons in the conformable sedimentary units of the Finlayson belt (Stone, 2008a), further suggesting that exposed felsic terranes similar in age and composition to the Marmion gneisses were eroded into the basin before the greenstone belt was deformed. Although the age of Diversion stock is poorly constrained, the structural relations demonstrate that it intruded along the already established contact between the Finlayson belt and Marmion TTGs. From published maps (Stone, 2008a) the boundary between the Finlayson belt and Diversion Stock is expected to be exposed along shoreline outcrops in the Marmion Lake and Red Paint Lake to the east and north of Finlayson Lake, respectively. At each expected boundary location a preferentially eroded 30 m to 50 m wide zone was observed, separating Finlayson mafic volcanics (chlorite schists) from Diversion Stock granitoids. One location showed remnant slivers of the Diversion Stock granitoid in contact with the greenstone belt. From this location we were able to measure the strike and dip of the eastern boundary. On average the contact strikes 050° (035° - 070°) and dips 75° (60° - 80°) to the southeast. The boundary zone is characterized by well foliated mafic volcanics and a series of granitoid dykes that increase in density towards the main Diversion Stock intrusion over approximately 50 to 100 m. The granitoid dykes are parallel to to the boundary and greenstone belt fabric and are petrographically identical to the main Diversion Stock intrusion. Although some dykes are undeformed, many have been fractured, suggesting localized brittle deformation postdating their intrusion.

The western boundary

In the west the Finlayson belt is bounded by two different TTG terranes, the 2.93 Ga Dashwa gneiss and the 2.94 Ga Hardtack gneiss. Both are younger than the 3.0 Ga Marmion TTGs and the Finlayson belt. The Dashwa TTGs, amongst other Wabigoon subprovince gneiss domes, have been cited amongst the key examples of solid state gneiss diapirism within the Superior Province (Schwerdtner et al., 1979; Schwerdtner, 1984, and unpublished fieldwork: Borowski, 2013). They document concentric foliation patterns, the younger 2.68 Ga Eye-Dashwa intrusive core, steeply plunging ductile lineation structures and greenstone belt-down kinematics supporting diapiric tectonic processes. Schwerdtner (1990) refuted the diapiric model based on structural tests of relative timing of folding and doming, suggesting that upright folding in the TTGs occurred prior to the doming phase. We observed better preserved ductile deformation close to the western margins of the Finlayson belt, consistent with our observations of decreasing retrogression from east to west.

The northwestern contact of the Finlayson belt to the Hardtack gneisses has only been documented in published maps (Stone & Kamineni, 1989; Stone, 2008a). We observed the contact to the Hardtack gneiss at Red Paint Lake (Fig. 3–1a), where the northern extent of the Finlayson Lake greenstone belt is exposed. The contact is faulted and the Hardtack tonalites brecciated. The amount of offset, kinematics or preexisting structures were not identified from this limited exposure. We were not able to investigate this contact any further.

3.4 Strain interpretations

The Finlayson Lake greenstone belt shows consistent kinematic indicators across the entire belt with early ductile fabrics, retrogressive overprint and late stage minor brittle faulting. In this section we discuss and compare the strain that resulted in the various structures described above in order to constrain the deformational history of the greenstone belt.

3.4.1 Sinistral transpression at amphibolite facies

The prograde foliation (S_1), which is preserved as inclusions within lineated hornblende (L_2), has been almost entirely overprinted and cannot be conclusively oriented. However, S_1 records an early deformation with the fabric formed at an angle of $\sim 30°$ to L_2 (Fig. 3–2f). The S_2 deformation occurred at amphibolite facies as seen from preserved hornblende lineations in the western portion of the Finlayson belt. Structures include sinistral folds with steep fold axes parallel to L_2 and local sinistral shear zones (Section 3.3.3). Both types of structures are kinematically consistent with sinistral transpression during formation of S_2 - L_2. All these fabrics can be explained by a horizontal north-south shortening.

3.4.2 Pure shear at greenschist facies

The S_3 retrogressive chlorite foliation clearly cross-cuts and overprints the S_2 - L_2 fabric (Section 3.3.4). There is no textural evidence for simple shear during the development of S_3 and all outcrops display fabrics showing flattening during chlorite retrogression. The well developed chlorite foliation of the eastern Finlayson suggests a southeast-northwest trending horizontal shortening axis, perpendicular to the eastern boundary (Fig. 3–2c and Fig. 3–6c). The orientation of the greenschist facies shortening axis can be contrasted to the shortening axis interpreted from the older amphibolite facies structures and records a 40° to 50° change in the shortening direction. The amount of shortening measured in three quartz veins that post-date S_2 and show only S_3 shortening decreases away from the boundary from 63% at the boundary, to 54% at 1 km and 50% at 2 km away perpendicular to boundary. Our observations demonstrate that the Finlayson belt has at least two different sub-parallel fabrics from separate deformation events.

3.4.3 Brittle reactivation

Late-stage small brittle faults in the eastern portion of the Finlayson belt show slip on pre-existing S_2 and S_3 fabrics. The orientations of sinistral and dextral faults are subdivided (Fig. 3–6) and define a southeast-northwest compression parallel to the shortening direction interpreted for S_3. Therefore, we infer that shortening continued in the same orientation through the transition from ductile to brittle deformation.

3.5 Metamorphic constraints

Field and petrographic observations show that the western portion of the Finlayson belt preserves the highest metamorphic grades, and older deformation event. Metamorphic assemblages indicate that peak metamorphism took place at amphibolite-facies conditions, and was followed by progressive retrogression to lower-greenschist-facies conditions. The dominant peak assemblages are amphibole + plagioclase + ilmenite, amphibole + plagioclase + ilmenite + quartz and amphibole + plagioclase + epidote + ilmenite ± quartz, depending on bulk rock composition. Garnet has not been observed anywhere in the belt. The L_2 mineral lineations (Fig. 3–2f) of peak-metamorphic amphibole are consistent with the sinistral transpression, and position this deformation event at peak metamorphism.

The peak metamorphic minerals, and amphibole in particular, contain a characteristic inclusion assemblage consisting of amphibole + plagioclase + quartz + ilmenite + epidote ± calcite. Plagioclase inclusions (S_1) have a subtly higher X_{An} compared to peak metamorphic (S_2) matrix plagioclase, and the adjacent measured amphibole is higher in Al and Ca, and lower in Mg, Fe and Na for D_2 (Table 3–1). The most largest variation is the difference in the Al content of the amphibole.

Retrogression is progressive, with initial replacement and overgrowth of peak-amphibole by a new, acicular amphibole generation (Fig. 3–2g). Epidote and quartz

Table 3–1: Average hornblende and plagioclase mineral composition for mineral data used in geothermobarometry. Minerals analysed from Sample MS008. Inclusion compositions measured for D_1 (n = 5 mineral pairs) and matrix compositions measured for D_2 (n = 6 mineral pairs).

	Inclusion (D_1) Amphibole	Plagioclase	Matrix (D_2) Amphibole	Plagioclase
SiO_2 wt.%	45.25	61.87	44.49	60.84
TiO_2	0.27	n.d.	0.30	0.01
Al_2O_3	10.72	23.91	12.67	24.37
FeO	17.44	0.36	17.05	0.26
MgO	9.85	0.00	9.26	0.00
MnO	0.29	n.d.	0.25	0.01
CaO	11.45	5.14	11.86	5.82
Na_2O	1.34	8.56	1.22	8.16
K_2O	0.28	0.11	0.35	0.11
Total	96.88	99.95	97.46	99.58
X_{Ab}	-	0.72	-	0.75
X_{An}	-	0.28	-	0.25
T (°C)	600 ± 45		625 ± 25	
P (MPa)	820 ± 40		635 ± 135	

(re-)appear in samples where they did not form part of the peak metamorphic assemblage. More intensely retrogressed samples are dominated by chlorite + albite ± actinolite, and may contain carbonate. The retrograde path is accompanied by pure shear kinematics to form the chlorite-defined S_3 foliation. Euhedral titanite growth records a final, static equilibration after the formation of S_3.

The best-preserved amphibolite facies metamorphic assemblages are from the coarse gabbroic unit. In order to further constrain metamorphic conditions, a pseudosection was calculated for the bulk-rock composition of sample MS008 from this unit, using the PerpleX suite of programs (Connolly, 2005). We use the 2002 version of the Holland & Powell (1998) thermodynamic database for mineral end-members, and solid solution models from Holland & Powell (1996, clinopyroxene), Holland & Powell (1998, epidote), Holland *et al.* (1998, chlorite), Newton *et al.* (1981, plagioclase), Diener *et al.* (2007) and Diener & Powell (2012, amphibole), White *et al.* (2000, ilmenite) and White *et al.* (2007, garnet) as implemented and modified in PerpleX 6.6.8. Calculations were run at water saturated conditions and with the oxygen fugacity buffered at Ni-NiO. The resulting diagram is shown in Figure 3–7.

For sample MS008, the peak paragenesis is plagioclase + amphibole + ilmenite, and it contains an inclusion paragenesis of plagioclase + amphibole + ilmenite + quartz ± epidote. Combining the pseudosection P-T fields with thermobarometry (Holland & Blundy, 1994) on coexisting plagioclase-amphibole pairs in these two assemblages, suggests conditions of close to 600°C, 820 MPa for the prograde inclusions (n = 5 mineral pairs), and 625°C and 635 MPa for the peak conditions (n = 6 mineral pairs) (Fig. 3–7, error bars are the spread in P and T for the various pairs analysed). The peak and inclusion assemblages are used to constrain the P-T range within the respective fields in Figure 3–7. Retrograde conditions are bound by the reappearance of chlorite, which is at approximately 550°C for this bulk-rock composition. For sample MS008 static titanite re-enters the mineral assemblage at temperatures of $\sim$ 500°C. Based on our calculations the reappearance of quartz will

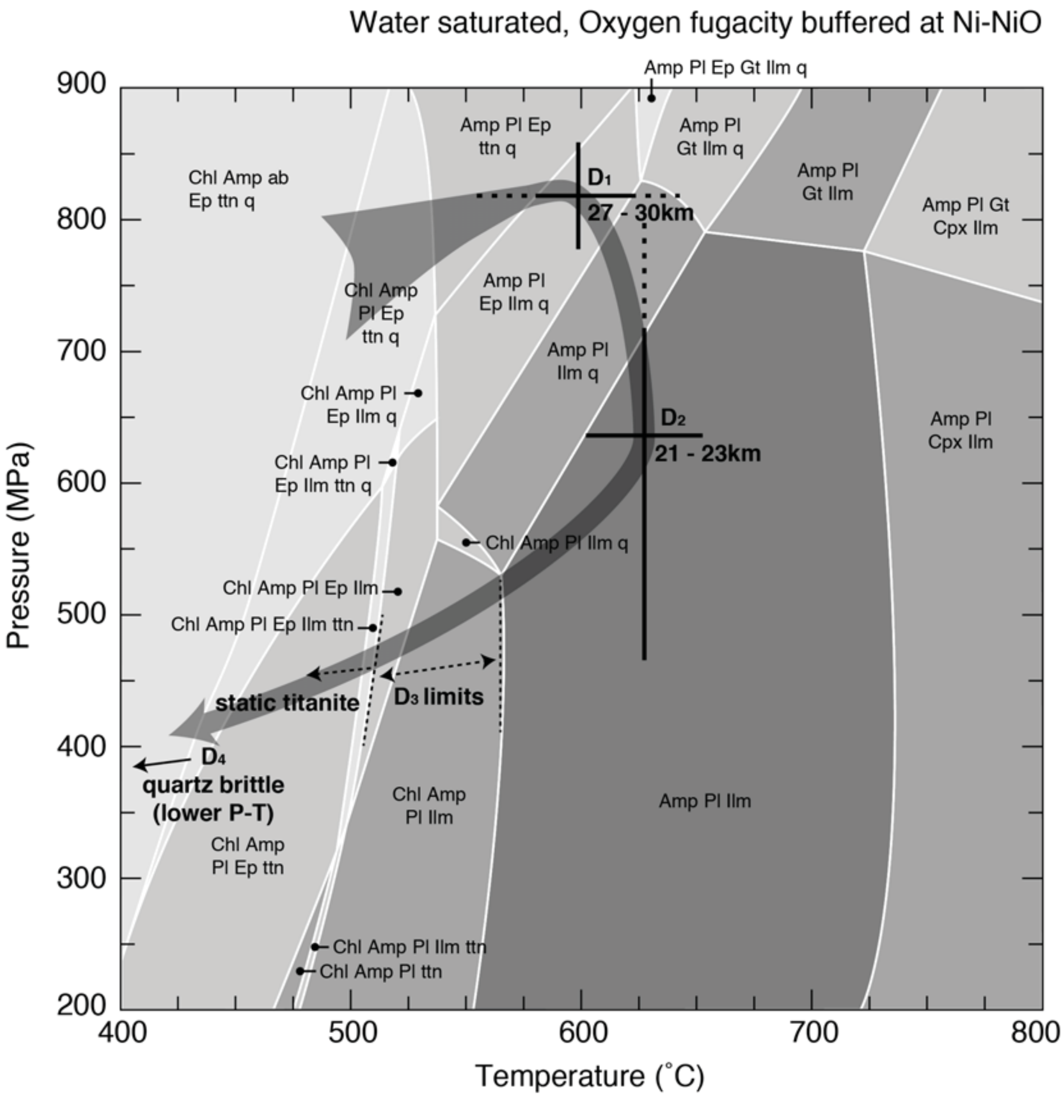

Figure 3–7: Pressure-temperature pseudosection calculated for gabbro sample MS008 using published mineral abbreviations (Kretz, 1983). Solid solutions indicated with a capital letter. Prograde conditions (D_1) are constrained by the inclusion paragenesis pl+amp+ep+ilm+q and pl-amp geothermobarometry to 820 $\pm$ 40 MPa and 600 $\pm$ 45°C, whereas the D_2 peak metamorphic paragenesis of pl+amp+ilm formed at 635 $\pm$ 165 MPa and 625 $\pm$ 25°C. The retrograde paragenesis contains ep, tit and q, and is not well constrained and depends on the bulk composition of the rock. However, we can show that D_3 deformation is constrained by the appearance of retrogressive chlorite (syn-D_3) and the (re-)appearance of static titanite (post-D_3) within quartz-ductile P-T conditions (see arrows showing D_3 limits). The late-stage deformation (D_4) occurred within quartz brittle P-T conditions, which plots to lower pressure-temperature conditions, likely at $<$ 400 MPa ($\sim$ 15 km) and $<$ 350°C.

vary significantly depending on the bulk compositions, with either quartz preceding or postdating titanite retrogression, therefore sample MS008 is used as a guideline only for retrograde conditions.

3.6 Deformation History of the Finlayson belt

A summary sketch of the Finlayson belt along with its deformation history is shown in Figure 3–8. The earliest deformation event (D_1) is only recorded as aligned mineral inclusions and is not seen at the macroscopic scale. From mineral analyses of these inclusions we are able to constrain the pressure and temperature conditions during D_1 at 600 ± 45 °C and 820 ± 40 MPa (Fig. 3–7), which corresponds to a depth of approximately 27 - 30 km for typical greenstone belt densities of 2.7 to 3.0 g/cm^3 (Peschler *et al.*, 2004). The kinematics associated with D_1 are unknown.

The pressure and temperature conditions of D_2 sinistral transpression are coeval with peak metamorphism along a clockwise P-T path at 625 ± 25°C and 635 ± 125 MPa (Fig. 3–7), which corresponds to approximately 21 - 23 km depth. This implies that the Finlayson belt was exhumed by 4 - 9 km between D_1 and D_2 under near isothermal conditions. Sinistral transpression is recorded on both sides of the Finlayson Fault, which separates the outward facing pillow basalt domains (Fig. 3–8). Therefore, any major motion on the Finlayson Fault either predates or is synchronous with D_2. Although no kinematics are observed with the Finlayson Fault due to overprinting retrogression, it can be postulated that sinistral strike slip offset was prevalent, if the fault was active during D_2 sinistral transpression. The Finlayson Fault may represent the trace of the anticlinal fold axis that defines the belt-scale pillow facing geometry. There are no constraints to quantify significant fault offset

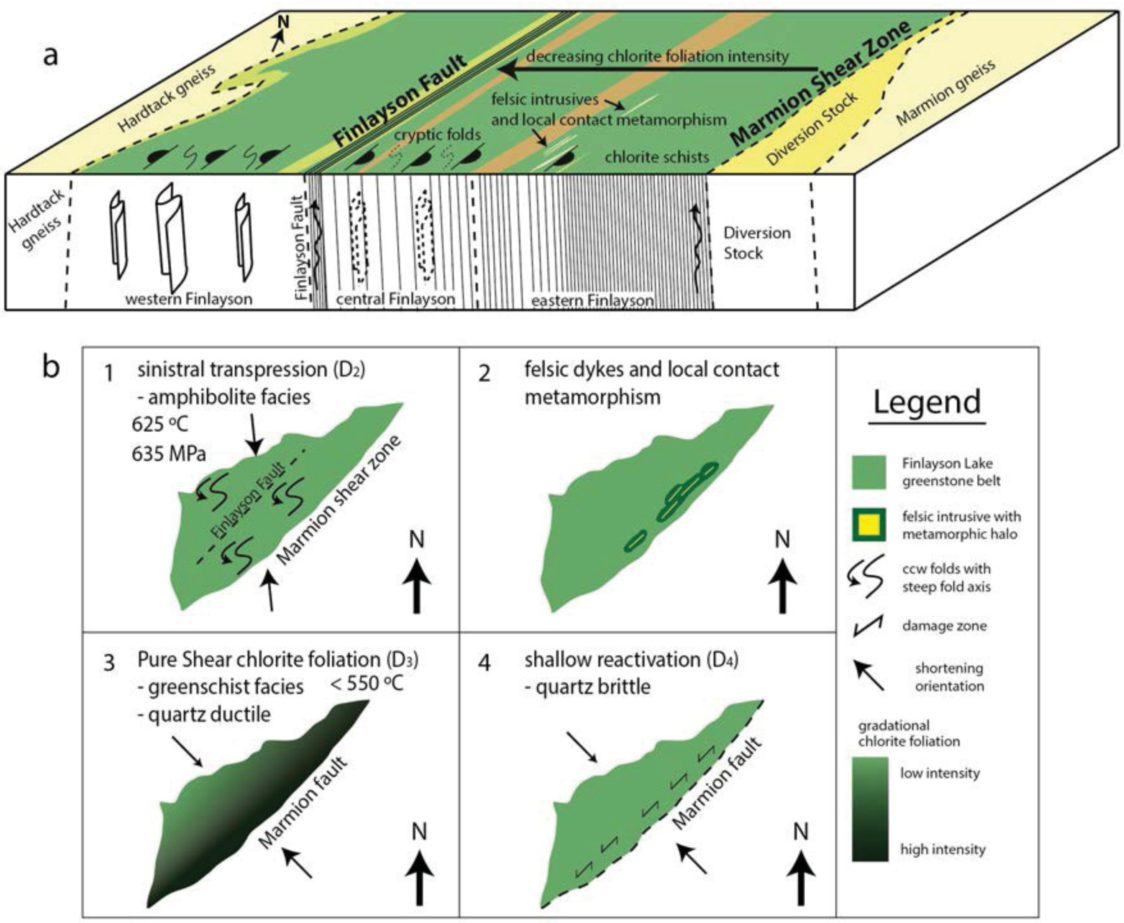

Figure 3–8: (a) Sketch cross section of the Finlayson Lake greenstone belt. Density of solid lines represent intensity of retrogressive chlorite foliation. Steeply plunging folds in western and central portion of the section indicate observed sinistral transpression (solid outline) and cryptic folds overprinted by chlorite foliation (dashed outline). Oppositely facing pillow domains are separated by the Finlayson Fault. (b) Breakdown of the deformation history of the Finlayson belt. (1) Sinistral transpression with approximately north-south shortening and sinistral folds. (2) Local felsic dykes and contact metamorphic aureoles, preserving zones of pillow basalts within the chlorite schist domain. (3) Greenschist facies pure shear chlorite foliation, showing increasing intensity towards the eastern boundary and the Marmion Fault. (4) Sinistral and dextral reactivation of pre-existing structures in the eastern Finlayson belt during shallow NW-SE shortening.

or just preferred flattening of the fold axis along the lineament, but the localized retrogression and alteration of the structure suggests a preferred fluid conduit and our interpretation as a major fault (Fig. 3–8a).

Magmatic activity was ongoing after sinistral transpression, evidenced by the intrusion of dykes along S_2 foliation (Fig. 3–1c). Some dykes show weak S_3 chlorite foliation and pure shear, plastically deformed quartz veins supporting the intrusion of dykes before S_3 flattening. Recrystallisation to the coarser texture of pillows related to contact metamorphism strengthens the rock, protecting it against pervasive S_3 chlorite retrogression and shortening. Retrogressive chlorite in these pillow basalts is confined to the margins of amphibole grains (Fig. 3–2k), also consistent with contact metamorphism occurring prior to the onset of greenschist facies retrogression.

Pure shear, greenschist facies deformation (D_3) is defined by the onset of chlorite retrogression and the development of S_3 foliation with no lineation. Chlorite becomes stable below approximately 550°C (Fig. 3–7), which marks the upper temperature limit for the onset of D_3 deformation. Titanite appears at approximately 500°C (Fig. 3–7). As ilmenite is still stable during D_3 flattening, the static overgrowth of titanite defines the lower bound for shortening associated with D_3. The pressure conditions for D_3 are unconstrained. The shortening axis rotated from approximately north-south during D_2 to northwest-southeast during D_3, perpendicular to the current orientation of the eastern boundary and the inferred Marmion Shear Zone. The flattening intensifies towards the Marmion Shear Zone from 50% to 63%. The strain estimate of 63% was measured in the contact metamorphic aureoles where strain is at a local minimum. Therefore, we infer that shortening in the chlorite schists was greater than 63% during D_3. The increased intensity of retrogression in the eastern Finlayson may be related to increased fluid flow closer to the eastern margin along the Marmion Shear Zone. Therefore the eastern boundary of the Finlayson belt is likely a crustal scale structure with enhanced greenschist facies retrogression in its proximity.

We have shown that coaxial shortening occurs across the transition from greenschist facies ductile flattening (D_3) into brittle faulting (D_4), presumably during exhumation (Fig. 3–7). The localisation of brittle deformation in the eastern part of the belt near the Marmion Shear Zone supports the hypothesis of continued activity on this structure during exhumation.

The exact ages of deformation events in the Finlayson belt are not known, but can be broadly tied into the tectonic evolution of the Superior Province. The early deformation events (D_1 and D_2) of the Finlayson belt are likely associated with the stabilisation of the 2.9 - 3.0 Ga Marmion terrane of the south-central Wabigoon subprovince. The larger Wabigoon subprovince is suggested to have formed by accretion of the Marmion, Winnipeg River, eastern and western Wabigoon terranes as early as 2.92 Ga (Tomlinson *et al.*, 2004; Percival, 2007a), which is consistent with the youngest ages of the Finlayson belt and adjacent gneiss terranes. A possible cause of the post-D_2 deformation could be related to the accretion of the Wawa, Wabigoon and Quetico subprovinces (Percival & Williams, 1989; Williams, 1990). Amalgamation of Archean subprovinces to form the Superior Province occurred between 2.72 - 2.68 Ga and has been suggested as a significant part of continental growth during Earth history (Polat & Kerrich, 2001). Brittle reactivation of structures in other greenstone belts in the Wawa subprovince have been tied to the activity of the Quetico Fault at around 2.7 Ga (Peterson & Zaleski, 1999), which lies just to the south of the Finlayson belt (Fig. 3–1a). Our interpreted NW-SE shortening direction for D_3 and D_4 deformation associated with the reactivation of the Marmion Shear Zone is kinematically consistent with dextral transpression on the Quetico Fault.

3.7 Resolving the tectonic settings for greenstone belts

The overall dome-and-keel geometry of TTG-greenstone belt provinces is common throughout Archean cratons, yet the tectonic processes and kinematics that formed them are still much debated. Dome-and-keel provinces globally have been compared and subdivided into three kinematically different settings that allow for orogenic collapse-, accretionary- and diapiric style tectonics (Marshak & Alkmim, 2012) . The subsurface geometry of the inter-dome greenstone belts has been interpreted by seismic and gravity surveys and vary from basin-shaped synclinal belts (Gibb *et al.*, 1988; Peschler *et al.*, 2004; Ranganai, 2012) to flat sheet-like geometries related to thrust faulting of allochthonous belts (Stettler *et al.*, 1988; de Wit, 1991; Stettler *et al.*, 1997). Ground-truthing of the model for synformal greenstone belt structures is drawn from symmetric metamorphic grades and synformal symmetry of mapped units, such as inward facing paleo way-up orientations of pillow basalts (Collins & Teyssier, 1990; Minnett & Anhaeusser, 1992; Lin, 2005). On the one hand, field evidence for synformal greenstone belt geometries has been reported in most Archean terranes, such as the Warrawoona greenstone belt, Pilbara (Collins & Teyssier, 1990) and the Barberton greenstone belt, Kaapvaal (Anhaeusser, 1984).

On the other hand, evidence for non-synformal geometries from asymmetric metamorphic grades and structures of the same greenstone belts is also reported (de Wit, 1982; Kloppenburg *et al.*, 2001). Although the tectonic implications are disputed, a common result from detailed structural studies in greenstone belts is a polydeformation history (de Wit, 1991; Peterson & Zaleski, 1999; Polat & Kerrich, 1999; Tomlinson *et al.*, 1999; Kloppenburg *et al.*, 2001; Lin, 2005; Kerrich & Polat, 2006; Lin & Beakhouse, 2013).

We emphasize here the complex and diverse tectonic histories recorded in Archean greenstone belt terranes and that multiple kinematic interpretations are presented for single greenstone belts globally, similar to the previous work for the Finlayson Lake greenstone belt. By combining detailed field mapping with structural and kinematic data we are able to establish the deformation history of greenstone belts and test the different hypotheses that exist for individual terranes. The consistent structural and kinematic evidence from across the Finlayson Lake greenstone belt supports the presence of a single volcanic package with a common deformation history. We show that the greenstone belt records a polydeformation history with sub-horizontal shortening axes and that the eastern boundary was an active structure during compressive deformation and exhumation. Thermodynamic data from mineral analyses show that the shortening axis was horizontal to depths of 27 - 30 km (D_1). Sinistral transpression of the Finlayson belt continued along the exhumation path past 21 km depth for D_2 and followed by flattening during the D_3 greenschist facies and D_4 brittle regimes. The overall structural geometry of the greenstone belt is not consistent with a synform as was previously proposed (Stone & Kamineni, 1989), but rather related to a belt-scale anticline, the hinge line of which we interpret as the trace of the Finlayson Fault. Local reversals in paleo way-up orientations within the Finlayson belt can be explained by counterclockwise folds and sinistral transpression kinematics during D_2. Measurements from the exposed eastern boundary show a steep slightly outward (southeast) dipping greenstone belt margin, in contrast to the inward-dipping basin-shaped structure that was interpreted from gravity studies (Gibb *et al.*, 1988).

It is important to highlight that siliciclastic sediments and clasts of tonalite similar in age and composition to the 3.0 Ga Marmion gneisses are incorporated within the Finlayson belt (Stone, 2010) (and this study). The age and structural relations between the Finlayson and exposed Marmion-equivalent terranes rule out the possibility of crustal buoyancy contrasts required for diapiric juxtaposition. The pressure-temperature calculations for maximum burial at D_1 and peak metamorphism at D_2 show a geothermal gradient of 20 and 30°C/km, respectively. This is significantly colder compared to geothermal gradients of 30 - 50°C/km expected for greenstone-TTG terranes in the Archean (Watson, 1978; Condie, 1984). The cold geothermal gradient from our calculated pressure-temperature path (Fig. 3–7) is typical for subduction-accretion models as suggested for other Archean terranes (Kisters *et al.*, 2012; Dziggel *et al.*, 2014). The pressure-temperature path of the Finlayson belt shows a steep exhumation path along near-isothermal conditions forming a clockwise pressure-temperature path (Fig. 3–7). Clockwise pressure-temperature paths are common for modern continental collision and subduction settings (Ernst, 1988; Handy *et al.*, 1999; Van Staal *et al.*, 2008). A modern example in the Alpine subduction-accretion setting (the Ivrea crustal section), shows a multistage deformation history of prograde and peak metamorphism accompanying the dominant structural fabrics, followed by overprinting greenschist facies retrogression during exhumation (Handy *et al.*, 1999).

The deformation fabrics in the Finlayson belt, specifically D_2 structures, have strong similarities to deformation fabrics described for the Schreiber-Hemlo greenstone belt in the Wawa subprovince, including steep fold axes that have been attributed to a transpressional setting (Polat & Kerrich, 1999; Kerrich & Polat, 2006). Polat and Kerrich (1999) interpret the tectonic setting of the Schreiber-Hemlo greenstone belt as a result of subduction-accretion. It is important when interpreting the paleo-tectonic setting of Archean rocks to account for the conditions of petrogenesis, deposition, deformation and metamorphism.

The lithologies of the Finlayson belt are comparable to any typical Archean greenstone belt, containing abundant pillow basalts and massive basaltic lavas as the predominant lithologies together with siliciclastic siltstone, sandstones and conglomerates and chemical sediments followed by younger felsic intrusives. No komatiites have been observed in the Finlayson belt, but komatiites have been mapped in the adjacent Lumby Lake greenstone belt, which is of the same age. These lithologies have been argued to be typical of oceanic plateaus (Desrochers *et al.*, 1993; Polat & Kerrich, 1999; Wang *et al.*, 2013), where magmatic production is more volumetrically significant than sedimentation, and water depth is somewhat shallow.

Comparing Archean greenstone belts to modern subduction-accretion settings based on lithologies is difficult, as the archetypal signature is the dominant sedimentary package, which are not observed in most greenstone belts. The depositional basins associated with Phanerozoic subduction settings are quite variable. Most trench deposition is characterized by voluminous, relatively immature clastic sediments, with minor volcanics and chemical sediments (Xiao *et al.*, 2002; Ota *et al.*, 2007). Tectonic mélanges, thought by many to be a structural signature of subduction, form most readily in subducting sediments (Moore *et al.*, 1985). However, many active subduction zones have little or no sediment deposited in the trench, and the subducting pile is dominated by oceanic magmatic rocks and chemical sediments. Thin subducting sediments are correlated with narrow, intense shearing, so the voluminous tectono-sedimentary mélanges known from Phanerozoic accretionary wedges are not expected (Meneghini *et al.*, 2009). Oceanic plate assemblages, subducted and then tectonically underplated, are preserved in the rock record (e.g. the Nicoya Ophiolite; Berrange & Thorpe (1988); Vannucchi *et al.* (2006)). This phenomenon may be favoured by thicker, more buoyant oceanic crust, even under modern conditions. Thus, a modern analog exists for developing an assemblage dominated by oceanic volcanism and minor sedimentation (oceanic plateau or proximal rift) and imposing a subduction-type metamorphic path on those rocks. The lithologies of the Finlayson belt do not discriminate between depositional settings (e.g. back arc, rift, oceanic plateau). Our observations, which focus on the detailed structural and metamorphic history of the Finlayson belt show similarities in structural and metamorphic evolution to modern subduction-accretion settings.

3.8 Conclusions

We have shown that the Finlayson Lake greenstone belt preserves a polydeformation history of at least four distinct events that follow a clockwise pressure-temperature path. The shortening axis remains horizontal throughout the deformation history, recording an older amphibolite facies sinistral transpression during peak metamorphism, which is followed by a retrogressive flattening and brittle faulting during exhumation. Our results are consistent with a subduction-accretion tectonic setting for the Finlayson Lake greenstone belt. Detailed kinematic and structural studies of greenstone belts worldwide show the importance of polydeformation histories with varied shortening orientation, often sub horizontal. Therefore, in order to correctly interpret the tectonic settings of greenstone-TTG terranes the details of the local and regional deformation histories need to be understood. In this study we show that by further defining the kinematics and deformation histories of Archean terranes, the tectonic processes that juxtaposed supracrustal and crustal terranes can be tested. This is a necessary step before we can truly resolve the tectonic processes that resulted in all representative greenstone belt geometries globally and further our understanding of early Earth processes.

CHAPTER 4
Deformation History of the Marmion Tonalite Gneiss

This Chapter focuses on the anastomosing deformation corridor in the Marmion tonalite gneiss and has been submitted to the Journal of Structural Geology as *"No Shear Thing: Deformation adjacent to a dormant shear zone"*. The abstract is as follows:

Deformation adjacent to faults and shear zones is traditionally thought to correlate with slip. Inherited structures may control damage geometry, localizing fluid flow and deformation even after shear zone activity has ceased. In this paper, we document a post-shearing anastomosing foliation and fracture network that developed to one side of the Mesoarchean Marmion Shear Zone. The shear zone juxtaposed a greenstone belt against tonalite gneiss, and was locked by an intrusion at $\sim$ *2.78 Ga. After cessation of activity, fluids channeled along fault- and intrusion-related fractures led to the pervasive sericitization of feldspars. Flattening in sericite-rich foliated zones resulted from the weakening of the tonalites during progressive alteration without any change in the regional NW-SE shortening direction. The anastomosing pattern may have been inherited from an earlier ductile fabric, but the fractures, alteration to sericite and flattening fabrics all formed post-shearing. Thus, the apparent foliated fracture network adjacent to the Marmion Shear Zone is a second-order effect of shear-related damage, distinct in time from shear activity. This phenomenon has implications for tectonic reconstructions and long-term fault zone permeability.*

4.1 Introduction

Zones of deformation, fluid flow, and alteration are commonly observed around major faults and shear zones and are attributed to slip-related damage. Most major shear zones have a long history of multiphase deformation and reactivation. Damage aureoles may reflect inherited structures, obscuring the relationship between fault core and damage zone. Once established, damage zones may act as a locus for fluid flow and deformation after activity on the shear zone that formed them has ceased.

In the traditional view, damage zones develop as the lower strain deformation around faults/shear zones and record distributed small offset fracturing ("damage") during progressive slip along principal slip surfaces (Chester & Logan, 1986; Chester & Chester, 1998; Gudmundsson *et al.*, 2001; Sibson, 2003; Kim *et al.*, 2004). The deformation intensity within damage zones typically shows a gradually decreasing fracture density away from the fault core (Chester & Logan, 1986; Rawling *et al.*, 2001; Shipton & Cowie, 2003; Faulkner *et al.*, 2003; Mitchell & Faulkner, 2009; Faulkner *et al.*, 2010; Savage & Brodsky, 2011). Permeability around fault zones is controlled by fluid conduits or barriers and can be localized or distributed (Caine *et al.*, 1996; Faulkner *et al.*, 2010). Fault zones and their associated wall-rock damage zones influence fluid flow through the crust and allow for deep crustal fluids to move to shallower depths (Sibson *et al.*, 1988; Sibson, 1992; Kennedy *et al.*, 1997; Cox, 2002; Kulongoski *et al.*, 2013). Fluid flow through fault zones is often recorded as hydrothermal alteration of the fault core and wall rock (Goddard & Evans, 1995; Clark *et al.*, 2005; Caine *et al.*, 2010; Morton *et al.*, 2012; Arancibia *et al.*, 2014). Concentrated flow of fluids through fault zones may also lead to the formation of economic ore deposits, which are commonly associated with damage zones of major crustal faults (Vearncombe, 1998; Sibson, 2001; Piessens *et al.*, 2002; Micklethwaite, 2009; Moir *et al.*, 2013).

We present detailed regional and micro-structural observations of a deformation aureole adjacent to the Mesoarchean Marmion Shear Zone (MSZ) in the southwestern Superior Province (Figure 4–1). The shear zone juxtaposed supracrustal mafic volcanics with crustal tonalites. Deformation and alteration around the shear zone are preferentially developed in the rheologically stronger tonalites, which also host the disseminated, low-grade Hammond Reef gold deposit. Strain in the tonalites is expressed as an anastomosing foliation. Anastomosing deformation networks have been related to shearing and described as the ductile style of damage zones in plastically deformed shear zones (Carreras *et al.*, 2010). In this paper we relate the observed deformation fabrics in the tonalites to the regional deformation history in order to reveal a disparity in relative timing of anastomosing foliation with respect to the activity of the Marmion Shear Zone.

4.2 Geological setting

The Superior Province of North America is composed of Mesoarchean to Neoarchean tonalite-trondhjemite-granodiorite (TTG) and greenstone belt terranes. Our study area sits within the south-central portion of the Wabigoon subprovince, which lies immediately to the north of the Quetico subprovince, across the Quetico fault (Figure 4–1). The Wabigoon subprovince is a mainly Mesoarchean crustal block that accreted together from the Marmion, Winnipeg River, eastern Wabigoon and western Wabigoon terranes at around 2.92 Ga (Tomlinson *et al.*, 2003, 2004; Percival, 2007a).

Younger, east-west-trending terrane boundaries record a progressive north-to-south amalgamation of subprovinces between 2.72 and 2.68 Ga (Corfu & Stott, 1986; Polat & Kerrich, 2001; Percival *et al.*, 2006; Percival, 2007a). The southern margin of the Wabigoon subprovince is the $\sim$ 2.7 Ga Quetico fault, which records dextral transpressional movement during accretion of the Quetico and Wawa subprovinces from the south (Corfu & Stott, 1986; Percival & Williams, 1989; Williams, 1990; Bauer *et al.*, 1992; Peterson & Zaleski, 1999), associated with northward subduction of the Wawa subprovince (Calvert *et al.*, 1995).

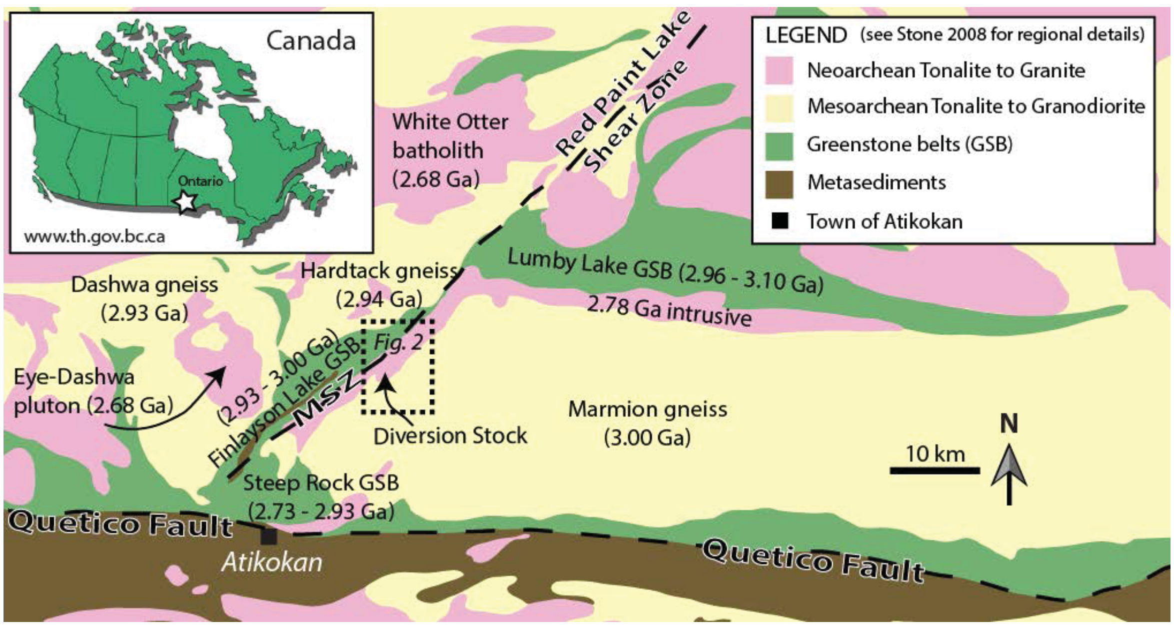

Figure 4–1: A simplified regional geological map of the south-central Wabigoon subprovince showing the ages of the Archean tonalite-trodhjemite-granodiorite (TTG) and greenstone belt terranes (Stone, 2008a). Major faults and shear zones are marked by dashed lines. The Marmion Shear Zone (MSZ) marks the eastern boundary of the Finlayson Lake greenstone belt as the southwestern continuation of the Red Paint Lake Shear Zone. The east-west trending dextral Quetico fault to the south of the field area separates the Wabigoon subprovince (north) from the Quetico subprovince (south). Inset map: The field area (star) is situated in the southwestern portion of the Superior Province in Ontario, Canada.

The Marmion Shear Zone juxtaposed the 2.93 Ga Finlayson Lake greenstone belt and 3.00 Ga Marmion tonalite gneiss, forming the southwestern continuation of the Red Paint Lake Shear Zone (Figure 4–1) (Davis & Jackson, 1988; Stone, 2008a). The shear zone core is not exposed, and the regional deformation history and pressure-temperature path have been inferred from structures and metamorphic assemblages of the Finlayson Lake greenstone belt (Backeberg *et al.*, 2014). The greenstone belt experienced deep (~820 MPa, or 27 – 30 km depth) oblique shortening along a NNW horizontal shortening axis, which has been tied to the earliest accretionary period of the Wabigoon subprovince at 2.92 Ga (Backeberg *et al.*, 2014). Two separate coaxial flattening events followed the NNW shortening and record a rotation of the shortening axis to NW during exhumation, perpendicular to the shear zone. The boundary between the Finlayson Lake greenstone belt and Marmion tonalites (the Marmion Shear Zone) is intruded by the Diversion Stock tonalite–granodiorite (Figure 4–1).

The age of the Marmion Shear Zone is constrained by cross-cutting relations. The upper limit of deformation is at 2.93 Ga, which marks the youngest deposition ages in the Finlayson Lake greenstone belt (Davis & Jackson, 1988; Tomlinson *et al.*, 1999, 2003; Stone, 2008a). The younger bound for any major displacement along the Marmion Shear Zone is limited by the cross-cutting of the $\sim$ 2.7 Ga Quetico fault to the south (Corfu & Stott, 1986; Williams, 1990; Bauer *et al.*, 1992). An anastomosing foliation runs parallel to the Marmion Shear Zone and overprints both the Marmion and Diversion Stock tonalites (Figure 4–2). The anastomosing network has also been referred to as the Marmion deformation corridor by the Osisko Mining Coorporation and other exploration companies (Osisko, 2013). Although both greenstone belt and tonalites have well-developed foliation zones, gold was only deposited in the anastomosing foliation zone in the tonalites, forming the Hammond Reef gold deposit (Figure 4–2). We study the deformation and alteration history of the shear zone-flanking anastomosing foliation to assess relative roles of strain and fluid flow along the western margin of the Marmion gneiss.

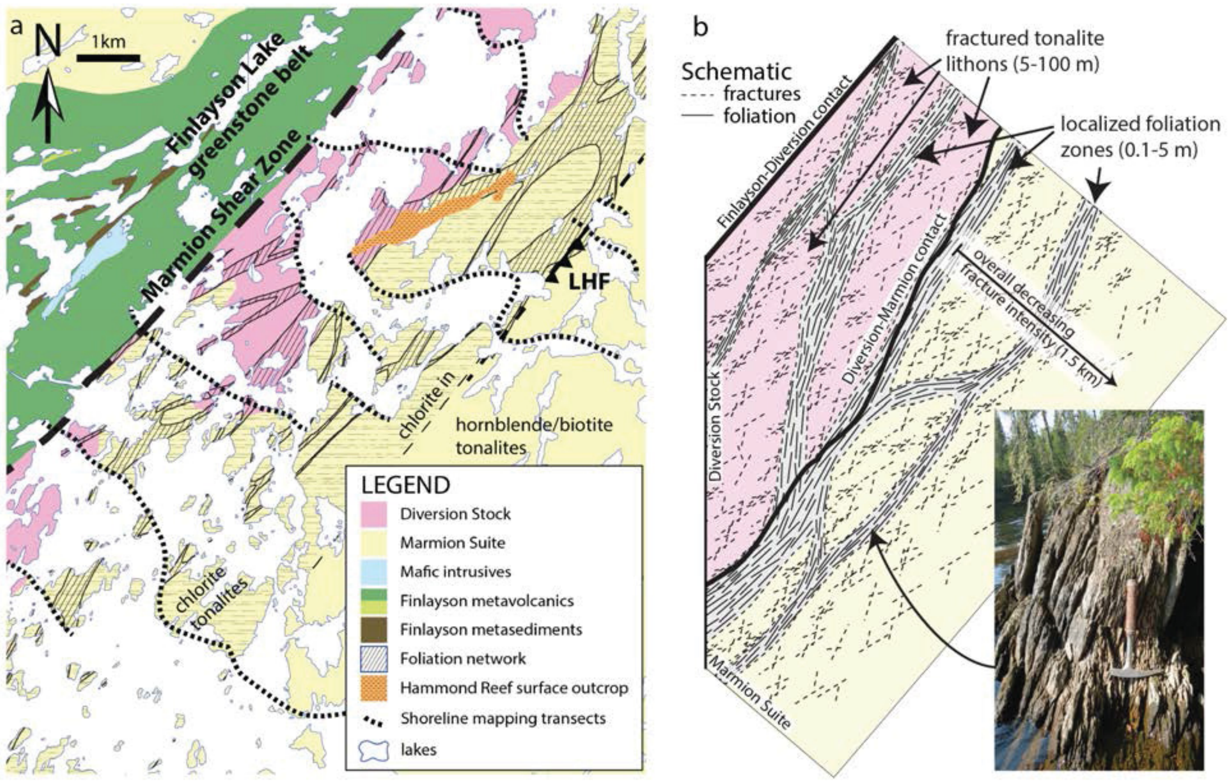

Figure 4–2: (a) Map of Marmion-Finlayson terrane boundary adapted from Stone (2008), showing the anastomosing foliation across the Diversion Stock and Marmion Suite. Lithological contacts are inferred due to lack of exposure and are only mapped along lake-shore exposures. Lakes are shown as translucent white areas. The southeastward extent of chlorite retrogression in the Marmion Suite is shown by the dashed “chlorite in” line, which lines up with known exposures of the Lynx Head Fault (LHF). The surface exposure of the Hammond Reef gold deposit is shown (orange area). (b) Schematic map of anastomosing foliation (not to scale), showing localized foliation zones (solid lines in grey-shaded area) and interfoliation lithons with fractures (dashed lines). Decreasing density of fractures in the Marmion Suite is schematically drawn. The photo shows a field exposure of a foliated tonalite.

4.3 Geology of the western margin of the Marmion gneiss

Field data and samples were collected from mapping transects along lake-shore exposures (Figure 4–2). Structural data were compiled to identify structural trends and variation in the observed fabrics. We developed a classification scheme for structural fabrics, which differentiates features related to alteration, pure shear and simple shear. Using structural fabrics and mineralogy, we define a detailed lithological classification to identify Diversion Stock and Marmion samples (Table 4–1), as the units have an overlapping bulk-composition and are therefore easily confused in the field. This distinction is used to establish cross-cutting relations between intrusion, alteration and deformation events.

4.3.1 Marmion Suite tonalites

The Marmion gneiss is a 3.002 Ga TTG terrane that covers over 200 km^2 (Figure 4–1). According to published maps, the Marmion gneiss is described as either a biotite or a hornblende-biotite tonalite (Stone, 2008b). Wasteneys (2011) identified pegmatites and leucotonalites as sub-units of the Marmion gneiss within the Hammond Reef area. We have differentiated four lithologic units based on cross-cutting relationships and group these together as the "Marmion Suite". In order of oldest to youngest, the Marmion Suite consists of: porphyritic tonalite, very fine-grained tonalite, main Marmion tonalite and leucotonalite (Table 4–1). The main Marmion tonalite is the most volumetrically significant and fits the description of the Marmion gneiss presented on geological maps (Stone, 2008b). The porphyritic and very fine-grained tonalites occur as xenoliths within the main tonalite, whereas

Table 4–1: Comparative table between the Diversion Stock intrusive and the Marmion Suite terrane. Mineralogy abbreviations correspond to quartz (Qtz), feldspar (Fsp), plagioclase (Pl), microcline (Mc), hornblende (Hbl), biotite (Bt) and muscovite (Ms). *correlated to intrusive south of Lumby Lake greenstone belt (Buse *et al.*, 2010a) **Stone (2010)

	Diversion Stock	Marmion Suite
Rock types	tonalite – granodiorite	4 tonalite sub-units: porphyritic, very fine, main and leucotonalites
Age (Ma)	? (2786 ± 1, correlated)*	3002 ± 3**
Primary Mineralogy	Qtz, Pl, Mc, Hbl, Ms	Qtz, Pl, Hbl, Bt
Outcrop characteristic	Qtz coarser than Fsp	Qtz finer than Fsp
Fabrics	none	aligned Hbl
Alteration to chlorite	weak, not aligned	pervasive, aligned
Alteration to sericite	pervasive, locally flattened	pervasive, locally flattened

the leucotonalite is volumetrically very minor and only found as small dykes intruding the main tonalite. All lithological variants of the Marmion Suite, except for the leucotonalite, have a weak gneissic fabric due to aligned crystals of metamorphic amphibole. They are composed of the same minerals with 20 - 30 wt.% mafic minerals, though variable in grain size. Even in tonalites with a weak gneissosity, amphibole grains are lineated. Rare folds are observed in the tonalites, where the gneissosity is more strongly developed. Plagioclase along the western margin of the tonalites have very low calcium contents with compositions of An_{02-07}, which we obtained by electron microprobe. Eastward away from the western margin, (to east of the Lynx Head Fault (LHF), Figure 4–2) the calcium content is only slightly higher with compositions of An_{17-20}.

4.3.2 Diversion Stock tonalite–granodiorite

The Diversion Stock is up to 2 km wide and intrudes along the original Finlayson Lake greenstone belt and Marmion Suite contact, i.e. the Marmion Shear Zone (Figure 4–2). A similar intrusive unit, mapped between the Marmion Suite and Lumby Lake greenstone belt to the north, has an age of 2.786 Ga (Buse *et al.*, 2010a) and is inferred to be contiguous with the Diversion Stock (see Figure 4–1). However, this correlation is uncertain due to lack of exposure and lack of Diversion Stock geochronology. The contact of the Diversion Stock with the Finlayson Lake greenstone belt is expressed as a zone of alternating mafic and felsic zones spanning an area of 50 to 100 m. This has been interpreted as felsic dykes of the Diversion Stock intruding parallel to the well-developed chlorite foliation of the greenstone belt's eastern margin (Backeberg *et al.*, 2014). The Diversion Stock locally contains K-feldspar (microcline), which is absent in the Marmion Suite (Table 4–1). The calcium content of plagioclase in the Diversion Stock is low, identical to the Marmion Suite (An_{02-07}). Furthermore, the Diversion Stock has preserved magmatic features, including primary hornblende and a micrographic intergrowth of quartz and feldspar. No ductile fabrics, such as gneissic banding, folding or mineral lineations were observed (Table 4–1).

Both the Diversion Stock and the Marmion Suite are cut by Proterozoic mafic dykes trending WNW across the Archean structural fabrics (seen on magnetic anomaly maps, Ontario Geological Survey, 2009). Older mafic dykes are common in the Marmion Suite, but are absent in the Diversion Stock, therefore inferred to be Archean in age. These dykes are highly altered to calcite and chlorite. The Archean dykes show similar flattening deformation and chlorite alignment, as seen along the eastern margin of the Finlayson Lake greenstone belt, where the original basalts have all been altered to chlorite schists (Backeberg *et al.*, 2014), consistent with alteration and flattening occurring prior to the emplacement of the Diversion Stock.

4.3.3 Alteration to chlorite

Within a 3–4 km wide zone southeast of the Marmion Shear Zone, hornblende and biotite are partially to completely replaced by chlorite (Figure 4–2). Hornblende and biotite are better preserved east of the Lynx Head Fault (LHF, Figure 4–2). In the Marmion Suite, chlorite is preferentially aligned parallel to the Marmion Shear Zone, whereas chlorite in the Diversion Stock is only weakly aligned (Table 4–1). A transect in the southern portion of the field area reveals a gradational appearance of chlorite at about 4 – 5 km southeast of the Marmion Shear Zone. The chlorite-in limit lines up approximately along strike of the Lynx Head Fault (Figure 4–2).

4.3.4 Alteration to sericite

A zone of altered plagioclase overlaps with the chlorite-altered zone. Plagioclase alters to very fine-grained micas (sericite), epidote and albite, which we observed using the electron microprobe. Alteration to sericite is characterized by a variable intensity of alteration in both the Diversion Stock and Marmion Suite (Figure 4–3). Where feldspar is partially altered, sericite is concentrated along fractures and grain boundaries (Figure 4–3b). Pervasively sericite-altered tonalites may preserve the original rock texture as pseudomorphs after feldspars (Figure 4–3d) and in Diversion Stock tonalites, even micrographic textures are preserved.

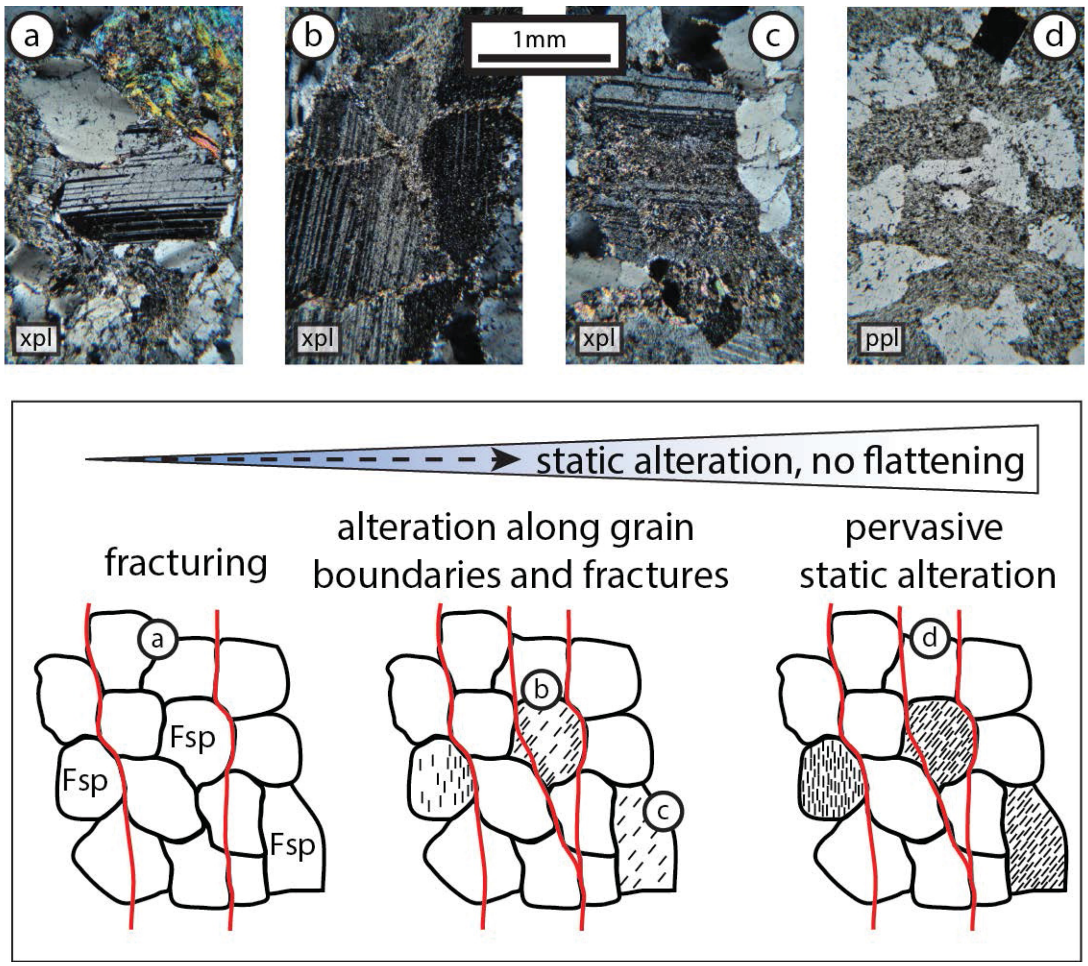

Figure 4–3: Variations in intensity of sericite alteration of feldspar (Fsp) without strain accommodation as seen throughout the Marmion Suite and Diversion Stock. (a) Unaltered plagioclase. (b) Fracture and grain-boundary localized sericite alteration. (c) Partially sericite-altered plagioclase. (d) Pervasive sericite alteration preserving plagioclase pseudomorphs.

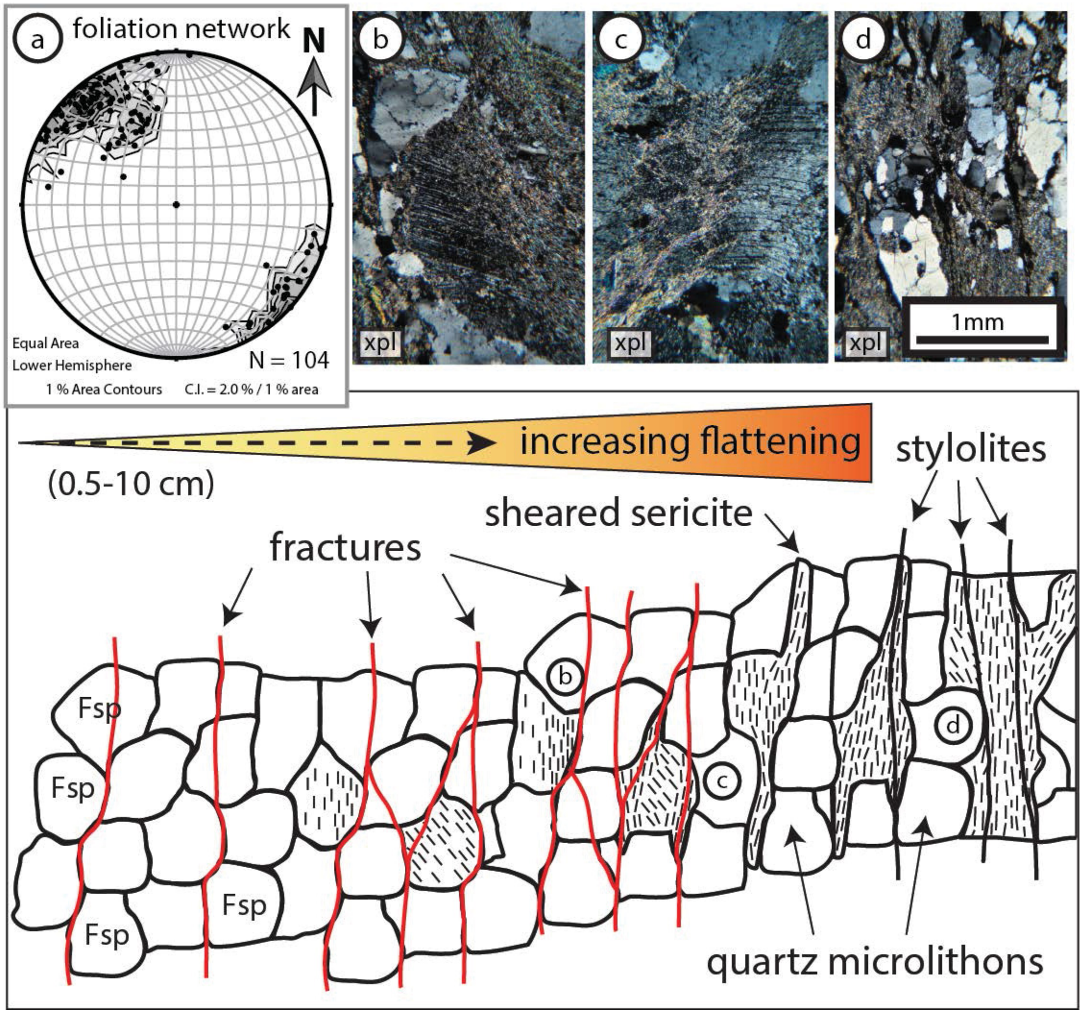

Figure 4–4: Progressive flattening of sericite flakes from altered feldspars (plagioclase and microcline) aligns to form foliation in tonalites. (a) Stereonet of poles to foliation-plane orientations showing a well-developed NE–SW strike and sub-vertical dip. (b, c) Partially altered feldspars show alignment of sericite flakes parallel to foliation, concentrated along fractures. Photo b also shows preferential alteration of plagioclase to one side, where the other side is shielded from alteration by the surrounding quartz. (d) Pervasively altered tonalites preserve no feldspar and sericite is aligned, defining the foliation fabric. Fractured quartz microlithons and stylolites are aligned parallel to foliation.

4.3.5 Anastomosing foliation

Stone (2008) mapped a zone of anastomosing deformation along the western margin of the tonalites, known as the Marmion deformation corridor (Osisko, 2013). Although the deformation fabric is more strongly developed in the Marmion Suite, it also cross-cuts the Diversion Stock (Figure 4–2). The deformation fabric extends up to 3 km away from the Finlayson Lake greenstone belt boundary (Figure 4–2). The anastomosing pattern is defined by localized foliation zones that strike on average 050° (035° – 075°) with a dip of 60° – 80° to the southeast (Figure 4–4a), parallel to the Marmion Shear Zone.

Individual foliated strands range between 0.1 m and 5 m wide with a gradual decay in the foliation intensity on either side. The deformation correlates to the degree of alignment of sericite in the altered feldspars (Figure 4–4). Remnant feldspars within highly sericitized tonalites are preserved where surrounded by quartz (Figure 4–4b). In cases where a significantly altered feldspar is strained, the sericite is flattened and sheared into foliation-parallel fractures (Figure 4–4c). Aggregates of quartz are preserved as aligned boudins in the foliated sericite (Figure 4–4d). The overall foliation intensity is correlated to the phyllosilicate content, including sericite and chlorite. Stylolites are developed parallel to sericite foliation and generally intersect with the quartz grain boundaries (Figure 4–4d). Small opening-mode quartz veins ($<$ 1 mm thick) are also observed parallel to foliation.

The unfoliated tonalite lithons in between the foliated strands do not show any direct evidence of flattening, despite the partial to pervasive alteration of plagioclase

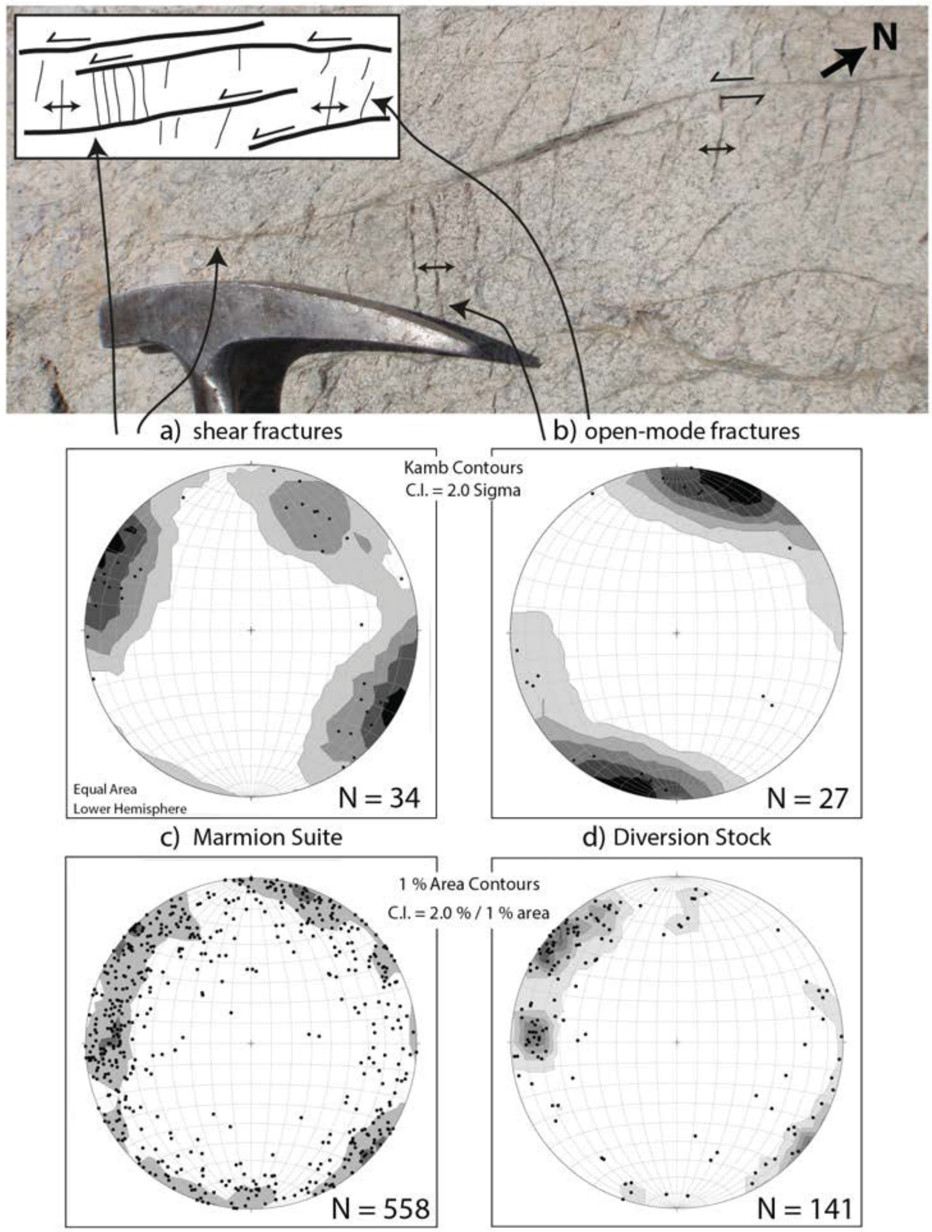

Figure 4–5: Fracture pattern preserved in tonalite lithons (see Figure 4–2b). The fracture pattern in the Marmion Suite is defined by two perpendicular sets of long curvilinear sinistral shear fractures striking NNE and short, WNW-trending opening-mode fractures that terminate along shear fractures. (a and b) Outcrops where both (a) shear fracture and (b) open-mode fracture sets are well exposed together. (c and d) Owing to the lack of exposure and weathering intensity, the fractures across the study area were mostly recorded as undifferentiated (see text). (c) Fractures measured in the Marmion Suite, excluding the data presented in stereonets a and b. (d) Fractures measured in the Diversion Stock.

to sericite (Figure 4–3). The lithons are fractured with a density of 10s to 100s of fractures per meter. Glacially polished exposures of the Marmion Suite, stripped during exploration activities, show a pattern of perpendicular shear and opening-mode fractures (Figure 4–5). Long curvilinear shear fractures (mostly sinistral) trend approximately NNE and have a typical spacing of > 5 cm (Figure 4–5a). Shorter open-mode fractures terminate at the intersection with the shear fractures and trend WSW with a fracture spacing of < 1 cm (Figure 4–5b). Away from stripped outcrops, weathered exposures do not allow for the classification of shear versus opening-mode fractures. Therefore, we documented undifferentiated fractures throughout the western margin of the study area. The undifferentiated fracture data define the same pattern of NNE- and WSW-trending subvertical fractures in the Marmion Suite (Figure 4–5c). Only the NE- to NNE-trending fracture group is observed in the Diversion Stock, but the pervasive WSW-striking opening-mode fractures are absent (Figure 4–5d).

4.3.6 Late-stage brittle faults

Late brittle faults cross-cut the anastomosing foliation. These faults strike northeast with a dip of approximately 40° to the southeast and commonly display down-dip lineations. The slip surface is coated with sericite, giving it a greenish sheen. These faults have thrust kinematics, observed from small-scale drag folding of the foliation as well as fault-surface roughness of the smeared sericite, down-stepping in the direction of slip. Thrust kinematics have previously been reported in the area together with shallow-dipping faults (Wasteneys, 2011).

The largest of these faults is the Lynx Head Fault (LHF) to the east of the Hammond Reef deposit (Figure 4–2). The trace of the fault can be drawn from magnetic anomaly maps (Ontario Geological Survey, 2009), where the fault is cut by a Proterozoic mafic dyke. The fault displaces unaltered hornblende-biotite tonalites with pristine feldspar towards the NW over chlorite- and sericite-altered tonalites (Figure 4–6), consistent with reverse motion. The upper footwall tonalite is foliated parallel to the Lynx Head Fault (Figure 4–6). The structural stratigraphy of the fault shows two series of large fault-parallel quartz veins (Figure 4–6). Both quartz veins include blocks of altered tonalites as either centimetre-scale inclusions or as large metre-sized clasts within a megabreccia (Figure 4–6), further suggesting that the Lynx Head Fault was active after the sericite alteration of the western Marmion and Diversion Stock tonalites.

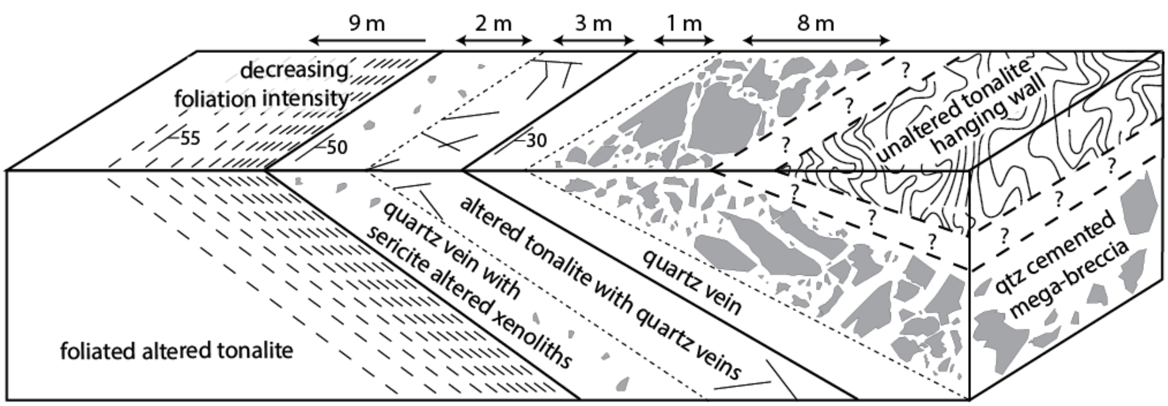

Figure 4–6: Fault stratigraphy of the Lynx Head Fault (LHF). The fault strikes 50° and dips 30° to the southeast, juxtaposing unaltered tonalites in the hanging wall next to altered, foliated tonalites in the footwall. Two large quartz veins are emplaced along the fault. The lower quartz vein carries clasts of altered tonalite and the upper quartz vein has a zone of coarse breccia in its hanging wall, also made up of altered tonalite.

4.3.7 Quartz Microstructures

We have observed overprinting brittle and ductile deformation in the tonalites to the east of the Marmion Shear Zone. In order to further differentiate the effect of the Marmion Shear Zone on the deformation textures in the tonalites, we have documented the quartz microfractures and grain-boundary microstructures (Figure 4–7).

Quartz grain boundary morphology is similar in the Diversion Stock and Marmion Suite tonalites, however, it is different in unfoliated and foliated tonalites. Within unfoliated tonalite lithons quartz grain boundaries are well preserved and show a weak bulging grain-boundary migration (Figure 4–7a). In contrast, a moderate to weak bulging and sub-grain recrystallization (Passchier & Trouw, 2005; Stipp *et al.*, 2002) is observed in quartz aggregates of foliated tonalites within the anastomosing network (Figure 4–7b). This is observed as quartz-quartz grain contact recrystallization and appearance of sub-grains along the majority of grain boundaries.

We compared healed micro-fractures in quartz-rich zones along the western margin of the Marmion Suite (2 samples) with samples collected 3 km east of the Marmion Suite – Diversion Stock contact (2 samples) (Figure 4–7d – e). Following Mitchell & Faulkner (2009), healed micro-fractures are interpreted from the planar alignment of fluid inclusions in quartz (see dashed lines in Figure 4–7). Distal samples in the Marmion Suite to the east (Figure 4–7e) clearly show a lower fluid inclusion density compared to samples in close proximity to the Diversion Stock contact to the west (Figure 4–7d). The micro-fracture density in the Diversion Stock (3 samples) is somewhat consistent across the intrusion, with a moderate to high fracture density (Figure 4–7c), similar to that of the western-most Marmion Suite.

The sample distribution presented here is insufficient to quantitatively describe the fracture density gradient across the anastomosing deformation network. However,

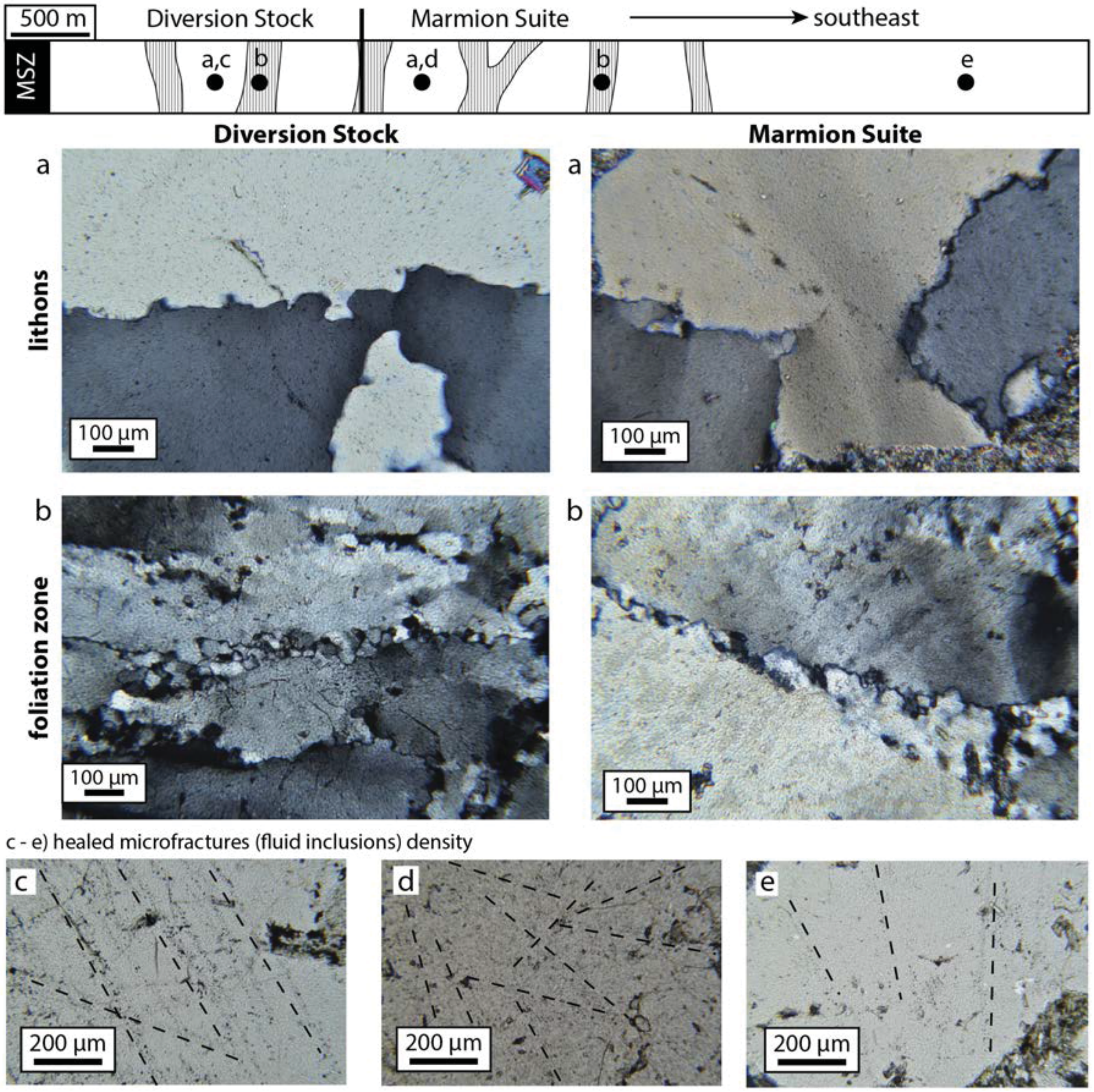

Figure 4–7: Photomicrographs of quartz-rich zones in the Marmion (right) and Diversion Stock (left). Top strip shows the relative position within the anastomosing foliation (striped area) away from the Marmion Shear Zone (MSZ). (a) Weak bulging grain-boundary migration of quartz-quartz grain boundary in unfoliated lithons of Diversion Stock and Marmion Suite. (b) Quartz aggregates (microlithons) in foliated tonalites show weak bulging recrystallization along quartz grain boundaries. (c - e) Healed microfracture density observed by planar alignment of fluid inclusions (selected dashed lines aligned next to micro-fractures for examples). (c) Moderate fracture density observed across the Diversion Stock. (d) High fracture density of western Marmion Suite, with a very high overall fluid inclusion density, giving the quartz a darker colour. (e) Lower (background) fracture density of Marmion Suite away from the western margin.

our data are consistent with an overall decrease in micro-fracture density in the Marmion Suite, away from the Diversion Stock intrusive contact.

4.4 Deformation history

Because of a lack of exposure and later overprinting, the early deformation history associated with the Marmion Shear Zone is difficult to constrain. Any kinematic reconstruction must be inferred from the deformation recorded in the adjoining terranes. In this section we focus on the deformation history of the Marmion Suite and the constraints on timing and conditions of suturing with the Finlayson Lake greenstone belt. We place the observed deformation fabrics in context with the deformation history from results of the Finlayson Lake greenstone belt (Figure 4–8) and discuss the possible implications of the observed microtextures.

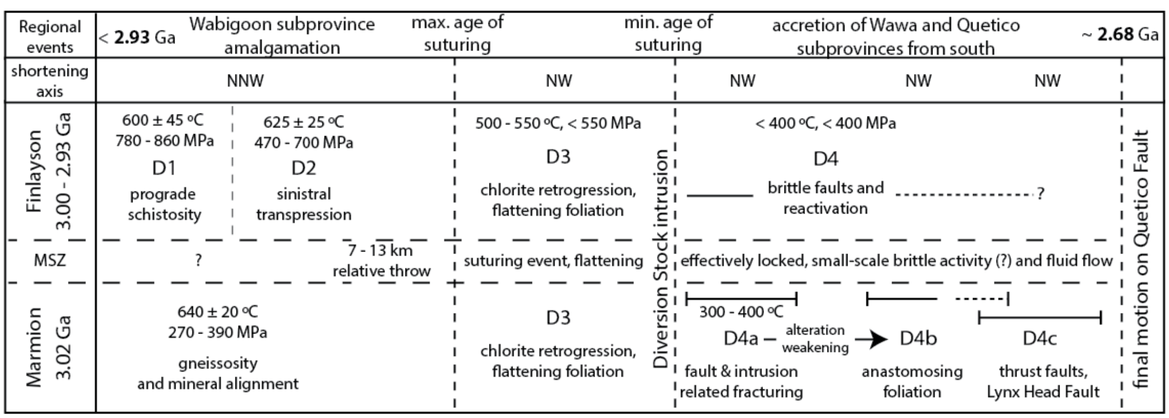

Figure 4–8: Summary of deformation history for the Marmion Suite and Finlayson Lake greenstone belt. Pressure–temperature estimates in greenstone belt taken from Backeberg et al. (2014). Maximum age of 2.93 Ga for D_1 deformation taken from youngest depositional age in the Finlayson Lake greenstone belt (Stone, 2010). Diversion Stock intrusion age of 2.78 Ga correlated to intrusive body north of Marmion Suite (Buse *et al.*, 2010a). Latest fault slip along Quetico Fault at 2.68 Ga estimated from cross-cut intrusive bodies (Williams, 1990).

4.4.1 Summary of Finlayson Lake greenstone belt deformation history

The Finlayson Lake greenstone belt preserves a more detailed structural and metamorphic history (Backeberg *et al.*, 2014). Briefly, the Finlayson Lake greenstone belt records early ductile sinistral transpression associated with a NNW horizontal shortening axis (D_1) down to a maximum depth of $\sim$29 km at 600$\pm$ 45°C. The NE-SW trending structural fabrics correspond to the D_2 peak metamorphism at 625 $\pm$ 25°C and 21 – 23 km depth. During exhumation, retrogression of amphiboles to chlorite and flattening are focused close to the eastern margin of the greenstone belt and record NW-SE shortening (D_3). Later D_4 brittle faults cross-cut and reactivate D_3 foliation at quartz-brittle conditions and record the same NW-SE shortening. These brittle faults are preferentially developed in close proximity to the Marmion Shear Zone. The Diversion Stock intrudes the shear zone along the well-developed chlorite foliation, suggesting emplacement after D_3 flattening (Backeberg *et al.*, 2014).

4.4.2 Ductile deformation

Ductile deformation structures observed in the Marmion Suite occur as lineated metamorphic amphibole, folding of gneissic fabrics and flattening of chlorite retrogressed from amphibole. Flattening of chlorite is aligned subparallel to the Marmion Shear Zone and occurs coaxially in both the Marmion Suite and the Finlayson Lake greenstone belt. Alignment of chlorite is not observed in the Diversion Stock, suggesting that chlorite flattening in the Marmion Suite is coeval with the strong chlorite foliation observed in the Finlayson Lake greenstone belt during D_3 (Figure 4–8). Amphibole lineation and folding record deformation in the Marmion Suite prior to D_3. We measured coexisting lineated amphibole and plagioclase pairs by electron microprobe for pressure–temperature constraints during amphibole lineation using the thermobarometry by Holland & Blundy (1994). Given that these mineral assemblages are stable over large pressure-temperature conditions for tonalites, the amphibole-plagioclase thermobarometry provides a best estimate, which we can relate to the deformation history and pressure-temperature conditions of the Finlayson Lake greenstone belt, which were determined by the same method (see Chapter 3). Samples were chosen east of the Lynx Head Fault, where amphibole and plagioclase are best preserved (Figure 4–2). The resulting temperature is 640 $\pm$ 20 °C at pressures of 330 $\pm$ 60 MPa for amphibole alignment (Table 4–2). These pressures correspond to a depth of 10 – 14 km, for an average tonalite density of 2.7 kg/m^3, which equates to a hot geothermal gradient of 45 – 65°C/km. Prior to D_3 deformation, the Finlayson Lake greenstone belt is at 21 – 23 km depth (Backeberg *et al.*, 2014). The depth differences between the Finlayson and Marmion requires 7 – 13 km of relative throw along the steep Marmion Shear Zone prior to or leading up to D_3 chlorite flattening (Figure 4–8).

4.4.3 Diversion Stock emplacement

Intrusion of the Diversion Stock after D_3 represents the final stitching of the two terranes and the latest time for suturing of the Finlayson Lake greenstone belt and the Marmion gneiss (Figure 4–8). All deformation fabrics during and after D_3 record NW shortening in both the Finlayson Lake greenstone belt (Backeberg *et al.*, 2014) and in the Marmion gneiss (this study), perpendicular to the Marmion Shear Zone. The regional NW-SE shortening axis is not favourable for slip along the Marmion

Table 4–2: Average hornblende and plagioclase composition (n = 4 mineral pairs) used in thermobarometry. Minerals analyzed from Sample MS071 east of the Lynx Head Fault.

	Amphibole	Plagioclase
SiO_2	47.86	63.60
TiO_2	0.52	0.05
Al_2O_3	7.64	22.30
FeO	17.29	0.13
MgO	12.78	0.00
CaO	11.97	3.55
Na_2O	0.86	8.84
K_2O	0.80	0.26
Total	99.71	98.73
X_{Ab}	-	0.80
X_{An}	-	0.20
T (°C)	640 ± 20	
P (MPa)	330 ± 60	

Shear Zone. Therefore, the suturing of the terranes and the emplacement of the Diversion Stock also imply the end of any major offset along the Marmion Shear Zone, thus making the shear zone effectively dormant.

4.4.4 Brittle deformation

All post D_3 quartz-brittle deformation fabrics in both the Finlayson Lake greenstone belt and Marmion gneiss record coaxial NW-SE shortening perpendicular to the Marmion Shear Zone. We subdivide the D_4 structures in the Marmion Suite into distributed deformation (D_{4a} and D_{4b}) and localized faulting (D_{4c}).

Distributed deformation

Perpendicular sinistral and open-mode fracture sets compatible with NW-SE shortening (D_{4a}) are observed in the Marmion Suite (Figure 4–5). Alteration to sericite is concentrated along D_{4a} fractures (Figure 4–3b). Flattening of sericite (D_{4b}) into anastomosing foliation strands subparallel to the Marmion Shear Zone (Figure 4–2b) records the continuation of NW-SE shortening (Figure 4–4a). Bulging and subgrain recrystallization textures observed in the foliated tonalites along quartz-quartz grain boundaries (Figure 4–7b) are comparable with experimental textures from low temperature deformation at 300 – 400°C (Hirth & Tullis, 1992; Stipp *et al.*, 2002). These temperatures are consistent with the predicted exhumation path for D_4 structures in the Finlayson Lake greenstone belt (Backeberg *et al.*, 2014).

Localized faults

Shallowly dipping NE-striking faults (e.g. the Lynx Head Fault) cross-cut sericite-altered tonalites and the anastomosing foliation. These faults record a change from distributed deformation ($D_{4a,b}$) to localized faulting (D_{4c}), while maintaining coaxial NW-SE shortening (Figure 4–8). At the Lynx Head Fault, we observed sericite foliation in the footwall parallel to the fault surface (Figure 4–6). As sericite-bearing tonalites are inherently weaker owing to the high modal proportion of phyllosilicates, we interpret this shallower foliation as drag and flattening coeval with D_{4c} thrust faulting. Therefore, flattening of sericite was further promoted during D_{4c} shortening. Although the direction of shortening did not change, we have documented a transition of deformation from distributed to localized (Figure 4–8).

4.5 Deformation adjacent to a dormant shear zone

The structures and fabrics in the Marmion Suite reveal overprinting stages of the late shallow deformation associated with close proximity to the Marmion Shear Zone. Combined with the details of early ductile stages of deformation preserved in the adjacent Finlayson Lake greenstone belt (Backeberg *et al.*, 2014), these results provide a continuous regional deformation path that spans the docking of the two terranes and ongoing post-docking fluid activity. In this section, we discuss the implications of the late-stage deformation along a kinematically dormant shear zone.

4.5.1 Fault- or intrusion-related damage?

In the Finlayson Lake greenstone belt, late-stage brittle fracturing is localized within < 100 m of the eastern boundary and slip is recorded predominantly by offset veins and steep slickenlines on foliation surfaces of chlorite schists (Backeberg *et al.*, 2014). In the Marmion and Diversion Stock tonalites to the southeast of the shear zone, there are less well developed pre-existing structures. The deformation in the tonalites extends up to 3 km away from the greenstone belt boundary (~ 1.5 km southeast of the Marmion-Diversion contact, Figure 4–2b). General observations of a decreasing fracture intensity in the Marmion Suite away from its western edge are comparable with documented brittle damage zones (Chester & Logan, 1986; Chester *et al.*, 2004; Mitchell & Faulkner, 2009; Faulkner *et al.*, 2010; Savage & Brodsky, 2011). Also, a relatively wider damage zone in the rheologically stronger tonalites is expected for asymmetric damage zones (Evans, 1990; Chester *et al.*, 2005; Mitchell *et al.*, 2011; Savage & Brodsky, 2011). The pattern of lower density shear fractures and higher density perpendicular open-mode fractures (Figure 4–5) has been observed in other damage zones related to fault slip (Gudmundsson *et al.*, 2001). However, the stitching of the Finlayson and Marmion terranes by the Diversion Stock precludes any major offset along the Marmion Shear Zone after emplacement. A damage zone related to fault motion could not have developed in the Marmion Shear Zone wall rocks after stitching, as damage zones require significant offset along structures in order to widen (Savage & Brodsky, 2011). Subsidiary shear and open-mode fractures were only positively identified on outcrop scale in the Marmion Suite and not in the younger Diversion Stock, although similar micro-fracture densities are observed in both units. A possible explanation is that the intrusion of the Diversion Stock displaced an older damage zone in the Marmion Suite eastward, away from the greenstone belt contact and shear zone. Any deformation after emplacement of the Diversion Stock can only have been related to the intrusion and cooling of the stock, fluid pulses, and/or small-scale slip along the two intrusive contacts either side of the Diversion Stock. Small-scale reactivation is consistent with observations of post-Diversion Stock deformation in the Finlayson Lake greenstone belt (Backeberg *et al.*, 2014). Therefore, the perpendicular fracture sets in the Marmion Suite may record pre-stitching fault activity, with associated decrease in fracture density away from the shear zone.

Considering the negligible displacement along the Marmion Shear Zone during post-D_3 deformation, it is necessary to consider other features that may have contributed to post-shearing fracturing in the Diversion Stock and pervasive alteration to sericite in both the Marmion Suite and Diversion Stock. In addition to a fault-related damage zone in the Marmion Suite, fracturing may also have occurred during the intrusion of the Diversion Stock and progressive exhumation. Intrusion-derived fluids promoting fracturing and alteration of the intrusive body as well as the country rock after cooling and crystallisation (Essaifi *et al.*, 2004; Pollard *et al.*, 2005). In this case, the intrusion of the Diversion Stock provided the fluids during exhumation and fracturing required to alter the Marmion Suite wall rock as well as the cooling Diversion Stock.

Both fault- and intrusion-related deformation likely played a role in developing the damage geometry around the Marmion Shear Zone, which bears many similarities to classical fault damage zones. However, the micro-fractures and alteration to sericite clearly cross-cuts the Diversion Stock. Therefore, we propose that the permeability structure that initiated pervasive alteration postdates any major fault motion adjacent to a dormant shear zone.

4.5.2 Fluid flow

The emplacement of the Diversion Stock affected the overall fault geometry and permeability structure of the Marmion Shear Zone. Preferential flow of a fluid along the Diversion Stock – Marmion Suite contact can be inferred from the preferential alteration close to the contact, as well as the location of the Hammond Reef gold deposit, which straddles that contact (Figure 4–2).

Fluid flow in the Marmion Suite and Diversion Stock led to the pervasive alteration of feldspar to sericite. The alteration to sericite, which was focused along fractures and grain boundaries (Figure 4–3b), did not seal flow pathways. Therefore the fluid flow resulted in incremental alteration that was distributed though the rock on the grain-scale without any strain (Figure 4–3d). This suggests that even though the tonalite was being and potassium was introduced to the plagioclase to form sericite, there was no reduction in pore connectivity to retard fluid flow. Furthermore, the gold deposit at Hammond Reef, which is intricately associated with the anastomosing foliation and is not associated with any discrete structures, must have been enriched by pervasive, grain-scale fluid flow.

4.5.3 Anastomosing foliation

Sericitized zones are locally flattened (Figure 4–4) and on the map-scale form a discontinuous anastomosing network (Figure 4–2). On the grain-scale, we observe a pattern that is defined by the alignment of sericite around undeformed quartz aggregates (microlithons), which is comparable to the definition of a continuous "rough" cleavage (Gray, 1978; Fossen, 2010). Networks of anastomosing foliation are typically associated with shear deformation (Carreras *et al.*, 2010; Ponce *et al.*, 2010). However, in the case of the deformation in the tonalites adjacent to the Marmion Shear Zone, the anastomosing deformation fabric postdates shearing and records predominantly flattening perpendicular to the shear zone.

It is unclear what the overall controls are on the initiation of localized flattening in foliation strands, which define the map-scale anastomosing network. Grain-scale textures in partially altered feldspars (Figure 4–4b and c) suggest that flattening is at least in part coeval with sericite alteration. Therefore, we interpret that the foliation formed due to a decreasing yield strength of the tonalites, during progressive alteration to weaker sericite. Reaction-weakening in the cores of shear zones has been shown to localize ductile deformation (Cox, 2002). Flattening occurred where the modal proportion of sericite became high enough to form interlinking rough cleavage. For the most part, we observe bulging and sub grain recrystallization of quartz grain boundaries together with the anastomosing foliation. Grain boundary recrystallization in quartz is unlikely to occur during sericite flattening, because all of the strain is accommodated by the much weaker phyllosilicates. This crystal plastic deformation may be a precursor fabric that initiated the map-scale anastomosing network and was preferentially flattened during alteration. This implies that the map-scale anastomosing pattern is inherited from the final stages of ductile shearing along the Marmion Shear Zone, even though the sericite foliation records only flattening.

4.6 Linking the deformation to a regional tectonic setting

The deformation history of the Marmion Suite is summarized in Figure 4–8 together with the deformation history of the Finlayson Lake greenstone belt (Backeberg *et al.*, 2014). The comparison allows us to constrain the deformation along the Marmion Shear Zone during the formation of the early fabrics, leading up to the docking of the two terranes prior to, or during D_3 (Figure 4–8). Backeberg et al. (2014) postulated the D_3 and D_4 structural events observed in the greenstone belt were related to the reactivation of the Marmion Shear Zone during the amalgamation of the Wawa, Quetico and Wabigon subprovinces with dextral transpression along the Quetico Fault estimated at ~ 2.7 Ga (Percival, 1989; Williams, 1990). Dextral transpression across the Quetico Fault is consistent with an approximate NW-SE horizontal shortening axis, that we interpret for structures in the Marmion Suite and Diversion Stock.

The Lithoprobe geophysical study across the Superior Province interpreted predominantly northward directed subduction of Archean subprovinces (Calvert *et al.*, 1995). If we infer a relative northwestward subduction for the Wawa subprovince subducting under the Wabigoon subprovince (Williams, 1990), the regional NW-SE shortening axis across the Marmion Shear Zone could have been caused by the continued subduction.

The alteration-weakening in the tonalites that formed the anastomosing foliation reflects the same NW-SE shortening axis. Therefore, no changes in the regional tectonic stress regime were necessary to initiate flattening. Rather, flattening may have occurred within the same regional stress regime, driven only by sericite alteration and bulk rock weakening of a pervasively permeable tonalite. The style of deformation in the Marmion Suite changes from distributed alteration and flattening (D_{4b}) to localized faults (D_{4c}), while still maintaining coaxial shortening during exhumation. It is unclear whether changes in far-field tectonic stress magnitudes caused the transition from distributed to localized deformation. The transition could be explained by either exhumation or increased strain rate associated with the Quetico

Fault activity and subduction. Regional maps show a persistent NE-SW fabric emphasized by river drainage across the entire Marmion Suite (Stone, 2008b). These all align parallel to the Lynx Head Fault and could be surface expressions of similar thrust faults recording NW-SE shortening, suggesting that significant shortening was accommodated in the Marmion Suite (and southern Wabigoon subprovince) during its late, shallow deformation history.

4.7 Conclusion

The Marmion Shear Zone has a long lived history of (i) ductile shearing juxtaposing greenstone supracrustal with tonalite crustal rocks, followed by (ii) stitching of the two terranes and "locking" of the shear zone during the emplacement and cooling of the Diversion Stock intrusive, to (iii) post-slip fluid flow and alteration leading to deformation and mineralization of the Hammond Reef gold deposit adjacent to a dormant shear zone (Figure 4–8). Fracturing in the tonalites of the Marmion Suite and Diversion Stock adjacent to the shear zone was caused by a combination of fault- and intrusion-related damage. Fractures were flushed with fluids that led to the pervasive alteration of feldspars to sericite without further fracturing. Alteration weakened the tonalites. Without any displacement along the Marmion Shear Zone and without a change in the orientation of regional shortening, the sericite locally flattened into foliation zones. The overall foliation pattern arranged into an anastomosing network of foliated tonalites that possibly mimic an earlier, weak grain-scale fabric. The NW-SE shortening axis observed for all events postdating the locking of the Marmion Shear Zone can be traced to regional tectonics associated with the activity of the $\sim$ 2.7 Ga Quetico Fault during the amalgamation of the Superior Province.

CHAPTER 5
Hammond Reef Gold Mineralization

This Chapter focuses on the Hammond Reef gold deposit within the context of the regional deformation history presented above. This chapter is in preparation for submission to Economic Geology or Lithos as *"Damaged Goods: Structural and tectonic setting of the Hammond Reef gold deposit, Ontario."*. The abstract is as follows:

Hammond Reef is a disseminated gold deposit spanning the intrusive contact of the Neoarchean Diversion Stock and Mesoarchean Marmion tonalite gneiss, 2 km east of the Finlayson Lake greenstone belt. Typically, Archean gold deposits worldwide are hosted within greenstone belt terranes or also in terrane-bounding faults and not in the adjacent TTGs, making Hammond Reef unusual and situated within an under-explored setting with respect to gold occurrences. The deposit is hosted within an anastomosing deformation corridor of chlorite and sericite altered tonalites, that developed parallel to the dormant Marmion Shear Zone. Gold mineralization occurred 100 to 200 million years after peak metamorphism and deformation of the host rocks. The mineralized alteration assemblage at Hammond Reef consists of sericite, pyrite and ankerite ± hematite, magnetite and fuchsite in chlorite-free tonalites. The alteration initiated around fractures and pervasive alteration was promoted along broad reaction fronts related to grain-scale fluid flow. Enhanced fluid-rock reactions and

pervasive wall-rock sulfidation were localized at Hammond Reef due to the higher concentration of more mafic lithological heterogeneities, which are absent elsewhere along strike of the anastomosing foliation. Auriferous quartz-carbonate veins at Hammond Reef record a change in the style of fluid flow from broad and pervasive (disseminated gold) to channelized flow (lode gold) within the same tectonic setting. Kinematic consistency of the anastomosing foliation and cross-cutting shallow thrust faults record NW-SE shortening. This ties the gold mineralization and fluid flow to a regional supra-subduction setting in the Neoarchean during the accretion of the Wabigoon and Wawa subprovinces at around 2.7 Ga. The alteration assemblages and tectonic setting classify the disseminated and vein-hosted gold as a mesothermal "orogenic" gold deposit that formed at the same time as many other prominent 2.7 Ga goldfields in the Superior Province.

5.1 Introduction

Gold occurs in mono- and multi-metal deposits in a variety of geological settings across geological time. Archean cratons worldwide are known to be rich in significant quantities of gold, typically hosted within shear structures cutting greenstone belt terranes (Böhlke, 1982; Groves *et al.*, 1989; Kerrich & Wyman, 1990; Hodgson, 1993; Groves *et al.*, 1998; Goldfarb *et al.*, 2001). The Canadian Superior Province is no exception and extensive gold deposits have been found, most markedly in the Neoarchean Timmins–Val d'Or gold belt of the Abitibi subprovince (Robert *et al.*, 2005; Percival, 2007b). The Abitibi subprovince is dominated by greenstone belt terranes sutured across prominent east-west striking shear zones, such as the Larder–Cadillac and Destor–Porcupine breaks, along which most of the quartz-carbonate vein-hosted gold deposits have been found (Poulsen *et al.*, 2000; Dubé & Gosselin, 2007). East-west trending structures are common throughout the Superior Province and are interpreted to record the accretionary history at around 2.72 – 2.68 Ga (Gower & Clifford, 1981; Card, 1990; Percival *et al.*, 2006; Percival, 2007a). Gold deposits throughout the Superior Province are all typically associated with these major east-west trending structures (Robert *et al.*, 2005; Percival, 2007b). Most major gold deposits were found by observed surface expressions of alteration or visible gold that led to further local exploration. Finding new gold fields has become increasingly difficult as most large, high-grade deposits with surface expressions are thought to have been found. Continued gold exploration relies on classification schemes that link the occurrence of known gold deposits to rock types and tectonic settings. Therefore, understanding the geological history of different types of gold deposits, and the terranes that host them, is the key to unlocking the potential of previously unexplored geological terranes.

Robert *et al.* (1997) subdivided gold deposits into 16 classifications related to crustal levels, tectonic- and volcanic settings. All gold deposits are essentially driven by hydrothermal processes that cover all 16 subdivisions, except for secondary placer deposits. Generally, deposits have been classified as either "orogenic", "epithermal-porphyry", "Carlin-type" or "intrusion-related", although a variety of classification schemes exist (Robert *et al.*, 1997; Groves *et al.*, 1998; Kerrich *et al.*, 2000; Goldfarb *et al.*, 2001). Orogenic, or mesothermal, gold deposits are typically found in transpressional convergent margins as part of the later stage, syn-deformational orogenic events typically related to subduction tectonics (Böhlke, 1982; Groves *et al.*, 1989;

Hodgson, 1993; Groves *et al.*, 1998; Goldfarb *et al.*, 2001). In such compressional regimes, gold can be emplaced as vein-hosted lode-gold, where fluctuations in deep pore fluid pressures reactivate pre-existing (steep) structures and rapidly emplace quartz-carbonate veins with significant gold quantities into the upper crust (Sibson *et al.*, 1988; Sibson, 1992). This rapid transport and gold "dumping" in veins has been linked to a broad range in pressure-temperature conditions of 1–5 kbar and 200–600°C (Groves, 1993). Other gold deposits formed by hydrothermal systems, have fluids that continually flux though the host rock and progressively enrich the metal content. These hydrothermal systems include the circulation of magmatic and/or meteoric fluids in porphyry and epithermal systems, or only meteoric fluids in non-magmatic geothermal systems (Heald *et al.*, 1987; Goldfarb *et al.*, 2001). Hydrothermal alteration and gold mineralization in sediments are known as Carlin-type gold deposits, typically expressed as "invisible" gold in pyrite and are associated with decarbonitization and argillization of silty carbonates (Cline *et al.*, 2005). Intrusion-related gold systems (IRGS) are a subdivision of deposits that fall within a combination of the characteristics described above, but form as low-grade, bulk tonnage gold mineralization hosted in intrusions and are typically post deformation (Sillitoe, 1991; Sillitoe & Thompson, 1998; Hart *et al.*, 2002). Classifications of gold deposits and their tectonic setting are often linked to "gold-only" and "gold-plus" deposits, based on metal contents adding to the economic value (Phillips, 1993), and the style fluid flow as either channelized lode-gold or diffuse disseminated gold with a broad reaction front (Couture & Pilote, 1993; Phillips & Powell, 2010).

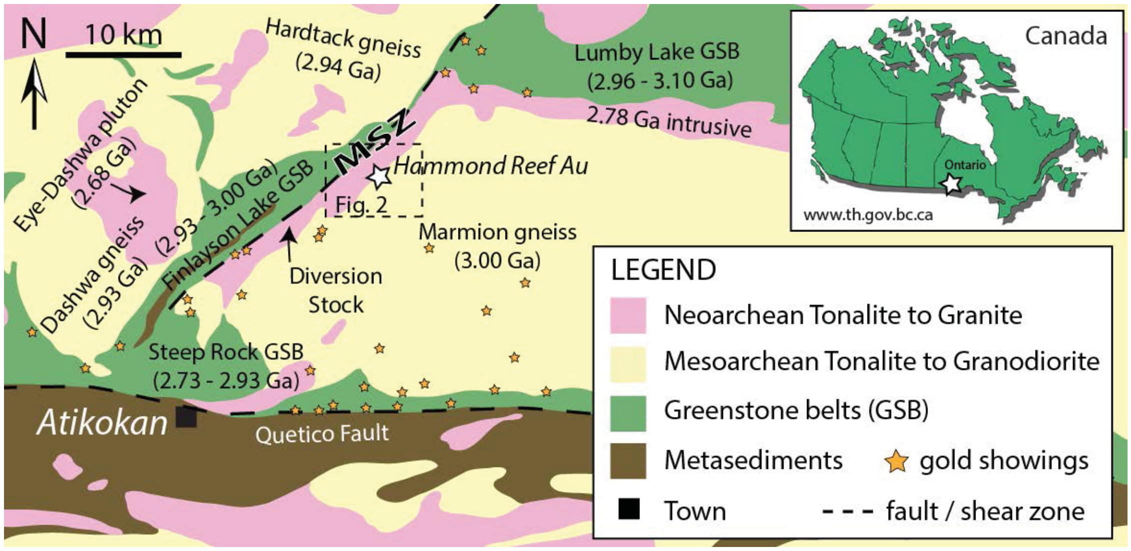

Figure 5–1: Simplified regional geological map with ages of the south–central Wabigoon subprovince granite–greenstone terranes (Stone, 2008a,b; Buse *et al.*, 2010a), showing the location of the Hammond Reef gold deposit (white star) in the Marmion gneiss adjacent to the Marmion Shear Zone (MSZ). Regional gold showings in the Marmion and Eye-Dashwa gneiss (Stone, 2008a,b) and at Lumby lake (Buse *et al.*, 2010b) are shown (gold stars). Gold showings around Hammond reef are shown in Figure 5–2. The east-west striking Quetico Fault separates the Wabigoon subprovince (north) from the Quetico subprovince (south).

The Hammond Reef gold deposit is hosted in the Mesoarchean 3.0 Ga Marmion gneiss tonalite–trondhjemite–granodiorites (TTGs) of the south-central Wabigoon subprovince, Superior Province (Figure 5–1). Hammond Reef is located adjacent to the Finlayson Lake greenstone belt, which does not host any significant gold mineralization. Typically, Archean gold deposits worldwide are hosted within greenstone belt terranes and not in the adjacent TTGs (Groves *et al.*, 1987; Robert, 1990; Ridley *et al.*, 1996; Thébaud *et al.*, 2006; Juul-Pedersen *et al.*, 2007). This places Hammond Reef within an under-explored terrane with respect to gold occurrences in the Archean. Furthermore, the deposit is associated with a northeast trending structure, the Marmion Shear Zone (MSZ, Figure 5–1), which is inferred to be Mesoarchean in age ($<$ 2.93 G, Backeberg *et al.* (2014)).

In this paper, we report the characteristic alteration and gold mineralization at Hammond Reef and place it into the context of the structural setting of the Marmion gneiss and relate the relative timing of mineralization to the regional deformation history. We then discuss the classification of the Hammond Reef gold deposit from its fluid sources and style of fluid flow within the regional tectonic setting, with implications to using general classification schemes.

5.2 Setting

The Wabigoon subprovince is a Mesoarchean crustal block made up of a mosaic of granite-greenstone terranes typical of Archean cratons worldwide. The assembly of the Wabigoon subprovince occurred in two stages, first with the accretion of the TTG-dominated terranes of the Marmion, Winnipeg River and central Wabigoon terranes from 2.92 Ga onwards, followed by the accretion of the greenstone-belt-dominated western Wabigoon terrane prior to 2.72 Ga (Tomlinson *et al.*, 2003; Percival & Helmstaedt, 2004; Tomlinson *et al.*, 2004; Percival, 2007a). Gold deposits in the Wabigoon subprovince are mostly found in the greenstone-belt-dominated western Wabigoon terrane, and mineralization is dated at $\sim$ 2.71 Ga (Mackasey *et al.*, 1974; Melling *et al.*, 1988; Davis & Smith, 1991). Hammond Reef is found in the Marmion tonalite gneiss of the TTG-dominated south-central portion of the Wabigoon subprovince, not typically known for significant gold deposits. Exploration has revealed only small-scale gold showings associated with quartz-carbonate veins to the north of the Quetico Fault (Figure 5–1). The Quetico Fault separates the Wabigoon subprovince from the Quetico subprovince metasedimentary rocks and is interpreted to be associated with the 2.72 – 2.68 Ga Kenoran orogeny and Superior

Province amalgamation (Corfu & Stott, 1986; Percival & Williams, 1989; Percival, 1989; Williams, 1990; Bauer *et al.*, 1992; Peterson & Zaleski, 1999). The Quetico subprovince metasediments are interpreted to have been deposited in an accretionary wedge (Langford & Morin, 1976; Percival & Williams, 1989; Valli *et al.*, 2004) that was deformed during the accretion and northward subduction of the Wawa subprovince from the south (Calvert *et al.*, 1995).

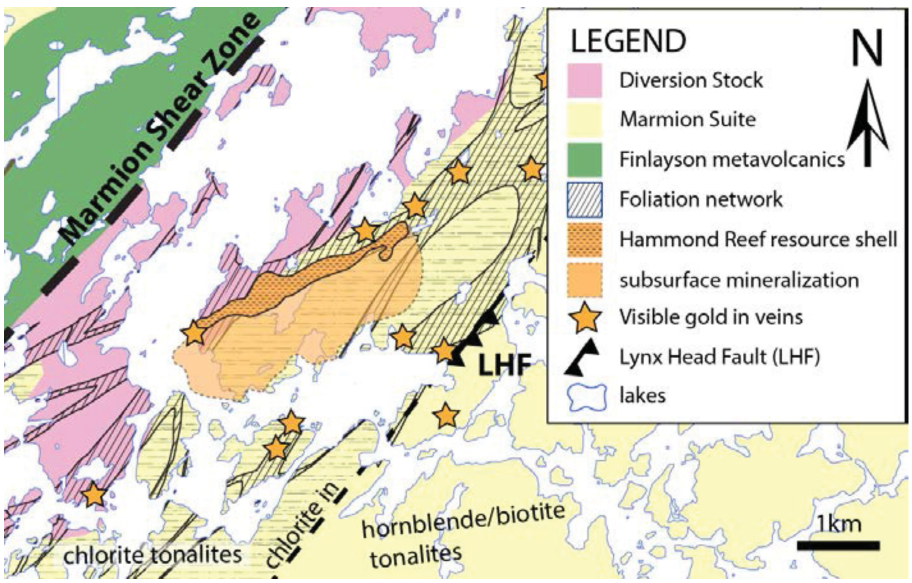

Figure 5–2: Local map showing the anastomosing deformation zone, which cuts the Marmion Suite and Diversion Stock tonalites (Stone, 2008a). Outline of the Hammond Reef gold deposit resource shell is shown (orange) with subsurface expression (transparent orange), which is defined by the gold mineralization at > 0.3 g/t Au. Exposure of the Lynx Head Fault (LHF) east of Hammond Reef is shown, which overlaps with the eastward extend of chlorite retrogression (chlorite-in line). Location of visible gold in large quartz-carbonate veins are shown (gold stars).

The Hammond Reef gold deposit is located approximately 20 km north of the Quetico Fault and 2 km east of the Finlayson Lake greenstone belt contact (Figure 5–1). The Marmion Shear Zone separates the 3.0 Ga Marmion gneiss from the 2.93 – 3.00 Ga Finlayson Lake greenstone belt and the contact is intruded by the Diversion Stock tonalite–granodiorite (Figure 5–2). The Diversion Stock has been mapped as a Neoarchean intrusive body (Stone, 2008a) and has been tentatively linked to the 2.786 Ga age of a petrographically similar boundary intrusive body between the Marmion Suite and the Lumby Lake greenstone belt to the north (Buse *et al.*, 2010a). The Marmion and Finlayson terranes become juxtaposed after 2.93 Ga (Backeberg *et al.*, 2014), which overlaps with the 2.92 Ga accretionary period of the Wabigoon subprovince (Tomlinson *et al.*, 2004; Percival, 2007a). Hammond Reef is spatially associated with an anastomosing deformation corridor to the east of the Marmion Shear Zone cross-cutting the Marmion gneiss and Diversion Stock (Figure 5–2, Stone (2008a)). The deformation corridor is defined by foliated tonalites aligned parallel to the Marmion Shear Zone and is interpreted as late-stage NW-SE flattening following the alteration of the feldspars to sericite (Backeberg *et al.*, submitted). The NW-SE shortening axis has been linked to dextral transpression along the Quetico Fault during accretion of the Wawa and Quetico subprovinces from the south (Backeberg *et al.*, 2014, submitted).

5.3 Hammond Reef

The outline of the Hammond Reef deposit resource (Figure 5–2) is characterized by a low-grade, disseminated mineralization of < 1 g/t Au (< 1 ppm) with high-tonnage of over 180 million tonnes (> 10 million ounces of gold) of measured and indicated resources based on an average grade of ~ 0.86 g/t at a cut-off of 0.5 g/t (Osisko, 2013). Visible gold in auriferous quartz-carbonate veins is also present in the Hammond Reef area (Figure 5–2) and has been mined historically in small-scale operations around Hammond Reef since its discovery in 1895. The disseminated deposit resource was defined by Brett Resources (2008), further developed by Osisko

Mining Corporation to the current resource estimates (2010 – 2014) and taken over in a partnership by Agnico Eagle and Yamana Gold (2014).

5.3.1 Lithologies

Hammond Reef is hosted in the Marmion gneiss and Diversion Stock within the anastomosing foliation that straddles the intrusive contact of the Diversion Stock, although it is preferentially expressed in the Marmion gneiss (Figure 5–2). Here we describe the lithological variations of different rock units that are found along the western margin adjacent to the Marmion Shear Zone.

Marmion gneiss

The Marmion gneiss extends over 100 km long (east-west) by $\sim$ 20 km wide (north-south) along the southern margin of the Wabigoon subprovince and is also referred to as the Marmion batholith in the literature (Davis & Jackson, 1988; Tomlinson *et al.*, 2003; Percival, 2007a). The Marmion gneiss consists of hornblende and biotite tonalite gneisses with a weak to moderate gneissosity (Stone, 2008a). The peak metamorphic assemblage of quartz, plagioclase, hornblende and biotite is preserved to the east of the anastomosing foliation zone (Backeberg *et al.*, submitted). Along the western margin, amphibole and biotite have been replaced by chlorite, and feldspar is partially to pervasively altered to sericite (Backeberg *et al.*, submitted). Backeberg *et al.* (submitted) investigated the anastomosing foliation zone along the western margin adjacent to the Marmion Shear Zone and subdivided the Marmion gneiss into four cross-cutting tonalite gneiss units as part of the Marmion Suite (Figure 5–3a). The dominant unit in the Marmion Suite is a fine- to medium-grained chlorite-bearing tonalite (main Marmion tonalite with 20 – 30 % chlorite, Figure

5–3a_3). It corresponds to the unit described as the Marmion gneiss on published maps (Stone, 2008a). Two older tonalites, a porphyritic tonalite and very fine-grained tonalite, are found as xenoliths within the main Marmion tonalite (Figure 5–3$a_{1,2}$). These xenoliths tend to have a slightly more mafic compositions (> 30% chlorite). The colour differences seen in Figure 5–3a are the result from the grain size differences. The porphyritic tonalite has aligned plagioclase porphyroclasts with gneissic augen textures (Figure 5–3a_1). A younger leucotonalite cuts the three mafic tonalites. Except for the lack of mafic minerals, it is petrographically identical to the main Marmion tonalite. (Figure 5–3a_4). Late pegmatite dykes are also commonly observed and have been reported in the area (Wasteneys, 2011). The four units of the Marmion Suite and pegmatites are preferentially found in the Hammond Reef area and are rarely observed elsewhere along the western margin of the Marmion gneiss.

Diversion Stock

The Diversion Stock was emplaced along the boundary of the Marmion gneiss and Finlayson Lake greenstone belt. It is up to 2 km wide (Figure 5–2). The mineralogy consists of quartz, plagioclase, microcline, hornblende and muscovite and the unit is classified as tonalite – granodiorite (Stone, 2008a; Backeberg *et al.*, submitted). Amphibole grains in the Diversion Stock are not aligned and more weakly altered to chlorite, compared to amphibole in the Marmion Suite. The feldspars in the Diversion Stock are also partially to pervasively altered to sericite (Backeberg *et al.*, submitted). Although petrographically very similar to the main Marmion tonalite of the Marmion Suite, the intrusive Diversion Stock is typically coarser grained and

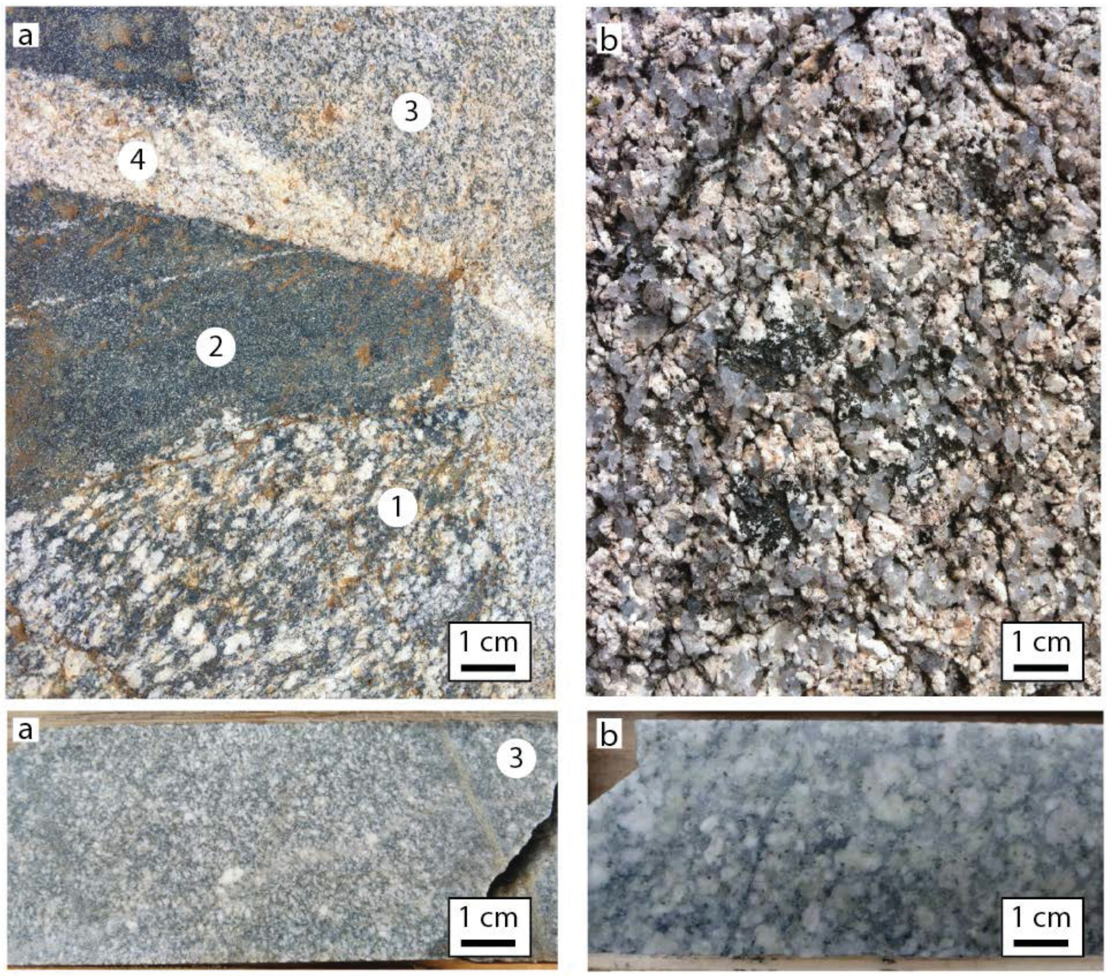

Figure 5–3: Lithologies of Hammond Reef. (a) Marmion Suite tonalites numbered in decreasing age. 1 – porphyritic tonalite with coarse feldspars and augen texture. 2 – very fine-grained tonalite. 1 and 2 occur as xenoliths in 3. 3 – fine- to medium-grained main Marmion tonalite, which corresponds to the Marmion gneiss represented on published maps (Stone, 2008a,b). 4 – leucotonalite, found as dykes cutting 1, 2 and 3. (b) Diversion Stock granodiorite with equigranular quartz and feldspar and higher modal quartz. Bottom images show samples of main Marmion tonalite (a) and Diversion Stock (b) in drill core at Hammond Reef.

has less amphibole or chlorite (10 – 15 % chlorite, Figure 5–3b). Other petrographic distinctions for the Diversion Stock include a higher modal quartz content, presence of potassium feldspar and absence of ductile deformation fabrics (Backeberg *et al.*, submitted).

We remapped the lake-shore exposures around the Hammond Reef peninsula using these petrographic classifications. Our observations place the contact of the Diversion Stock up to 500 m farther east of where it was previously drawn (c.f. Stone, 2008b). This places the exposed Hammond Reef mineralization across the intrusive contact (Figure 5–2). Samples of Diversion Stock are observed in drill core that cut the western edge of the Hammond Reef mineralization, consistent with the new map. The chronology revealed by this revision to the map is important for establishing the controls and history of the deposit.

Mafic dykes

Regionally, there are Proterozoic mafic dykes best observed on magnetic maps that trend northwest and cut across the Archean terranes (Stone, 2010). At Hammond Reef, smaller mafic dykes are common in the Marmion Suite, but are absent in Diversion Stock. Backeberg *et al.* (submitted) interpreted these dykes as Archean in age probably related to the mafic magmatism of the Finlayson Lake greenstone belt. Along the western margin in the Marmion gneiss, there seems to be a higher concentration of mafic dykes in the Hammond Reef area, confirmed by common intersections of drill core with mafic dykes. Unlike the Proterozoic dykes, these Archean dykes are all altered to chlorite and calcite.

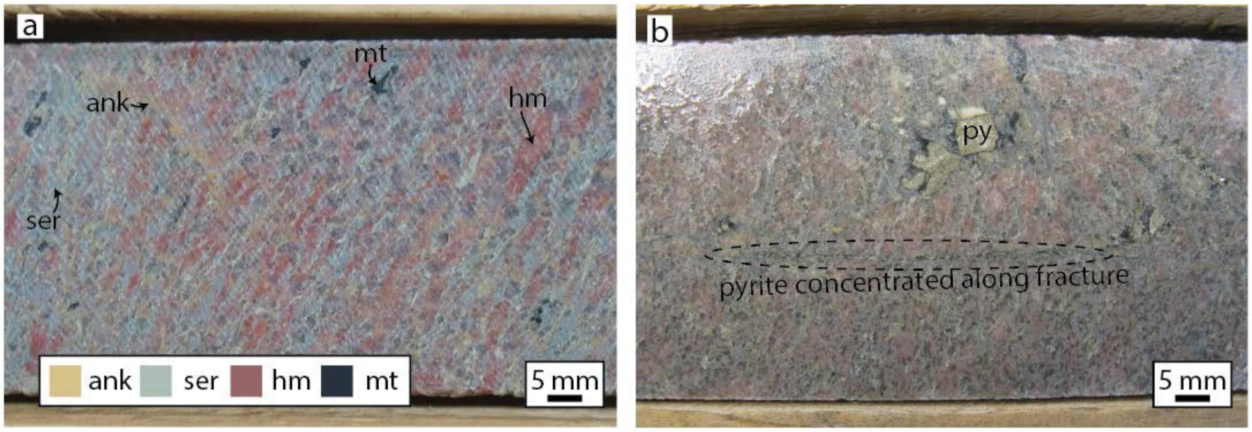

Figure 5–4: Two examples of intensely altered tonalite at Hammond Reef. (a) Highly altered, weakly foliated tonalite with the main alteration assemblage of green sericite (ser), reddish stain to quartz from hematite (hm), yellow ankerite (ank) and black magnetite (mt). Pyrite is not visible at this scale, but may be abundant as fine-grained crystals. (b) Highly altered, unstrained tonalite with abundant coarse-grained pyrite (py). Pyrite tends to be disseminated throughout the tonalite, but commonly is concentrated along fractures and foliation surfaces.

5.3.2 Alteration assemblages

The disseminated Hammond Reef gold mineralization is localized in the northern portion of the anastomosing foliation (Figure 5–2). Backeberg *et al.* (submitted) separated two hydrothermal alteration events along the western margin of the Marmion gneiss within the anastomosing foliation. The first was the alteration of amphibole to chlorite during exhumation and docking with the Finlayson Lake greenstone belt prior to the emplacement of the Diversion Stock. The second was the pervasive alteration of feldspar to sericite in both the Marmion gneiss and Diversion Stock that led to localized flattening and development of the anastomosing foliation (Backeberg *et al.*, submitted). Here we describe the localized alteration at Hammond Reef that is associated with disseminated gold mineralization, which overlaps spatially with the sericite alteration within the anastomosing deformation corridor.

The Hammond Reef alteration modified the colour of the tonalites to light greens and brick reds (Figure 5–4), which are the characteristic colours of the Hammond Reef orebody (Osisko, 2013). The mineralized alteration is found in both foliated and unstrained tonalites at Hammond Reef, although foliated zones are typically more intensely altered. The alteration assemblages at Hammond Reef can be characterized by variable mineral modes of sericite, pyrite, ankerite, hematite, magnetite and in some cases, fuchsite (Figure 5–4a). Chlorite is absent in the Hammond Reef alteration assemblages, resulting in the overall paler green colour at Hammond Reef compared to the dark chlorite tonalites along the rest of the western margin (Figure 5–3a). The most common alteration assemblage at Hammond Reef is pale-green sericite with pyrite and ankerite. The distinct pale-green alteration colour associated with sericite is not found outside of Hammond Reef, even though sericite alteration is pervasive across the entire anastomosing foliation zone. Pyrite is highly abundant at Hammond Reef and has a variable grain size, up to cm-sized grains. It is typically distributed pervasively throughout the tonalites, but high concentrations of pyrite are generally found along fractures and foliation planes (Figure 5–4b). Pyrite is also found as rare small disseminated grains throughout the western margin outside of Hammond Reef. Hematite occurs as very fine grains that stain the translucent quartz to show a brick-red colour. Hematite staining is observed throughout the deposit and can occur as pervasive or with a patchy distribution, but it does not occur outside of Hammond Reef. Magnetite and fuchsite are less common, but observed locally throughout the alteration zone. In the most intensely altered tonalites, euhedral magnetite occurs together with the hematite red-stained alteration (Figure 5–3a).

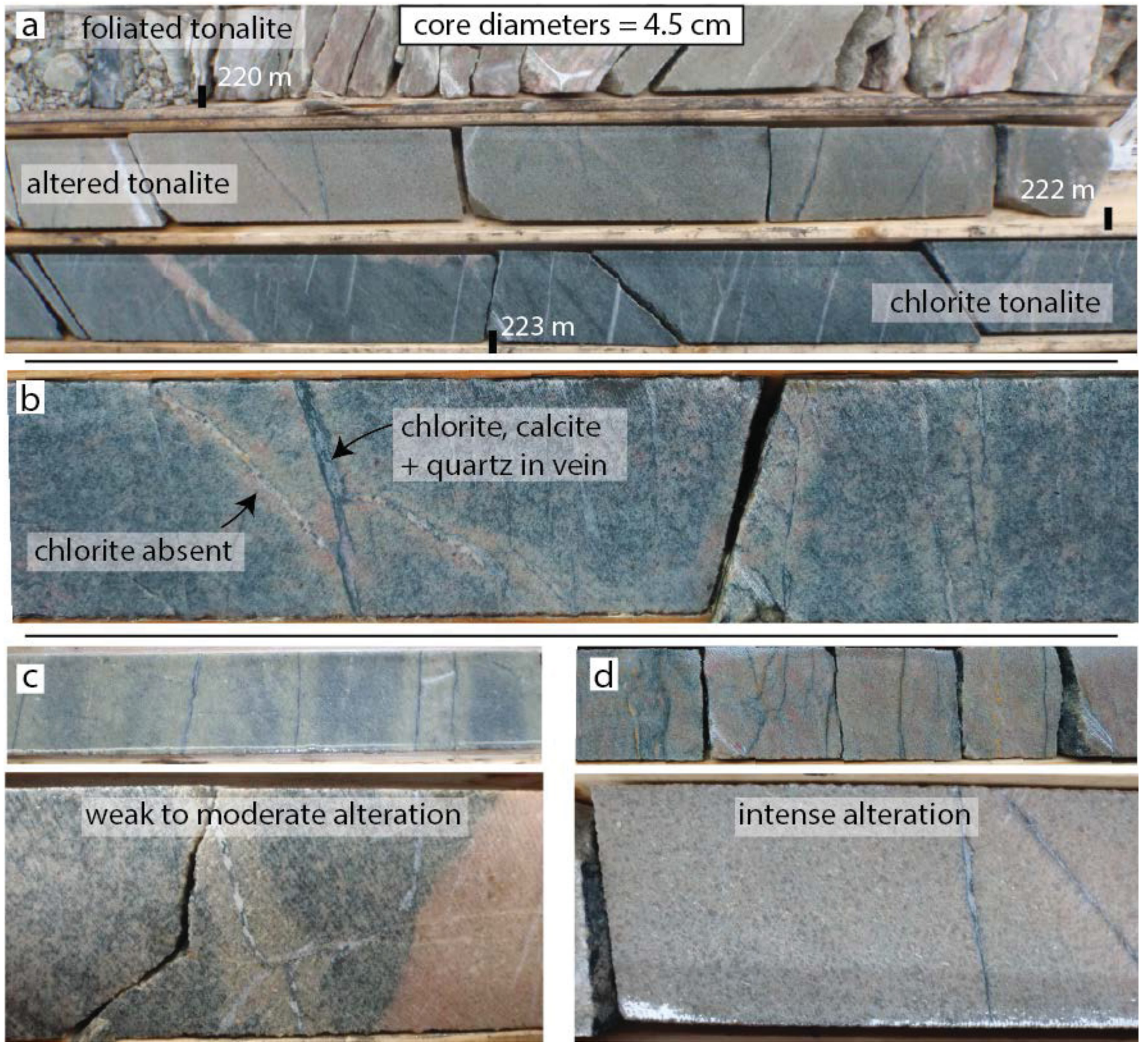

Figure 5–5: Drill-core samples showing leaching of chlorite out of host tonalite around fractures with quartz, calcite and chlorite precipitated in veins that fill the fractures. (a) Gradational decrease of hydrothermal alteration adjacent to foliated tonalites at the edge of the Hammond Reef deposit. Core meter marks for 220, 222 and 223 meters shown by black ticks. The decrease in chlorite abundance towards the foliation corresponds to the overall colour change. Veins in chlorite tonalites are composed of only quartz and carbonate with no chlorite. (b) Localized chlorite-leached halos around fractures. Note the appearance of the patchy green-red tonalite around the vein, typical for pervasively altered tonalites at Hammond Reef. (c) Weak to moderately altered tonalite with multiple alteration halos around fractures with chlorite in the vein. (d) Pervasively altered tonalite with chlorite absent and pale green-red colours.

The intensity of the Hammond Reef alteration at the edge of the deposit is gradational. Where the hydrothermal alteration margin overlaps closely with foliation, there is a 2 - 5 m gradational zone of decreasing alteration intensity from a pale green sericite tonalite into dark green chlorite tonalites (Figure 5–5a). The stark colour contrast comes from the absence of chlorite in the Hammond Reef altered tonalites, which is clearly observed around fractures and veins (Figure 5–5). There are a variety of veins less than 1 cm wide. These veins include predominantly quartz, ankerite, calcite, chlorite or epidote with mutually cross-cutting relations. Quartz-ankerite-chlorite veins are the most common at Hammond Reef, usually with quartz-ankerite crystallized along the walls and chlorite filling in the central void. Some veins show a halo of the chlorite-leaching in the tonalites leading to the patchy pale green-red colours (Figure 5–5b,c). More weakly altered tonalites show an array of chlorite leaching halos around fractures (Figure 5–5c). In more strongly altered tonalites, chlorite-leaching is pervasive, such that chlorite is only observed in veins that cut the pale green tonalites (Figure 5–5d). Therefore, the third phase of alteration along the western margin of the tonalites can be characterized by sericite tonalites that experienced the removal of chlorite and the addition of pyrite, ankerite ± hematite, magnetite and locally fuchsite.

5.3.3 Geochemistry

Samples were collected from surface exposures and drill core throughout the Marmion Suite and Diversion Stock for geochemical analyses (n = 31, Appendix B). In this section, we describe and compare the geochemical variations of the main Marmion tonalites (n = 12), xenoliths in main Marmion tonalite (n = 6), Diversion

Stock (n = 5) and altered tonalites from the Hammond Reef ore zone (n = 8). The Marmion tonalite and Diversion Stock samples were collected from the western margin within the anastomosing foliation, which experienced partial to pervasive alteration of amphibole to chlorite and feldspar to sericite.

Major elements

The variations in major element compositions show a continuous trend from 60 – 76 wt.% SiO_2 across all rock types (Figure 5–6). The Marmion gneiss (main Marmion tonalite, Figure 5–3a$_3$) shows the largest variations in chemical compositions. Xenoliths of porphyritic and very fine-grained tonalites (Figure 5–3a$_{1,2}$) show the least evolved compositions with consistently higher Fe and Mg contents in those samples. The Diversion Stock plots consistently as the most evolved felsic compositions with $> 70\ wt.\%\ SiO_2$, compared to the Marmion Suite with a range from 64 – 72 wt.% SiO_2. This is consistent with observations of higher quartz contents in the Diversion Stock described above. Variations in K_2O show the least well-defined trend, likely because of the alteration of the feldspar to sericite. The concentrations overlap for samples from the Marmion tonalite and Diversion Stock, likely related to the pervasive sericite alteration in both rock types. Altered samples from the Hammond Reef gold deposit overlap with the full range of SiO_2 concentrations and substantiate our field interpretations that the Diversion Stock contact extends into the Hammond Reef ore zone (see triangles in Figure 5–6). Sulfur and carbon are elevated in the altered samples from Hammond Reef. Altered tonalites are enriched in K_2O and depleted in Na_20 and SiO_2 (Figure 5–6).

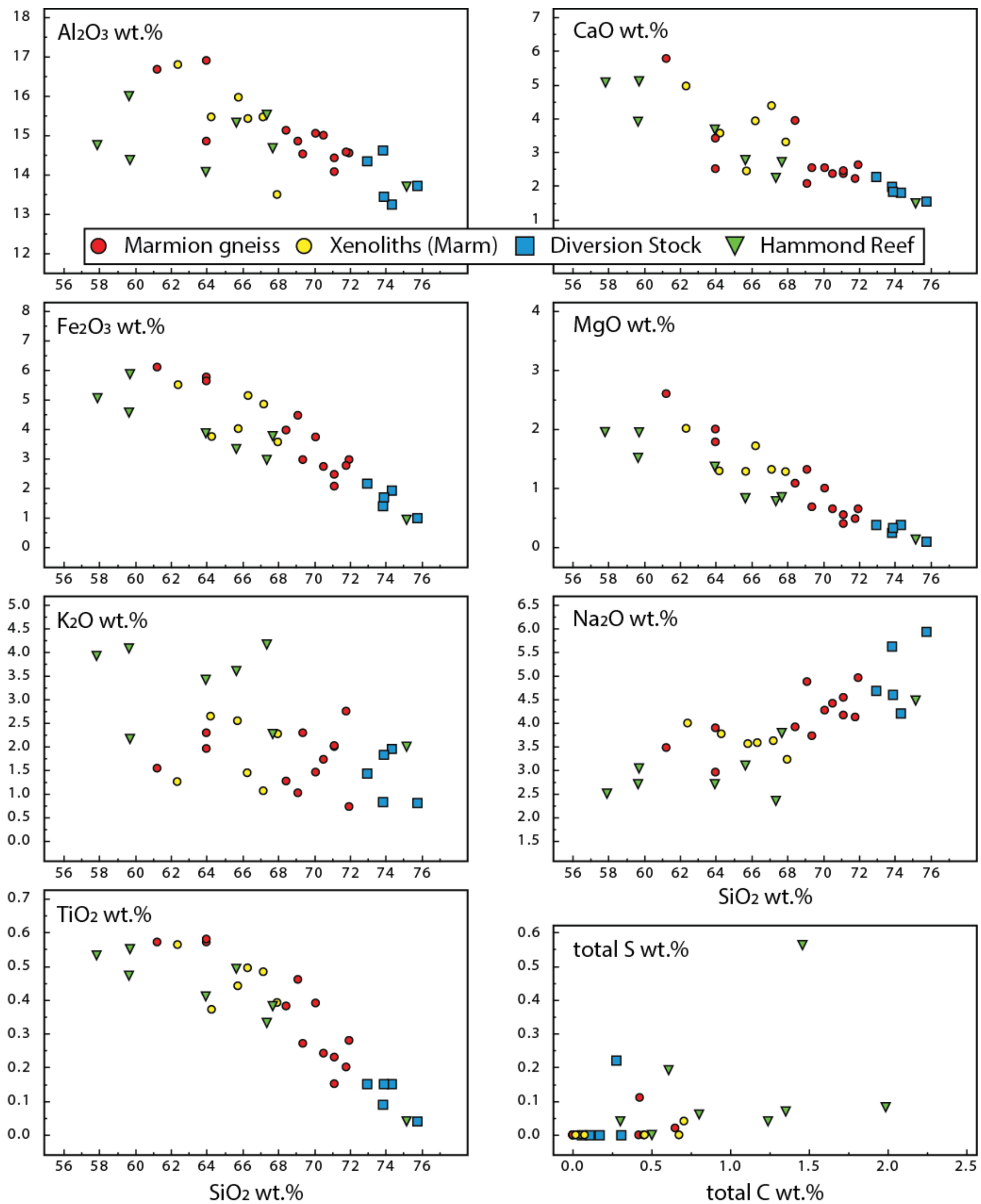

Figure 5–6: Major element geochemical variations and total carbon and sulfur (all in weight %) for the main Marmion tonalite (red circles), porphyritic and fine-grained tonalite xenoliths (yellow circle) Diversion Stock (blue squares) and altered tonalites from the Hammond Reef ore zone (green triangles).

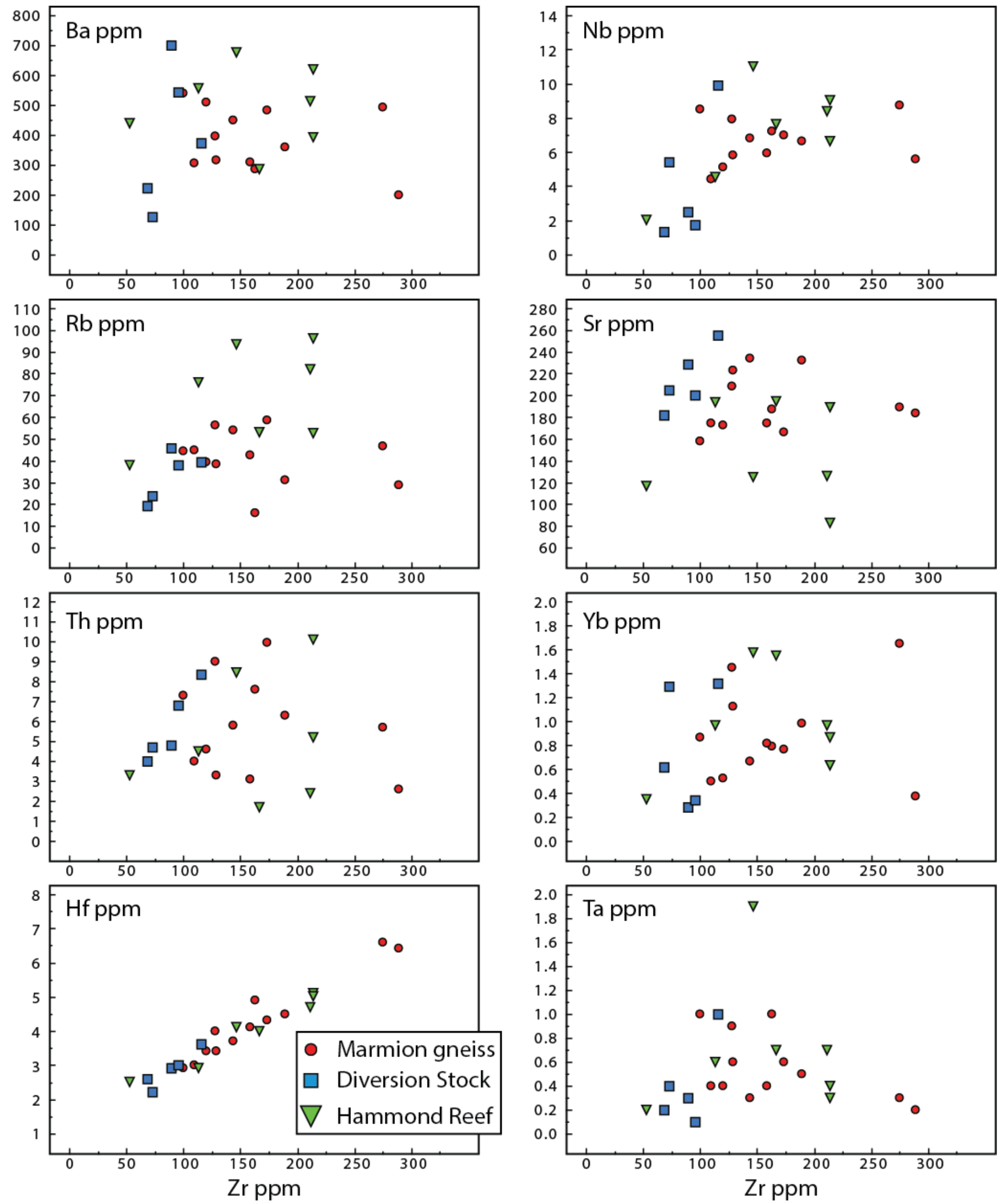

Figure 5–7: Trace element geochemical variations plotted against Zr for the main Marmion tonalite (circles), Diversion Stock (squares) and altered tonalites from the Hammond Reef ore zone (triangles).

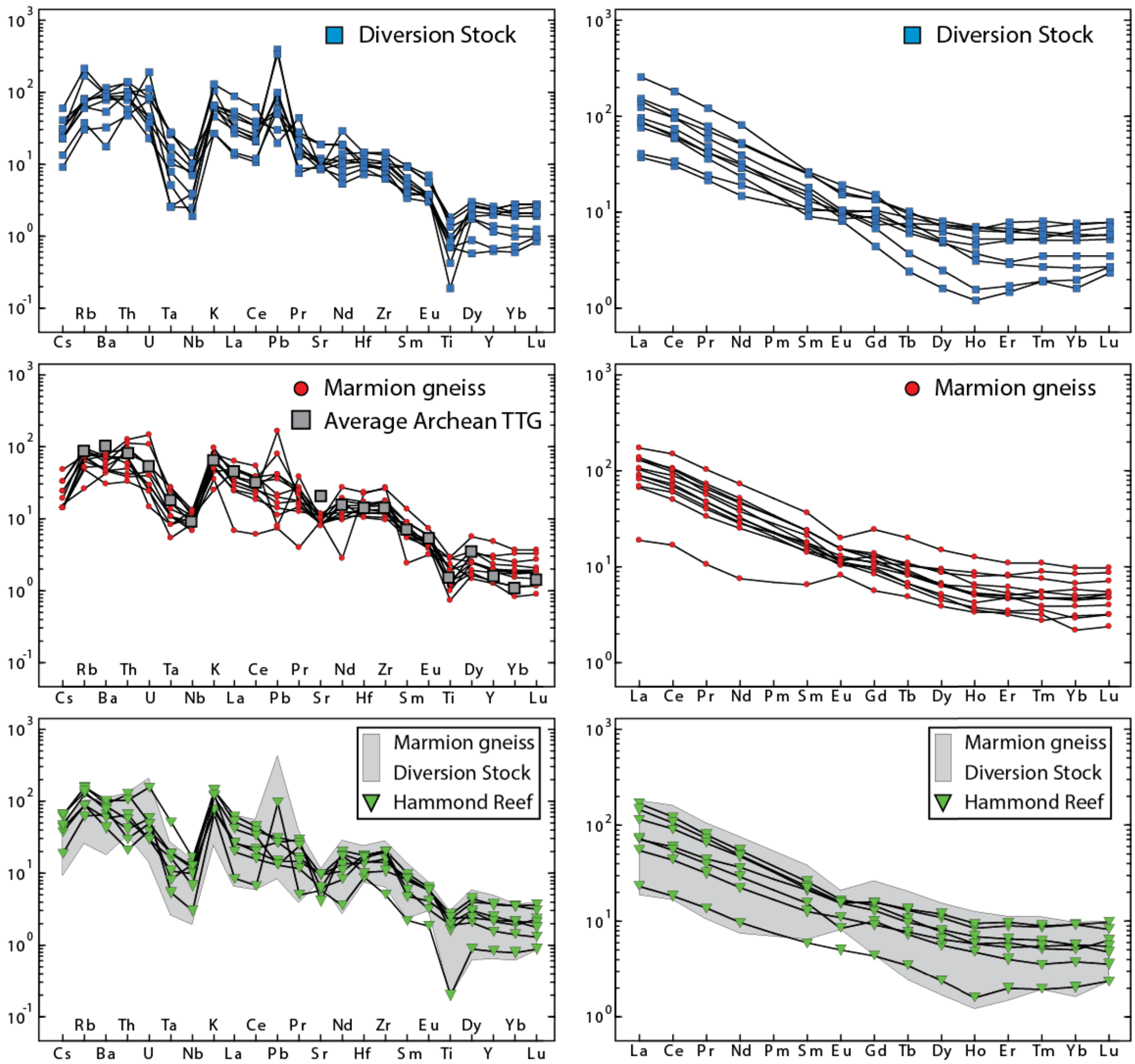

Figure 5–8: Normalized trace element profiles of the Diversion Stock (squares, top row), Marmion tonalite gneiss (circle, middle row) and altered tonalites from Hammond Reef overlain onto Diversion Stock and Marmion tonalite profiles (triangles, bottom row). (left column) Primitive-mantle-normalized trace element profiles. (right column) Chondrite-normalized rare earth element profiles. Average Archean TTG composition (Condie, 2005; Xiong, 2006) overlain on Marmion gneiss primitive mantle normalized trace element profiles. Primitive mantle and chondrite values take from McDonough & Sun (1995).

Trace elements

Trace element variations are scattered and overlap for both the Marmion tonalites and Diversion Stock. Only Zr and Hf concentrations fall along a well-defined trend, with relatively higher Zr and Hf concentrations in the Marmion tonalites (Figure 5–7). Other trace element variations overlap in both rock types and typical petrochemical markers such as Zr/Y and Ta/Nb do not differentiate between the Marmion gneiss and the Diversion Stock. The geochronology and structural relationships require that they are different units. The altered tonalites from Hammond Reef also show no clear deviations in trace element concentrations (see triangles in Figure 5–7). The same altered sample that overlaps with the Diversion Stock SiO_2 contents has a similar low Zr and Hf content (Figure 5–6).

Primitive-mantle-normalized trace element profiles show the same enrichments in both rock units, as well as altered tonalites from Hammond Reef (Figure 5–8). The profiles emphasize negative Ta, Nb, and Ti anomalies and a positive Pb anomaly, although some samples from the Marmion tonalites also show a negative Pb anomaly (Figure 5–8). All of the anomalies are more pronounced in the Diversion Stock. Chondrite-normalized rare earth element (REE) profiles also show overlapping profiles for the Marmion tonalites and Diversion Stock (Figure 5–8). Two samples from the Diversion Stock have a more heavy-REE-depleted profile. The Marmion tonalites have a mostly well-defined negative Eu anomaly, except for one sample with less enriched light REE and a positive Eu anomaly.

Comparison to other Archean TTGs

Archean TTGs have been widely discussed in the literature. The discussion is focussed on early Earth processes and melting of Archean oceanic crust that led to this first appearance of felsic crust and stabilization of the earliest continents (De Wit *et al.*, 1992; Zegers & van Keken, 2001; Smithies *et al.*, 2003; Rapp *et al.*, 2010; Hoffmann *et al.*, 2014). Typical TTG series are absent in the formation of modern crust. Modern felsic crust is granitic, rather than part of the TTG series (e.g. Frost *et al.*, 2006) and, therefore, adakites, which formed from the foundering of thickened crust are sometimes compared to TTGs as a modern equivalent (e.g. Martin, 1999; Martin *et al.*, 2005; Ma *et al.*, 2015).

The variations in trace elements of the Marmion gneiss and Diversion Stock overlap with the multi-element profiles and anomalies reported for the average Archean TTG terranes worldwide (Foley *et al.*, 2003; Condie, 2005; Xiong, 2006; Foley, 2008; Rollinson, 2008, 2009). Examples of TTGs from the Fiskenaesset complex in Greenland (Polat *et al.*, 2009; Huang *et al.*, 2013) show the identical chemical characteristics as the Marmion gneiss and Diversion Stock. These TTGs have been interpreted to form by the melting of a thickened mafic root under an arc (Polat *et al.*, 2009; Polat, 2012; Huang *et al.*, 2013). The formation of Archean TTGs generally is thought to recrystallize from partial melts from foundered (delaminated or subducted) garnet amphibolites in thickened oceanic crust (deep hydrous basalts) in arc settings (Foley *et al.*, 2003; Polat *et al.*, 2009; Rollinson, 2008; Huang *et al.*, 2013), although the geochemical characteristics of arc magmatism are still disputed (Bédard *et al.*, 2013).

5.3.4 Structural geology

The structures we observed at Hammond Reef are dominated by foliated tonalites and shallowly dipping cross-cutting faults. All the structures observed at Hammond Reef are identical with structures and cross-cutting relationships found in the Marmion tonalites and Diversion Stock along the entire extent of the western margin, adjacent to the Marmion Shear Zone. The details of the structural geology of the western margin are presented in Backeberg *et al.* (submitted). Here, we present a summary of the structural features.

The boundary to the Finlayson Lake greenstone belt is the Marmion Shear Zone, which strikes 050° and dips $\sim 75°$ to the southeast. The shear zone is intruded by the Diversion Stock, which is up to 2 km wide (Figure 5–2). The shear zone is inferred to have been mostly locked since the emplacement of the Diversion Stock (Backeberg *et al.*, submitted).

Fractures are common along the western margin of the Marmion gneiss and in the Diversion Stock. The fractures have a pattern of perpendicular shear and open-mode fractures and the overall fracture pattern in the tonalites is caused by a combination of fault- and intrusion-related damage by the Marmion Shear Zone and Diversion Stock, respectively (D_{4a} deformation: Backeberg *et al.*, submitted). We measured a high fracture density in drill core and on surface exposures at Hammond Reef. The average fracture density at Hammond Reef is ~ 25 fractures per meter with a range from < 10 to > 100 fractures per meter. These fractures and microfractures (observed in thin section) are thought to provide the original grain scale permeability in the tonalites that initiated alteration to sericite (Backeberg *et al.*, submitted).

The prevalent structural fabric along the entire western margin of the tonalites is an anastomosing deformation corridor parallel to the Marmion Shear Zone. The deformation is characterized by foliation striking 035° – 075° and dipping 60° – 80° to the southeast. The foliation is formed by the localized flattening and alignment of sericite from altered feldspars in both the Marmion Suite and Diversion Stock. The foliation records a horizontal NW-SE shortening axis, perpendicular to the shear zone and formed after cessation of shearing along the Marmion Shear Zone (D_{4b} deformation: Backeberg *et al.*, submitted). The intensity of foliation grades into unstrained tonalite lithons within the anastomosing network. Although mostly unstrained, the feldspars in the tonalite lithons are also partially to pervasively altered to sericite. At Hammond Reef the sericite gives the rock a pale-green colour, not observed outside of the ore deposit.

The foliation is cut by shallowly dipping thrust faults, consistent with coaxial NW-SE shortening (D_{4c} deformation: Backeberg *et al.*, submitted). Thrust faults strike ∼050° and dip 040° to the southeast. Breccias and fault gouges are commonly associated with these thrust faults. The largest of these faults, the Lynx Head Fault (LHF), is located 1.5 km to the southeast of Hammond Reef (Figure 5–2). The Lynx Head Fault displaces fresh, "unaltered" tonalites with preserved feldspar, biotite and hornblende over the chlorite- and sericite-altered tonalites of the western margin (Backeberg *et al.*, submitted). Fault breccias are observed in drill core at Hammond Reef. We infer these to be associated with these late-stage thrust faults.

5.3.5 Gold

There is disseminated and vein-hosted occurrences of gold along the western margin of the Marmion gneiss and within the Diversion Stock. The distribution of gold occurrences is shown in Figure 5–1 and Figure 5–2. The bulk of the gold tonnage is in the form of disseminated mineralization that defines the Hammond Reef gold deposit (Figure 5–9a). The highest gold grades occurs as free gold in large quartz-carbonate veins all along the anastomosing foliation zone (Figure 5–9b).

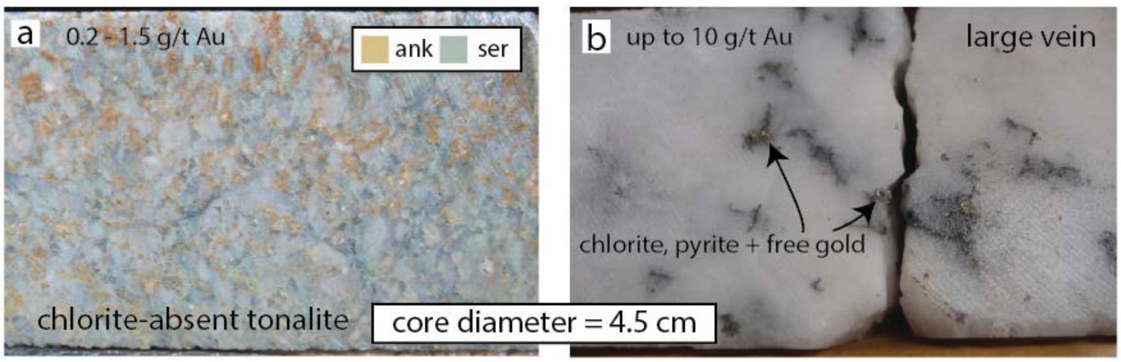

Figure 5–9: Gold mineralization at Hammond Reef. (a) Example of a sample with disseminated gold mineralization. This sample has 1.5 g/t Au (Sample MS173, Appendix B) and shows pervasive chlorite leaching, green sericite and yellow ankerite alteration with no hematite staining. Grades at Hammond Reef range between 0.2 – 1.5 g/t Au. (b) Large quartz-carbonate vein with visible gold and pyrite.

Disseminated gold mineralization

The Hammond reef gold deposit is defined by a disseminated mineralized zone (> 0.3 g/t Au) associated with chlorite-free tonalites altered to pale-green and/or brick-red colours (Figure 5–9a). The disseminated gold mineralization is spatially related to the sericite-altered tonalites and the anastomosing foliation zone across the intrusive contact of the Diversion Stock, but is preferentially developed in the Marmion tonalites (Figure 5–2). Mineralization occurs in both foliated tonalites and undeformed tonalite lithons. The deposit is 100 to 300 m wide along 1500 m of strike length trending $\sim 050°$. Extensive drilling from exploration activities indicates that the mineralized alteration zone dips 60 - 75° to the southeast at its western edge. At depths of 200 – 300 m, the dip shallows to $< 15°$ to sub-horizontal (Osisko, 2013). Below the subhorizontal dip of the mineralization and at the edges of the deposit, the intensity of the Hammond Reef alteration decreases gradually into chlorite tonalites (Figure 5–4a).

Gold is not visible to the naked eye in the Hammond Reef alteration zone, but it is always associated with pyrite. Gold grades range between 0.2 and 1.5 g/t (Osisko, 2013). We observed only minor amounts of disseminated pyrite throughout the western margin of the tonalites outside of Hammond Reef. A study by Kolb (2010) showed that gold occurs as inclusions or along fractures in pyrite, as well as within quartz strain shadows within foliation around euhedral or brecciated pyrite. There is abundant pyrite without gold mineralization at Hammond Reef (Osisko, 2013). Therefore, pyrite is not always a reliable indicator of gold. The intensity of alteration is not correlated with gold occurrences at Hammond Reef. Gold enrichment is observed in core logged as strongly, moderately and weakly altered tonalites (Osisko, 2013).

Visible gold in quartz-carbonate veins

Large quartz-carbonate veins up to 1 meter in width and with a strike length of over 100 meters are present throughout the western margin of the tonalites (Figure 5–10). The veins are made up of mostly quartz with carbonates (mainly ankerite, but also calcite) as a minor phase. Visible gold associated with large quartz-carbonate veins is reported throughout the region (see Figure 5–1, Stone (2008a,b)). Strike-slip

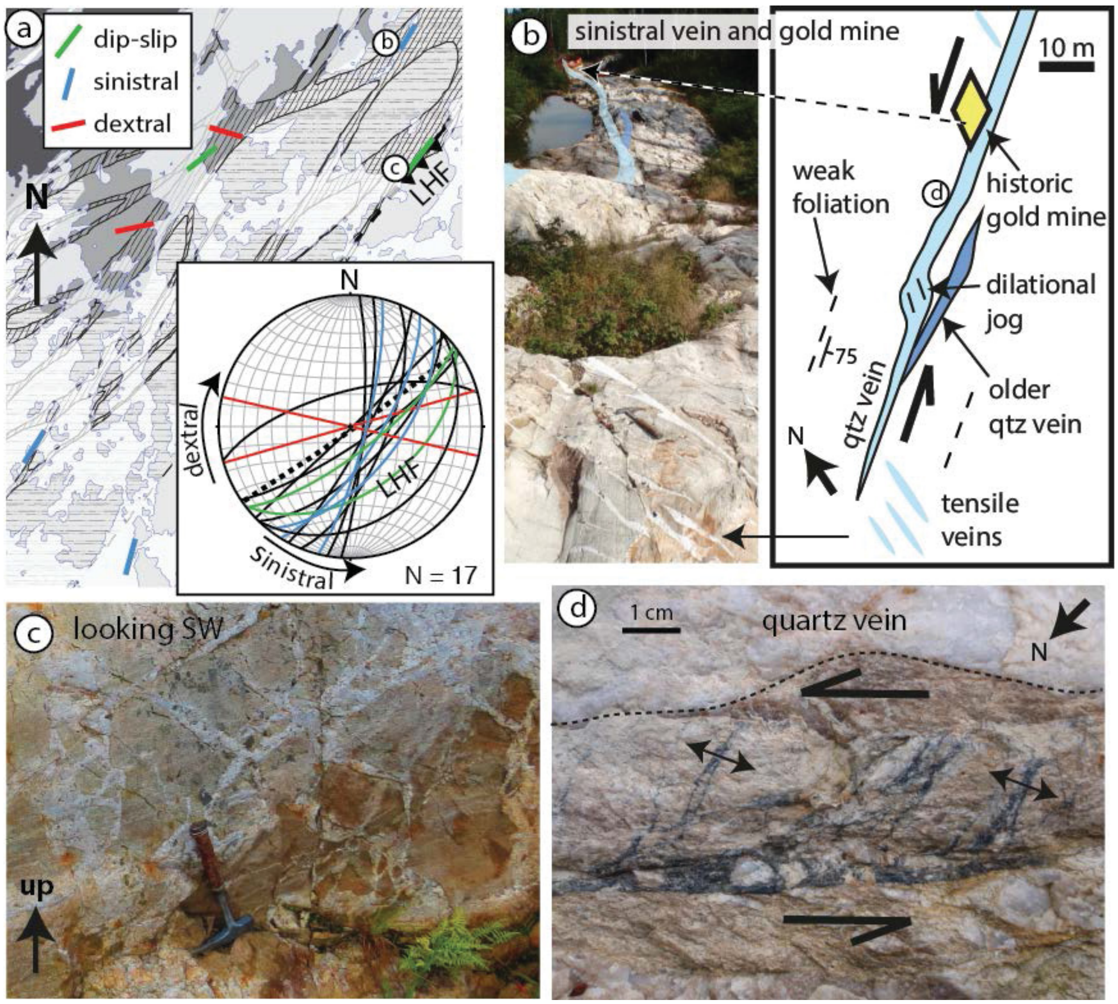

Figure 5–10: Large (auriferous) quartz-carbonate veins. (a) Map showing location of mapped quartz veins with kinematics displayed (green - dip-slip; blue - sinistral; red - dextral). Stereonet of large veins showing domains of sinistral and dextral kinematics, separated around the mean foliation plane (dashed line). Shallow Lynx Head Fault (LHF) vein is labelled. (b) Example of auriferous vein with sinistral offset, cross-cutting subparallel veins and a historic gold mine (yellow diamond). (c) Brecciated tonalite with vein stockwork in the hanging wall of the Lynx Head Fault vein. Hammer for scale. (d) Fault breccia with sinistral off-set is cut by a quartz vein, subparallel to the fault.

offsets along large quartz veins reach up to 5 m, measured from offset dykes. The dominant sense of offset is sinistral, but both dextral and sinistral offset are observed and are separated about the strike of the mean foliation (Figure 5–10a). The veins are emplaced parallel to pre-existing structures (Figure 5–10d), such as the local foliation or younger faults and therefore strike predominantly NE-SW (Figure 5–10a). Therefore, it is possible that the observed offset stems from the earlier structures, along which the veins were emplaced. Most veins are subvertical, but more shallowly dipping veins are also observed, for example where emplaced along shallowly dipping thrust faults, such as the Lynx Head Fault (Figure 5–10a). At the Lynx Head Fault, there are two parallel large veins (Backeberg *et al.*, submitted), whereas some locations show a mutually cross-cutting relationship of subparallel veins (Figure 5–10b). Hydrofractured breccias are commonly associated with these veins, especially in the hanging wall of shallowly dipping structures (Figure 5–10c). Visible gold is commonly associated with these large quartz-carbonate veins. Some veins with visible gold have been mined in the past (Figure 5–10b). Quartz-carbonate veins with visible gold are also observed cutting the Diversion Stock, along the eastern edge of the Finlayson Lake greenstone belt and also all along the Quetico Fault (Figure 5–1).

5.4 Discussion

The characteristics of the Hammond Reef gold deposit can be summarized as (1) gold only, (2) tonalite-hosted, (3) low-grade, (4) disseminated mineralization across (5) an intrusive contact and is (6) not related to shear zone deformation. Using the published criteria for gold deposit classifications, Hammond Reef can be broadly classified as a "non-carbonate stockwork-disseminated gold deposit" (classification number 11, Robert *et al.* (1997)). As Robert *et al.* (1997) emphasized, this class is a poorly defined group. Hammond Reef shows many similarities to deposits interpreted as "intrusion-related gold systems" (IRGS) (Couture & Pilote, 1993; Sillitoe & Thompson, 1998; Thompson *et al.*, 1999; Lang & Baker, 2001; Robert, 2001). In this section, we discuss Hammond Reef within the context of the deformation, alteration and intrusion history from detailed structural studies (Backeberg *et al.*, 2014, submitted), which will lead to a different classification of the Hammond Reef gold deposit.

5.4.1 Timing of mineralization

The relative timing of any ore deposit is identified by understanding the local cross-cutting relationships of structures, intrusions, fluid flow and alteration. There are many examples of gold deposits that formed coevally with active faults and shear zones (Sibson *et al.*, 1988; Castroviejo, 1990; de Ronde *et al.*, 1992; Vearncombe, 1998). Similarly, gold deposits around intrusions related to hydrothermal fluid flow during the cooling of the intrusive body are also well documented (Sillitoe, 1991; Sillitoe & Thompson, 1998; Thompson *et al.*, 1999; Cooke *et al.*, 2005). Hammond Reef is located across an intrusive contact in tonalites, adjacent to a shear zone that separates it from a greenstone belt. Understanding the details of the cross-cutting relationships is key in order to understand the source and timing of the mineralizing fluid(s).

The onset of deformation in the Marmion gneiss and Finlayson Lake greenstone belt occurred at ~ 2.92 Ga (Tomlinson *et al.*, 2003, 2004; Backeberg *et al.*, 2014).

Both disseminated and vein-hosted gold at Hammond Reef postdate the emplacement of the Diversion Stock, after the suturing of the Finlayson Lake greenstone belt and Marmion gneiss. The Diversion Stock is loosely linked in age to a similar intrusive body north of the Marmion gneiss dated at $\sim$ 2.786 Ga (Stone, 2008a; Buse *et al.*, 2010a). This provides the upper age-limit on mineralization. Pressure-temperature constraints from metamorphic assemblages in the Finlayson Lake greenstone show that deformation after the suturing of the Finlayson and Marmion terranes occurred during exhumation (see D_4 deformation event in Backeberg *et al.*, 2014). Exhumation of the Marmion tonalites is consistent with previous structural work at Hammond Reef showing an uplift-related regime inferred from the pattern of a high density of small fractures and veins (Barclay, 1996; Wasteneys, 2011). The D_{4a} fractures that cut the Marmion gneiss and Diversion Stock (Figure 5–11) provided the initial permeability structure that led to sericite alteration adjacent to the dormant Marmion Shear Zone (Backeberg *et al.*, submitted). The kinematics of the anastomosing foliation and cross-cutting thrust faults that followed (e.g. Lynx Head Fault) link fluid flow and deformation at Hammond Reef to a NW-SE shortening axis and dextral transpression of the active Quetico Fault to the south of the Marmion Shear Zone (Backeberg *et al.*, 2014, submitted). The Quetico Fault is related to the accretion of the Wawa subprovince at $\sim$ 2.72 – 2.68 Ga (Gower & Clifford, 1981; Card, 1990; Williams, 1990; Bauer *et al.*, 1992; Percival, 2007a) and was locked prior to 2.68 Ga (Corfu & Stott, 1986), which provides the lower age-limit on mineralization. These lines of evidence imply that Hammond Reef is a Neoarchean gold deposit hosted in a predominantly Mesoarchean terrane that saw the majority of its deformation 100 to 200 million years before mineralization (Figure 5–11).

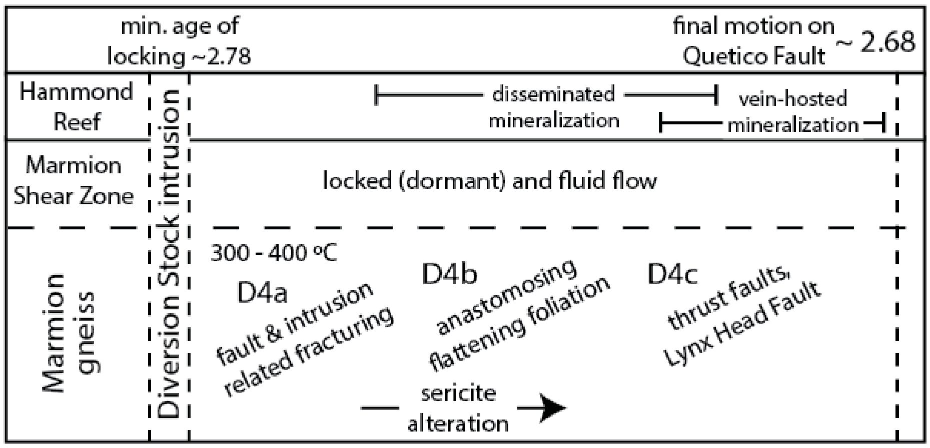

Figure 5–11: Timing of Hammond Reef disseminated and vein-hosted mineralization. Figure highlights the possible overlap in timing. Figure adapted from Backeberg et al. (submitted). Minimum age of locking interpreted from intrusion age inferred for Diversion Stock (Stone, 2008a; Buse *et al.*, 2010a). Final motion on Quetico Fault interpreted from intrusions that postdate offset (Corfu & Stott, 1986).

Disseminated gold, found together with pyrite and hydrothermal alteration of tonalites to pale green-red colours at Hammond Reef, is spatially associated with the sericite alteration found regionally within the anastomosing deformation corridor. Both types of alteration are pervasive and are found in foliation zones and in unstrained tonalite lithons in between. The presence of gold within quartz strain shadows around pyrite in foliated tonalites (Kolb, 2010) suggests that flattening occurred syn- to post-precipitation of gold. Flattening of sericite-altered tonalites has been linked to distributed NW-SE shortening, related to the progressive alteration of the feldspar that weakened the Marmion gneiss and Diversion Stock (Backeberg *et al.*, submitted). The spatial and structural overlap of the Hammond Reef style and regional sericite alteration style suggests that both were coeval prior to and during D_{4b} flattening (Figure 5–11). Alternatively auriferous fluids postdate the regional sericite alteration and fluid flow was focussed at Hammond Reef. However, the structures at Hammond Reef are identical to the structures all along the western margin, which suggests that fluid flow should be relatively homogeneous along strike. We discuss possible controls that led to the localization of mineralization at Hammond Reef in the sections below.

Gold is also hosted in large quartz-carbonate veins that follow pre-existing structures, including the latest shallow thrust faults (D_{4c}, Figure 5–11). The quartz-carbonate veins are mutually cross-cutting, which suggests that they were emplaced episodically during the later stages of deformation. Hydrofractured breccias in the hanging walls of quartz-carbonate veins are also consistent with the high fluid pressures, expected for episodic fluid flow. Backeberg *et al.* (submitted) showed that thrust faulting, which also accommodated the same NW-SE shortening, could have further developed flattening in the weak sericite-altered tonalites during thrusting. This suggests a temporal overlap between fluid flow, D_{4b} and D_{4c} deformation (Backeberg *et al.*, submitted). Quartz-carbonate veins were emplaced along reactivated D_{4c} faults; therefore vein-hosted gold is likely the latest mineralization event, even though there may have been some overlap with disseminated gold mineralization (Figure 5–11).

5.4.2 Deposit geometry

Hammond Reef has been extensively drilled during exploration activities (over 900 km of core at 15 - 20 m drill-core spacings), showing a $\sim$ 300 m wide mineralized zone with a steeply dipping western edge and a shallowly eastward-dipping (subhorizontal) base beginning at depths of around 300 – 400 m (Osisko, 2013). The exploration drilling data were interpreted in a structural model that included two foliated zones, known as the upper- and lower shear, that bound the deposit along the shallowly and steeply dipping sections (Osisko, 2013). However, the detailed mapping that identified the anastomosing deformation corridor along the western margin of the Marmion gneiss (Stone, 2008a) is defined by foliated zones of sericite-altered tonalites with a predominantly steep eastward-facing dip (Backeberg *et al.*, submitted). The distribution of foliation data at Hammond Reef is identical to the measurements made elsewhere within the anastomosing foliation zone, showing a range in dip from 50 to 80° facing to the southeast (see stereonet in Figure 5–12). No shallowly dipping foliation of less than 40° dip is observed in the tonalites. Furthermore, reexamination of the core logs and photo archives of drill core shows that foliated zones are not always present at the base of the mineralization. Therefore, we do not favour a subhorizontal dip for foliated tonalites at depth to conform to a upper- and lower-shear model. It is more likely that the deposit overlaps with the anastomosing foliation at depth, which has a similar geometry to what is observed at the surface (Figure 5–13).

We re-examined selected drill cores that intersected with the steep western edge and the deepest base of the shallowly dipping mineralized alteration zone at Hammond Reef. The Diversion Stock is observed in drill core that cuts the steep western edge of the alteration zone (Figure 5–12), consistent with the new map and geochemical data that places Hammond Reef across the intrusive contact. We interpret

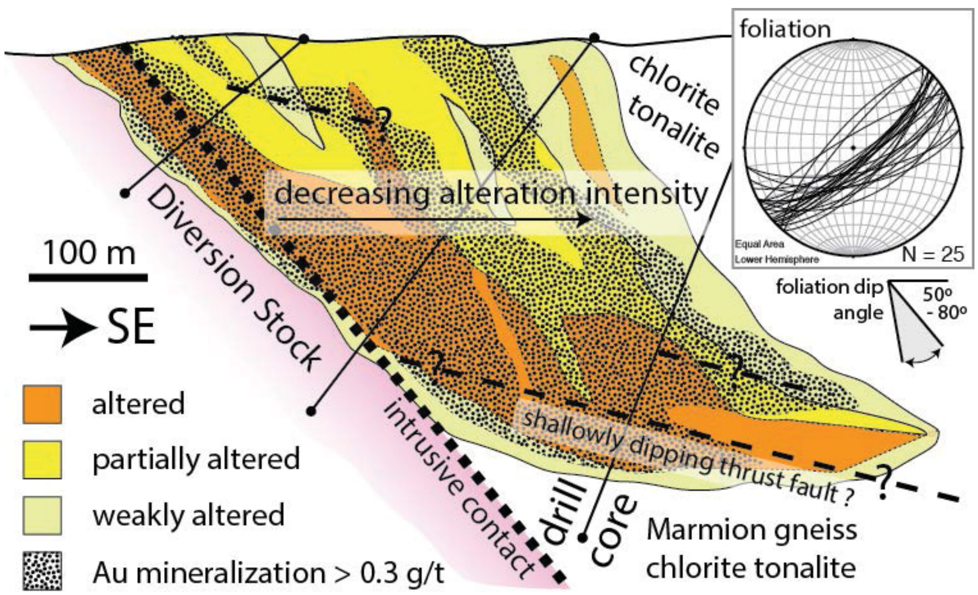

Figure 5–12: Schematic cross-section that summarizes the Hammond Reef mineralization, adapted from core logging and cross-sections by the Osisko Mining Corporation. No vertical exaggeration. Stereonet shows range of foliation data collected from surface exposures at Hammond Reef. We interpret the steep edge to the northwest of the deposit as being subparallel to the steep foliation and Diversion Stock intrusive contact (dotted line). Shallow southeastward dip of mineralization away from the intrusive contact possibly follows shallow thrust faults (dashed lines), related to the Lynx Head Fault. The outline of the resource shell overlaps with leaching of chlorite from the host tonalite.

the steep dip of the mineralized zone to be subparallel to the Diversion Stock intrusive contact and steep foliation (Figure 5–12), which are subparallel to the Marmion Shear Zone. The shallower, subhorizontal dip at the base of the deposit is more difficult to explain. The shallow eastward-facing dip of the disseminated mineralization is subparallel to the Lynx Head Fault (Figure 5–13). Subsidiary thrust faults that cut the sericite foliation are observed west of the Lynx Head Fault (Wasteneys, 2011; Backeberg *et al.*, submitted) and we observe fault breccias in the drill core that probably represent similar thrust faults at Hammond Reef. These shallow thrust faults may provide the dominant structural control for the shallowly dipping geometry of the mineralized Hammond Reef alteration zone (Figure 5–12), which emphasizes the temporal overlap between D_{4b} foliation and D_{4c} thrust faulting described above. The base and margins of the Hammond Reef alteration are gradual and are expressed as the gradational decrease of chlorite, which is absent in the mineralized zone. We found that where the base of the deposit intersects the foliation, the Hammond Reef alteration intensity shows a more pronounced gradational decrease (Figure 5–5a). In contrast, where the base of the hydrothermal alteration does not closely overlap with foliation, the decrease in alteration is more patchy and is correlated with the local frequency of veins around which chlorite was removed (for example Figure 5–5c).

5.4.3 Fluid flow adjacent to the Marmion Shear Zone

In Archean granite-greenstone terranes, TTGs are volumetrically prevalent over the thin slivers of greenstone belts pinched in between them. Yet nearly all of the known Archean gold deposits are found along steep crustal structures in greenstone belts (Groves *et al.*, 1989; Ward, 1995; Goldfarb *et al.*, 2001; Dubé & Gosselin, 2007;

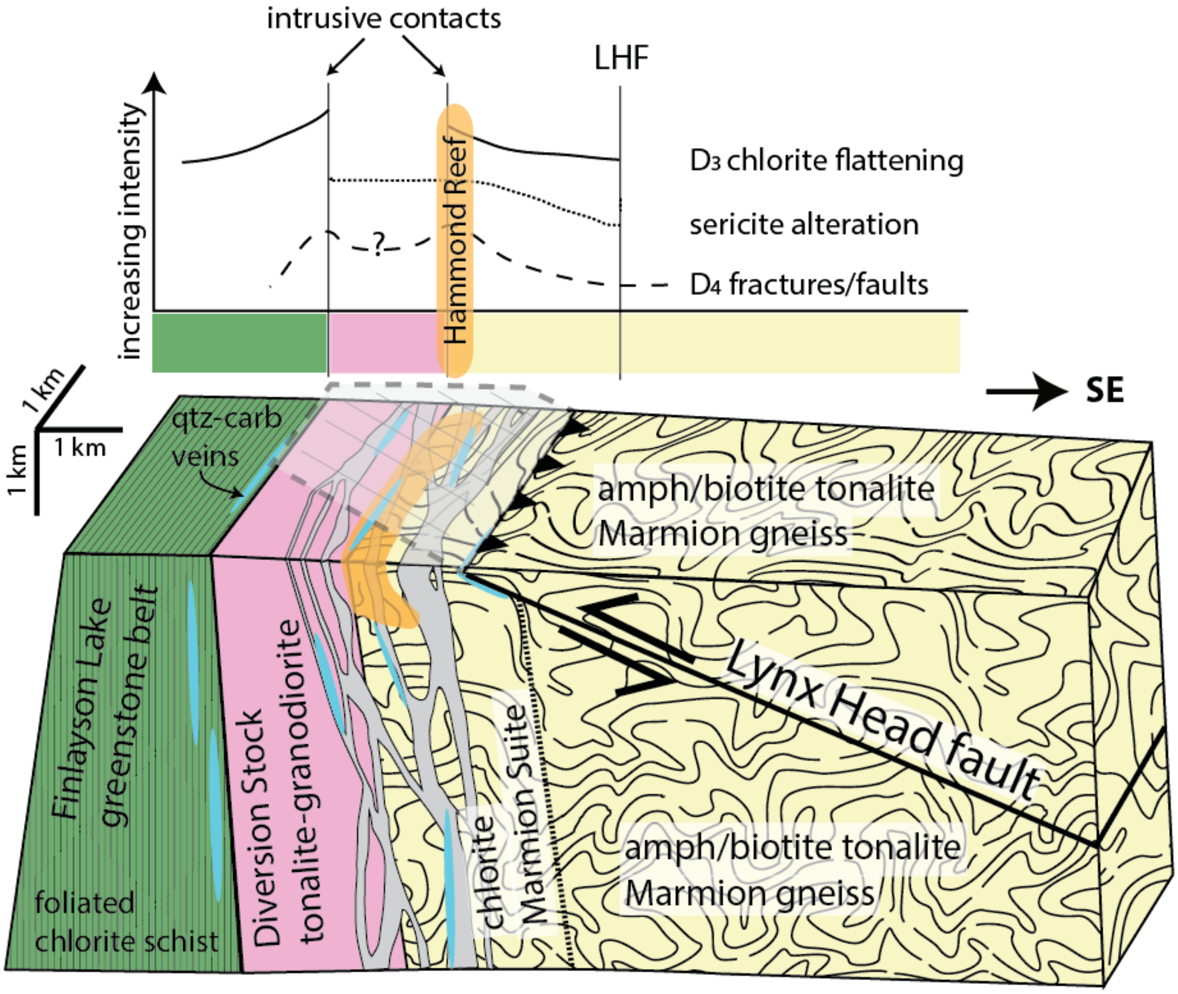

Figure 5–13: 3D block diagram of the Finlayson Lake greenstone belt, Marmion gneiss and Diversion Stock. The anastomosing foliation is drawn schematically and is not to scale. Dashed faults (f) are smaller D_{4c} faults parallel to the Lynx Head Fault (LHF). Quartz-carbonate veins (blue) drawn in parallel to pre-existing structures. The location of the chlorite – amphibole reaction front below the Lynx Head Fault is schematic (not observed). Top graph summarizes observations of alteration and D_3–D_4 deformation from the Finlayson Lake greenstone belt (Backeberg *et al.*, 2014), Diversion Stock and Marmion Suite (Backeberg *et al.*, submitted) with the Hammond Reef deposit overlain (transparent orange).

Juul-Pedersen *et al.*, 2007). Steep shear zones preferentially develop in the weaker finer-grained mafic volcanics that accommodated the majority of the plastic deformation (and shearing) during crustal-scale tectonic processes and the juxtaposition of greenstone belts and TTGs (Park, 1981; Jaguin *et al.*, 2012). Prominent steep shear zones either within or along the margins of the greenstone belts are thought to be the dominant pathways for fluids that led to many world-class gold deposits, such as in Abitibi (Poulsen *et al.*, 2000; Robert *et al.*, 2005). The Finlayson Lake greenstone belt, adjacent to the Marmion gneiss, was extensively shortened perpendicular to its southeastern margin ($> 50\%$) during the ductile deformation history of the region and its eastern margin is highly foliated, related to the steep crustal-scale Marmion Shear Zone (Backeberg *et al.*, 2014). Carbonation, most prominently observed by the addition of ankerite, of highly foliated units of the Finlayson Lake greenstone belt is also observed (Backeberg *et al.*, 2014), which is a common marker of fluid flow associated with auriferous quartz-carbonate veins (Dubé & Gosselin, 2007). Gold-bearing quartz-carbonate veins are observed on the very eastern margin of the Finlayson Lake greenstone belt (Figure 5–1; Stone (2008a)), suggesting that auriferous fluids migrated through the greenstone belt adjacent to the Marmion Shear Zone (Figure 5–13). Therefore, the Finlayson seems to have all the required ingredients for prospective gold mineralization. However, gold mineralization adjacent to the Marmion Shear Zone is preferentially developed in the adjacent Marmion gneiss and occurs as both vein-hosted and disseminated gold (Figure 5–13). The contrasting occurrences of gold at Hammond Reef can be explained by differences in the style of fluid transport as broad zones in disseminated mineralization related to pervasive grain-scale fluid flow (Couture & Pilote, 1993; Phillips & Powell, 2010) or channelized flow leading to higher-grade concentrations (Phillips & Powell, 2010).

Distributed fluid flow

The bulk of gold mineralization adjacent to the Marmion Shear Zone occurs as disseminated gold at Hammond Reef with a resource of over 10 million ounces of gold. Hammond Reef is located in the northern portion of pervasively sericite-altered tonalites (Figure 5–13), which developed into anastomosing foliation (aligned sericite) around undeformed tonalite lithons (sericite pseudomorphs after feldspar) (Backeberg *et al.*, submitted). The alteration of feldspar to sericite with and without the accommodation of strain did not seal the microstructural permeability of the tonalites, allowing for pervasive alteration to occur (Backeberg *et al.*, submitted). Chlorite leaching and gold-associated alteration at Hammond Reef were initiated around vein-filled fractures, as seen at the margins of the deposit (Figure 5–5) and are pervasive throughout the disseminated gold-mineralized zone. Microstructural grain-scale permeability identical to the description of the regional sericite alteration in the anastomosing deformation corridor thus also accommodated the pervasive flow of auriferous fluids at Hammond Reef. Sericite in the pervasively altered tonalites at Hammond Reef are also locally aligned into foliation zones. The foliation formed in response to the alteration-weakening of the tonalites as feldspar altered to sericite, as seen all along the western margin of the TTGs (Backeberg *et al.*, submitted). Examples of disseminated sericite alteration and gold mineralization in Archean intrusive rocks have been reported, but even those tend to have intruded shear zones within greenstone belts (e.g. in Abitibi: Couture & Pilote, 1993; Robert, 2001). The

Francoeur-Wasa Shear Zone in Abitibi shows a similar pervasive gold mineralization in intrusive bodies (Couture & Pilote, 1993). Couture & Pilote (1993) associate disseminated alteration and mineralization with pervasive fluid flow, where the host rocks remained permeable during the hydrothermal events, preventing episodic fluctuations in fluid pressure. Pervasive fluid flow is key to allow for disseminated gold mineralization to form along broader fluid-rock reaction fronts (Hofstra *et al.*, 1991; Couture & Pilote, 1993; Li *et al.*, 2013). Disseminated gold deposits in intrusive rocks are typically associated with magmatic-hydrothermal alteration processes related to local intrusions of magma(Thompson *et al.*, 1999; Sillitoe, 1991; Sillitoe & Thompson, 1998; Lang & Baker, 2001; Baker, 2002). The close spatial relationship of Hammond Reef to the Diversion Stock makes an intrusive-related interpretation for gold mineralization very attractive, but the detailed sequence of events (Backeberg *et al.*, 2014, submitted) clearly separates the two (Figure 5–11).

Channelized fluid flow

The highest gold grades in the Marmion gneiss occur as auriferous quartz-carbonate veins that cut the anastomosing foliation. These veins were emplaced episodically along discrete channels in pre-existing faults and foliation (Figure 5–13) and post-date the disseminated mineralisation (Figure 5–11). Vein-hosted gold deposits associated with cyclic, channelized fluid flow are reported in transpressive regimes and are classified as lode gold or mesothermal gold deposits (Sibson *et al.*, 1988; Kerrich & Wyman, 1990; Groves, 1993; Ridley *et al.*, 1996; Phillips & Powell, 2010). Episodic emplacement of large veins can be caused by the cyclic pore-fluid pressure build-up to above the lithostatic load followed by the sudden release of fluids along steep structures, known as fault-valving (Sibson *et al.*, 1988; Sibson, 1992). Subhorizontal veins known as flats, which occur perpendicular to steep shear zones can provide good evidence that fluids achieved supralithostatic pore-fluid pressures (Sibson, 1992). Gold deposits associated with subhorizontal quartz veins adjacent to shear zones have been reported (e.g. Gaboury & Daigneault, 2000; Tunks *et al.*, 2004; Chi & Guha, 2011). We only locally observed smaller-scale sub-horizontal veins at Hammond Reef and not extensive characteristically large flats. The mutually cross-cutting relationship of quartz-carbonate veins record episodic emplacement all along the western margin of the Marmion gneiss and together with hydro-fractured breccias are consistent with cyclic, channelized flow of fluids.

5.4.4 Source and nature of fluids

Hydrothermal alteration assemblages record the interaction of hydrothermal fluids in disequilibrium with surrounding wallrocks and can provide insight into the chemical composition of a fluid (Evans *et al.*, 2006; Thébaud *et al.*, 2006; Zhu *et al.*, 2011; Tomkins, 2013). The characteristic alteration at Hammond Reef consists of the removal of chlorite and the addition of sericite, pyrite and carbonates to the tonalites. These alteration characteristics are identical to alteration assemblages of other gold-only disseminated and lode gold deposits (Couture & Pilote, 1993; Phillips, 1993; Lang & Baker, 2001; Robert, 2001; Evans *et al.*, 2006; Phillips & Powell, 2010). Hydrothermal sericite and hematite are also common in these gold deposits (Cameron & Hattori, 1987; Evans *et al.*, 2006; Phillips & Powell, 2010). Auriferous fluids associated with these alteration assemblages are typically characterized as weakly oxidized, low-salinity fluids rich in CO_2 and sulfur (Cameron & Hattori, 1987; Phillips, 1993; Phillips & Evans, 2004; Evans *et al.*, 2006; Phillips & Powell, 2010; Tomkins, 2013). The precipitation of gold responds to changes in physicochemical conditions of the fluid and surrounding wallrock during transport, which affects the solubility of gold in the fluid (Böhlke, 1989; Gammons & Williams-Jones, 1997; Williams-Jones *et al.*, 2009; Zhu *et al.*, 2011; Tomkins, 2013). Gold precipitation occurs predominantly at temperatures of 300 – 400°C (Kerrich, 1999; Tomkins, 2013). This temperature range overlaps with the predicted pressure–temperature path of the Marmion gneiss and Hammond Reef during D_4 deformation (Backeberg *et al.*, 2014, submitted) (see Figure 5–11).

The source of auriferous fluids is still strongly debated in the literature. Gold enrichment in fluids is linked to either metamorphic devolatilization reactions of metabasic rocks (Phillips, 1993; Goldfarb *et al.*, 2005; Phillips & Powell, 2010) or fluids given off during crystallization of felsic to intermediate magmas (Cameron & Hattori, 1987; Couture & Pilote, 1993; Goldfarb *et al.*, 2005; Richards, 2009). Gold fields in Archean terranes occur predominantly as vein-hosted lode gold in shear zones cutting greenstone belts and are classified as mesothermal "orogenic" gold deposits (Böhlke, 1982; Groves *et al.*, 1989; Kerrich & Wyman, 1990; Hodgson, 1993; Groves *et al.*, 1998; Goldfarb *et al.*, 2001), for which the source of the fluids is predominantly thought to be metamorphic (Phillips, 1993; Goldfarb *et al.*, 2005; Phillips & Powell, 2010). On the other hand, less common disseminated gold in Archean terranes hosted in plutons is thought to be related to magmatic fluids (Thompson *et al.*, 1999; Sillitoe, 1991; Sillitoe & Thompson, 1998; Lang & Baker, 2001; Baker, 2002). Goldfarb *et al.* (2005) highlighted the temporal overlap observed between magmatic events and lode gold deposits throughout Archean terranes. Regardless of the fluid source, both styles of gold deposits have similar alteration characteristics and are linked to subduction-style tectonics in collisional orogens (Groves *et al.*, 1998; McCuaig & Kerrich, 1998; Goldfarb *et al.*, 2001; Lang & Baker, 2001; Goldfarb *et al.*, 2005; Richards, 2009). The interaction of partial melts from subducted slabs with the mantle wedge has been shown to produce magmas typically associated with large Au (and Cu) deposits (Mungall, 2002; Sun *et al.*, 2004) The correlation of gold to subduction and accretionary systems is observed throughout Earth history (Kerrich & Wyman, 1990; Groves *et al.*, 1998; Kerrich *et al.*, 2000; Goldfarb *et al.*, 2001). Examples of gold occurrences spatially associated with active subduction-accretion settings are reported for lode-gold deposits (Koons & Craw, 1991; Goldfarb *et al.*, 1998; Sibson & Scott, 1998; Haeussler *et al.*, 1995; Cox *et al.*, 2006; Pitcairn *et al.*, 2006; MacKenzie & Craw, 2007) and intrusion-related deposits (Baker & Tullemans, 1990; Bakke, 1995; Simmons *et al.*, 1996; Thompson *et al.*, 1999; Lang & Baker, 2001).

We do not present direct fluid data for the Hammond Reef gold deposit, but show that the resultant alteration assemblages are comparable to many known gold settings described above. Our results do show that the structural and metamorphic data of the western margin of the Marmion gneiss clearly show late-stage, brittle deformation at temperatures below ~400°C leading up to D_4 deformation (Figure 5–11). We relate the localisation of alteration of feldspar to sericite along fractures to fluid flow and fluid-rock reactions. Even though we do not report any fluid data, unaltered tonalites away from the western margin of the TTGs (e.g. east of the Lynx Head Fault), supports the presence of a fluid that caused alteration along the structural contact with the Finlayson Lake greenstone belt. The tectonic setting and source for auriferous fluids of Hammond Reef are even more cryptic than in other studied gold deposits, because the deposit formed adjacent to a dormant shear zone and overlaps with an intrusive contact, but the structural evidence suggests that mineralization postdates local magmatic activity. Hammond Reef also hosts large quartz-carbonate veins that post-date the timing of disseminated mineralization (Figure 5–11). This overlap of two different styles of mineralization at Hammond Reef shows that both types can occur in the same structural setting. The kinematic consistency and relative timing of cross-cutting structures in the Finlayson Lake greenstone belt and Marmion gneiss link the regional NW-SE shortening leading up to and during gold mineralization to the accretionary tectonics of the Wawa and Wabigoon subprovinces along the Quetico Fault $\sim$ 20 km to the south (D_3 and D_4 deformation events, Backeberg *et al.*, 2014, submitted). Felsic magmatism at 2.70 – 2.68 Ga is widespread in the southwestern Superior Province, associated with the Neoarchean accretion (Card, 1990; Percival *et al.*, 2006). However, the closest intrusive body of that age to Hammond Reef is the Eye-Dashwa pluton, which lies $\sim$ 20 km west of Hammond Reef (Stone, 2008a). The difficulty of interpreting the source of fluids at Hammond Reef relates to the distal relationship of alteration and mineralization to both active tectonism and magmatism.

5.4.5 Why is disseminated gold at Hammond Reef?

Pervasive alteration to sericite of the tonalites within the anastomosing deformation corridor, suggests that grain-scale permeability was enhanced during progressive sericite-alteration (Backeberg *et al.*, submitted). Therefore, pervasive fluid flow can be inferred to have occurred along the entire western margin of the TTGs, which is consistent with the occurrence of disseminated pyrite throughout the sericite-altered tonalites. Similarly, auriferous quartz-carbonate veins are also found along the length of the anastomosing foliation, showing that auriferous fluids migrated along the entire strike-length of the Marmion Shear Zone and damage aureole. However, the pale green-red hydrothermal alteration and disseminated gold mineralization (> 0.2 g/t) are only localized at Hammond Reef in the northern portion of the anastomosing network.

We do not observe specific structures or set of structures that explain the localization of gold mineralization at Hammond Reef. Therefore, it is necessary to explore alternative controls that promoted localized wallrock sulfidation (i.e. pyrite alteration) and gold mineralization. The most pronounced difference that we observed within the anatomising deformation corridor is the higher density of more mafic tonalite xenoliths and mafic dykes at Hammond Reef (Figure 5–3). Lithological heterogeneities have been shown to enhance fluid-rock interactions by bringing the fluid out of chemical equilibrium with the surrounding wallrock (e.g. Böhlke, 1989; Evans *et al.*, 2006). The xenoliths in the Marmion gneiss have a higher mafic mineral content (up to 30% chlorite), specifically increasing the availability of Fe, which enhances the alteration potential for pyrite (wallrock sulfidation) and associated gold precipitation (Neall & Phillips, 1987; Evans *et al.*, 2006; Zhu *et al.*, 2011). More abundant mafic dykes at Hammond Reef compared to elsewhere along the margin provide an even higher Fe content, ideal for sulfidation. These mafic dykes also provide a local source of chromium for the fuchsite alteration observed only at Hammond Reef.

The minor lithological heterogeneities caused by more mafic xenoliths and more abundant mafic dykes found at Hammond Reef are the most likely candidate observed to promote sulfidation and gold precipitation of the tonalite wall rocks at Hammond Reef. We showed that disseminated gold and the characteristic alteration at Hammond Reef overlapped with the development of the anastomosing foliation after regional sericite alteration along the western margin of the tonalites (Figure 5–11). This implies, that if enhanced wallrock sulfidation and gold mineralization was *only* controlled by lithological heterogeneities, the pervasive sericite alteration along the entire western margin of the TTGs adjacent to the Finlayson Lake greenstone belt formed by the same auriferous fluid.

5.4.6 Hammond Reef classification

For most ore deposits, it is typically assumed that mineralization is directly related to the local geological events, such as the intrusion of magma or deformation along major faults and shear zones. However, results from Hammond Reef show that mineralization postdated both shearing along the nearby Marmion Shear Zone as well as the local Diversion Stock magmatism. Rather, the relative timing of gold mineralization at Hammond Reef is related to the regional accretion of the Superior Province. Gold mineralization throughout the Superior Province is known to be strongly associated with the beginning of the Neoarchean era at around 2.7 Ga (Goldfarb *et al.*, 2001) and the prominent east-west-trending structures that record the accretionary tectonism at that time (Card, 1990; Poulsen *et al.*, 2000; Robert *et al.*, 2005; Percival *et al.*, 2006; Dubé & Gosselin, 2007; Percival, 2007a). Even though Hammond Reef is located in a Mesoarchean terrane that accreted at 2.92 Ga (Tomlinson *et al.*, 2004; Percival, 2007a), the mineralization is associated with late-stage deformation and fluid flow along a steep structure in a supra-subduction setting during the $\sim$ 2.7 Ga tectonism (Backeberg *et al.*, 2014, submitted) and is not sourced from local intrusions. The temporal and structural overlap of the disseminated gold and alteration with the channelized auriferous quartz-carbonate veins reflects different styles of flow flow of auriferous fluids along a dormant structural contact between the Finlayson Lake greenstone belt and Marmion gneiss TTGs from a distal source related to subduction. This makes the Hammond Reef fit with a mesothermal orogenic gold classification.

5.5 Conclusion

Hammond Reef is located in an anastomosing deformation zone in tonalites adjacent to the northwest striking Mesoarchean Marmion Shear Zone, which was located in a suprasubduction setting during the accretionary tectonics of the Wabigoon and Wawa subprovinces at around 2.7 Ga. The gold mineralization can be classified as of mesothermal "orogenic" type related to accretionary tectonics, even though Hammond Reef is not located close to any zone of active tectonism and magmatism.

Rather, Hammond Reef is hosted in a terrane that experienced peak metamorphism and deformation up to 200 million years before mineralization. Gold mineralization occurs as disseminated and vein-hosted styles related to broad pervasive and channelized fluid flow, respectively. Disseminated gold mineralization was coeval to the pervasive fluid flow that led to the regional sericite alteration and anastomosing foliation of the tonalites adjacent to the Marmion Shear Zone. Gold mineralization was localized at Hammond Reef within the anastomosing deformation zone because of the presence of lithological heterogeneities of relatively more mafic mineral compositions that promoted fluid-rock reactions and gold precipitation.

CHAPTER 6
Synthesis and Conclusions

As a result of detailed structural field work in the adjoining Finlayson Lake greenstone belt and Marmion tonalite gneiss, I describe the deformation, alteration and fluid flow history and the association with the Marmion Shear Zone (MSZ, Figure 6–1). The focus of this thesis is to understand the overall structural controls and timing of the Hammond Reef gold deposit that lies within the Marmion gneiss. The interpretations of cross-cutting relationships place gold mineralization during Neoarchean fluid flow through the damage aureole in the tonalites adjacent to the dormant Marmion Shear Zone (Figure 6–1). In this chapter, I summarize and combine the results from the previous chapters into a coherent timeline and present a schematic model to illustrate the evolution of the Finlayson Lake greenstone belt, Marmion gneiss and Marmion Shear Zone (Figure 6–2).

The timeline begins with the Finlayson Lake greenstone belt deposited between 3.00 and 2.93 Ga into a submarine setting, possibly a rift basin (Figure 6–2a). Sedimentation in the Finlayson Lake greenstone belt included a source of exposed tonalite-trondhjemite-granodiorite (TTG) crust, similar in age and composition to the Marmion gneiss tonalites (Figure 6–2a). Evidence for an exposed 3.0 Ga felsic crust comes from inherited crystals of zircon of that age and large, angular tonalite boulders in the conformable sediments of the greenstone belt. Deformation of the greenstone belt may have begun by 2.92 Ga during the amalgamation of the Wabigoon subprovince (Tomlinson *et al.*, 2004; Percival, 2007a). The deformation history and clockwise pressure-temperature path for the Finlayson Lake greenstone belt described below show a relatively cold and deep setting and point to a subduction-accretion setting (see Ernst, 1988; Handy *et al.*, 1999; Van Staal *et al.*, 2008, for modern examples). There are no constraints on the direction or kinematics of subduction. In this chapter, we illustrate subduction of the Finlayson belt as dipping to the east, with the exposed 3.0 Ga felsic crust in the overriding plate (Figure 6–2 b-d). It is also important to note that are no constraints on the subduction angle. The dip angle of modern subduction zones is typically related to the relative rate of convergence and dynamics of mantle convection (Luyendyk, 1970; Yokokura, 1981; King, 2001), as well as the age and thermal cooling of the subducted oceanic crust, which increases in density with time (Carlson & Herrick, 1990; Cloos, 1993; Crosby *et al.*, 2006; Hynes, 2013). During the Archean it is sometime argued that subduction, if any, should have been shallowly dipping (Abbott *et al.*, 1994; Foley *et al.*, 2003; Johnson *et al.*, 2014), but new numerical models and physicochemical constraints on subduction slabs are showing that steep subduction is viable in the hotter Archean environment (van Hunen *et al.*, 2008; van Hunen & Moyen, 2012; Hynes, 2013). We have illustrated steep subduction in Figure 6–2c.

The onset of deformation of the Finlayson Lake greenstone belt corresponds to a regional compressive regime and closure of the basin (Figure 6–2b). We utilize the thermobarometry published by Holland & Blundy (1994) on coexisting plagioclase-amphibole mineral pairs in both the Finlayson Lake greenstone belt and the Marmion gneiss. The uncertainties of pressure-temperature calculations are discussed in the literature (e.g. Hodges & McKenna, 1987; Kohn & Spear, 1991) and need to be considered before any meaningful interpretations can be made. We report the range of results from different mineral pairs measured within the samples, which greatly exceeds the analytical error of the thermobarometry, therefore we believe the resultant pressure-temerature path to be an accurate range in possibilities that represent the history of the measured events. Relative uncertainties related to systematic errors of experimental conditions can be eliminated by using the same thermobarometer for different metamorphic events within a suite of samples (Hodges & McKenna, 1987). This allows for comparative thermobarometry between the pressure-temperature conditions of separate metamorphic and deformation events. We report the resultant pressure-temperature conditions for three separate settings together with metamorphic mineral assemblages and structural relationships. Prograde metamorphism preserved in aligned mineral inclusions recorded a foliation that developed at 780 – 860 MPa at 600 ± 45°C during D_1 deformation (Figure 6–2c). The mineral assemblage that makes up the aligned inclusions associated with D_1 consists of plagioclase, epidote, ilmenite and quartz preserved within D_2 amphiboles. The robustness of pressure-temperature conditions of plagioclase inclusions is well knows and provides good estimates for conditions of deformation during the development of the fabric preserved in the inclusion assemblage (?). The D_1 deformation is only observed in one location within the greenstone belt and is, therefore, poorly constrained. The prograde foliation has been overprinted by the peak metamorphic assemblage and deformation during D_2. The kinematic consistency of overprinting deformation structures across the entire greenstone belt was used to argue a common deformation history for the entire belt (see Chapter 3) and, therefore, we retain a simplified interpretation of common deformation events in the Finlayson Lake greenstone belt during D_1. The error in pressure-temperature settings for the two deformation events in the Finlayson Lake greenstone belt overlap partially (D_1 and D_2, Figure 3–7), but together with the varying mineral assemblages described below, the two are clearly separated. All possible variations in pressure and temperature conditions for these deformation events require a clockwise pressure-temperature pathway. Next, the Finlayson Lake greenstone belt experienced peak metamorphism and D_2 deformation at 470 – 700 MPa at 625 ± 25°C during subhorizontal compression (Figure 6–2d). Folds and shear zones in the greenstone belt preserve belt-scale sinistral transpression during D_2, which led to the development of the overall anticlinal geometry observed today (Figure 6–2c). Along the approximate axis of the anticline, we observe a tabular zone of intense foliation and veining, which we call the Finlayson fault. The timing of development of this structure has not been determined. The anticlinal structure could be a result of a fault-propagation fold or the fault could represent high-strain flattening of the anticline's fold hinge. The belt-scale structural architecture and anticline is kinematically consistent with D_2 deformation. Therefore we include the Finlayson fault during D_2 deformation (Figure 6–2d), although it may have modified pre-existing fabrics inherited from D_1 deformation. The pressure ranges for the two deformation events in the greenstone belt require 4 – 9 km of exhumation between D_1 and D_2 deformation (Figure 3–7). The present day exposed Marmion gneiss is estimated to have been at 300 – 360 MPa and 640 ± 20°C prior to D_3 deformation, suggesting that it was shallower (and hotter) than the adjacent greenstone belt during D_1 and D_2. We do not know when metamorphism in the Marmion gneiss took place, but the relative difference in pressure conditions emphasizes that the two terranes were in crust with entirely different thermal structures ($\sim 30°$C/km in the greenstone belt and $\sim 60°$C/km in the gneiss) and could not have been adjacent at the time. Therefore, exhumation of the Finlayson Lake greenstone belt prior to, during and after D_2 is illustrated as greenstone-belt-up displacement relative to the Marmion gneiss, possibly related to deformation along the Marmion Shear Zone (MSZ, Figure 6–2d). No kinematics are preserved for displacement along the Marmion Shear Zone, which has been overprinted by late stage suturing and emplacement by the Diversion Stock (see below). The structure is drawn with a steep dip with predominantly sinistral strike-slip displacement that also accommodated vertical displacement of the greenstone belt. Inferred sinistral kinematics along the Marmion Shear Zone are consistent with the D_2 deformation structures described above.

We interpret the exhumation of the greenstone belt as following under-plating and D_2 deformation (Figure 6–2d). Mechanisms for the exhumation of subducted crust have been shown to be accommodated by underplating into the overriding plate, through down-stepping of the subduction fault or the arrival of a back-stepped "new" subduction zone, which deactivates older subduction zones (Groves *et al.*, 1998; Kusky & Polat, 1999; Meneghini *et al.*, 2009). The schematic in Figure 6–2d includes slab break-off. We observe no constraints on slab break-off in the field area, but include slab break-off in the schematic, because it is thought to be a more common occurrence in hotter Archean subduction zones (van Hunen & Moyen, 2012). Furthermore, slab break-off has been suggested to also provide a mechanism to help drive exhumation of the subducted crust (Warren, 2013). The occurrence or absence of slab break-off does not affect the tectonic evolution described here. The D_2 deformation of the Finlayson Lake greenstone belt followed by exhumation are associated with the final stages of the Wabigoon amalgamation and associated local NNW-SSE horizontal shortening (Figure 6–2).

The next stage in the local tectonic evolution is recorded by a regional change in shortening axis to NW-SE, preserved in foliation and aligned chlorite (D_3) during retrogression of amphibole (Figure 6–2e). The D_3 deformation records flattening perpendicular to the Marmion Shear Zone and is observed in both the Marmion gneiss and the Finlayson Lake greenstone belt (Figure 6–2e). The pressure constraints to either side of the Marmion Shear Zone separate the Finlayson and Marmion by 7 - 13 km prior to D_3. Chlorite alignment and foliation do not preserve any simple shear. We thus propose 7 - 13 km of relative throw (Finlayson up) leading up to D_3 deformation (Figure 6–2e). The D_3 deformation marks the earliest time of compressional suturing and cessation of shear along the Marmion Shear Zone (Figure 6–1). The regional NW-SE shortening places the Marmion Shear Zone at a high angle (perpendicular) to the shortening axis, making slip impossible (Anderson, 1905; Simpson, 1997) and is consistent with cessation of simple shear leading up to D_3. The pervasive retrogression to chlorite and flattening along the eastern margin of the Finlayson Lake greenstone belt associated with the proximity to the Marmion Shear Zone overprints any pre-existing kinematic markers. The shortening estimate of 64% during D_3 along the eastern margin of the greenstone belt presented in Chapter 3 is a minimum estimate of shortening, as the shortening was estimated in units that did not experience pervasive alteration to chlorite and flattening associated with D_3 foliation (see Chapter 3). The minimum age of suturing of the Marmion gneiss and Finlayson Lake greenstone belt is constrained by the late- to post-D_3 emplacement of the Diversion Stock at approximately 2.78 Ga and effectively locks the Marmion Shear Zone (Figure 6–2f). The Diversion Stock has geochemical characteristics identical other "TTGs" interpreted to have formed in magmatic arc settings (see Figure 5–8) (e.g. Foley *et al.*, 2003; Polat *et al.*, 2009; Rollinson, 2008; Huang *et al.*, 2013). It results from melts intruding the overriding plate, emplaced along the crustal-scale Marmion Shear Zone. Emplacement of the pluton promoted fracturing and microfracturing (D_{4a}) of the solidified Diversion Stock itself, as well as the adjacent Marmion gneiss, which likely had prior fault-related damage associated with offset along the Marmion Shear Zone (Figure 6–2f). By D_{4a} deformation, the Finlayson Lake greenstone belt and Marmion gneiss have thermally equilibrated (Figure 6–1). The fracture network provided the initial permeability structure in the damage aureole adjacent to the Marmion Shear Zone, for fluids to migrate through (Figure 6–2g). Auriferous fluids altered felspar in the Marmion gneiss and Diversion Stock to sericite, which promoted grain-scale permeability and pervasive alteration. Gold was locally precipitated where more mafic rocks enhanced fluid-rock reactions and wallrock alteration, such as at Hammond Reef. The sericite alteration weakened the tonalites, which locally flattened (D_{4b}) during progressive sericitization, in response to the regional NW-SE shortening and developed into an anastomosing foliation parallel to the Marmion Shear Zone (Figure 6–2g). Continued NW-SE shortening developed NE-striking shallowly dipping thrust faults (D_{4c}) that cut the sericitized tonalites, such as the Lynx Head Fault to the east of Hammond Reef (Figure 6–2h). We observed only one such fault (the Lynx Head Fault), but lineaments in aerial photos in similar orientation suggest these faults may be expressed regionally by river drainage throughout the Marmion gneiss (see Stone, 2008b). Thrust faulting was kinematically consistent with sericite-induced foliation and could have promoted further foliation of sericitized tonalites. This suggests a temporal overlap in D_{4b} and D_{4c} deformation (Figure 6–1). Large gold-bearing quartz-carbonate veins record the youngest activity in the region. They are emplaced episodically along pre-existing foliation and thrust faults. The quartz-carbonate veins record a change in fluid-flow style from pervasive flow with broad reaction fronts and disseminated gold to channelized flow with higher-grade lode gold. The timing of gold mineralization at Hammond Reef and along the western margin of the Marmion gneiss emphasizes that it is located adjacent to an inactive structure and is not related to local magmatic activity. Rotation of the shortening axis to NW-SE during the late-stage deformation of the Marmion gneiss is associated with the regional convergence and northward-directed subduction of the Quetico and Wawa subprovinces from the south (Calvert *et al.*, 1995; Whalen *et al.*, 2002; White *et al.*, 2003; Musacchio *et al.*, 2004) and is kinematically consistent with dextral transpression recorded across the Quetico Fault (Corfu & Stott, 1986; Percival & Williams, 1989; Williams, 1990; Bauer *et al.*, 1992; Peterson & Zaleski, 1999). This places the steep and dormant Marmion Shear Zone in a suprasubduction zone setting (Figure 6–2 e-h). The spatial and temporal relationship between auriferous fluids and subduction systems have long been identified

(Groves *et al.*, 1998; McCuaig & Kerrich, 1998; Goldfarb *et al.*, 2001; Lang & Baker, 2001; Mungall, 2002; Goldfarb *et al.*, 2005; Richards, 2009). Therefore, gold mineralization at Hammond Reef (and regionally) is interpreted as subduction-related during the regional accretion with the Wawa and Quetico subprovinces at ~ 2.7 Ga. Gold deposits throughout the Superior Province are associated with the 2.72 – 2.68 Ga accretion along prominent east-west striking sutures, such as the Quetico Fault. The Hammond Reef deposit is related to the spike in gold occurrences during the Neoarchean, even though it is hosted in a Mesoarchean terrane that saw the majority of its deformation up to 200 million years prior to mineralization.

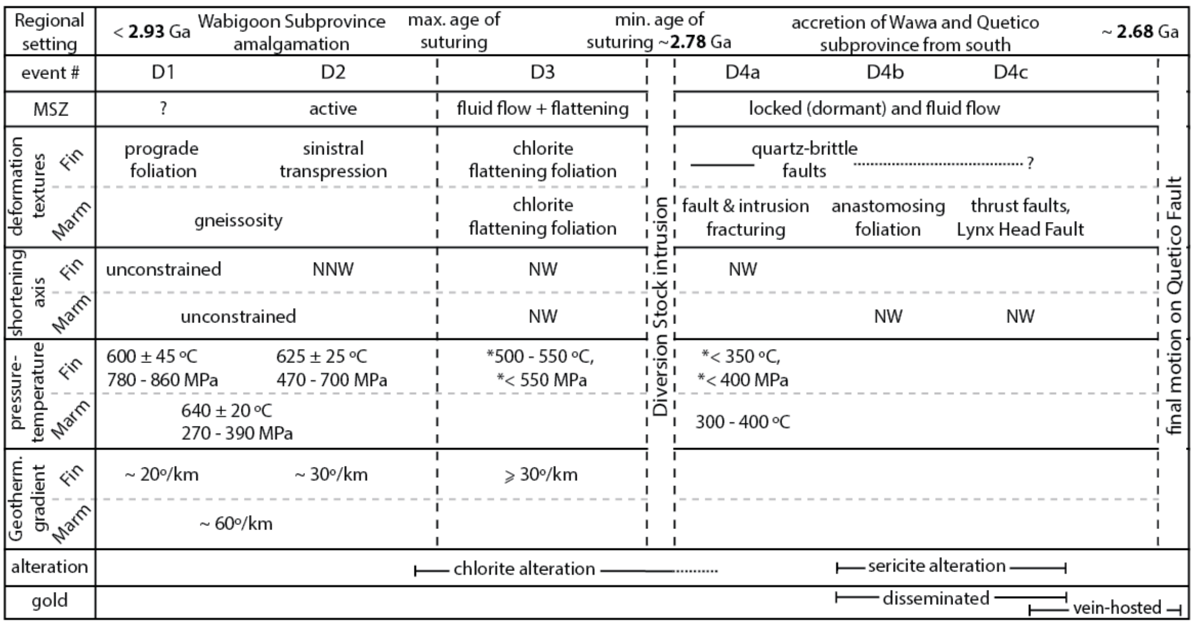

Figure 6–1: Summary of the deformation events in the Finlayson Lake greenstone belt (Fin), Marmion gneiss (Marm) and Marmion Shear Zone (MSZ). This figure is complementary to Figure 6–2, which provides a graphical illustration. The pressure range is given, rather than the uncertainty, because of the thermodynamic constraints from metamorphic assemblages. * Unconstrained pressure-temperature for D_3 and D_4 deformation in the Finlayson Lake greenstone belt estimated from the clockwise pressure-temperature pathway (Backeberg *et al.*, 2014). Hammond Reef mineralization overlaps with the late-stage D_4 deformation events. Rotation of shortening axis observed in Finlayson deformation events (Backeberg *et al.*, 2014). The NW-SE shortening axis for D_3 and D_4 is perpendicular to the Marmion Shear Zone and kinematically consistent with dextral transpression across the Quetico Fault to the south. The transition from the regional Mesoarchean Wabigoon subprovince tectonism to Neoarchean Superior Province tectonism is linked to the change in the subhorizontal shortening axis from NNW to NW, respectively. Ages shown are < 2.93 Ga for onset of Wabigoon accretion (Tomlinson *et al.*, 2003), 2.78 Ga for intrusion of Diversion Stock (Buse *et al.*, 2010a) and 2.68 Ga for undeformed intrusive bodies cutting the Quetico Fault (Corfu & Stott, 1986).

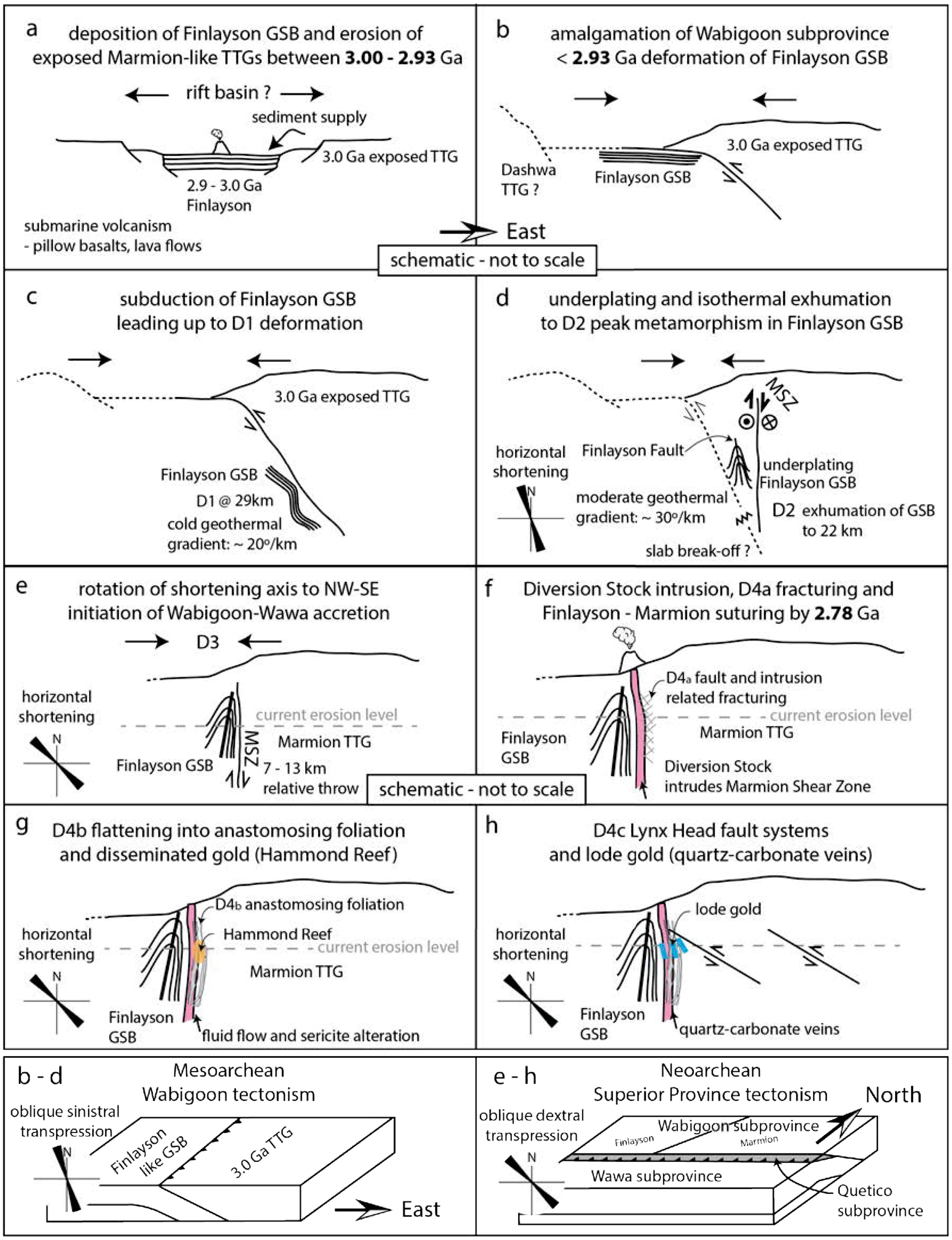

a deposition of Finlayson GSB and erosion of exposed Marmion-like TTGs between 3.00 - 2.93 Ga
rift basin ?
sediment supply
3.0 Ga exposed TTG
2.9 - 3.0 Ga Finlayson
submarine volcanism - pillow basalts, lava flows
b amalgamation of Wabigoon subprovince < 2.93 Ga deformation of Finlayson GSB
3.0 Ga exposed TTG
Dashwa TTG ?
Finlayson GSB
East
schematic - not to scale
c subduction of Finlayson GSB leading up to D1 deformation
3.0 Ga exposed TTG
Finlayson GSB
D1 @ 29km
cold geothermal gradient: ~ 20º/km
d underplating and isothermal exhumation to D2 peak metamorphism in Finlayson GSB
MSZ
horizontal shortening
Finlayson Fault
underplating Finlayson GSB
moderate geothermal gradient: ~ 30º/km
D2 exhumation of GSB to 22 km
slab break-off ?
e rotation of shortening axis to NW-SE initiation of Wabigoon-Wawa accretion
D3
horizontal shortening
current erosion level
MSZ
Marmion TTG
Finlayson GSB
7 - 13 km relative throw
schematic - not to scale
f Diversion Stock intrusion, D4a fracturing and Finlayson - Marmion suturing by 2.78 Ga
D4a fault and intrusion related fracturing
current erosion level
Marmion TTG
Finlayson GSB
Diversion Stock intrudes Marmion Shear Zone
g D4b flattening into anastomosing foliation and disseminated gold (Hammond Reef)
D4b anastomosing foliation
horizontal shortening
Hammond Reef
current erosion level
Marmion TTG
Finlayson GSB
fluid flow and sericite alteration
h D4c Lynx Head fault systems and lode gold (quartz-carbonate veins)
lode gold
horizontal shortening
Finlayson GSB
quartz-carbonate veins
b - d Mesoarchean Wabigoon tectonism
oblique sinistral transpression
Finlayson like GSB
3.0 Ga TTG
East
e - h Neoarchean Superior Province tectonism
North
oblique dextral transpression
Wabigoon subprovince
Finlayson
Marmion
Wawa subprovince
Quetico subprovince
N

Figure 6–2: (Previous page) Schematic reconstruction of Finlayson Lake greenstone belt (GSB), Marmion gneiss tonalite-trondhjemite-granodiorite (TTG) and Marmion Shear Zone (MSZ). This figure is complementary to Figure 6–1, which provides a tabulated summary. See text for details of the reconstruction. Sketch is not drawn to scale, but represents a schematic representation to illustrate relative depth of the Finlayson Lake greenstone belt and Marmion gneiss with relative displacement along the Marmion Shear Zone. The western Finlayson and Dashwa gneiss TTG are unconstrained in this thesis (dashed). Bottom strip illustrates the regional governing tectonic setting that was active during the deformation history. (b-d) Mesoarchean subduction of the Finlayson Lake greenstone during Wabigoon subprovince tectonism with NNW-SSE subhorizontal shortening. (e-f) Neoarchean northward subduction of the Wawa subprovince beneath the Wabigoon subprovince during Superior Province tectonism with NW-SE subhorizontal shortening.

6.1 List of key findings

The key findings of this research, which contribute to the better understanding of the geological history of the Finlayson Lake greenstone belt and Marmion gneiss, are listed here in chronological order. The implications of some of these key results for future research are emphasized in the sections that follow.

1. 3.00 Ga tonalite crust was exposed and eroded into conformable sediments of the Finlayson prior to deformation.
2. The prograde metamorphic assemblage and deformation of the Finlayson record subduction with a cool (for the Archean) geothermal gradient of $\sim 20°$/km during the amalgamation of the Wabigoon subprovince at around 2.92 Ga.
3. The peak metamorphic assemblages of the Marmion and Finlayson record contrasting geothermal gradients of $\sim 60°$/km and $\sim 30°$/km, respectively.
4. The Finlayson exhumed 10 - 20 km from its deepest recorded pressures prior to docking with the Marmion gneiss.
5. The temperature-pressure paths of the Marmion gneiss and Finlayson Lake greenstone belt during the early deformation history record significantly different geothermal gradients, and therefore the two terranes cannot have been in contact prior to juxtaposition along the Marmion Shear Zone.

6. The Diversion Stock intruded the Marmion Shear Zone at approximately 2.78 Ga, which effectively locked the shear zone.
7. Auriferous hydrothermal fluids passed along microfracture networks in the Diversion Stock and adjacent damage zone in the Marmion Gneiss, which promoted alteration in the Marmion gneiss and Diversion Stock.
8. Hydrothermal alteration manifested as the pervasive alteration of feldspars to sericite ± fine-grained disseminated pyrite without deformation, suggesting that grain-scale permeability was not sealed during progressive alteration.
9. Higher degree of fluid-rock reactions and gold precipitation were locally associated with zones of the Marmion gneiss that host more mafic lithologies (xenoliths and dykes), such as at Hammond Reef.
10. Sericite-altered zones locally flattened during progressive alteration and developed an anastomosing foliation around undeformed altered tonalite lithons, recording NW-SE shortening.
11. Shallow thrust faults, such as the Lynx Head Fault, cut the anastomosing foliation and are kinematically consistent with NW-SE shortening.
12. The latest activity in the area is recorded by gold-bearing quartz-carbonate veins, which were emplaced along pre-existing foliation and thrust faults.
13. NW-SE shortening is kinematically consistent with dextral transpression across the Quetico Fault associated with the amalgamation of the Wawa, Quetico and Wabigoon subprovinces at 2.72 – 2.68 Ga.

14. Linking fluid flow along the Marmion Shear Zone to the ~ 2.7 Ga Neoarchean tectonism places the Wabigoon subprovince and source of fluids in a suprasubduction setting above the northward directed subduction of the Quetico and Wawa subprovinces.
15. Mineralization at Hammond Reef post-dates the emplacement of the Diversion Stock (~ 2.78 Ga), however it could correspond to much younger regional events at ~ 2.7 Ga.
16. Gold fields throughout the Superior Province are commonly associate with 2.7 Ga east-west-trending terrane boundaries (such as the Quetico Fault) that record the amalgamation of the Superior Province.
17. Hammond Reef is a Neoarchean gold deposit hosted within a Mesoarchean terrane that saw peak metamorphism and deformation up to 200 million years prior to mineralization.
18. Although Hammond Reef shows similarities with intrusion-related or porphyry-style gold deposits, gold mineralization is associated with orogenic mesothermal fluids.
19. Other Hammond Reef type deposits could be found in steep crustal structures located above ancient subduction zones.

6.2 Mesoarchean tectonic reconstruction of the Wabigoon

From the results presented in this thesis, the deformation history and pressure-temperature path of the Finlayson Lake greenstone belt is interpreted within a subduction-accretion setting (Figure 6–2). Burial of the Finlayson Lake greenstone belt began after $\sim$ 2.93 Ga, based on the youngest depositional ages. The greenstone bely returns to shallow depths by the emplacement of the Diversion Stock, which constrains the period during which burial and exhumation took place. The timing and tectonic setting interpreted for deformation have implications for the Mesoarchean tectonic reconstruction of the Wabigoon subprovince. The consensus concerning the evolution of the Wabigoon subprovince involves the accretion of the Winnipeg River, western Wabigoon, central Wabigoon and Marmion terranes during two accretionary events at $\sim$ 2.92 Ga and prior to 2.72 Ga (Figure 6–3) (Tomlinson *et al.*, 2003, 2004; Percival *et al.*, 2006; Percival, 2007a). The Marmion terrane is thought to be a stable crustal block during accretion with the Winnipeg River and the central Wabigoon terrane at $\sim$ 2.92 Ga (Figure 6–3a) (Tomlinson *et al.*, 2003; Percival & Helmstaedt, 2004; Percival, 2007a). However, the Marmion Shear Zone is located in the centre of the proposed Marmion terrane (see dashed line Figure 6–3). Therefore, the Marmion terrane cannot be treated as a stable crustal block at 2.92 Ga, because crustal-scale terrane displacements occurred within the Marmion terrane at that time. The individual local TTG blocks (Marmion, Dashwa, Hardtack etc.) and greenstone belts (Finlayson, Lumby etc.) were actively deforming during this proposed accretionary period and may need to be considered as separate crustal terranes during the accretion with the Winnipeg River and central Wabigoon terranes at 2.92 Ga (Figure 6–3b). Furthermore, these results show that subduction-accretion style tectonics deformed the Finlayson Lake greenstone belt and emphasize that modern-style plate tectonics operated during the Mesoarchean by 2.92 Ga. This is consistent with authors who argue for plate tectonics by at least 3.0 Ga (Calvert *et al.*, 1995; Lin, 2005; Lin *et al.*, 2005; Lin & Beakhouse, 2013; Shirey & Richardson, 2011).

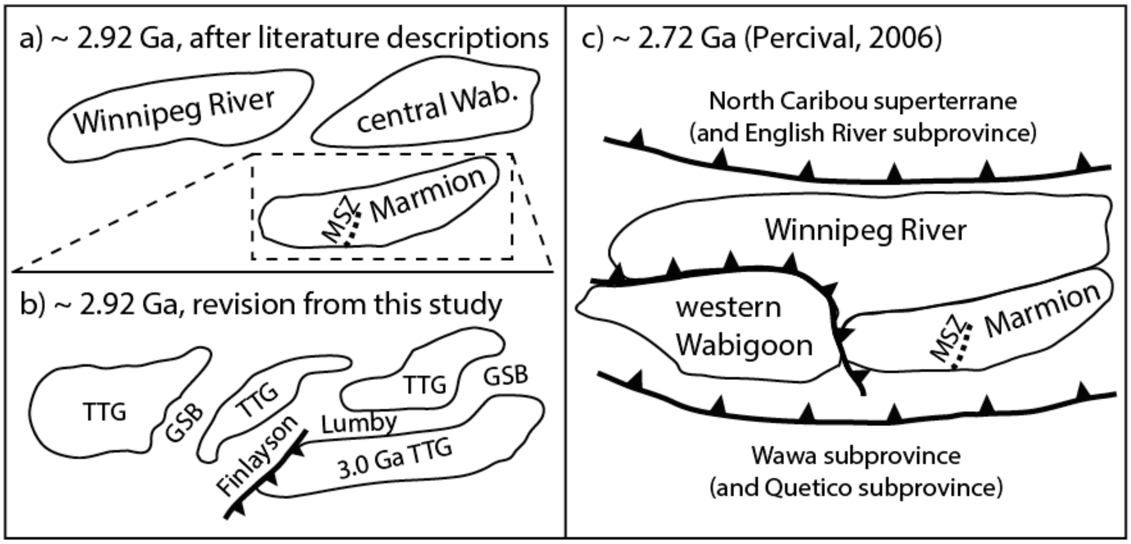

Figure 6–3: Schematic evolution of accretionary growth for the Wabigoon subprovince. (a) Winnipeg-River, central Wabigoon and Marmion terrane configuration drawn from literature description for 2.92 Ga accretion (after Tomlinson *et al.*, 2003, 2004; Percival *et al.*, 2006; Percival, 2007a). Location of Marmion Shear Zone (dashed line, MSZ) is drawn for reference. (b) Revision to Marmion terrane configuration, showing smaller crustal fragments (TTG) and greenstone belts (GSB) that deformed during the 2.92 Ga accretion. We only show the Finlayson subduction, suggested from the results of this study. (c) Accretion of the western Wabigoon subprovince and final assembly of the Wabigoon subprovince (taken from Percival *et al.*, 2006; Percival, 2007a). The major east-west-trending northward-directed subduction systems are associated with accretion of the 2.72 – 2.68 Ga Superior Province.

6.3 Deformation adjacent to shear zones

Damage zones form as a result of off-fault fracturing with an increasing fracture intensity correlated with the amount of displacement along a principal slip surface (Chester & Logan, 1986; Chester & Chester, 1998; Gudmundsson *et al.*, 2001; Rawling *et al.*, 2001; Shipton & Cowie, 2003; Sibson, 2003; Faulkner *et al.*, 2003, 2010; Kim *et al.*, 2004; Mitchell & Faulkner, 2009; Savage & Brodsky, 2011). Therefore, where deformation zones flank faults and shear zones, it is typically assumed that the parent fault or shear zone was actively shearing in order to accommodate offset and develop a damage aureole. The anastomosing foliation adjacent to the Marmion Shear Zone is one example, where near-fault deformation was offset in time from displacement along the parent structure, but was caused by the inherited permeability. Fluids were flushed through the dormant Marmion Shear Zone and damage aureole. These fluids led to the alteration of strong feldspar to weak fine grained-mica (sericite). This weakened the bulk strength of the tonalite and sericite aligned in response to a regional far-field stresses that were not related to the dynamics of the immediately adjacent shear zone. The sericite in the Marmion tonalite is aligned parallel to the shear zone and perpendicular to the regional shortening axis, which existed after slip along the Marmion Shear Zone had ceased. The Coulomb failure criterion shows that reactivation of steep faults or shear zones within a compressional setting is unfavourable (see MSZ in Figure 6–4), unless pore fluid pressures greater than the lithostatic load are introduced (Sibson *et al.*, 1988). Typically, reactivated steep structures are identified in the field, where large horizontal veins (or flats) indicate that fluid pressure did overcome the lithostatic load and that channelized fluid flow (large veins) occurred parallel to or along the main structure (Sibson *et al.*, 1988; Sibson, 1992; Wilson *et al.*, 2009; Chi & Guha, 2011). However, distributed deformation such as the anastomosing foliation seen in the Marmion gneiss is not expected. Deformation at this scale associated with a dormant structure has not been previously described. The majority of the strain related to the NW-SE shortening axis was likely accommodated by the late NW-verging shallow thrust faults in the Marmion gneiss (Figure 6–4). Therefore, it may be possible to infer other late-stage deformation aureoles of faults not directly related to displacement, by interpreting the shortening axis that formed them and the relative angle to the parent structure. In order to confidently show that deformation around a fault is not related to offset, the cross-cutting relations, deformation history and locking of the shear zone need to be clearly defined.

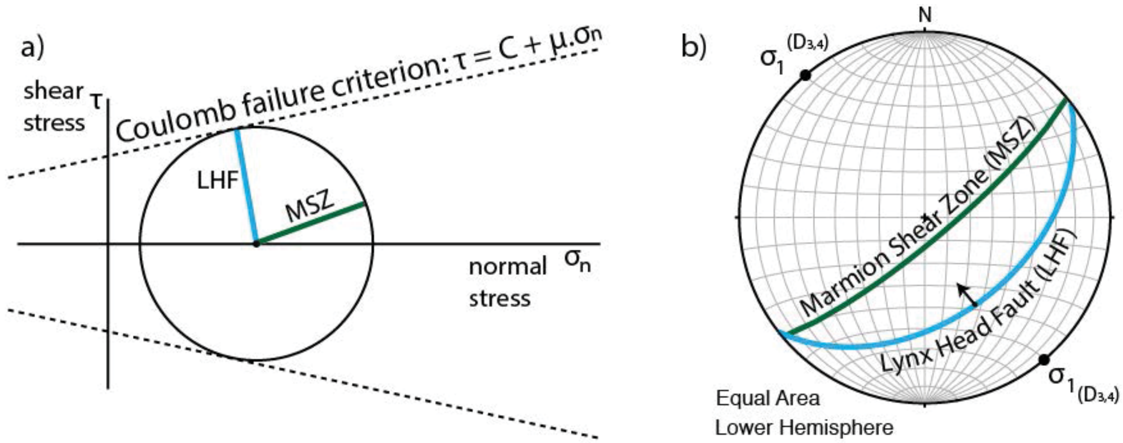

Figure 6–4: Schematic Mohr diagram and Coulomb failure criterion (a) and stereonet (b) showing the orientation of the Marmion Shear Zone (MSZ) and Lynx Head Fault (LHF) relative to the NW-SE shortening axis (σ_1) during D_3 and D_4 deformation.

6.4 Interpreting the origin of ore deposits

Classification criteria for gold deposits are published in the literature and are tied to the geological settings in which they can be found (Robert *et al.*, 1997; Groves *et al.*, 1998; Kerrich *et al.*, 2000; Goldfarb *et al.*, 2001). These classifications summarize observations and interpretations from exploration and research projects and the results drive exploration targets towards known deposit styles and known geological settings, which is true for any commodity (e.g. Guilbert & Park Jr, 2007). The Hammond Reef gold deposit is located in Archean tonalites, which are not typically known to host gold deposits. Furthermore, gold mineralization at Hammond Reef is somewhat ambiguous with regards to its deposit-type classification. It shows some similarities to porphyry deposits and intrusion-related gold systems, such as low-grade, high-tonnage, disseminated mineralization and it is hosted in plutonic rocks (Thompson *et al.*, 1999; Sillitoe, 1991; Sillitoe & Thompson, 1998; Lang & Baker, 2001; Robert, 2001; Baker, 2002). Understanding the detailed deformation, metamorphic, intrusions, alteration and mineralization history at Hammond Reef shows that gold mineralization is related to fluids in a suprasubduction setting, not sourced from local magmatism (Figure 6–2). The deformation history links mineralization to an orogenic event up to 200 million years younger than the peak metamorphism and deformation of the tonalites that host the deposit (Figure 6–1). Therefore, Hammond Reef falls within the mesothermal category of classifications in orogenic gold deposits. This research shows that detailed structural work and an understanding of the regional deformation history are an integral part in interpreting the origin and setting of ore deposits, not only restricted to gold.

6.5 Final remarks: Are there other Hammond Reef style deposits?

Hammond Reef is a very low-grade deposit (< 1 g/t or ppm). With respect to gold, it is located in an underexplored Archean tonalite setting. Therefore, it warrants the question: where could other Hammond Reef style gold deposits with similar structural controls be found? The fluid flow and alteration of feldspar to sericite of the Marmion tonalite gneiss adjacent to the Marmion Shear Zone are pervasive and found all along western margin of the Marmion gneiss. The 0.3 g/t cut-off grade for the Hammond Reef resource shell is localized along the anastomosing foliation at Hammond Reef. The results suggest that small lithological heterogeneities related to locally more mafic units along the margin of Marmion gneiss and its contact with the

Diversion Stock may have enhanced fluid-rock reactions at Hammond Reef, allowing for the localized and disseminated gold precipitation. The auriferous fluids migrated along the entire steep Marmion Shear Zone and deformation aureole (Figure 6–2) and there may be similar local enrichments in gold around more mafic segments of the Marmion gneiss within the anastomosing foliation zone below the currently exposed surface.

The combined results from the Finlayson Lake greenstone belt and Marmion gneiss place the Hammond Reef gold deposit within a steeply dipping, crustal scale, dormant shear zone that provided a fluid conduit above an ancient subduction zone related to the 2.7 Ga amalgamation of the Superior Province. Gold prospects similar to Hammond Reef throughout the Superior Province and possibly any Archean terrane could be found in similar steep structures that overlie ancient subduction systems. Exploration in the Superior Province has shown the importance of the east-west-trending terrane boundaries for high-grade gold mineralization. According to the new insights from Hammond Reef, older structures that intersect with the east-west sutures may have been favourable for the migration of auriferous fluids.

References

Abbott, D., Drury, R., & Smith, W. H. F. (1994). Flat to steep transition in subduction style. *Geology*, *22*(10), 937–940.

Anderson, E. M. (1905). The dynamics of faulting. *Transactions of the Edinburgh Geological Society*, *8*(3), 387–402.

Anhaeusser, C. R. (1984). Structural elements of Archaean granite-greenstone terranes as exemplified by the Barberton Mountain Land, southern Africa. In A. Kroner & R. Greiling (Eds.), *Precambrian Tectonics Illustrated*. Schweizerbart, Stuttgart, 57–78.

Anhaeusser, C. R., Mason, R., Viljoen, M. J., & Viljoen, R. P. (1969). A reappraisal of some aspects of Precambrian Shield geology. *Geological Society of America Bulletin*, *80*(11), 2175–2200.

Arancibia, G., Fujita, K., Hoshino, K., Mitchell, T. M., Cembrano, J., Gomila, R., Morata, D., Faulkner, D. R., & Rempe, M. (2014). Hydrothermal alteration in an exhumed crustal fault zone: Testing geochemical mobility in the Caleta Coloso Fault, Atacama Fault System, Northern Chile. *Tectonophysics*, *623*, 147–168.

Backeberg, N. R., Rowe, C. D., & Barshi, N. (submitted). No shear thing: Deformation adjacent to a dormant shear zone. *submitted to Journal of Structural Geology*.

Backeberg, N. R., Rowe, C. D., van Hinsberg, V. J., & Bellefroid, E. J. (2014). Structural and metamorphic evidence for Mesoarchaean subduction in the Finlayson Lake greenstone belt, Superior Province, Ontario. *Precambrian Research*, *249*, 100–114.

Baker, E. M. & Tullemans, F. J. (1990). Kidston gold deposit. In F. E. Hughes (Ed.), *Geology of the mineral deposits of Australia and Papua New Guinea*. vol. 2, 1461–1465.

Baker, T. (2002). Emplacement depth and carbon dioxide-rich fluid inclusions in intrusion-related gold deposits. *Economic Geology*, *97*(5), 1111–1117.

Bakke, A. A. (1995). The Fort Knox “porphyry” gold deposit: Structurally controlled stockwork and shear quartz vein, sulfide-poor mineralization hosted by a Late Cretaceous pluton, east-central Alaska. In T. G. Schroeter (Ed.), *Porphyry Deposits of the northwestern Cordillera of North America*. vol. 46, 795–802.

Barclay, W. A. (1996). Vein arrays and possible controls on gold mineralization on the Hammond Reef property, northwest Ontario. Tech. rep., Pentland Firth Ventures Ltd.

Bauer, R. L., Hudleston, P. J., & Southwick, D. L. (1992). Deformation across the western Quetico subprovince and adjacent boundary regions in Minnesota. *Canadian Journal of Earth Sciences*, *29*(10), 2087–2103.

Bédard, J. H., Harris, L. B., & Thurston, P. C. (2013). The hunting of the snArc. *Precambrian Research*, *229*, 20–48.

Bercovici, D. (2003). The generation of plate tectonics from mantle convection. *Earth and Planetary Science Letters*, *205*(3), 107–121.

Berrange, J. P. & Thorpe, R. S. (1988). The geology, geochemistry and emplacement of the Cretaceous—Tertiary ophiolitic Nicoya Complex of the Osa Peninsula, southern Costa Rica. *Tectonophysics*, *147*(3), 193–220.

Blackburn, C. E., Johns, G. W., Ayer, J., & Davis, D. W. (1991). Wabigoon subprovince. In P. C. Thurston, H. R. Williams, H. R. Sutcliffe, & G. M. Stott (Eds.), *Geology of Ontario*. Ontario Geological Survey, vol. 4, Part 1, 303–381.

Bloem, E. J. M., Dalstra, H. J., Ridley, J. R., & Groves, D. I. (1997). Granitoid diapirism during protracted tectonism in an Archaean granitoid-greenstone belt, Yilgarn Block, Western Australia. *Precambrian Research*, 147–171.

Böhlke, J. K. (1982). Orogenic (metamorphic-hosted) gold-quartz veins. *US Geological Survey Open File Report*, *795*, 70–76.

Böhlke, J. K. (1989). Comparison of metasomatic reactions between a common CO_2-rich vein fluid and diverse wall rocks; intensive variables, mass transfers, and Au mineralization at Alleghany, California. *Economic Geology*, *84*(2), 291–327.

Borowski, R. (2013). *Understanding the tectonics of Archean gneisses in the western Wabigoon terrane: Evidence from the Dashwa Gneiss, Atikokan, Ontario*. Master's thesis, McGill University.

Borradaile, G. J. & Schwerdtner, W. M. (1984). Horizontal shortening of upward-facing greenstone structures in the southern Superior Province, Canadian Shield. *Canadian Journal of Earth Sciences*, *21*(5), 611–615.

Breaks, F. W. (1991). English River subprovince. In P. C. Thurston, H. R. Williams, H. R. Sutcliffe, & G. M. Stott (Eds.), *Geology of Ontario*. Ontario Geological Survey, vol. 4, Part 1, 239–277.

Buse, S., Lewis, D., Davis, D. W., & Hamilton, M. A. (2010a). U/Pb Geochronological Results from the Lumby Lake Greenstone Belt, Wabigoon Subprovince, Northwestern Ontario. Tech. Rep. Project Unit 09-007, Ontario Geological Survey.

Buse, S., Lewis, D., & Magnus, S. (2010b). Precambrian geology of the Lumby Lake greenstone belt, Preliminary Map P.3619. Tech. rep., Ontario Geological Survey.

Caine, J. S., Bruhn, R. L., & Forster, C. B. (2010). Internal structure, fault rocks, and inferences regarding deformation, fluid flow, and mineralization in the seismogenic Stillwater normal fault, Dixie Valley, Nevada. *Journal of Structural Geology*, *32*(11), 1576–1589.

Caine, J. S., Evans, J. P., & Forster, C. B. (1996). Fault zone architecture and permeability structure. *Geology*, *24*(11), 1025–1028.

Calvert, A. J., Sawyer, E. W., Davis, W. J., & Ludden, J. N. (1995). Archean subduction inferred from seismic images of a mantle suture in the Superior Province. *Nature*, *375*, 670–674.

Cameron, E. M. & Hattori, K. (1987). Archean gold mineralization and oxidized hydrothermal fluids. *Economic Geology*, *82*(5), 1177–1191.

Card, K. D. (1990). A review of the Superior Province of the Canadian Shield, a product of Archean accretion. *Precambrian Research*, *48*, 99–156.

Carlson, R. L. & Herrick, C. N. (1990). Densities and porosities in the oceanic crust and their variations with depth and age. *Journal of Geophysical Research: Solid Earth (1978–2012)*, *95*(B6), 9153–9170.

Carreras, J., Czeck, D. M., Druguet, E., & Hudleston, P. J. (2010). Structure and development of an anastomosing network of ductile shear zones. *Journal of Structural Geology*, *32*(5), 656–666.

Castroviejo, R. (1990). Gold ores related to shear zones, West Santa Comba-Fervenza Area (Galicia, NW Spain): a mineralogical study. *Mineralium Deposita*, *25*(1), 42–52.

Cawood, P. A., Kröner, A., Collins, W. J., Kusky, T. M., Mooney, W. D., & Windley, B. F. (2009). Accretionary orogens through Earth history. *Geological Society, London, Special Publications*, *318*(1), 1–36.

Chardon, D., Choukroune, P., & Jayananda, M. (1998). Sinking of the Dharwar Basin (South India): implications for Archean tectonics. *Precambrian Research*, *91*, 15–39.

Chester, F. M. & Chester, J. S. (1998). Ultracataclasite structure and friction processes of the Punchbowl fault, San Andreas system, California. *Tectonophysics*, *295*(1), 199–221.

Chester, F. M., Chester, J. S., Kirschner, D. L., Schulz, S. E., & Evans, J. P. (2004). Structure of large-displacement, strike-slip fault zones in the brittle continental crust. *Rheology and Deformation in the Lithosphere at Continental Margins*, *1*, 223–260.

Chester, F. M. & Logan, J. M. (1986). Implications for mechanical properties of brittle faults from observations of the Punchbowl fault zone, California. *Pure and Applied Geophysics*, *124*(1-2), 79–106.

Chester, J. S., Chester, F. M., & Kronenberg, A. K. (2005). Fracture surface energy of the Punchbowl fault, San Andreas system. *Nature*, *437*(7055), 133–136.

Chi, G. & Guha, J. (2011). Microstructural analysis of a subhorizontal gold-quartz vein deposit at Donalda, Abitibi greenstone belt, Canada: Implications for hydrodynamic regime and fluid-structural relationship. *Geoscience Frontiers*, *2*(4), 529–538.

Clark, C., Mumm, A. S., & Faure, K. (2005). Timing and nature of fluid flow and alteration during Mesoproterozoic shear zone formation, Olary Domain, South Australia. *Journal of Metamorphic Geology*, *23*(3), 147–164.

Cline, J. S., Hofstra, A. H., Muntean, J. L., Tosdal, R. M., & Hickey, K. A. (2005). Carlin-type gold deposits in Nevada: critical geologic characteristics and viable models. *Economic Geology 100th anniversary volume*, 451–484.

Cloos, M. (1993). Lithospheric buoyancy and collisional orogenesis: Subduction of oceanic plateaus, continental margins, island arcs, spreading ridges, and seamounts. *Geological Society of America Bulletin*, *105*(6), 715–737.

Collins, W. J. (1989). Polydiapirism of the Archean Mount Edgar Batholith, Pilbara Block, Western Australia. *Precambrian Research*, *43*, 41–62.

Collins, W. J. & Teyssier, C. (1990). Mount Edgar Batholith and Warrawoona Syncline. In S. E. Ho, J. E. Glover, J. S. Myers, & J. R. Muhling (Eds.), *Third International Archean Symposium*, Perth: University of Western Australia, vol. 21. 36–45.

Collins, W. J., Van Kranendonk, M. J., & Teyssier, C. (1998). Partial convective overturn of Archean crust in the east Pilbara Craton, Western Australia: driving mechanisms and tectonic implications. *Journal of Structural Geology*, *20*(9/10), 1405–1424.

Condie, K. C. (1984). Archean geotherms and supracrustal assemblages. *Tectonophysics*, *105*(1), 29–41.

Condie, K. C. (2005). TTGs and adakites: are they both slab melts? *Lithos*, *80*(1), 33–44.

Connolly, J. A. D. (2005). Computation of phase equilibria by linear programming: a tool for geodynamic modeling and its application to subduction zone decarbonation. *Earth and Planetary Science Letters*, *236*, 524–541.

Conrad, C. P. & Lithgow-Bertelloni, C. (2002). How mantle slabs drive plate tectonics. *Science*, *298*(5591), 207–209.

Cooke, D. R., Hollings, P., & Walshe, J. L. (2005). Giant porphyry deposits: characteristics, distribution, and tectonic controls. *Economic Geology*, *100*(5), 801–818.

Corfu, F. & Stott, G. M. (1986). U-Pb ages for late magmatism and regional deformation in the Shebandowan Belt, Superior Province, Canada. *Canadian Journal of Earth Sciences*, *23*, 1075–1082.

Couture, J. F. & Pilote, P. (1993). The geology and alteration patterns of a disseminated, shear zone-hosted mesothermal gold deposit; the Francoeur 3 Deposit, Rouyn-Noranda, Quebec. *Economic geology*, *88*(6), 1664–1684.

Cox, L., MacKenzie, D. J., Craw, D., Norris, R. J., & Frew, F. (2006). Structure and geochemistry of the Rise and Shine Shear Zone mesothermal gold system, Otago Schist, New Zealand. *New Zealand Journal of Geology and Geophysics*, *49*, 429–442.

Cox, S. F. (2002). Fluid flow in mid-to deep crustal shear systems: Experimental constraints, observations on exhumed high fluid flux shear systems, and implications for seismogenic processes. *Earth, planets and space*, *54*(11), 1121–1125.

Crosby, A. G., McKenzie, D., & Sclater, J. G. (2006). The relationship between depth, age and gravity in the oceans. *Geophysical Journal International*, *166*(2), 553–573.

Cruden, A. R., Davis, D., Melnyk, M., Robin, P. Y. R., & Menard, T. (1998). Structural and geochronological observations at Kenora: Implications for the style and timing of deformation during the Kenoran orogeny, NW Ontario. In *Western Superior Transect Fourth Annual Workshop: Lithoprobe Secretariat, University of British Columbia, Lithoprobe Report*. vol. 65, 54–62.

Davies, G. F. (1992). On the emergence of plate tectonics. *Geology*, *20*(11), 963–966.

Davis, D. W. & Jackson, M. C. (1988). Geochronology of the Lumby Lake greenstone belt: A 3 Ga complex within the Wabigoon subprovince, northwest Ontario. *Geological Society of America Bulletin*, *100*, 818–824.

Davis, D. W. & Smith, P. M. (1991). Archean gold mineralization in the Wabigoon Subprovince, a product of crustal accretion: evidence from U-Pb geochronology in the Lake of the Woods area, Superior Province, Canada. *The Journal of Geology*, 337–353.

de Ronde, C. E. J., Spooner, E. T. C., de Wit, M. J., & Bray, C. J. (1992). Shear zone-related, Au quartz vein deposits in the Barberton greenstone belt, South Africa: Field and petrographic characteristics, fluid properties, and light stable isotope geochemistry. *Economic Geology*, *87*, 366–402.

de Wit, M. J. (1982). Gliding and overthrust nappe tectonics in the Barberton greenstone belt. *Journal of Structural Geology*, *4*(2), 117–136.

de Wit, M. J. (1991). Archaean greenstone belt tectonism and basin development: some insights from the Barberton and Pietersburg greenstone belts, Kaapvaal Craton, South Africa. *Journal of African Earth Sciences (and the Middle East)*, *13*(1), 45 – 63.

de Wit, M. J. (1998). On Archean granites, greenstones, cratons and tectonics: Does the evidence demand a verdict? *Precambrian Research*, *91*, 181–226.

De Wit, M. J., de Ronde, C. E., Tredoux, M., Roering, C., Hart, R. J., Armstrong, R. A., Green, R. W., Peberdy, E., & Hart, R. A. (1992). Formation of an Archaean continent. *Nature*, *357*, 553–562.

Desrochers, J.-P., Hubert, C., Ludden, J. N., & Pilote, P. (1993). Accretion of Archean oceanic plateau fragments in the Abitibi, greenstone belt, Canada. *Geology*, *21*(5), 451–454.

Diener, J. F. A. & Powell, R. (2012). Revised activity-composition models for clinopyroxene and amphibole. *Journal of Metamorphic Geology*, *30*, 131–142.

Diener, J. F. A., Powell, R., White, R. W., & Holland, T. J. B. (2007). A new thermodynamic model for clino- and orthoamphiboles in the system Na_2O–CaO–FeO–MgO–Al_2O_3–SiO_2–H_2O–O. *Journal of Metamorphic Geology*, *25*, 631–656.

Dubé, B. & Gosselin, P. (2007). Greenstone-hosted quartz-carbonate vein deposits. In W. Goodfellow (Ed.), *Mineral Deposits of Canada: A synthesis of major deposit-types, district metallogeny, the evolution of geological provinces, and exploration methods: Geological Association of Canada, Mineral Deposits Division, Special*

Publication. 5, 49–73.

Dziggel, A., Diener, J. F. A., Kolb, J., & Kokfelt, T. F. (2014). Metamorphic record of accretionary processes during the Neoarchaean: the Nuuk region, southern West Greenland. *Precambrian Research*, *242*, 22–38.

Ernst, W. G. (1988). Tectonic history of subduction zones inferred from retrograde blueschist PT paths. *Geology*, *16*(12), 1081–1084.

Ernst, W. G. (2009). Archean plate tectonics, rise of Proterozoic supercontinentality and onset of regional episodic stagnant-lid behaviour. *Gondwana Research*, *15*, 243–253.

Essaifi, A., Capdevila, R., Fourcade, S., Lagarde, J. L., Ballvère, M., & Marignac, C. H. (2004). Hydrothermal alteration, fluid flow and volume change in shear zones: the layered mafic-ultramafic Kettara intrusion (Jebilet Massif, Variscan belt, Morocco). *Journal of Metamorphic Geology*, *22*, 25–43.

Evans, J. P. (1990). Thickness-displacement relationships for fault zones. *Journal of Structural Geology*, *12*(8), 1061–1065.

Evans, K. A., Phillips, G. N., & Powell, R. (2006). Rock-buffering of auriferous fluids in altered rocks associated with the Golden Mile-style mineralization, Kalgoorlie gold field, Western Australia. *Economic Geology*, *101*(4), 805–817.

Faulkner, D. R., Jackson, C. A. L., Lunn, R. J., Schlische, R. W., Shipton, Z. K., Wibberley, C. A. J., & Withjack, M. O. (2010). A review of recent developments concerning the structure, mechanics and fluid flow properties of fault zones. *Journal of Structural Geology*, *32*(11), 1557–1575.

Faulkner, D. R., Lewis, A. C., & Rutter, E. H. (2003). On the internal structure and mechanics of large strike-slip fault zones: Field observations of the Carboneras fault in southeastern Spain. *Tectonophysics*, *367*(3), 235–251.

Fayon, A. K., Whitney, D. L., & Teyssier, C. (2004). Exhumation of orogenic crust: Diapiric ascent versus low-angle normal faulting. *Geological Society of America Special Papers*, *380*, 129–139.

Foley, S. F. (2008). A trace element perspective on Archean crust formation and on the presence or absence of Archean subduction. *Geological Society of America Special Papers*, *440*, 31–50.

Foley, S. F., Buhre, S., & Jacob, D. E. (2003). Evolution of the Archaean crust by delamination and shallow subduction. *Nature*, *421*(6920), 249–252.

Forsyth, D. & Uyeda, S. (1975). On the relative importance of the driving forces of plate motion. *Geophysical Journal International*, *43*(1), 163–200.

Fossen, H. (2010). *Structural Geology*. Cambridge, U.K.: Cambridge University Press.

Frost, C. D., Frost, B. R., Kirkwood, R., & Chamberlain, K. R. (2006). The tonalite-trondhjemite-granodiorite (TTG) to granodiorite-granite (GG) transition in the late Archean plutonic rocks of the central Wyoming Province. *Canadian Journal of Earth Sciences*, *43*(10), 1419–1444.

Fyson, W. K. (1978). Structures induced by granite diapirs in the Archaean greenstone belt at Yellowknife, Canada: Implications for Archaean geotectonics: A discussion. *Journal of Geology*, *86*(6), 767–769.

Gaboury, D. & Daigneault, R. (2000). Flat vein formation in a transitional crustal setting by self-induced fluid pressure equilibrium—an example from the Geant Dormant gold mine, Canada. *Ore Geology Reviews*, *17*(3), 155–178.

Gammons, C. & Williams-Jones, A. E. (1997). Chemical mobility of gold in the porphyry-epithermal environment. *Economic Geology*, *92*(1), 45–59.

Gibb, R. A., Nagy, D., Coderre, J., Fogarasi, A., & Thomas, M. D. (1988). Gravity surveys and interpretation, Eye-Dashwa lakes pluton, Atikokan (RA 4), Ontario. Tech. rep., Geological Survey of Canada.

Goddard, J. V. & Evans, J. P. (1995). Chemical changes and fluid-rock interaction in faults of crystalline thrust sheets, northwestern Wyoming, USA. *Journal of Structural Geology*, *17*(4), 533–547.

Goldfarb, R. J., Baker, T., Dubé, B., Groves, D. I., Hart, C. J., & Gosselin, P. (2005). Distribution, character, and genesis of gold deposits in metamorphic terranes. *Economic Geology, 100th anniversary volume*, *40*, 407 – 450.

Goldfarb, R. J., Groves, D. I., & Gardoll, S. (2001). Orogenic gold and geologic time: a global synthesis. *Ore Geology Reviews*, *18*(1), 1–75.

Goldfarb, R. J., Phillips, G. N., & Nokleberg, W. J. (1998). Tectonic setting of synorogenic gold deposits of the Pacific Rim. *Ore Geology Reviews*, *13*(1), 185–218.

Gower, C. F. & Clifford, P. M. (1981). The structural geometry and geological history of Archean rocks at Kenora, north-western Ontario - a proposed type area for the Kenoran Orogeny. *Canadian Journal of Earth Sciences*, *18*(6), 1075–1091.

Gray, D. R. (1978). Cleavages in deformed psammitic rocks from southeastern Australia: their nature and origin. *Geological Society of America Bulletin*, *89*(4), 577–590.

Groves, D. I. (1993). The crustal continuum model for late-Archaean lode-gold deposits of the Yilgarn Block, Western Australia. *Mineralium Deposita*, *28*(6), 366–374.

Groves, D. I., Barley, M. E., & Ho, S. E. (1989). Nature, genesis, and tectonic setting of mesothermal gold mineralization in the Yilgarn Block, Western Australia. *Econ. Geol. Monogr*, *6*, 71–85.

Groves, D. I., Goldfarb, R. J., Gebre-Mariam, M., Hagemann, S. G., & Robert, F. (1998). Orogenic gold deposits: a proposed classification in the context of their crustal distribution and relationship to other gold deposit types. *Ore Geology Reviews*, *13*(1), 7–27.

Groves, D. I., Phillips, G. N., Ho, S. E., Houstoun, S. M., & Standing, C. A. (1987). Craton-scale distribution of Archean greenstone gold deposits; predictive capacity of the metamorphic model. *Economic Geology*, *82*(8), 2045–2058.

Gudmundsson, A., Berg, S. S., Lyslo, K. B., & Skurtveit, E. (2001). Fracture networks and fluid transport in active fault zones. *Journal of Structural Geology*, *23*(2), 343–353.

Guilbert, J. M. & Park Jr, C. F. (2007). *The geology of ore deposits*. Waveland Press.

Haeussler, P. J., Bradley, D., Goldfarb, R. J., Snee, L. W., & Taylor, C. (1995). Link between ridge subduction and gold mineralization in southern Alaska. *Geology*, *23*(11), 995–998.

Hamilton, W. B. (1998). Archean magmatism and deformation were not products of plate tectonics. *Precambrian Research*, *91*, 143–179.

Handy, M. R., Franz, L., Heller, F., Janott, B., & Zurbriggen, R. (1999). Multistage accretion and exhumation of the continental crust (Ivrea crustal section, Italy and Switzerland). *Tectonics*, *18*(6), 1154–1177.

Hart, C. J., Goldfarb, R. J., Qiu, Y., Snee, L., Miller, L. D., & Miller, M. L. (2002). Gold deposits of the northern margin of the North China Craton: multiple late Paleozoic–Mesozoic mineralizing events. *Mineralium Deposita*, *37*(3-4), 326–351.

Heald, P., Foley, N. K., & Hayba, D. O. (1987). Comparative anatomy of volcanic-hosted epithermal deposits; acid-sulfate and adularia-sericite types. *Economic Geology*, *82*(1), 1–26.

Herzberg, C., Condie, K. C., & Korenaga, J. (2010). Thermal history of the Earth and its petrological expression. *Earth and Planetary Science Letters*, *292*, 79–88.

Hirth, G. & Tullis, J. (1992). Dislocation creep regimes in quartz aggregates. *Journal of Structural Geology*, *14*(2), 145–159.

Hodges, K. V. & McKenna, L. W. (1987). Realistic propagation of uncertainties in geologic thermobarometry. *American Mineralogist*, *72*(7-8), 671–680.

Hodgson, C. J. (1993). Mesothermal lode-gold deposits. *Geological Association of Canada (Special Paper)*, *40*, 635–678.

Hoffmann, J. E., Nagel, T. J., Münker, C., Næraa, T., & Rosing, M. T. (2014). Constraining the process of Eoarchean TTG formation in the Itsaq Gneiss Complex, southern West Greenland. *Earth and Planetary Science Letters*, *388*, 374–386.

Hofstra, A. H., Leventhal, J. S., Northrop, H. R., Landis, G. P., Rye, R. O., Birak, D. J., & Dahl, A. R. (1991). Genesis of sediment-hosted disseminated-gold deposits by fluid mixing and sulfidization: Chemical-reaction-path modeling of ore-depositional processes documented in the Jerritt Canyon district, Nevada. *Geology*, *19*(1), 36–40.

Holland, T., Baker, J., & Powell, R. (1998). Mixing properties and activity-composition and relationships of chlorites in the system MgO-FeO-Al_2O_3-SiO_2-H_2O. *European Journal of Mineralogy*, *10*(3), 395–406.

Holland, T. & Blundy, J. (1994). Non-ideal interactions in calcic amphiboles and their bearing on amphibole-plagioclase thermometry. *Contributions to Mineralogy and Petrology*, *116*(4), 433–447.

Holland, T. & Powell, R. (1996). Thermodynamics of order-disorder in minerals: II. Symmetric formalism applied to solid solutions. *American Mineralogist*, *81*(11), 1425–1437.

Holland, T. & Powell, R. (1998). An internally-consistent thermodynamic dataset for phases of petrological interest. *Journal of Metamorphic Geology*, *16*, 309–344.

Holm, D. K. & Lux, D. R. (1996). Core complex model proposed for gneiss dome development during collapse of the Paleoproterozoic Penokean orogen, Minnesota. *Geology*, *24*(4), 343–346.

Huang, H., Polat, A., & Fryer, B. J. (2013). Origin of Archean tonalite–trondhjemite–granodiorite (TTG) suites and granites in the Fiskenæsset region, southern West Greenland: Implications for continental growth. *Gondwana Research*, *23*(2), 452–470.

Hynes, A. (2013). How feasible was subduction in the Archean? *Canadian Journal of Earth Sciences*, *51*(3), 286–296.

Jaguin, J., Gapais, D., Poujol, M., Boulvais, P., & Moyen, J.-F. (2012). The Murchison greenstone belt (South Africa): a general tectonic framework. *South African Journal of Geology*, *115*(1), 65–76.

James, D. T. & Mortensen, J. K. (1992). An Archean metamorphic core complex in the southern Slave Province: basement-cover structural relations between the Sleepy Dragon Complex and the Yellowknife Supergroup. *Canadian Journal of Earth Sciences*, *29*(10), 2133–2145.

Johnson, T. E., Brown, M., Kaus, B. J. P., & VanTongeren, J. A. (2014). Delamination and recycling of Archaean crust caused by gravitational instabilities. *Nature Geoscience*, *7*(1), 47–52.

Jones, R. R. & Tanner, P. W. G. (1995). Strain partitioning in transpression zones. *Journal of Structural Geology*, *17*(6), 793–802.

Juul-Pedersen, A., Frei, R., Appel, P. W. U., Persson, M. F., & Konnerup-Madsen, J. (2007). A shear zone related greenstone belt hosted gold mineralization in the Archean of West Greenland. A petrographic and combined Pb–Pb and Rb–Sr geochronological study. *Ore Geology Reviews*, *32*(1), 20–36.

Kennedy, B. M., Kharaka, Y. K., Evans, W. C., Ellwood, A., DePaolo, D. J., Thordsen, J., Ambats, G., & Mariner, R. H. (1997). Mantle fluids in the San Andreas fault system, California. *Science*, *278*(5341), 1278–1281.

Kerrich, R. (1999). Nature's gold factory. *Science*, *284*(5423), 2101–2102.

Kerrich, R., Goldfarb, R. J., Groves, D. I., Garwin, S., & Jia, Y. (2000). The characteristics, origins, and geodynamic settings of supergiant gold metallogenic provinces. *Science in China Series D: Earth Sciences*, *43*(1), 1–68.

Kerrich, R. & Polat, A. (2006). Archean greenstone-tonalite duality: Thermochemical mantle convection models or plate tectonics in the early Earth global dynamics? *Tectonophysics*, *415*(1), 141–165.

Kerrich, R. & Wyman, D. (1990). Geodynamic setting of mesothermal gold deposits: An association with accretionary tectonic regimes. *Geology*, *18*, 882–885.

Kim, Y.-S., Peacock, D. C. P., & Sanderson, D. J. (2004). Fault damage zones. *Journal of Structural Geology*, *26*(3), 503–517.

King, S. D. (2001). Subduction zones: observations and geodynamic models. *Physics of the Earth and Planetary Interiors*, *127*(1), 9–24.

Kisters, A. F. M., Stevens, G., Dziggel, A., & Armstrong, R. A. (2003). Extensional detachment faulting and core-complex formation in the southern Barberton granite–greenstone terrain, South Africa: evidence for a 3.2 Ga orogenic collapse. *Precambrian Research*, *127*(4), 355–378.

Kisters, A. F. M., van Hinsberg, V. J., & Szilas, K. (2012). Geology of an Archaean accretionary complex–The structural record of burial and return flow in the Tartoq Group of South West Greenland. *Precambrian Research*, *220*, 107–122.

Kloppenburg, A., White, S. H., & Zegers, T. E. (2001). Structural evolution of the Warrawoona Greenstone Belt and adjoining granitoid complexes, Pilbara Craton, Australia: implications for Archean tectonic processes. *Precambrian Research*, *112*, 107–147.

Kohn, M. J. & Spear, F. S. (1991). Error propagation for barometers: 1. Accuracy and precision of experimentally located end-member reactions. *American Mineralogist*, *76*, 128–137.

Kolb, M. J. (2010). *A microstructural study of Musselwhite Mine and Hammond Reef shear-zone-hosted gold deposits*. Master's thesis, Lakehead University.

Koons, P. O. & Craw, D. (1991). Gold mineralization as a consequence of continental collision: an example from the Southern Alps, New Zealand. *Earth and Planetary Science Letters*, *103*(1), 1–9.

Kretz, R. (1983). Symbols for rock-forming minerals. *American Mineralogist*, *68*, 277–279.

Kulongoski, J. T., Hilton, D. R., Barry, P. H., Esser, B. K., Hillegonds, D., & Belitz, K. (2013). Volatile fluxes through the Big Bend section of the San Andreas Fault, California: Helium and carbon-dioxide systematics. *Chemical Geology*, *339*, 92–102.

Kusky, T. M., Li, X., Wang, Z., Fu, J., Ze, L., & Zhu, P. (2014). Are Wilson cycles preserved in Archean cratons? A comparison of the North China and Slave cratons. *Canadian Journal of Earth Sciences*, *51*, 297–311.

Kusky, T. M. & Polat, A. (1999). Growth of granite-greenstone terranes at convergent margins, and stabilization of Archean cratons. *Tectonophysics*, *305*(1), 43–73.

Kusky, T. M. & Vearncombe, J. R. (1997). Structural Aspects. In M. J. de Wit & L. D. Ashwal (Eds.), *Greenstone Belts*, Oxford University Press, chap. 2.3. 91–124.

Labrosse, S. & Jaupart, C. (2007). Thermal evolution of the Earth: secular changes and fluctuations of plate characteristics. *Earth and Planetary Science Letters*, *260*, 465–481.

Lana, C., Kisters, A., & Stevens, G. (2010). Exhumation of Mesoarchean TTG gneisses from the middle crust: Insights from the Steynsdorp core complex, Barberton granitoid-greenstone terrain, South Africa. *Geological Society of America Bulletin*, *122*(1-2), 183–197.

Lang, J. R. & Baker, T. (2001). Intrusion-related gold systems: the present level of understanding. *Mineralium Deposita*, *36*(6), 477–489.

Langford, F. F. & Morin, J. A. (1976). The development of the Superior Province of northwestern Ontario by merging island arcs. *American Journal of Science*, *276*(9), 1023–1034.

Li, X.-C., Fan, H.-R., Santosh, M., Hu, F.-F., Yang, K.-F., & Lan, T.-G. (2013). Hydrothermal alteration associated with Mesozoic granite-hosted gold mineralization at the Sanshandao deposit, Jiaodong Gold Province, China. *Ore Geology Reviews*, *53*, 403–421.

Lin, S. (2005). Synchronous vertical and horizontal tectonism in the Neoarchean: Kinematic evidence from a synclinal keel in the northwestern Superior craton, Canada. *Precambrian Research*, *139*, 181–194.

Lin, S. & Beakhouse, G. P. (2013). Synchronous vertical and horizontal tectonism at late stages of Archean cratonization and genesis of Hemlo gold deposit, Superior craton, Ontario, Canada. *Geology*, *41*(3), 359–362.

Lin, S., Jiang, D., & Williams, P. F. (1998). Transpression (or transtension) zones of triclinic symmetry: natural example and theoretical modelling. *Geological Society, London, Special Publications*, *135*(1), 41–57.

Lin, S., Parmenter, A., & Parks, J. (2005). Synchronous vertical and horizontal tectonism at the late stage of Archean cratonization: an important process in gold mineralization? In J. Mao & F. Bierlein (Eds.), *Mineral Deposits Research: Meeting and Global Challenge*. Proceedings of the 8th Biennial SGA Meeting, Beijing, China: Springer Verlag, vol. 1, 29–32.

Lin, S., Percival, J. A., & Skulski, T. (1996). Structural constraints on the tectonic evolution of a late Archean greenstone belt in the northeastern Superior Province, northern Quebec (Canada). *Tectonophysics*, *265*, 151–167.

Lister, G. S. & Baldwin, S. L. (1993). Plutonism and the origin of metamorphic core complexes. *Geology*, *21*(7), 607–610.

Luyendyk, B. P. (1970). Dips of downgoing lithospheric plates beneath island arcs. *Geological Society of America Bulletin*, *81*(11), 3411–3416.

Ma, Q., Zheng, J.-P., Xu, Y.-G., Griffin, W. L., & Zhang, R.-S. (2015). Are continental "adakites" derived from thickened or foundered lower crust? *Earth and Planetary Science Letters*, *419*, 125–133.

Mackasey, W. O., Blackburn, C. E., & Trowell, N. F. (1974). *A regional approach to the Wabigoon-Quetico belts and its bearing on exploration in northwestern Ontario*, vol. 58. Ontario Division of Mines.

MacKenzie, D. J. & Craw, D. (2007). Contrasting hydrothermal alteration mineralogy and geochemistry in the auriferous Rise Shine Shear Zone, Otago, New Zealand. *New Zealand Journal of Geology and Geophysics*, *50*, 67–79.

Marshak, S. (1999). Deformation style way back when: thoughts on the contrasts between Archean/Paleoproterozoic and contemporary orogens. *Journal of Structural*

Geology, *21*(8), 1175–1182.

Marshak, S. & Alkmim, F. (2012). Contrasting mechanisms for gneiss-dome formation in Precambrian dome-and-keel provinces: a record of evolving styles of crustal flows. In *Geological Society of America Abstract*. vol. 44, 70.

Marshak, S., Alkmim, F., & Jordt-Evangelista, H. (1992). Proterozoic crustal extension and the generation of dome-and-keel structure in an Archaean granite–greenstone terrane. *Nature*, *357*, 491–493.

Marshak, S., Tinkham, D., Alkmim, F., Brueckner, H., & Bornhorst, T. (1997). Dome-and-keel provinces formed during Paleoproterozoic orogenic collapse-core complexes, diapirs, or neither?: examples from the Quadrilátero Ferrífero and the Penokean orogen. *Geology*, *25*(5), 415–418.

Martin, H. (1999). Adakitic magmas: modern analogues of Archaean granitoids. *Lithos*, *46*(3), 411–429.

Martin, H., Smithies, R. H., Rapp, R., Moyen, J.-F., & Champion, D. (2005). An overview of adakite, tonalite–trondhjemite–granodiorite (TTG), and sanukitoid: relationships and some implications for crustal evolution. *Lithos*, *79*(1), 1–24.

Martínez-Martínez, J. M., Soto, J. I., & Balanyá, J. C. (2002). Orthogonal folding of extensional detachments: structure and origin of the Sierra Nevada elongated dome (Betics, SE Spain). *Tectonics*, *21*(3), 3–1.

McCuaig, T. C. & Kerrich, R. (1998). P—T—t—deformation—fluid characteristics of lode gold deposits: evidence from alteration systematics. *Ore Geology Reviews*, *12*(6), 381–453.

McDonough, W. F. & Sun, S.-S. (1995). The composition of the Earth. *Chemical Geology*, *120*(3), 223–253.

Melling, D. R., Blackburn, C. E., Watkinson, D. H., & Parker, J. R. (1988). Geological setting of gold, western Wabigoon Subprovince, Canadian Shield: exploration targets in mixed volcanic successions. *Canadian Journal of Earth Sciences*, *25*(12), 2075–2088.

Meneghini, F., Marroni, M., Moore, J. C., Pandolfi, L., & Rowe, C. D. (2009). The processes of underthrusting and underplating in the geologic record: structural diversity between the Franciscan Complex (California), the Kodiak Complex (Alaska) and the Internal Ligurian Units (Italy). *Geological Journal*, *44*(2), 126–152.

Micklethwaite, S. (2009). Mechanisms of faulting and permeability enhancement during epithermal mineralisation: Cracow goldfield, Australia. *Journal of Structural Geology*, *31*(3), 288–300.

Minnett, R. C. A. & Anhaeusser, R. C. (1992). Gravitational and diapiric structural history of the eastern portion of the Archaean Murchison greenstone belt, South Africa. *Journal of African Earth Sciences*, *15*(3/4), 429–440.

Mitchell, T. M., Ben-Zion, Y., & Shimamoto, T. (2011). Pulverized fault rocks and damage asymmetry along the Arima-Takatsuki Tectonic Line, Japan. *Earth and Planetary Science Letters*, *308*(3), 284–297.

Mitchell, T. M. & Faulkner, D. R. (2009). The nature and origin of off-fault damage surrounding strike-slip fault zones with a wide range of displacements: A field study from the Atacama fault system, northern Chile. *Journal of Structural Geology*, *31*(8), 802–816.

Moir, H., Lunn, R. J., Micklethwaite, S., & Shipton, Z. K. (2013). Distant off-fault damage and gold mineralization: The impact of rock heterogeneity. *Tectonophysics*, *608*, 461–467.

Moore, J. C., Cowan, D. S., & Karig, D. E. (1985). Structural styles and deformation fabrics of accretionary complexes. *Geology*, *13*(1), 77–79.

Morton, N., Girty, G. H., & Rockwell, T. K. (2012). Fault zone architecture of the San Jacinto fault zone in Horse Canyon, southern California: A model for focused post-seismic fluid flow and heat transfer in the shallow crust. *Earth and Planetary Science Letters*, *329*, 71–83.

Mungall, J. E. (2002). Roasting the mantle: slab melting and the genesis of major Au and Au-rich Cu deposits. *Geology*, *30*(10), 915–918.

Musacchio, G., White, D. J., Asudeh, I., & Thomson, C. J. (2004). Lithospheric structure and composition of the Archean western Superior Province from seismic refraction/wide-angle reflection and gravity modeling. *Journal of Geophysical Research: Solid Earth (1978–2012)*, *109*.

Neall, F. B. & Phillips, G. N. (1987). Fluid-wall rock interaction in an Archean hydrothermal gold deposit; a thermodynamic model for the Hunt Mine, Kambalda. *Economic Geology*, *82*(7), 1679–1694.

Newton, R. C., Wood, B. J., & Kleppa, O. J. (1981). Thermochemistry of silicate solid solutions. *Bulletin de Minéralogie*, *104*, 162–171.

Nisbet, E. G., Cheadle, M. J., Arndt, N. T., & Bickle, M. J. (1993). Constraining the potential temperature of the Archaean mantle: a review of the evidence from komatiites. *Lithos*, *30*(3), 291–307.

Osisko (2013). Executive summary: Hammond Reef gold project. Tech. rep., Osisko Mining Corporation.

Ota, T., Utsunomiya, A., Uchio, Y., Isozaki, Y., Buslov, M. M., Ishikawa, A., Maruyama, S., Kitajima, K., Kaneko, Y., Yamamoto, H., *et al.* (2007). Geology of the Gorny Altai subduction–accretion complex, southern Siberia: tectonic evolution of an Ediacaran–Cambrian intra-oceanic arc-trench system. *Journal of Asian Earth Sciences*, *30*(5), 666–695.

Park, R. G. (1981). Shear-zone deformation and bulk strain in granite-greenstone terrain of the Western Superior Province, Canada. *Precambrian Research*, *14*(1), 31–47.

Parmenter, A. C., Lin, S., & Corkery, M. T. (2006). Structural evolution of the Cross Lake greenstone belt in the northwestern Superior Province, Manitoba: implications for relationship between vertical and horizontal tectonism. *Canadian Journal of Earth Sciences*, *43*(7), 767–787.

Passchier, C. W. & Trouw, R. A. J. (2005). *Microtectonics*. Springer, 2 ed.

Percival, J. A. (1989). A regional perspective of the Quetico metasedimentary belt, Superior Province, Canada. *Canadian Journal of Earth Sciences*, *26*(4), 677–693.

Percival, J. A. (2007a). Eo- to Mesoarchean terranes of the Superior Province and their tectonic context. In M. J Van Kranendonk, R. H. Smithies, & V. C. Bennet

(Eds.), *Earth's Oldest Rocks*. vol. 15, Developments in Precambrian Geology, 1065–1085.

Percival, J. A. (2007b). Geology and metallogeny of the Superior Province, Canada. In W. D. Goodfellow (Ed.), *Mineral Deposits of Canada: A Synthesis of Major Deposit-Types, District Metallogeny, the Evolution of Geology Provinces, and Exploration Methods*. Geological Association of Canada, Mineral Deposits Devision, Special Publication No. 5, 903–928.

Percival, J. A. & Helmstaedt, H. (2004). Insights on Archean continent-ocean assembly, western Superior Province, from new structural, geochemical and geochronological observations: Introduction and summary. *Precambrian Research*, *132*, 209–212.

Percival, J. A., McNicoll, V., Brown, J. L., & Whalen, J. B. (2004). Convergent margin tectonics, central Wabigoon subprovince, Superior Province, Canada. *Precambrian Research*, *132*, 213–244.

Percival, J. A., Sanborn-Barrie, M., Skulski, T., Stott, G. M., Helmstaedt, H., & White, D. J. (2006). Tectonic evolution of the western Superior Province from NATMAP and Lithoprobe studies. *Canadian Journal of Earth Sciences*, *43*, 1085–1117.

Percival, J. A. & Williams, H. R. (1989). Late Archean Quetico accretionary complex, Superior province, Canada. *Geology*, *17*(1), 23–25.

Peschler, A. P., Benn, K., & Roest, W. R. (2004). Insights on Archean continental geodynamics from gravity modelling of granite–greenstone terranes. *Journal of Geodynamics*, *38*(2), 185–207.

Peterson, V. L. & Zaleski, E. (1999). Structural history of the Manitouwadge greenstone belt and its volcanogenic Cu-Zn massive sulphide deposits, Wawa subprovince, south-central Superior Province. *Canadian Journal of Earth Sciences*, *36*(4), 605–625.

Phillips, G. N. (1993). Metamorphic fluids and gold. *Mineralogical Magazine*, *57*, 365–374.

Phillips, G. N. & Evans, K. A. (2004). Role of CO_2 in the formation of gold deposits. *Nature*, *429*, 860–863.

Phillips, G. N. & Powell, R. (2010). Formation of gold deposits: A metamorphic devolatilization model. *Journal of Metamorphic Geology*, *28*(6), 689–718.

Piessens, K., Muchez, P., Dewaele, S., Boyce, A., De Vos, W., Sintubin, M., Debacker, T. N., Burke, E. A. J., & Viaene, W. (2002). Fluid flow, alteration and polysulphide mineralisation associated with a low-angle reverse shear zone in the Lower Palaeozoic of the Anglo-Brabant fold belt, Belgium. *Tectonophysics*, *348*(1), 73–92.

Pitcairn, I. K., Teagle, D. A. H., Craw, D., Olivo, G. R., Kerrich, R., & Brewer, T. S. (2006). Sources of metals and fluids in orogenic gold deposits: insights from the Otago and Alpine Schists, New Zealand. *Economic Geology*, *101*(8), 1525–1546.

Polat, A. (2012). Growth of Archean continental crust in oceanic island arcs. *Geology*, *40*(4), 383–384.

Polat, A., Appel, P. W. U., Fryer, B., Windley, B., Frei, R., Samson, I. M., & Huang, H. (2009). Trace element systematics of the Neoarchean Fiskenæsset anorthosite complex and associated meta-volcanic rocks, SW Greenland: evidence for a magmatic arc origin. *Precambrian Research*, *175*(1), 87–115.

Polat, A. & Kerrich, R. (1999). Formation of an Archean tectonic mélange in the Schreiber-Hemlo greenstone belt, Superior Province, Canada: Implications for Archean subduction-accretion process. *Tectonics*, *18*(5), 733–755.

Polat, A. & Kerrich, R. (2001). Geodynamic processes, continental growth, and mantle evolution recorded in late Archean greenstone belts of the southern Superior Province, Canada. *Precambrian Research*, *112*(1), 5–25.

Polat, A., Kerrich, R., & Wyman, D. A. (1998). The late Archean Schreiber-Hemlo and White River-Dayohessarah greenstone belts, Superior Province: collages of oceanic plateaus, oceanic arcs, and subduction-accretion complexes. *Tectonophysics*, *289*(4), 295–326.

Pollard, P. J., Taylor, R. G., & Peters, L. (2005). Ages of intrusion, alteration, and mineralization at the Grasberg Cu-Au deposit, Papua, Indonesia. *Economic Geology*, *100*(5), 1005–1020.

Ponce, C., Carreras, J., & Druguet, E. (2010). Development of "lozenges" in anastomosing shear zone networks in foliated rocks. *Geologia Estructural y Tectónica*, *48*, 207–210.

Poulsen, K. H., Robert, F., & Dubé, B. (2000). *Geological classification of Canadian gold deposits*. Geological Survey of Canada, Bulletin 540.

Ramberg, H. (1981). *Gravity, deformation, and the earth's crust: In theory, experiments, and geological application*. Academic press.

Ranganai, R. T. (2012). Gravity and aeromagnetic studies of the Filabusi greenstone belt, Zimbabwe Craton: Regional and geotectonic implications. *International Journal of Geosciences*, *3*(5), 1048–1064.

Rapp, R. P., Norman, M. D., Laporte, D., Yaxley, G. M., Martin, H., & Foley, S. F. (2010). Continent formation in the Archean and chemical evolution of the cratonic lithosphere: melt–rock reaction experiments at 3–4 GPa and petrogenesis of Archean Mg-diorites (sanukitoids). *Journal of Petrology*, *51*(6), 1237–1266.

Rawling, G. C., Goodwin, L. B., & Wilson, J. L. (2001). Internal architecture, permeability structure, and hydrologic significance of contrasting fault-zone types. *Geology*, *29*(1), 43–46.

Reimold, W. U. & Gibson, R. L. (2006). *Processes on the early Earth*, vol. 405. Geological society of America.

Rey, P. F., Philippot, P., & Thébaud, N. (2003). Contribution of mantle plumes, crustal thickening and greenstone blanketing to the 2.75–2.65 Ga global crisis. *Precambrian Research*, *127*(1), 43–60.

Richards, J. P. (2009). Postsubduction porphyry Cu-Au and epithermal Au deposits: Products of remelting of subduction-modified lithosphere. *Geology*, *37*(3), 247–250.

Ridley, J., Mikucki, E. J., & Groves, D. I. (1996). Archean lode-gold deposits: fluid flow and chemical evolution in vertically extensive hydrothermal systems. *Ore Geology Reviews*, *10*(3), 279–293.

Riller, U., Schwerdtner, W. M., Halls, H. C., & Card, K. D. (1999). Transpressive tectonism in the eastern Penokean orogen, Canada: Consequences for Proterozoic crustal kinematics and continental fragmentation. *Precambrian Research*, *93*(1), 51–70.

Robert, F. (1990). An overview of gold deposits in the Eastern Abitibi Subprovince. *Geological Survey of Canada, Contribution Series 44089*, *open file report*, 93–105.

Robert, F. (2001). Syenite-associated disseminated gold deposits in the Abitibi greenstone belt, Canada. *Mineralium Deposita*, *36*, 503–516.

Robert, F., Poulsen, K. H., Cassidy, K. F., & Hodgson, C. J. (2005). Gold metallogeny of the Superior and Yilgarn cratons. *Economic geology*, *100*, 1001–1033.

Robert, F., Poulsen, K. H., & Dubé, B. (1997). Gold deposits and their geological classification. In A. G. Gubins (Ed.), *Proceedings of Exploration*. Fourth Decennial International Conference on Mineral Exploration, vol. 97, 209–220.

Robin, C. M. I. & Bailey, R. C. (2009). Simultaneous generation of Archean crust and subcratonic roots by vertical tectonics. *Geology*, *37*(6), 523–526.

Rollinson, H. (2008). Secular evolution of the continental crust: Implications for crust evolution models. *Geochemistry, Geophysics, Geosystems*, *9*(12), 1–14.

Rollinson, H. (2009). *Early Earth systems: a geochemical approach*. Blackwell Publishing.

Savage, H. M. & Brodsky, E. E. (2011). Collateral damage: Evolution with displacement of fracture distribution and secondary fault strands in fault damage zones. *Journal of Geophysical Research: Solid Earth (1978–2012)*, *116*(B3), 1–14.

Schwerdtner, W. M. (1982). Salt stocks as natural analogues of Archean gneiss diapirs. *Geologiche Rundschau*, *71*(1), 370–379.

Schwerdtner, W. M. (1984). Foliation patterns in large gneiss bodies of the Archean Wabigoon Subprovince, southern Canadian shield. *Journal of Geodynamics*, *1*, 313–337.

Schwerdtner, W. M. (1990). Structural tests of diapir hypotheses in Archean crust of Ontario. *Canadian Journal of Earth Sciences*, *27*, 387–402.

Schwerdtner, W. M., Stone, D., Osadetz, K., Morgan, J., & Stott, G. M. (1979). Granitoid complexes and the Archean tectonic record in the southern part of northwestern Ontario. *Canadian Journal of Earth Sciences*, *16*, 1965–1977.

Shipton, Z. K. & Cowie, P. A. (2003). A conceptual model for the origin of fault damage zone structures in high-porosity sandstone. *Journal of Structural Geology*, *25*(3), 333–344.

Shirey, S. B. & Richardson, S. H. (2011). Start of the Wilson Cycle at 3 Ga shown by diamonds from subcontinental mantle. *Science*, *333*, 434–436.

Sibson, R. H. (1992). Implications of fault-valve behaviour for rupture nucleation and recurrence. *Tectonophysics*, *211*(1), 283–293.

Sibson, R. H. (2001). Seismogenic framework for hydrothermal transport and ore deposition. *Reviews in Economic Geology*, *14*, 25–50.

Sibson, R. H. (2003). Thickness of the seismic slip zone. *Bulletin of the Seismological Society of America*, *93*(3), 1169–1178.

Sibson, R. H., Robert, F., & Poulsen, K. H. (1988). High-angle reverse faults, fluid-pressure cycling, and mesothermal gold-quartz deposits. *Geology*, *16*(6), 551–555.

Sibson, R. H. & Scott, J. (1998). Stress / fault controls on the containment and release of overpressured fluids: Examples from gold-quartz vein systems in Juneau, Alaska; Victoria, Australia and Otago, New Zealand. *Ore Geology Reviews*, *13*, 293–306.

Sillitoe, R. H. (1991). Intrusion-related gold deposits. In R. P. Foster (Ed.), *Gold metallogeny and exploration*, Springer. 165–209.

Sillitoe, R. H. & Thompson, J. F. H. (1998). Intrusion-related vein gold deposits: Types, tectono-magmatic settings and difficulties of distinction from orogenic gold deposits. *Resource Geology*, *48*(4), 237–250.

Simmons, H. W., Pollard, P. J., Steward, J. L., Taylor, I. A., & Taylor, R. G. (1996). Granite hosted disseminated gold mineralisation at Timbarra, New South Wales. In *Mesozoic Geology of the eastern Australian plate conference*. 507–509.

Simpson, R. W. (1997). Quantifying Anderson's fault types. *Journal of Geophysical Research*, *102*(B8), 17909–17919.

Sleep, N. H. & Windley, B. F. (1982). Archean plate tectonics: Constraints and inferences. *Journal of Geology*, *90*(4), 363–379.

Smithies, R. H., Champion, D. C., & Cassidy, K. F. (2003). Formation of Earth's early Archaean continental crust. *Precambrian Research*, *127*(1), 89–101.

Soula, J.-C., Debat, P., Brusset, S., Bessière, G., Christophoul, F., & Déramond, J. (2001). Thrust-related, diapiric, and extensional doming in a frontal orogenic wedge: example of the Montagne Noire, Southern French Hercynian Belt. *Journal of Structural Geology*, *23*(11), 1677–1699.

Spence, W. (1987). Slab pull and the seismotectonics of subducting lithosphere. *Reviews of Geophysics*, *25*(1), 55–69.

Stern, R. J. (2005). Evidence from ophiolites, blueschists, and ultrahigh-pressure metamorphic terranes that the modern episode of subduction tectonics began in Neoproterozoic time. *Geology*, *33*(7), 557–560.

Stettler, E. H., de Beer, J. H., Eberle, D., Ludden, J., & Mareschal, M. (1997). Greenstone-belt boundaries, surrounding-rock terrains, and ther interrelations: Geophysics and deep structure. In M. J. de Wit & L. D. Ashwal (Eds.), *Greenstone Belts*, Oxford University Press, chap. 4.1. 339–375.

Stettler, E. H., Du Plessis, J. G., & De Beer, J. H. (1988). The structure of the Pietersburg greenstone belt, South Africa, as derived from geophysics. *South African Journal of Geology*, *91*(2), 292–303.

Stipp, M., Stünitz, H., Heilbronner, R., & Schmid, S. M. (2002). The eastern Tonale fault zone: A 'natural laboratory' for crystal plastic deformation of quartz over a temperature range from 250 to 700 °C. *Journal of Structural Geology*, *24*(12), 1861–1884.

Stone, D. (2008a). Precambrian geology, Atikokan Area, Preliminary Map P.3349-Revised. Tech. rep., Ontario Geological Survey.

Stone, D. (2008b). Precambrian geology, Sapawe Area, Preliminary Map P.3350-Revised. Tech. rep., Ontario Geological Survey.

Stone, D. (2010). Precambrian geology of the central Wabigoon subprovince area, northwest Ontario. Tech. Rep. Open File Report 5422, Ontario Geological Survey.

Stone, D. & Kamineni, D. C. (1989). Geology, Atikokan Area, Ontario, Map 1666A, scale 1:50 000. Tech. rep., Geological Survey of Canada.

Stone, D., Kamineni, D. C., & Jackson, M. C. (1992). Precambrian geology of the Atikokan Area, northwestern Ontario. Tech. Rep. Bulletin 405, Geological Survey of Canada.

Sun, W., Arculus, R. J., Kamenetsky, V. S., & Binns, R. A. (2004). Release of gold-bearing fluids in convergent margin magmas prompted by magnetite crystallization. *Nature*, *431*(7011), 975–978.

Thébaud, N., Philippot, P., Rey, P., & Cauzid, J. (2006). Composition and origin of fluids associated with lode gold deposits in a Mesoarchean greenstone belt (Warrawoona Syncline, Pilbara Craton, Western Australia) using synchrotron radiation X-ray fluorescence. *Contributions to Mineralogy and Petrology*, *152*(4), 485–503.

Thébaud, N. & Rey, P. F. (2013). Archean gravity-driven tectonics on hot and flooded continents: controls on long-lived mineralised hydrothermal systems away from continental margins. *Precambrian Research*, *229*, 93–104.

Thompson, J. F. H., Sillitoe, R. H., Baker, T., Lang, J. R., & Mortensen, J. K. (1999). Intrusion-related gold deposits associated with tungsten-tin provinces. *Mineralium Deposita*, *34*(4), 323–334.

Thurston, P. C., Osmani, I. A., & Stone, D. (1991). Northwestern Superior Province: review and terrane analysis. In P. C. Thurston, H. R. Williams, H. R. Sutcliffe, & G. M. Stott (Eds.), *Geology of Ontario*. Ontario Geological Survey, vol. 4, Part 1, 81–144.

Tomkins, A. G. (2013). On the source of orogenic gold. *Geology*, *41*(12), 1255–1256.

Tomlinson, K. Y., Davis, D. W., Stone, D., & Hart, T. R. (2003). U-Pb age and Nd isotopic evidence for Archean terrane development and crustal recycling in the south-central Wabigoon subprovince, Canada. *Contributions to Mineralogy and Petrology*, *144*, 684–702.

Tomlinson, K. Y., Hughes, D. J., Thurston, P. C., & Hall, R. P. (1999). Plume magmatism and crustal growth at 2.9 to 3.0 Ga in the Steep Rock and Lumby Lake area, Western Superior Province. *Lithos*, *46*, 103–136.

Tomlinson, K. Y., Stone, D., & Hattori, K. H. (2004). Basement terranes and crustal recycling in the western Superior Province: Nd isotopic character of granitoid and felsic volcanic rocks in the Wabigoon subprovince, N. Ontario, Canada. *Precambrian Research*, *132*, 245–274.

Tunks, A. J., Selley, D., Rogers, J. R., & Brabham, G. (2004). Vein mineralization at the Damang gold mine, Ghana: controls on mineralization. *Journal of structural geology*, *26*(6), 1257–1273.

Valli, F., Guillot, S., & Hattori, K. H. (2004). Source and tectono-metamorphic evolution of mafic and pelitic metasedimentary rocks from the central Quetico metasedimentary belt, Archean Superior Province of Canada. *Precambrian Research*, *132*(1), 155–177.

van Hunen, J. & Moyen, J.-F. (2012). Archean subduction: fact or fiction? *Annual Review of Earth and Planetary Sciences*, *40*, 195–219.

van Hunen, J., van Keken, P. E., Hynes, A., & Davies, G. F. (2008). Tectonics of early Earth: Some geodynamic considerations. In K. C. Condie & V. Pease (Eds.), *When Did Plate Tectonics Begin on Planet Earth?*, Geological Society of America, Special Paper 440. 157–171.

Van Kranendonk, M. J. (2011). Cool greenstone drips and the role of partial convective overturn in Barberton greenstone belt evolution. *Journal of African Earth Sciences*, *60*(5), 346–352.

Van Kranendonk, M. J. (2011). Onset of plate tectonics. *Science*, *333*, 413–414.

Van Kranendonk, M. J., Collins, W. J., Hickman, A., & Pawlay, M. J. (2004). Critical tests of vertical vs. horizontal tectonic models for the Archean East Pilbara granite-greenstone terrane, Pilbara Craton, Western Australia. *Precambrian Research*, *131*, 173–211.

Van Kranendonk, M. J., Hickman, A., Smithies, R. H., & Nelson, D. R. (2002). Geology and tectonic evolution of the Archean North Pilbara terrain, Pilbara Craton, Western Australia. *Economic Geology*, *97*, 695–732.

Van Staal, C. R., Currie, K. L., Rowbotham, G., Rogers, N., & Goodfellow, W. (2008). Pressure-temperature paths and exhumation of Late Ordovician–Early Silurian blueschists and associated metamorphic nappes of the Salinic Brunswick subduction complex, northern Appalachians. *Geological Society of America Bulletin*, *120*(11-12), 1455–1477.

Van Thienen, P., Vlaar, N. J., & Van den Berg, A. P. P. (2004). Plate tectonics on the terrestrial planets. *Physics of the Earth and Planetary Interiors*, *142*(1), 61–74.

Vannucchi, P., Fisher, D. M., Bier, S., & Gardner, T. W. (2006). From seamount accretion to tectonic erosion: Formation of Osa Mélange and the effects of Cocos Ridge subduction in southern Costa Rica. *Tectonics*, *25*(2), 1–19.

Vearncombe, J. R. (1998). Shear zones, fault networks, and Archean gold. *Geology*, *26*(9), 855–858.

Vlaar, N. J., Van Keken, P. E., & Van den Berg, A. P. (1994). Cooling of the Earth in the Archaean: consequences of pressure-release melting in a hotter mantle. *Earth and Planetary Science Letters*, *121*(1), 1–18.

Wang, J., Kusky, T. M., Polat, A., Wang, L., Deng, H., & Wang, S. (2013). A late Archean tectonic mélange in the Central Orogenic Belt, North China Craton. *Tectonophysics*, *608*, 929–946.

Ward, J. H. W. (1995). Geology and metallogeny of the Barberton greenstone belt: a survey. *Journal of African Earth Sciences*, *21*(2), 213–240.

Warren, C. J. (2013). Exhumation of (ultra-) high-pressure terranes: concepts and mechanisms. *Solid Earth*, *4*(1), 75–92.

Wasteneys, H. (2011). Report on Kabakong, Lynx Head Bay and Snail Bay Map Areas for Osisko Hammond Reef Gold Inc. Tech. rep., Hammond Reef Geological Mapping Programme 2010.

Watson, J. V. (1978). Precambrian thermal regimes. *Philosophical Transactions of the Royal Society of London. Series A, Mathematical and Physical Sciences*, *288*(1355), 431–440.

Whalen, J. B., Percival, J. A., McNicoll, V. J., & Longstaffe, F. J. (2002). A mainly crustal origin for tonalitic granitoid rocks, Superior Province, Canada: implications for late Archean tectonomagmatic processes. *Journal of Petrology*, *43*(8), 1551–1570.

White, D. J., Musacchio, G., Helmstaedt, H. H., Harrap, R. M., Thurston, P. C., Van der Velden, A., & Hall, K. (2003). Images of a lower-crustal oceanic slab: Direct evidence for tectonic accretion in the Archean western Superior province. *Geology*, *31*(11), 997–1000.

White, R. W., Powell, R., & Holland, T. (2007). Progress relating to calculation of partial melting equilibria for metapelites. *Journal of Metamorphic Geology*, *25*(5), 511–527.

White, R. W., Powell, R., Holland, T., & Worley, B. A. (2000). The effect of TiO_2 and Fe_2O_3 on metapelitic assemblages at greenschist and amphibolite facies conditions: mineral equilibria calculations in the system K_2O–FeO–MgO–Al_2O_3–SiO_2–H_2O–TiO_2–Fe_2O_3. *Journal of Metamorphic Geology*, *18*(5), 497–512.

White, S. H., Burrows, S. E., Carreras, J., Shaw, N. D., & Humphreys, F. J. (1980). On mylonites in ductile shear zones. *Journal of Structural Geology*, *2*(1), 175–187.

Whitney, D. L., Teyssier, C., Rey, P., & Buck, W. R. (2013). Continental and oceanic core complexes. *Geological Society of America Bulletin*, *125*(3-4), 273–298.

Wilks, M. E. & Nisbet, E. G. (1988). Stratigraphy of the Steep Rock Group, northwest Ontario: a major Archaean unconformity and Archaean stromatolites. *Canadian Journal of Earth Sciences*, *25*(3), 370–391.

Williams, H. R. (1990). Subprovince accretion tectonics in the south-central Superior Province. *Canadian Journal of Earth Sciences*, *27*(4), 570–581.

Williams-Jones, A. E., Bowell, R. J., & Migdisov, A. A. (2009). Gold in solution. *Elements*, *5*, 281–287.

Wilson, C. J. L., Robinson, J. A., & Dugdale, A. L. (2009). Quartz vein fabrics coupled to elevated fluid pressures in the Stawell gold deposit, south-eastern Australia. *Mineralium Deposita*, *44*(3), 245–263.

Xiao, W. J., Windley, B. F., Chen, H. L., Zhang, G. C., & Li, J. L. (2002). Carboniferous-Triassic subduction and accretion in the western Kunlun, China: Implications for the collisional and accretionary tectonics of the northern Tibetan Plateau. *Geology*, *30*(4), 295–298.

Xiong, X.-L. (2006). Trace element evidence for growth of early continental crust by melting of rutile-bearing hydrous eclogite. *Geology*, *34*(11), 945–948.

Yin, A. (2004). Gneiss domes and gneiss dome systems. In D. L. Whitney, C. Teyssier, & C. S. Siddoway (Eds.), *Gneiss domes in orogeny*. Geological Society of America, Special Papers 380, 1–14.

Yokokura, T. (1981). On subduction dip angles. *Tectonophysics*, *77*(1), 63–77.

Zegers, T. E., Nelson, D. R., Wijbrans, J. R., & White, S. H. (2001). SHRIMP U-Pb zircon dating of Archean core complex formation and pancratonic strike-slip deformation in the East Pilbara granite-greenstone terrain. *Tectonics*, *20*(6), 883–908.

Zegers, T. E. & van Keken, P. E. (2001). Middle Archean continent formation by crustal delamination. *Geology*, *29*(12), 1083–1086.

Zhu, Y., An, F., & Tan, J. (2011). Geochemistry of hydrothermal gold deposits: a review. *Geoscience Frontiers*, *2*(3), 367–374.

Appendix A - The composition of chlorite of the Finlayson Lake greenstone belt

Table 6–1: Chemical analyses of chlorite in samples collected throughout the Finlayson Lake greenstone belt used in Chapter 3. Locations separated into west, central and east Finlayson.

Name	MS002	MS004	MS004	MS004	MS004	MS008	MS008	MS017	MS017	MS017
Finlayson:	West	West	West	West	West	West	West	East	East	East
Element oxides (wt.%)										
Na2O	0.02	0.02	0.01	0.08	0.04	0.00	0.02	0.00	0.00	0.00
MgO	14.74	9.92	15.80	9.36	9.05	16.03	16.39	13.41	15.22	14.47
CaO	0.14	0.09	0.01	0.15	0.07	0.05	0.00	0.02	0.06	0.00
K2O	0.04	0.03	0.00	0.07	0.05	0.03	0.01	0.02	0.02	0.03
FeO	25.88	32.62	25.40	31.98	33.26	23.84	24.17	27.38	24.77	26.57
SiO2	26.67	24.50	24.95	25.94	25.17	25.31	25.37	24.07	25.56	24.92
Al2O3	19.86	20.89	21.41	19.72	21.11	19.95	19.78	22.52	19.90	21.86
Cr2O3	0.00	0.00	0.05	0.05	0.02	0.02	0.05	0.37	0.00	0.15
TiO2	0.03	0.09	0.04	0.31	0.02	0.08	0.07	0.02	0.02	0.02
MnO	0.38	0.27	0.22	0.22	0.25	0.26	0.27	0.02	0.06	0.03
Total	87.74	88.43	87.90	87.87	89.05	85.58	86.12	87.83	85.61	88.06

Name	MS023	MS023	MS023	MS023	MS023	MS023	MS023	MS023	MS023	MS023
Finlayson:	East	East	East	East	East	East	East	East	East	East
Element oxides (wt.%)										
Na2O	0.00	0.02	0.01	0.00	0.00	0.05	0.00	0.01	0.00	0.01
MgO	12.56	12.25	12.25	13.73	12.62	11.24	12.53	12.33	12.10	12.37
CaO	0.02	0.01	0.02	0.02	0.03	0.03	0.01	0.03	0.05	0.05
K2O	0.02	0.02	0.18	0.03	0.03	1.20	0.01	0.02	0.05	0.02
FeO	28.36	28.11	27.11	26.94	28.41	25.86	28.42	28.72	28.77	28.59
SiO2	23.92	23.96	23.78	24.37	23.88	26.35	23.90	23.44	23.67	23.88
Al2O3	22.81	22.66	22.19	22.53	22.67	23.97	22.93	23.11	22.97	22.80
Cr2O3	0.02	0.00	0.00	0.01	0.03	0.00	0.00	0.00	0.02	0.04
TiO2	0.05	0.04	0.05	0.03	0.02	0.06	0.06	0.03	0.01	0.01
MnO	0.13	0.11	0.15	0.12	0.15	0.11	0.11	0.12	0.13	0.13
Total	87.90	87.18	85.73	87.78	87.83	88.86	87.96	87.80	87.76	87.89

Name	MS023	MS023	MS027	MS027	MS027	MS027	MS027	MS027	MS027	MS027
Finlayson:	East	East	East	East	East	East	East	East	East	East
Element oxides (wt.%)										
Na2O	0.00	0.01	0.01	0.02	0.02	0.01	0.00	0.00	0.01	0.00
MgO	12.58	12.56	14.83	13.94	14.72	15.14	14.29	14.42	13.99	14.22
CaO	0.01	0.03	0.05	0.11	0.05	0.07	0.06	0.08	0.05	0.04
K2O	0.01	0.02	0.02	0.19	0.02	0.01	0.03	0.02	0.01	0.03
FeO	28.10	28.41	23.95	24.67	24.83	23.99	24.78	24.79	25.01	24.72
SiO2	23.98	24.06	25.23	24.66	24.71	25.33	24.23	24.62	24.25	24.47
Al2O3	22.50	22.75	22.66	23.60	23.62	22.59	23.46	23.46	23.32	23.14
Cr2O3	0.00	0.00	0.13	0.15	0.02	0.00	0.06	0.13	0.24	0.23
TiO2	0.04	0.01	0.03	0.06	0.03	0.03	0.02	0.01	0.00	0.04
MnO	0.13	0.12	0.08	0.04	0.06	0.08	0.07	0.05	0.07	0.08
Total	87.35	87.99	86.98	87.44	88.08	87.25	86.99	87.58	86.97	86.97

Name	MS027	MS032	MS032	MS032	MS032	MS032	MS032	MS032	MS032	MS032
Finlayson:	East	Central	Central	Central	Central	Central	Central	Central	Central	Central
Element oxides (wt.%)										
Na2O	0.01	0.00	0.00	0.00	0.00	0.02	0.00	0.01	0.00	0.00
MgO	14.11	23.68	23.11	22.31	19.34	21.30	24.01	23.90	23.66	24.46
CaO	0.10	0.04	0.00	0.04	0.00	0.03	0.03	0.04	0.01	0.03
K2O	0.01	0.01	0.02	0.03	0.01	0.02	0.00	0.02	0.01	0.03
FeO	24.76	13.34	14.31	14.73	18.85	16.77	13.43	13.46	13.87	12.57
SiO2	24.21	27.08	27.04	26.66	25.90	26.86	27.51	27.14	27.31	27.46
Al2O3	22.70	21.86	22.49	21.21	22.70	21.50	21.38	21.51	21.92	20.71
Cr2O3	0.23	0.07	0.22	0.74	0.36	0.05	0.16	0.41	0.17	0.78
TiO2	0.00	0.01	0.06	0.02	0.04	0.06	0.03	0.05	0.05	0.04
MnO	0.07	0.21	0.15	0.15	0.12	0.12	0.16	0.20	0.15	0.24
Total	86.21	86.30	87.40	85.87	87.32	86.72	86.72	86.73	87.16	86.31

Name	MS032	MS032	MS032	MS032	MS032	MS032	MS032	MS032	MS032	MS032
Finlayson:	Central	Central	Central	Central	Central	Central	Central	Central	Central	Central
Element oxides (wt.%)										
Na2O	0.02	0.01	0.00	0.00	0.01	0.03	0.01	0.02	0.00	0.01
MgO	21.96	17.16	23.27	21.19	23.47	22.73	24.44	16.57	21.10	23.14
CaO	0.03	0.08	0.06	0.07	0.01	0.03	0.04	0.06	0.00	0.04
K2O	0.01	0.02	0.01	0.02	0.02	0.02	0.01	0.01	0.03	0.02
FeO	15.55	20.53	13.81	15.73	13.64	13.81	12.99	21.27	16.70	13.99
SiO2	26.83	25.31	27.25	26.36	27.20	26.69	27.23	24.17	26.43	27.31
Al2O3	21.58	22.38	21.64	23.25	21.96	21.46	21.74	22.40	22.32	21.51
Cr2O3	0.00	0.30	0.26	0.19	0.16	0.29	0.22	0.39	0.36	0.20
TiO2	0.06	0.00	0.01	0.02	0.00	0.06	0.06	0.02	0.02	0.07
MnO	0.10	0.18	0.17	0.14	0.17	0.17	0.22	0.20	0.19	0.13
Total	86.13	85.96	86.47	86.95	86.64	85.29	86.95	85.12	87.13	86.43

Name	MS032	MS034	MS034	MS034	MS034	MS034	MS034	MS034	MS034	MS034
Finlayson:	Central	Central	Central	Central	Central	Central	Central	Central	Central	Central
Element oxides (wt.%)										
Na2O	0.00	0.01	0.00	0.00	0.00	0.00	0.00	0.03	0.00	0.00
MgO	19.65	18.25	18.48	18.50	18.44	18.35	18.19	17.89	18.21	18.33
CaO	0.04	0.05	0.45	0.06	0.08	0.04	0.02	0.03	0.03	0.04
K2O	0.03	0.02	0.02	0.01	0.01	0.01	0.00	0.02	0.02	0.02
FeO	18.54	20.69	20.20	20.52	20.65	21.03	21.02	21.21	20.69	20.97
SiO2	26.33	26.06	26.98	26.34	26.10	26.01	25.79	25.61	26.08	25.86
Al2O3	22.41	21.61	20.70	20.93	21.09	21.12	21.69	21.32	21.00	21.33
Cr2O3	0.41	0.07	0.07	0.14	0.04	0.01	0.06	0.06	0.05	0.05
TiO2	0.02	0.04	0.14	0.03	0.04	0.02	0.02	0.04	0.00	0.03
MnO	0.14	0.43	0.46	0.46	0.38	0.41	0.42	0.35	0.44	0.41
Total	87.56	87.23	87.50	86.98	86.82	87.00	87.21	86.55	86.54	87.05

Name	MS034	MS034	MS034	MS034	MS034	MS034	MS034	MS034	MS034	MS034
Finlayson:	Central	Central	Central	Central	Central	Central	Central	Central	Central	Central
Element oxides (wt.%)										
Na2O	0.00	0.00	0.00	0.01	0.01	0.02	0.00	0.01	0.00	0.01
MgO	18.68	18.38	18.24	18.28	18.30	18.40	18.88	18.53	18.71	18.04
CaO	0.02	0.02	0.01	0.07	0.07	0.04	0.07	0.08	0.09	0.04
K2O	0.02	0.02	0.01	0.03	0.00	0.01	0.00	0.00	0.01	0.01
FeO	20.36	20.97	21.12	20.67	20.47	20.87	20.51	20.93	20.18	21.10
SiO2	26.20	26.13	25.91	26.00	26.33	26.09	26.58	26.04	25.99	25.88
Al2O3	20.84	21.16	21.27	21.25	21.34	21.21	21.15	21.73	21.36	21.47
Cr2O3	0.05	0.06	0.09	0.03	0.10	0.06	0.14	0.10	0.10	0.10
TiO2	0.04	0.01	0.06	0.06	0.08	0.03	0.00	0.06	0.04	0.03
MnO	0.47	0.42	0.43	0.49	0.42	0.45	0.49	0.40	0.46	0.40
Total	86.68	87.19	87.15	86.88	87.13	87.17	87.83	87.88	86.95	87.07

Name	MS034	MS036	MS036	MS036	MS036	MS036	MS036	MS036	MS036	MS036
Finlayson:	Central	Central	Central	Central	Central	Central	Central	Central	Central	Central
Element oxides (wt.%)										
Na2O	0.00	0.01	0.00	0.01	0.00	0.00	0.01	0.01	0.00	0.02
MgO	18.14	19.63	19.45	19.68	20.08	20.13	20.01	19.77	20.00	19.60
CaO	0.03	0.13	0.07	0.09	0.08	0.09	0.16	0.08	0.03	0.78
K2O	0.03	0.02	0.01	0.03	0.03	0.02	0.02	0.02	0.03	0.02
FeO	20.91	20.04	20.02	19.97	19.70	19.87	19.65	19.38	19.43	19.57
SiO2	25.60	26.51	26.44	26.78	27.28	26.92	27.18	26.30	26.73	28.00
Al2O3	21.42	20.27	20.91	19.59	19.09	19.89	19.24	19.79	20.14	18.86
Cr2O3	0.10	0.22	0.14	0.09	0.08	0.11	0.81	1.22	0.58	0.54
TiO2	0.05	0.08	0.04	0.02	0.03	0.00	0.01	0.01	0.02	0.08
MnO	0.40	0.34	0.34	0.37	0.37	0.34	0.33	0.31	0.31	0.30
Total	86.69	87.24	87.43	86.64	86.73	87.37	87.41	86.89	87.27	87.76

Name	MS044	MS044	MS044	MS044	MS044	MS044	MS044	MS044	MS044	MS048
Finlayson:	West	West	West	West	West	West	West	West	West	East
Element oxides (wt.%)										
Na2O	0.00	0.00	0.01	0.00	0.01	0.01	0.01	0.02	0.00	0.00
MgO	14.63	14.30	15.05	15.17	16.14	16.77	14.79	15.30	14.94	17.74
CaO	0.08	0.07	0.07	0.07	0.06	0.04	0.12	0.08	0.11	0.05
K2O	0.02	0.02	0.03	0.01	0.01	0.01	0.02	0.01	0.01	0.02
FeO	26.42	26.33	25.94	25.98	24.61	23.67	26.42	25.08	25.53	21.88
SiO2	25.50	25.44	25.59	25.65	25.44	25.82	25.47	25.54	25.38	25.73
Al2O3	20.49	20.44	20.45	21.01	21.26	21.18	20.54	20.34	19.65	21.80
Cr2O3	0.00	0.02	0.05	0.06	0.04	0.04	0.03	0.07	0.01	0.12
TiO2	0.00	0.00	0.04	0.01	0.06	0.06	0.00	0.05	0.01	0.02
MnO	0.34	0.35	0.33	0.33	0.29	0.26	0.35	0.31	0.31	0.24
Total	87.48	86.97	87.55	88.29	87.91	87.86	87.74	86.78	85.95	87.59

Name	MS048	MS048	MS048	MS048	MS048	MS048	MS048	MS052	MS052	MS052
Finlayson:	East	East	East	East	East	East	East	Central	Central	Central
Element oxides (wt.%)										
Na2O	0.01	0.02	0.02	0.01	0.00	0.02	0.01	0.01	0.00	0.00
MgO	18.03	18.97	18.48	19.26	18.35	17.71	17.87	22.40	22.67	22.01
CaO	0.03	0.03	0.06	0.04	0.06	0.06	0.09	0.08	0.05	0.06
K2O	0.02	0.03	0.02	0.01	0.01	0.02	0.00	0.03	0.05	0.03
FeO	22.16	20.76	21.55	20.74	21.26	21.74	21.41	16.29	16.39	16.80
SiO2	25.75	26.27	26.44	27.07	26.07	25.72	25.39	28.14	28.06	26.98
Al2O3	21.60	20.12	20.55	19.42	21.08	21.50	21.47	18.39	19.96	19.40
Cr2O3	0.05	0.11	0.30	0.34	0.17	0.16	0.14	0.59	0.70	1.61
TiO2	0.03	0.03	0.04	0.05	0.04	0.02	0.04	0.02	0.03	0.03
MnO	0.26	0.25	0.22	0.23	0.26	0.25	0.25	0.18	0.15	0.17
Total	87.92	86.57	87.68	87.15	87.30	87.20	86.67	86.13	88.04	87.08

Name	MS052	MS054	MS054	MS054	MS054	MS054	MS054	MS054	MS054	MS054
Finlayson:	Central	East	East	East	East	East	East	East	East	East
Element oxides (wt.%)										
Na2O	0.01	0.01	0.00	0.01	0.00	0.01	0.00	0.01	0.00	0.00
MgO	23.27	19.18	18.63	18.58	19.35	19.61	18.29	19.15	18.17	18.55
CaO	0.07	0.05	0.11	0.06	0.08	0.03	0.04	0.05	0.05	0.04
K2O	0.07	0.02	0.01	0.02	0.02	0.01	0.02	0.02	0.02	0.04
FeO	15.59	20.45	20.52	20.51	20.23	20.26	21.03	20.62	21.01	20.84
SiO2	28.02	26.99	26.39	26.49	27.24	27.34	26.06	26.80	25.92	26.17
Al2O3	18.91	19.80	20.52	20.49	19.93	19.39	21.27	19.43	21.17	19.70
Cr2O3	0.37	0.27	0.15	0.27	0.14	0.15	0.18	0.36	0.35	0.14
TiO2	0.04	0.05	0.00	0.03	0.02	0.05	0.05	0.02	0.04	0.06
MnO	0.13	0.28	0.26	0.30	0.30	0.26	0.29	0.23	0.33	0.31
Total	86.49	87.10	86.58	86.76	87.33	87.11	87.24	86.68	87.05	85.84

Name	MS054	MS079	MS079	MS079	MS079	MS079	MS079	MS079	MS079	MS079
Finlayson:	East	Red Paint	Red Paint	Red Paint	Red Paint	Red Paint	Red Paint	Red Paint	Red Paint	Red Paint
Element oxides (wt.%)										
Na2O	0.01	0.00	0.00	0.00	0.00	0.00	0.00	0.00	0.02	0.02
MgO	18.02	13.06	13.67	13.71	13.07	13.27	13.73	13.76	13.71	12.60
CaO	0.07	0.04	0.02	0.05	0.07	0.06	0.04	0.04	0.08	0.06
K2O	0.01	0.02	0.03	0.02	0.01	0.02	0.04	0.02	0.02	0.01
FeO	20.90	29.00	28.89	28.72	28.82	28.93	28.38	28.43	28.41	29.32
SiO2	26.15	24.67	25.14	25.03	24.75	25.18	25.23	25.20	25.04	24.56
Al2O3	20.93	20.32	19.93	20.46	20.12	19.60	19.75	19.93	20.45	20.98
Cr2O3	0.12	0.00	0.01	0.00	0.00	0.00	0.01	0.00	0.02	0.00
TiO2	0.05	0.04	0.01	0.03	0.00	0.02	0.03	0.03	0.02	0.14
MnO	0.27	0.44	0.40	0.45	0.42	0.41	0.41	0.41	0.42	0.41
Total	86.53	87.58	88.11	88.47	87.26	87.49	87.62	87.81	88.18	88.10

Name	MS079	MS085	MS085	MS085	MS085	MS085	MS085	MS085	MS085	MS085	MS085
Finlayson:	Red Paint	East	East	East	East	East	East	East	East	East	East
Element oxides (wt.%)											
Na2O	0.00	0.00	0.00	0.00	0.02	0.01	0.03	0.05	0.05	0.10	0.06
MgO	14.56	13.70	14.26	13.58	14.18	13.58	14.10	13.99	14.47	13.34	14.25
CaO	0.06	0.06	0.04	0.03	0.43	0.08	0.19	0.14	0.05	0.06	0.10
K2O	0.04	0.01	0.02	0.02	0.02	0.01	0.05	0.07	0.07	0.05	0.06
FeO	27.89	28.23	27.10	27.52	27.51	27.92	27.42	27.44	27.30	27.68	27.28
SiO2	25.85	25.37	25.49	25.05	26.75	25.17	25.27	25.19	25.79	24.84	25.44
Al2O3	19.46	20.40	20.89	20.92	19.63	20.56	20.01	20.40	19.50	20.09	19.42
Cr2O3	0.01	0.06	0.16	0.04	0.05	0.02	0.02	0.01	0.01	0.00	0.02
TiO2	0.01	0.04	0.04	0.07	0.03	0.06	0.01	0.03	0.02	0.02	0.04
MnO	0.39	0.36	0.34	0.31	0.34	0.37	0.34	0.32	0.37	0.31	0.35
Total	88.26	88.22	88.32	87.55	88.96	87.78	87.45	87.63	87.62	86.48	87.02

Name	MS093	MS093	MS093	MS093	MS093	MS093	MS093	MS093	MS093	MS093	MS095
Finlayson:	West	West	West	West	West	West	West	West	West	West	Central
Element oxides (wt.%)											
Na2O	0.02	0.00	0.01	0.00	0.01	0.00	0.00	0.02	0.01	0.03	0.00
MgO	20.72	19.89	19.71	20.32	19.73	19.58	20.28	20.34	21.50	20.10	21.37
CaO	0.12	0.10	0.09	0.07	0.06	0.09	0.11	0.07	0.06	0.07	0.03
K2O	0.01	0.02	0.04	0.01	0.02	0.02	0.00	0.01	0.01	0.01	0.01
FeO	19.33	19.34	19.66	18.87	19.61	19.46	19.10	19.33	18.26	20.05	17.31
SiO2	27.90	27.05	26.62	26.91	26.61	26.39	27.29	27.44	28.27	27.11	27.24
Al2O3	17.76	17.82	17.90	18.71	19.25	19.08	18.30	18.48	17.78	18.18	19.62
Cr2O3	1.01	1.72	2.01	1.32	1.64	1.60	1.09	1.11	0.59	1.33	0.69
TiO2	0.07	0.03	0.02	0.05	0.03	0.06	0.05	0.06	0.06	0.03	0.05
MnO	0.15	0.14	0.17	0.14	0.16	0.12	0.15	0.16	0.14	0.15	0.21
Total	87.09	86.10	86.22	86.40	87.13	86.39	86.37	87.02	86.68	87.05	86.53

Name	MS095	MS095	MS095	MS095	MS095	MS095	MS095	MS095	MS095	MS099	MS099
Finlayson:	Central	Central	Central	Central	Central	Central	Central	Central	Central	Central	Central
Element oxides (wt.%)											
Na2O	0.00	0.01	0.01	0.00	0.00	0.01	0.00	0.01	0.01	0.00	0.03
MgO	19.25	21.64	21.00	21.02	21.53	20.81	20.79	21.26	20.57	15.10	14.27
CaO	0.06	0.09	0.02	0.07	0.07	0.08	0.08	0.09	0.09	0.04	0.08
K2O	0.02	0.04	0.03	0.02	0.31	0.02	0.02	0.02	0.02	0.02	0.04
FeO	17.13	17.50	18.66	17.90	17.59	18.16	18.42	17.61	18.40	24.64	25.04
SiO2	25.01	28.67	27.62	26.95	29.05	26.54	27.51	27.11	27.57	25.00	24.53
Al2O3	18.86	16.88	19.21	19.85	17.95	20.03	19.07	19.26	18.08	22.21	23.06
Cr2O3	0.73	0.66	0.61	0.56	0.61	0.75	0.66	0.49	0.76	0.19	0.21
TiO2	0.04	0.02	0.04	0.06	0.11	0.06	0.05	0.05	0.04	0.07	0.09
MnO	0.18	0.17	0.20	0.22	0.19	0.19	0.23	0.19	0.21	0.22	0.20
Total	81.27	85.66	87.40	86.65	87.39	86.64	86.81	86.08	85.76	87.48	87.54

Name	MS099	MS101	MS101	MS101	MS101	MS101	MS101	MS101	MS101	MS101	MS101
Finlayson:	Central	East	East	East	East	East	East	East	East	East	East
Element oxides (wt.%)											
Na2O	0.07	0.00	0.01	0.03	0.00	0.03	0.01	0.00	0.00	0.01	0.01
MgO	14.73	18.24	19.30	20.02	19.66	19.55	19.84	19.32	19.95	20.00	18.79
CaO	0.07	0.02	0.04	0.08	0.05	0.03	0.04	0.03	0.02	0.06	0.04
K2O	0.03	0.01	0.00	0.01	0.03	0.03	0.02	0.02	0.02	0.02	0.02
FeO	24.77	21.42	20.63	20.10	20.42	20.48	20.20	20.44	20.29	19.80	21.68
SiO2	25.23	25.86	26.67	26.64	26.52	26.54	26.81	26.72	27.00	26.81	25.81
Al2O3	22.30	20.58	19.75	19.67	19.29	18.91	18.86	19.09	19.20	18.52	21.33
Cr2O3	0.23	0.01	0.28	0.38	0.83	1.08	0.74	0.93	0.73	0.98	0.05
TiO2	0.09	0.01	0.03	0.00	0.01	0.03	0.07	0.00	0.00	0.01	0.02
MnO	0.23	0.36	0.32	0.37	0.33	0.34	0.31	0.33	0.35	0.31	0.32
Total	87.74	86.51	87.03	87.31	87.15	87.01	86.90	86.87	87.57	86.52	88.06

Appendix B - Major- and trace-element compositions of the Marmion gneiss and Diversion Stock

Table 6–2: Major and trace element concentrations of the Marmion Suite units (1 - porphyritic tonalite, 2 - very fine-grained tonalite, 3 - main Marmion tonalite), the Diversion Stock and altered tonalites from Hammond Reef (Hammond).

Sample	MS073	MS126	MS127	MS128	MS133	MS134	MS135	MS136	MS138
Unit	Marmion 3	Diversion	Diversion	Marmion 2	Diversion	Diversion	Marmion 3	Marmion 1	Marmion 1
Major element oxides (wt.%)									
SiO2	69.14	73.85	72.99	67.22	74.34	73.89	69.4	64.3	67.98
Al2O3	14.85	14.62	14.35	15.44	13.24	13.44	14.52	15.45	13.46
Fe2O3	4.46	1.39	2.14	4.81	1.92	1.69	2.94	3.72	3.54
MgO	1.31	0.24	0.37	1.29	0.37	0.33	0.68	1.27	1.26
CaO	2.07	1.97	2.26	4.37	1.8	1.82	2.52	3.54	3.28
Na2O	4.87	5.61	4.67	3.61	4.2	4.59	3.72	3.76	3.22
K2O	1.02	0.82	1.42	1.04	1.95	1.83	2.29	2.61	2.25
TiO2	0.46	0.09	0.15	0.48	0.15	0.15	0.27	0.37	0.39
P2O5	0.12	0.02	0.03	0.14	0.03	0.03	0.06	0.11	0.12
MnO	0.04	0.03	0.05	0.06	0.02	0.02	0.04	0.07	0.06
Cr2O3	<0.002	<0.002	<0.002	0.003	<0.002	<0.002	0.002	<0.002	<0.002
LOI	1.6	1.3	1.5	1.4	1.9	2.1	3.4	4.6	4.3
Total	99.9	99.96	99.9	99.86	99.88	99.9	99.88	99.86	99.9
Trace elements (ppm)									
Sc	5	2	3	7	<1	1	3	7	6
Ba	200	124	373	311	699	543	483	434	291
Be	2	<1	<1	<1	<1	<1	1	<1	<1
Co	5.8	1.6	2.2	8.1	6.5	2	4.7	8.7	8.2
Cs	0.3	0.3	0.5	0.3	0.7	0.5	0.7	1.2	1
Ga	16.3	15.1	15.9	16.5	12.3	11.8	15.2	16.2	14.4
Hf	6.4	2.2	3.6	5.9	2.9	3	4.3	3.2	3.5
Nb	5.6	5.4	9.9	7.1	2.5	1.7	7	5.9	6.1
Rb	28.6	23.6	39.3	27.8	45.4	38	58.4	61.7	54.1
Sn	<1	<1	2	1	<1	<1	1	1	1
Sr	183.7	204.1	254.9	286.8	227.9	200.1	166.3	266.2	198.5
Ta	0.2	0.4	1	0.3	0.3	0.1	0.6	0.9	0.8
Th	2.6	4.7	8.3	3.5	4.8	6.8	9.9	11.3	5.2
U	0.5	4.1	2.4	0.7	0.5	0.7	3	1.6	0.9
V	38	13	18	49	11	19	22	53	57
W	<0.5	<0.5	<0.5	<0.5	<0.5	<0.5	<0.5	0.5	0.8
Zr	289.3	73.4	115.7	237.7	89.8	96	174	109.7	131.3
Y	5.5	10.7	10.7	13.1	2.8	3.1	7.7	9	7.4
La	4.5	9	20.6	20.8	18.4	23.3	31	48.1	23.4
Ce	10.2	18.9	40.2	39.9	36	45.9	59.4	91.4	42.1
Pr	1.02	2.04	4.06	4.46	3.43	4.67	5.64	9.9	4.77
Nd	3.5	6.9	14.7	15.7	11	15	18.9	33.6	17.8
Sm	0.98	1.61	2.47	2.93	1.42	2.06	2.73	4.51	2.66
Eu	0.48	0.62	0.58	0.87	0.48	0.6	0.65	0.74	0.59
Gd	1.16	1.53	2.18	2.93	0.92	1.41	2.02	3.08	2.1
Tb	0.18	0.29	0.33	0.47	0.09	0.14	0.25	0.4	0.28
Dy	0.99	1.92	1.93	2.65	0.41	0.63	1.3	1.91	1.51
Ho	0.19	0.38	0.4	0.48	0.07	0.09	0.24	0.35	0.28
Er	0.55	1.32	1.04	1.22	0.25	0.29	0.78	0.86	0.75
Tm	0.08	0.21	0.18	0.18	0.05	0.05	0.12	0.12	0.12
Yb	0.37	1.29	1.31	1.22	0.28	0.34	0.76	0.9	0.76
Lu	0.06	0.2	0.2	0.16	0.06	0.07	0.12	0.13	0.11

Sample	MS073	MS126	MS127	MS128	MS133	MS134	MS135	MS136	MS138
Unit	Marmion 3	Diversion	Diversion	Marmion 2	Diversion	Diversion	Marmion 3	Marmion 1	Marmion 1
Carbon and Sulfur (wt. %)									
TOT/C	0.02	0.06	0.17	0.02	0.28	0.31	0.45	0.71	0.68
TOT/S	<0.02	<0.02	<0.02	<0.02	0.22	<0.02	<0.02	0.04	<0.02
Additional trace elements* (ppm)									
Mo	<0.1	0.2	0.2	0.2	0.2	0.2	0.3	<0.1	0.1
Cu	5.7	3.6	4.7	16.5	8.9	12.7	7.3	35.5	16.1
Pb	1.1	11.7	14.1	2.7	62.2	53.1	`	6.7	5.6
Zn	50	27	43	76	21	10	52	65	56
Ni	6.5	1.6	2.6	9.9	2.3	1.8	4.7	8.5	8.3
As	0.8	<0.5	1	9.9	2	1.5	<0.5	<0.5	<0.5
Cd	<0.1	<0.1	<0.1	<0.1	<0.1	<0.1	<0.1	<0.1	<0.1
Sb	<0.1	<0.1	<0.1	<0.1	<0.1	<0.1	<0.1	<0.1	<0.1
Bi	<0.1	<0.1	<0.1	<0.1	<0.1	<0.1	<0.1	<0.1	<0.1
Ag	<0.1	<0.1	<0.1	<0.1	<0.1	<0.1	<0.1	<0.1	<0.1
Au (ppb)	<0.5	<0.5	<0.5	<0.5	<0.5	<0.5	<0.5	<0.5	<0.5
Hg	<0.01	<0.01	<0.01	<0.01	<0.01	<0.01	<0.01	<0.01	<0.01
Tl	<0.1	<0.1	<0.1	<0.1	<0.1	<0.1	<0.1	<0.1	<0.1
Se	<0.5	<0.5	<0.5	<0.5	<0.5	<0.5	<0.5	<0.5	<0.5

Sample	MS142	MS143	MS144	MS147	MS152	MS156	MS157	MS161	MS165
Unit	Hammond	Hammond	Hammond	Marmion 3	Marmion 1	Hammond	Hammond	Hammond	Marmion 3
Major element oxides (wt.%)									
SiO2	75.15	72.06	63.96	68.47	66.32	65.67	57.91	67.35	71.16
Al2O3	13.69	13.41	14.06	15.11	15.39	15.3	14.71	15.51	14.42
Fe2O3	0.93	1.85	3.84	3.94	5.12	3.33	5.01	2.96	2.06
MgO	0.12	0.68	1.36	1.08	1.69	0.82	1.92	0.77	0.4
CaO	1.47	2.05	3.67	3.92	3.88	2.76	5.07	2.23	2.43
Na2O	4.47	2.74	2.7	3.9	3.57	3.1	2.49	2.34	4.53
K2O	1.99	2.96	3.41	1.27	1.42	3.6	3.89	4.15	2.01
TiO2	0.04	0.19	0.41	0.38	0.49	0.49	0.53	0.33	0.15
P2O5	<0.01	0.05	0.13	0.1	0.14	0.15	0.08	0.09	0.05
MnO	0.01	0.03	0.06	0.05	0.08	0.04	0.08	0.04	0.03
Cr2O3	<0.002	<0.002	<0.002	0.002	0.003	<0.002	<0.002	<0.002	<0.002
LOI	2.1	3.9	6.3	1.7	1.7	4.6	8.2	4.1	2.7
Sum	99.94	99.89	99.86	99.88	99.85	99.88	99.86	99.86	99.92
Trace elements (ppm)									
Sc	<1	2	7	6	8	4	11	5	2
Ba	438	694	556	360	249	512	425	619	304
Be	<1	<1	<1	<1	1	3	3	1	2
Co	0.8	3.2	8.4	7.1	10.7	5.5	14	4.8	4.3
Cs	0.4	0.6	1	0.3	0.4	1.4	1.4	1.4	0.5
Ga	12.5	13	14	16.7	16.3	19.6	15.6	18.6	14.8
Hf	2.5	2.2	2.9	4.5	3.9	4.7	3.4	5.1	3
Nb	2	2.8	4.5	6.6	6.3	8.4	5.1	9	4.4
Rb	37.7	63	75.9	30.9	47.6	81.7	94.3	95.9	44.8
Sn	<1	<1	<1	1	2	2	1	1	<1
Sr	116.3	132.9	193.1	232.2	262.5	125.7	137.2	82.6	174.3
Ta	0.2	0.3	0.6	0.5	0.7	0.7	0.6	0.3	0.4
Th	3.3	7.1	4.5	6.3	6.9	2.4	3.6	10.1	4
U	1.2	0.8	0.6	1.2	1.2	1	1	1	0.6
V	9	31	58	39	68	50	82	39	17
W	0.7	1.8	2.2	<0.5	<0.5	7.2	9.8	4.2	<0.5
Zr	53	69	113.2	189.5	152.1	211.5	131.1	213.6	109.8
Y	3.6	4.1	11	10	11.1	9.5	10.5	9.4	5.8
La	5.5	32.5	27.2	32.3	45.3	13.1	18.9	40.3	19.1
Ce	11.2	63.3	55.4	63.4	82.6	26.7	37.2	74.6	38.5
Pr	1.29	6.33	6.24	6.46	8.31	3	4.03	7.55	3.99
Nd	4.5	20.5	22.1	22	27.6	10.4	14.8	25.5	13.6
Sm	0.9	2.63	3.37	3.58	3.47	1.93	2.8	4.01	2.16
Eu	0.29	0.6	0.9	0.9	0.86	0.64	0.76	0.97	0.64
Gd	0.9	1.81	2.64	2.81	2.85	1.87	2.47	3	1.71
Tb	0.13	0.19	0.36	0.39	0.37	0.29	0.36	0.4	0.23
Dy	0.61	0.81	2.07	2.35	1.81	1.65	2.02	1.94	1.12
Ho	0.09	0.13	0.39	0.37	0.36	0.33	0.36	0.33	0.21
Er	0.33	0.35	1.09	1.01	1.1	0.87	1.03	1	0.57
Tm	0.05	0.05	0.16	0.14	0.15	0.14	0.17	0.13	0.09
Yb	0.35	0.35	0.96	0.98	1.05	0.96	1	0.86	0.5
Lu	0.06	0.06	0.14	0.14	0.15	0.12	0.14	0.16	0.08

Sample	MS142	MS143	MS144	MS147	MS152	MS156	MS157	MS161	MS165
Unit	Hammond	Hammond	Hammond	Marmion 3	Marmion 1	Hammond	Hammond	Hammond	Marmion 3
Carbon and Sulfur (wt. %)									
TOT/C	0.3	0.65	1.35	0.08	0.06	0.8	1.99	0.61	0.43
TOT/S	0.04	<0.02	0.07	<0.02	<0.02	0.06	0.08	0.19	0.11
Additional trace elements* (ppm)									
Mo	0.4	1.5	0.1	0.2	0.1	1.2	<0.1	1.7	0.2
Cu	4.3	4.1	16.5	30.3	105.3	27.4	47.1	20	79
Pb	14.6	4.1	2	6.2	6.4	2	2.9	4	24.5
Zn	8	11	24	62	85	18	35	22	35
Ni	1	1.7	3.3	10.3	11.4	1.2	5.8	1.6	2.3
As	<0.5	<0.5	<0.5	9.1	6.3	<0.5	<0.5	<0.5	<0.5
Cd	<0.1	<0.1	<0.1	<0.1	<0.1	<0.1	<0.1	<0.1	<0.1
Sb	<0.1	<0.1	<0.1	<0.1	<0.1	<0.1	<0.1	<0.1	<0.1
Bi	0.1	<0.1	<0.1	<0.1	<0.1	<0.1	<0.1	<0.1	<0.1
Ag	<0.1	<0.1	0.1	<0.1	0.3	0.1	<0.1	0.1	0.2
Au (ppb)	9.1	12.4	42.2	2.4	<0.5	101.8	37.1	146.6	12.6
Hg	<0.01	<0.01	<0.01	<0.01	<0.01	<0.01	<0.01	<0.01	<0.01
Tl	<0.1	<0.1	<0.1	<0.1	<0.1	<0.1	<0.1	<0.1	<0.1
Se	<0.5	<0.5	<0.5	<0.5	<0.5	<0.5	<0.5	<0.5	<0.5

Sample	MS167	MS173	MS175	MS176	MS178	MS180	MS188	MS190	MS203	MS204
Unit	Marmion 1	Hammond	Diversion	Marmion 1	Hammond	Hammond	Diversion	Marmion 3	Marmion 3	Marmion 3
Major elment oxides (wt.%)										
SiO2	65.78	59.68	75.77	62.41	59.69	67.71	72.43	61.23	63.98	64
Al2O3	15.94	15.98	13.71	16.76	14.36	14.67	13.96	16.67	16.9	14.85
Fe2O3	3.97	4.55	0.98	5.48	5.86	3.75	2.18	6.1	5.74	5.62
MgO	1.26	1.51	0.1	1.99	1.95	0.85	0.49	2.59	1.99	1.78
CaO	2.45	3.88	1.52	4.95	5.09	2.69	1.82	5.77	2.49	3.4
Na2O	3.56	2.7	5.93	3.98	3.03	3.78	4.34	3.46	3.88	2.95
K2O	2.51	4.08	0.81	1.22	2.15	2.26	1.95	1.54	1.94	2.29
TiO2	0.44	0.47	0.04	0.56	0.55	0.38	0.18	0.57	0.57	0.58
P2O5	0.09	0.14	<0.01	0.15	0.13	0.14	0.05	0.1	0.14	0.17
MnO	0.04	0.09	0.01	0.07	0.07	0.03	0.02	0.09	0.07	0.06
Cr2O3	<0.002	0.002	<0.002	<0.002	0.005	<0.002	<0.002	<0.002	<0.002	0.003
LOI	3.8	6.8	1.1	2.2	7	3.6	2.5	1.7	2.1	4.1
Sum	99.87	99.84	99.95	99.83	99.85	99.88	99.86	99.85	99.84	99.83
Trace elements (ppm)										
Sc	4	9	<1	9	12	4	2	13	8	9
Ba	464	676	222	254	284	393	796	316	447	492
Be	<1	1	1	<1	<1	<1	2	1	<1	3
Co	8	11.2	0.7	12.9	17	6.1	2.8	16.2	10.6	10.5
Cs	1	1.3	0.2	0.5	0.8	0.9	0.9	0.3	0.7	1
Ga	16	19.9	13.5	18.6	17.1	16.9	13.6	16.1	18.8	16.7
Hf	4.2	4.1	2.6	3.6	4	5	4.3	3.4	3.7	6.6
Nb	6.6	11	1.3	5.1	7.6	6.6	2.7	5.8	6.8	8.7
Rb	61.2	93.4	18.9	36.4	53	52.6	45.8	38.5	53.7	46.7
Sn	1	2	<1	1	1	1	<1	1	1	2
Sr	180.3	125	181.4	554.7	194.4	188.8	202.3	222.8	234.1	188.6
Ta	0.6	1.9	0.2	0.6	0.7	0.4	0.1	0.6	0.3	0.3
Th	6.9	8.4	4	2.5	1.7	5.2	11.4	3.3	5.8	5.7
U	1	3.2	1.7	0.6	0.8	0.6	0.9	0.9	0.3	0.5
V	63	73	20	88	102	38	14	102	78	69
W	1.9	6.9	<0.5	<0.5	3	3.4	<0.5	<0.5	1.2	<0.5
Zr	165	146.7	68.3	148.8	166.4	213.9	148.3	129.4	144	275
Y	6.4	16.3	6.2	10.3	15.8	6.7	5.2	12.2	7.8	20.6
La	26	34.4	9.8	13.6	17	17.5	34	15.8	21.1	41.4
Ce	50.4	65.1	20.8	27.2	36.9	33.7	60.1	30.8	44.4	90.7
Pr	4.9	6.85	2.33	3.34	4.21	3.74	5.68	3.15	4.55	9.77
Nd	16.6	22.8	9	14.3	16.9	13.7	18.4	11.9	15.3	34.3
Sm	2.28	3.57	1.74	2.53	3.24	2.38	2.77	2.24	2.4	5.53
Eu	0.58	0.91	0.58	0.87	0.89	0.49	0.61	0.71	0.59	1.15
Gd	1.89	3.23	1.77	2.41	3.24	2.08	2.09	2.29	2.06	5.05
Tb	0.25	0.49	0.23	0.35	0.5	0.27	0.25	0.38	0.31	0.74
Dy	1.17	2.73	1.23	1.92	3.02	1.41	1.26	2.39	1.68	3.85
Ho	0.21	0.48	0.21	0.36	0.53	0.27	0.18	0.49	0.29	0.71
Er	0.52	1.46	0.51	1.02	1.59	0.66	0.48	1.3	0.8	1.81
Tm	0.07	0.22	0.09	0.15	0.23	0.09	0.07	0.19	0.1	0.28
Yb	0.44	1.57	0.61	1.09	1.55	0.63	0.45	1.12	0.66	1.65
Lu	0.08	0.25	0.09	0.15	0.21	0.09	0.07	0.18	0.1	0.25

Sample	MS167	MS173	MS175	MS176	MS178	MS180	MS188	MS190	MS203	MS204
Unit	Marmion 1	Hammond	Diversion	Marmion 1	Hammond	Hammond	Diversion	Marmion 3	Marmion 3	Marmion 3
Carbon and Sulfur (wt. %)										
TOT/C	0.46	1.46	0.11	0.08	1.24	0.5	0.28	<0.02	<0.02	0.65
TOT/S	<0.02	0.56	<0.02	<0.02	0.04	<0.02	<0.02	<0.02	<0.02	0.02
Additional trace elements* (ppm)										
Mo	0.1	4.1	0.2	0.1	0.1	0.2	0.1	0.4	0.2	0.2
Cu	26.5	21.5	4.2	32.2	158.5	6.7	9.7	44.2	24.5	26.8
Pb	2.5	4.7	8.9	3.6	4	2.2	7.8	2.1	2.5	1.2
Zn	67	26	7	67	119	64	25	49	97	67
Ni	8.8	6.5	1.2	14.1	21.2	3.5	3.8	18.3	12.3	9.4
As	<0.5	<0.5	0.6	3.9	<0.5	<0.5	0.6	0.7	2.8	<0.5
Cd	<0.1	<0.1	<0.1	<0.1	0.1	<0.1	<0.1	<0.1	<0.1	<0.1
Sb	<0.1	<0.1	<0.1	<0.1	<0.1	<0.1	<0.1	<0.1	<0.1	<0.1
Bi	<0.1	0.2	<0.1	<0.1	<0.1	<0.1	<0.1	<0.1	<0.1	<0.1
Ag	<0.1	0.6	<0.1	<0.1	0.2	<0.1	<0.1	<0.1	<0.1	<0.1
Au (ppb)	3.4	1573.2	3.4	1.2	3.4	<0.5	<0.5	<0.5	0.6	<0.5
Hg	<0.01	<0.01	<0.01	<0.01	<0.01	<0.01	<0.01	<0.01	<0.01	<0.01
Tl	<0.1	<0.1	<0.1	<0.1	<0.1	<0.1	<0.1	<0.1	<0.1	<0.1
Se	<0.5	<0.5	<0.5	<0.5	<0.5	<0.5	<0.5	<0.5	<0.5	<0.5

Sample	MS221	MS224	MS225	MS230	MS232	MS235	MS238
Unit	Diversion	Marmion 3	Marmion 3	Marmion 3	Marmion 3	Marmion 3	Diversion
Major element oxides (wt.%)							
SiO2	66.75	70.54	70.1	71.82	71.99	71.16	68.74
Al2O3	16.31	14.98	15.03	14.57	14.54	14.07	14.93
Fe2O3	2.35	2.72	3.73	2.74	2.96	2.44	3.53
MgO	1.24	0.65	0.99	0.48	0.64	0.54	1.11
CaO	2.11	2.34	2.52	2.2	2.6	2.34	3.41
Na2O	3.24	4.4	4.26	4.11	4.95	4.16	3.96
K2O	3.91	1.71	1.45	2.74	0.72	1.99	1.96
TiO2	0.28	0.24	0.39	0.2	0.28	0.23	0.35
P2O5	0.1	0.06	0.12	0.09	0.1	0.08	0.12
MnO	0.05	0.05	0.05	0.05	0.04	0.03	0.06
Cr2O3	<0.002	0.002	<0.002	<0.002	<0.002	<0.002	<0.002
LOI	3.5	2.2	1.2	0.9	1	2.8	1.6
Sum	99.81	99.86	99.86	99.84	99.86	99.85	99.8
Trace elements (ppm)							
Sc	3	3	5	3	2	3	6
Ba	657	394	308	538	284	509	615
Be	<1	<1	<1	<1	<1	<1	<1
Co	2.6	2.9	4.7	2.1	3.6	3.3	6.7
Cs	1.3	0.4	0.5	0.3	<0.1	0.3	0.5
Ga	21.9	17.2	17.3	15.4	15.9	14.8	14.7
Hf	4.4	4	4.1	2.9	4.9	3.4	3.2
Nb	7.2	7.9	5.9	8.5	7.2	5.1	4.9
Rb	134.3	56.2	42.5	44.1	15.8	39	49.8
Sn	1	2	1	1	1	<1	<1
Sr	185.7	208.4	173.7	157.6	187.4	172.3	397.9
Ta	1.1	0.9	0.4	1	1	0.4	0.5
Th	11.8	9	3.1	7.3	7.6	4.6	7.4
U	1.8	2.2	0.8	1.1	1.1	0.6	0.8
V	34	23	37	16	26	23	48
W	1.3	<0.5	<0.5	<0.5	<0.5	<0.5	<0.5
Zr	157.4	128.6	158.9	99.8	163.6	120.5	112.7
Y	9	13.3	8.7	8.5	8.4	5.7	10.3
La	61.1	24.7	16.3	24.8	30.3	21	36.2
Ce	110.7	48.3	36.1	54	65.3	41.5	69
Pr	11.75	5.38	3.79	6.22	6.99	4.47	7.58
Nd	37.7	17.8	13.2	21.6	23.9	14.9	25
Sm	4.12	3.22	2.72	3.64	3.65	2.56	3.92
Eu	1.14	0.67	0.76	0.89	0.89	0.66	0.9
Gd	3.19	2.66	2.23	2.42	2.63	1.9	2.8
Tb	0.3	0.41	0.32	0.31	0.34	0.25	0.39
Dy	1.32	2.21	1.67	1.6	1.66	1.22	1.81
Ho	0.26	0.45	0.35	0.3	0.28	0.2	0.37
Er	0.86	1.37	0.88	0.84	0.77	0.52	1.05
Tm	0.14	0.23	0.12	0.14	0.12	0.07	0.15
Yb	1.1	1.45	0.81	0.86	0.79	0.52	0.95
Lu	0.18	0.22	0.12	0.13	0.13	0.08	0.15

Sample	MS221	MS224	MS225	MS230	MS232	MS235	MS238
Unit	Diversion	Marmion 3	Marmion 3	Marmion 3	Marmion 3	Marmion 3	Diversion
Carbon and Sulfur (wt. %)							
TOT/C	0.44	0.12	<0.02	<0.02	<0.02	0.42	0.05
TOT/S	<0.02	<0.02	<0.02	<0.02	<0.02	<0.02	<0.02
Additional trace elements* (ppm)							
Mo	0.1	0.2	0.2	0.2	0.2	0.1	0.1
Cu	5.2	5	8.8	5.4	4.8	5.6	10.6
Pb	3.1	6.2	1.7	5.4	3.2	3	4.8
Zn	25	41	55	51	51	38	37
Ni	2.5	4.5	4.6	2.8	3.4	2.5	7.7
As	1.4	1	0.7	1.9	0.8	5.5	0.7
Cd	<0.1	<0.1	<0.1	<0.1	<0.1	<0.1	<0.1
Sb	<0.1	<0.1	<0.1	<0.1	<0.1	<0.1	<0.1
Bi	<0.1	<0.1	<0.1	<0.1	<0.1	<0.1	<0.1
Ag	<0.1	<0.1	<0.1	<0.1	<0.1	<0.1	<0.1
Au (ppb)	1.3	1	<0.5	<0.5	<0.5	<0.5	<0.5
Hg	<0.01	<0.01	<0.01	<0.01	<0.01	<0.01	<0.01
Tl	<0.1	<0.1	<0.1	<0.1	<0.1	<0.1	<0.1
Se	<0.5	<0.5	<0.5	<0.5	<0.5	<0.5	<0.5